A MULTI-WAVELENGTH STUDY OF MASSIVE STAR FORMING REGION G188.95+0.89 IN PROBING THE DYNAMICS OF MASSIVE STAR FORMATION

MARTIN MULE MUTIE

B.Ed (Egerton), MSc.(KU)

SPPZ/06529P/2016

A Thesis Submitted in Partial Fulfilment of the Requirements for the Award of the Degree of Doctor of Philosophy in Physics

in

School of Physics and Earth Sciences

of

The Technical University of Kenya

(November, 2023)

DECLARATION

This thesis is my original work and has not been presented in any other institution for a degree award or other qualification.

MUTIE MARTIN MULE
REG NO. SPPZ/06529P/2016

Signature ——————————— Date ———————————

This thesis has been submitted with our approval as Supervisors:

Signature ——————————— Date ———————————

PROF. PAUL BAKI
PROFESSOR OF PHYSICS
THE TECHNICAL UNIVERSITY OF KENYA

Signature ——————————— Date ———————————

PROF. JAMES. O. CHIBUEZE
PROFESSOR OF ASTRONOMY AND ASTROPHYSICS
UNIVERSITY OF SOUTH AFRICA

Signature ——————————— Date ———————————

DR. KHADIJA EL BOUCHEFRY
RESEARCH FELLOW
HARTEBEESTHOEK RADIO ASTRONOMY OBSERVATORY
SOUTH AFRICA

DEDICATION

The time that a few people contributed to improving my knowledge of the formation of stars helped make it possible for me to complete the work that is contained in this PhD thesis. I would want to thank everyone who helped me in any way, be it monetarily or academically, and dedicate this dissertation to all of you. Special thanks to my dear wife Juster Muthoni Mule, to my Daughter- Anna Mumo Mule, to my Son- Eliud Mwendwa Mule, to my late mum Veronicah Kalenzele Mutie who passed on in 2023 and to my late Dad Naftali Mutie Nzomi who passed on in 2019. I really appreciate all the help and consideration you've given me over the years.

ACKNOWLEDGEMENTS

I would like to thank my supervisors Prof. Paul Baki, Dr. Khadija El Bouchefry and Prof. James.O. Chibueze for accepting me as their student. Khadija and other trainers at Hartebeesthoek Radio observatory (HartRAO) introduced me to methanol masers during Development in Africa with Radio Astronomy (DARA) training in 2016 and instilled in me a deep interest in these strange but wonderful objects. High tech skills using radio astronomy in a number of African countries will be developed by the DARA project.

I especially have to thank Prof. Chibueze for facilitang me to travel from Kenya to North West University in Potchefstroom to have an in-depth discussion with him on milimeter/submillimeter data reduction and imaging. I knew nothing about radio astronomy when I started at DARA training in Hartebeesthoek, but supervisors patiently guided me through the process of data reduction, imaging and reducing spectra. Prof Baki has been encouraging me to keep working hard despite enormous amount of data reduction and imaging. Special thanks to all my supervisors, whom despite their busy schedule, have always taken time to support and guide me in my research. Special appreciation to Dr. Gordon MaCleod of HartRAO for training me on radio data reduction using the lines software. You sacrificed your time to better my life and I appreciate it so much. I also want to render my appreciation to my late Mom (Mrs Mutie), Wife (Juster) and children (Anna and Eliud) for their encouragement, support and love throughout this amazing journey.

Thanks to all my siblings and friends for their support throughout. To name few, Juma and Obonyo, you guys were always there for a chat to lift my spirit when I was down. I would like to acknowledge the ALMA for use of data ADS/JAO. ALMA 2015.101454.S that can be accessed on the ALMA Science portal. ALMA is a partnership of ESO (representing its member states), NSF (USA) and NINS (Japan), together with NRC (Canada), MOST and ASIAA (Taiwan), and KASI (Republic of Korea), in cooperation with the Republic of Chile. The Joint ALMA Observatory is

operated by ESO, AUI/NRAO and NAOJ. Special thanks to HartRAO,for use of data products of the 26m single dish maser monitoring project. This paper made use of information from the Red MSX Source survey database at www.ast.leeds.ac.uk/RMS which was constructed with support from the Science and Technology Facilities Council of the UK. This research made use of Montage, funded by the National Aeronautics and Space Administration's Earth Science Technology Office, Computation Technologies Project, under Cooperative Agreement Number NCC5-626 between NASA and the California Institute of Technology. Montage is maintained by the NASA/IPAC Infrared Science Archive. This research has made use of NASA's Astro-physics Data System Bibliographic Services and the SIMBAD database operated at CDS, Strasbourg, France. Special appreciation to the the National Research Foundation (NRF) South Africa for their financial support that helped me to do my research to completion. Thank you all of you for your time in shaping my future, I highly appreciate it and it was a wonderful experience.

TABLE OF CONTENTS

DECLARATION ii
DEDICATION iii
ACKNOWLEDGEMENTS iv
LIST OF TABLES ix
LIST OF FIGURES x
ABBREVIATIONS xii
ABSTRACT xiii

1 INTRODUCTION **1**
1.1 OVERVIEW OF STAR FORMATION 2
1.2 PROBLEM STATEMENT 5
1.3 OBJECTIVES 6
1.3.1 Main Objective 6
1.3.1.1 Specific Objectives 6
1.4 MOTIVATION OF THE STUDY 7

2 THEORY AND LITERATURE REVIEW **8**
2.1 LOW AND INTERMEDIATE - MASS STAR FORMATION 8
2.2 HIGH - MASS STAR FORMATION 9
2.3 GIANT MOLECULAR CLOUDS 12
2.3.1 GMCs Formation 13
2.3.2 Criterion For a Molecular Cloud to Collapse 15
2.3.3 Stellar Initial Mass Function 19
2.4 HIGH MASS STAR EVOLUTIONARY SEQUENCE 21
2.4.1 Infra-Red Dark Clouds and Filaments 22
2.4.2 High-Mass Protostellar Objects (HMPOs) 23
2.4.3 Hot Molecular Cores (HMCs) 24
2.4.4 HII Regions 25
2.4.5 Maser-Based Evolutionary Timeline 28
2.5 THEORIES OF THE FORMATION OF MASSIVE STARS 29
2.5.1 Core Accretion 30
2.5.2 Competitive Accretion Model 31
2.5.3 Stellar Collisions and Mergers 32
2.6 MASER THEORY 33
2.6.1 Rate Equations 34
2.6.2 Population Inversion 36
2.6.3 Maser Saturation 39
2.6.4 Radiative Transfer in Masers 40
2.7 ASTROPHYSICAL MASERS 40
2.8 METHANOL MASERS 45
2.8.1 Class I Methanol Masers 46
2.8.2 Class II Methanol Masers 48
2.8.3 6.7 GHz Methanol Masers 49
2.8.4 Methanol Molecular Structure 50

2.9 MASER VARIABILITY 51
2.9.1 Stochastic variations and flares 52
2.9.2 Periodic variation 54
2.9.3 Origin of the Periodic Variability in Methanol Masers 56
2.9.4 Masers as Evolutionary Probes of MSF 58

3 METHODOLOGY 60
3.1 DESCRIPTION OF RADIO TELESCOPES 60
3.1.1 Single Dish 61
3.2 SINGLE DISH OBSERVATION 61
3.2.1 Receivers 61
3.3 HartRAO 26 m TELESCOPE INSTRUMENTATION AND SIGNAL PROCESSING 63
3.4 THE HartRAO OBSERVATIONS 64
3.4.1 The Drift Scan 64
3.4.2 The 26-m HartRAO Telescope Calibration 66
3.4.2.1 Pointing Offset Correction 66
3.4.2.2 Calibration of a 4.5 cm receiver 69
3.4.3 Calibrating Continuum Drift Scans 69
3.4.3.1 Flux Density Calibration 70
3.4.3.2 6.7 GHz receiver point source sensitivity 71
3.4.3.3 Baseline and Amplitude Correction 72
3.4.4 Frequency to Velocity Conversion 73
3.4.5 Bandpass Correction 74
3.5 RADIO DATA REDUCTION PROCESSES 75
3.6 MASER SLECTION 76
3.7 RADIO INTERFEROMETRIC OBSERVATIONS 77
3.7.1 Interferometer Basics 77
3.7.2 The Two Element Interferometer 78
3.7.3 Radio Interferometric Imaging 80
3.8 BASELINES AND U-V COVERAGE 81
3.9 SUB-MILLIMETER INSTRUMENTATION 82
3.9.1 Submillimeter Observations 83
3.9.2 Sub-millimeter Data Calibration and Reduction 86
3.9.3 Calibration 87
3.9.3.1 Bandpass calibration 88
3.9.3.2 Gain Calibration (gaincal) 88
3.9.3.3 Time-dependent Phase/Amplitude Calibration 89
3.9.3.4 Imaging the complex visibilities 89
3.10 INFRARED OBSERVATIONS 90
3.11 INFRARED INSTRUMENTATION 91
3.11.1 Near Infrared Image Archives 92
3.11.2 Mid- and Far-infrared Image Archives 92

4 RESULTS AND DISCUSSION 94
4.1 SINGLE DISH RADIO RESULTS 94
4.1.1 Variability of the 6.7 GHz CH_3OH Maser Features 94

4.1.2 Time Series and Light curves of Maser components in 2D Contour Form . . . 100
4.1.3 Maser velocity drifts . . . 102
4.2 RADIO INTERFEROMETRIC RESULTS . . . 103
4.2.1 G188.95+0.89 Continuum Emission . . . 103
4.2.2 G188.95+0.89 Millimeter Line Emmission . . . 106
4.2.3 Main Morphological Features of G188.95+0.89 . . . 116
4.2.4 Molecular Outflows . . . 116
4.3 INFRARED RESULTS . . . 122
4.3.1 Dust emission . . . 122
4.3.2 Color–Color Diagrams . . . 123
4.3.3 Color-Magnitude Diagrams . . . 125
4.3.4 Spatial Distribution of YSOs and Cool Red Sources . . . 126
4.3.5 Mid-infrared data . . . 127
4.3.6 Counterparts at Other Wavelengths . . . 128
4.3.7 Methanol Masers and Star Formation Tracers . . . 130
4.3.8 Infrared Sources Coincident with Methanol Masers . . . 131
4.3.9 Results from the Point Source Catalogues . . . 132
4.4 DISCUSSION OF RESULTS . . . 133
4.4.1 Radio Results . . . 133
4.4.1.1 Methanol Maser Variability Implications . . . 133
4.4.2 Interferometric Results . . . 136
4.4.2.1 Binary System of G188.95+0.89-MM2 . . . 136
4.4.3 Infrared Results . . . 136

5 CONCLUSIONS 139
5.1 SUMMARY . . . 139
5.2 FUTURE RESEARCH PROSPECTS . . . 140

REFERENCES 142

A APPENDICES 173
A.1 FUNDAMENTALS OF A SINGLE DISH RADIO TELESCOPE . . . 173
A.1.1 Single Dish Radio Telescope . . . 173
A.1.2 Single-dish observing techniques . . . 175
A.1.3 RCP and LCP of G188.95+0.89 Before Addition . . . 176
A.2 FUNDAMENTALS OF INTERFEROMETRIC OBSERVATIONS . . . 177
A.2.1 Baselines and U-V Coverage . . . 177
A.2.2 Sub-millimeter Instrumentation . . . 178
A.2.3 Processing radio signals with the ALMA . . . 179
A.2.4 Frequency bands of receivers . . . 180
A.2.5 Zero Moment Maps of Some Detected Molecular Lines . . . 181
A.2.6 Spectra of Some Detected Molecular Lines lines . . . 182
A.3 Publication-2019 . . . 183
A.4 Publication-2021 . . . 184
A.5 Plagiarism Report . . . 185

LIST OF TABLES

2.1 Classes of Galactic molecular clouds. 13
2.2 Physical properties of the ionised hydrogen regions. 26
2.3 Some masing transitions in Class I and II methanol masers. 48
2.4 Periods Of Periodic Methanol Masers. 55

3.1 Specifications for the HartRAO 26-m telescope. 62
3.2 Average point source sensitivity values 72
3.3 Monitored sources linked with class II methanol masers. 77
3.4 Basic specifications for the ALMA Telescope 84
3.5 ALMA Observational Parameters. 86

4.1 Details of each five selected 6.7 GHz maser features. 100
4.2 Parameters of the detected dust cores. 106
4.3 Parameters of observed molecular species. 115
4.4 List of detected species in G188.95+0.89 115
4.5 Note. Columns are lobes, mass(M), momentum(P), kinetic energy(E), P/M ratio. 120
4.6 Counterparts to the methanol maser sample in IRAS, MSX, and NVSS sources catalogs 130
4.7 Presence or absence of counterparts 130
4.8 Distances between methanol masers and other objects. 131
4.9 Presence and absence of infrared sources coincicent with masers IRAS, MSX 132
4.10 Methanol masers, MSX, and IRAS flux densities in Jy. 132

A.1 Specifications of individual ALMA receivers. 180

LIST OF FIGURES

1.1 Protostars formation from molecular clouds (Christensen 2019). . . . 3
1.2 Protostar formation starting from dense core (Christensen 2019) . . . 4
1.3 The birth of new stars begins in a dense concentration of protostars within a molecular cloud (Christensen 2019). 5

2.1 A massive star showing core fusion processes. 11
2.2 HR diagram showing stellar evolutionary model. 12
2.3 The Eagle Nebula molecular. 14
2.4 Plot of various initial mass functions (IMF). 20
2.5 The schematic HII region (Deharveng et al. 2010) 25
2.6 Evolutionary sequence for masers associated with massive star formation regions (Breen et al. 2010) 29
2.7 A schematic two level system with energy ΔE. 35
2.8 A schematic of a three energy level model. 37
2.9 CH_3OH asymmetric top molecular structure 51

3.1 Examples of antenna reflector designs. 61
3.2 Elevation of HartRAO The 26-m telescope. 63
3.3 Image of HartRAO radio telescope dish. 64
3.4 A second-order polynomial fit to the peak of the source. 65
3.5 Pointing observation of the G188.95+0.89 maser source. 67
3.6 Fitting the peak power measured at the half-power points. 67
3.7 Schematic diagram for (4.5-cm) radio receiver. 69
3.8 Pointing correction factor applied to the peak amplitude. 73
3.9 Spectra of each polarisation for the frequency switched pair of the maser. 75
3.10 Illustration of a basic two-dish interferometer. 78
3.11 A graphical illustration of Deconvolution principle. 81
3.12 Imaging of the continuum 82
3.13 ALMA array. 84
3.14 The classification of low mass protostellar. 91

4.1 Spectrum of the 6.7 GHz methanol masers in G188.95+0.89. 95
4.2 Time series plots of selected 6.7 GHz features in G188.95+0.89. . . . 96
4.3 Flux density plots of five 6.7 GHz methanol features. 97
4.4 Flux density plots of the v_{LSR} =+10.70 km s^{-1} and the v_{LSR} =+10.44 km s^{-1} maser features. 98
4.5 Time series plot of selected $F_{\mathbf{Int_{6.7}}}$ for the exponentially decaying v_{LSR} =+11.45 km s^{-1} maser feature. 99
4.6 The dynamic spectrum of the 6.7 GHz methanol masers associated with G188.95+0.89. 101
4.7 A velocity drifts fit in the maser features. 102
4.8 ALMA 1.3 mm Continuum emission. 104
4.9 Band 6 ALMA 1.3 mm Continuum emission. 105
4.10 Dust continuum emission of G188.95+0.89 overlaid with WISE image. 107

4.11 CH_3OH 4(2,2)-3(1,2) thermal line channel map with dust continuum overlaid. 110
4.12 Spectrum and integrated map of CH_3OH 4(2,2)-3(1,2). 111
4.13 SiO ($J = 2-1$) thermal line channel map with dust continuum overlaid. 112
4.14 ^{12}CO ($J = 2-1$) thermal line channel map with dust continuum overlaid. 113
4.15 $C^{18}O$ ($J = 2-1$) channel map with dust continuum overlaid. 114
4.16 The spectra of the identified molecular lines. 116
4.17 Zero moment maps of detected molecular lines with emission at high velocities. 117
4.18 Spectra of ^{12}CO (2-1) and SiO (5-4) and Outflow traced by the ^{12}CO 2-1 and SiO (5-4) emission respectively. 119
4.19 Composite 3-color images of the G188.95+0.89. overlaid with Herschel. 122
4.20 Composite 3-color image of G188.95+0.89 overlaid with WISE. 123
4.21 Color picture of G188.95+0.89 from the Spitzer/IRAC archive. . . . 124
4.22 Color-color diagrams. 126
4.23 Color Magnitude diagram for the YSO candidates in AFGL 5180 showing J vs. (J-H) and K vs. (H-K). 127
4.24 Spatial distribution of the YSO color-excess candidates superposed on the K_s -band image with a logarithmic intensity scale. 128
4.25 A combined image of the MSX's E and A bands. 129
4.26 ^{12}CO and CH_3OH spectra (of G188.95+0.89 extracted with an ellipse of size ∼4" centred on MM2. 137

A.1 Time series and dynamic spectrum of G188.95+0.89. 176
A.2 LCP spectra linked with G188.95+0.89. 177
A.3 ALMA array, in an extended configuration. 178
A.4 Band 6, receiver cartridge. 180
A.5 Zero moment maps and integrated maps. 181
A.6 Molecular line spectra that have been identified. 182
A.7 Publication-2019. 183
A.8 Publication-2021. 184
A.9 Similarity Report 185

ABBREVIATIONS

ALMA	Atacama Large Millimeter/ sub-Millimeter Array
CNO	Carbon, Nitrogen and Oxygen cycle
GMCs	Giant Molecular Clouds
GLIMPSE	Galactic Legacy Infrared Mid-Plane Survey Extraordinaire
HartRAO	Hartebeesthoek Radio Astronomy Observatory
HCHII	Hyper-Compact HII
HII	Ionised hydrogen
HMSFRs	High Mass Star Forming Regions
HMSF	High Mass Star Formation
HMPOs	High-Mass Protostellar Objects
HR	Hertzsprung Russell
HMCs	Hot Molecular Cores
IMF	Initial Mass Function
IRAS	Infrared Astronomical Satellite
IRDCs	Infrared Dark Clouds
ISO	Infrared Space Observatory
LCP	Left Circular Polarization
LRF	Line Rest Frequency
MASER	Microwave Amplification by Stimulated Emission of Radiation
RCP	Right Circular Polarization
MSFRs	Massive Star Forming Regions
MIR	Mid In-frared
MMB	Methanol MultiBeam
MSLs	main sequence lifetimes
MSX	Midcourse Space Experiment
OAGH	Guillermo Haro Astrophysical Observatory
PDMF	Present-Day Mass Function
SFRs	Star Forming Regions
UCHII	Ultra Compact HII Region
VLBI	Very Long Baseline Interferometer
YMSOs	Young Massive Stellar Objects
yr	year
YSOs	Young Stellar Objects
ZAMS	Zero-Age Main Sequence

ABSTRACT

Massive stars are born in regions that are opaque to optical observations. This is a challenge in understanding the processes that involve their formation. In order to investigate their formations, a multi-wavelength approach in the infrared (IR) to radio wavelengths was employed to probe the environment around the core, where they are formed. To understand the dynamics of massive star formation, we probed the molecular cloud to check the chemical composition, bipolar outflows and detailed measurements of molecular velocity fields. G188.95+089 is the Massive Star Forming Region (MSFR) that was used in our study. The choice of the star-forming region was due to the fact that it is nearby, emits periodic masers and harbours multiple star-forming cores.

While there are many tracers that can be utilized to infer the presence of massive star formation, we relied on Class II methanol masers at 6.7 GHz. In executing the multi-wavelength investigation, radio data from the 26 m Hartebeesthoek Radio Astronomy Observatory (HartRAO) dish was used to analyse the observed spectra of 6.7 GHz methanol masers. Interferometric data from the Atacama Large Millimeter/ sub-Millimeter Array (ALMA) were used to check molecular line and continuum emissions of the source. Complementary infrared data from WISE, 2MASS, Hi-GAL, GLIMPSE, IRAS and MSX was used to probe the presence of extended sources surrounding the massive star forming region. Results from radio observations showed that the source had five velocity maser features that exhibited average periodicity of 397.6 days and at least two showed evidence of velocity drifts ranging from $-2.38 \times 10^{-5} kms^{-1}d^{-1}$ to $+1.88 \times 10^{-5} kms^{-1}d^{-1}$. One maser feature at 11.45 Km s^{-1} exhibited a varying spectra with exponential decay as from year 2003 to present. The spectra of the other maser velocity features have varied significantly since detection in 1991.

Using ALMA band 6 at $\sim$ 1.3 mm and band 7 at $\sim$ 0.93 mm data, we were able to identify eight continuum cores (MM1-MM8) in the source, with masses ranging from 0.40 to 8.20 solar masses. In the ALMA band 7 observations, G188.95+0.89 MM2 was resolved into two continuum cores separated by 0.1 arcsec. The thermal emission of CH_3OH ($4_(2,2)$ - $3_(1,2)$) linked with MM2 has a double peak. In MM2, SiO emission has a bow-shock morphology, but high 12CO evidence for an east-west bipolar outflow is provided by emission to the east and west of MM2. SiO emission shows bipolar outflow centered around MM2 core.

Using near- and mid-IR color-color diagrams, young sources were detected in this star-forming region. A total of 36 candidate YSOs, were detected within a 60″ radius of the G188.95+0.89 source. There is an IR cluster made up of nine of these YSOs just outside the UC HII zone. Only the H and Ks bands of the 2MASS data can reveal nine highly red shifted objects. These sources have redder colors than $H - K > 2$, indicating that the IR cluster is extremely young. It is unlikely that interstellar absorption alone is responsible for the reddening of the vectors; instead, the presence of a circumstellar disc and envelope must account for at least some of the IR excess. Although further investigation is needed, it appears that the velocity drifts were caused by gas falling into the inner radius of the accretion disk surrounding the protostar G188.95+0.89. The variability of 6.7 GHz methanol masers is a confirmation of on going accretion in the source. Although the presence of

accretion disks in the source cannot be confirmed with the existing measurements, the identification of outflows is consistent with their existence. The out-flowing material creates shocks when it encounters the quiescent gas of the envelop. The detection of SiO molecular lines is an effective tool for checking for the existence of shocks. The shock waves pushes the gas into ever denser physical states that allow it to cool and fragment more efficiently. We argue that MM2 has a massive multiple (at least binary) of young star objects, but more VLBI observations are needed to confirm that this is indeed the case.

Keywords: ISM: stars: formation – stars: masers–Jets and Outflows – stars: – infrared: stars – stars: colors– circumstellar matter – ISM–technique – interferometric.

CHAPTER ONE

INTRODUCTION

A star is a large self-luminous cosmic ball of gas, primarily hydrogen,that is kept together by its own gravity and shines by radiation produced by internal energy sources. The hydrostatic and thermal balance of a star is often maintained by the nuclear fusion that is occurring inside, in the hottest and densest parts, is exerting radiation pressure that is pushing outwards in addition to the object's inherent self-gravity pulling inwards.

Young stars are made of the same stuff as the molecular cloud from which they originally formed, with a hydrogen composition of approximately 74 percent, helium content of approximately 25 percent, and metal content of approximately one percent (Freedman & William III 2008). The aging of a star results in some of its component parts having undergone nuclear fusion, which results in the transformation of lighter elements into heavier ones. The star's inner core is typically where this conversion occurs, leaving the star surface unchanged. Stars can be classified as: low-mass $M_* < 2M_\odot$, intermediate-mass stars $2M_\odot - 8M_\odot$ and high-mass stars $M_* > 8M_\odot$ (Zinnecker & Yorke 2007). By studying the environment in which stars are formed and understanding of the process involved in their formation,information may be obtained on star evolution.

Through studying the environments inhabited during the earliest periods of their formation, a deeper comprehension of the development of these important objects is hoped to be found. In this introductory chapter, the importance and the motivation of the study of birth of massive stars are elaborated.

1.1 OVERVIEW OF STAR FORMATION

The vast bulk of the stars in the Milky Way are believed to have formed in Giant Molecular Clouds (GMCs), that are relatively thick accumulations of interstellar gas and dust. These clouds have typical sizes $\sim$ 20 - 100 parsecs and masses $\sim 10^4 - 10^6 M_\odot$, thus an average density of $nH_2 \sim 1.7 \times 10^{-20} gcm^{-3}$ (Larson 2003). They are extremely cold with temperatures in the range 10-20K. Atoms bind to one another at low temperatures and gases take on a molecular structure. In interstellar gas clouds, hydrogen (H_2) and carbon monoxide (CO) are the most prevalent molecules. The gas clusters to high densities due to the intense coldness and when the density reaches $1 \times 10^{-25} g/cm^{-3}$ for a cloud of 1000 $M_\odot$ it becomes a dark molecular cloud.

Within the GMCs are cold, dense regions called clumps. The larger clumps within the GMCs may have density averages roughly 10^3 H_2 cm^{-3} (Larson 2003). Within these clumps, there are even denser, smaller regions called cores (Impey & Fraknoi 2020). Small dense cloud cores with masses about 1 $M_\odot$ and diameters about 0.1 pc may develop into single stars or tiny multiple stars (Larson 2003). The small pre-stellar cloud cores may have densities of 10^5 H_2 cm^{-3} or more (Larson 2003). The cores are the embryos of stars. For stars to be formed in these cores, two conditions-low temperature and high density-are just what is required. The dense, dark nebula-shaped stellar nurseries are not visible to the naked eye. The process of star creation occurs in the in the dark nebulae. Telescopes that pick up infrared(IR) and radio waves are used to investigate them as they are opaque to visible light (Freedman & William III 2008).

A single, typically lower mass ($M_* < 10 M_\odot$) object evolving toward the formation of a star is thought to exist in isolated regions. A collection or a cluster of dense cores, typically of higher mass ($M_* \geq 10 M_\odot$), which appear to be forming multiple stars is thought to exist during star formation process. When the denser sections of the cloud core separate because of gravity or own weight, star formation takes place (Impey & Fraknoi 2020). The cores collapse first because they are denser than the

outer cloud.

It takes roughly 10 millions years for the cores to develop into protostars. Fig. 1.1 shows the formation of stars from molecular clouds. In light of the core collapse's transformation of potential energy to kinetic energy, majority of these cloud cores produce IR radiations. At some point the core of the collapsing clump becomes so thick that the radiation produced deep inside the clump is consrained,rapidly raising the cores's temperature. At this stage, the core can be thought of as a protostar, and it has a distinct gravity and identity (Fraknoi et al. 2016). The infalling gas generates heat as kinetic energy, raising the temperature and pressure in the protostar's core (Freedman & William III 2008). The creation of a protostar starting from a dense core is seen in Fig. 1.2. When the protostar's temperature reaches thousands of degrees it turns into an IR source (Freedman & William III 2008).

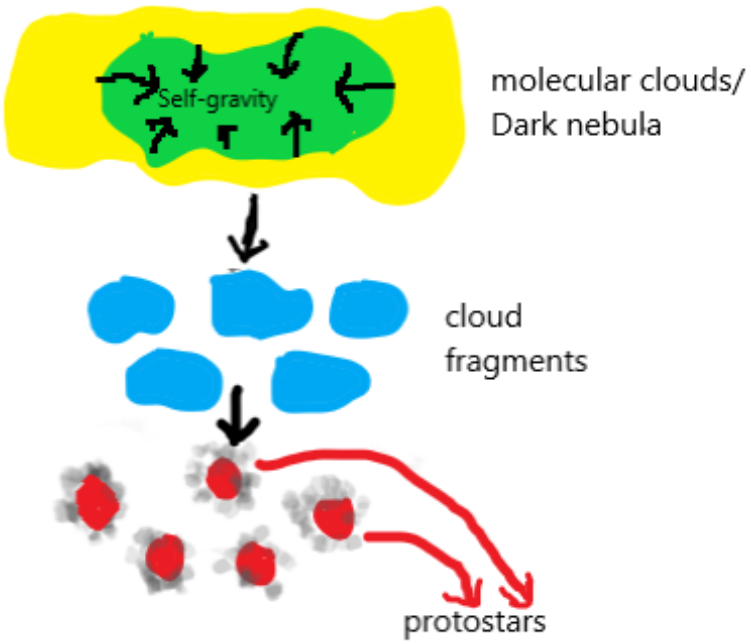

Figure 1.1: Protostars formation from molecular clouds (Christensen 2019).

The protostar keep up on growing as infalling material is accreted, initially it has about 1% of its final mass. After a few million years, its core begin undergo thermonuclear fusion, which causes the creation of powerful stellar wind that prevents the formation of new mass (Morison 2013). Since the protostar mass has been deter-

mined, it is currently thought of as a young star.

Strong stellar winds frequently appear along the spin axis, when a protostar evolves into a hydrogen-burning star. Bipolar outflow is a phenomena whereby many new-

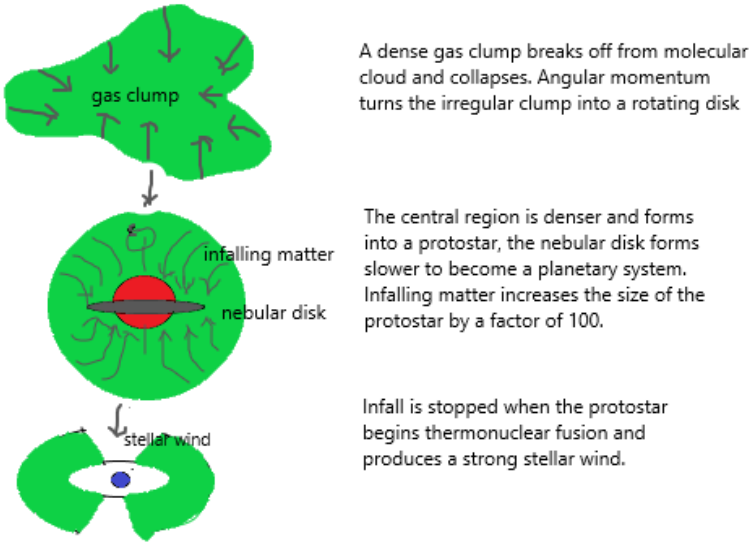

Figure 1.2: Protostar formation starting from dense core (Christensen 2019)

born stars shed mass by ejecting gas along two parallel, narrow jets or poles, that are observed by radio telescopes. T-Tauri phase is the first stage of a star's existence.

According to Freedman & William III (2008), young T-Tauri stars are frequently being encompassed by large, opaque, circumstellar discs that slowly accrete onto the stellar surface, emitting radiations from both the disc (at IR wavelengths) and the spot where the material hits the star (at optical and ultraviolet wavelengths). Within a highly collimated stellar jet, the matter that has been accreted onto the star is partially ejected in a course orthogonal to the disc's surface. Eventually, the circumstellar disc will dissipate, most likely when planets form.

A cluster of protostars at the heart of a molecular cloud give rise to young stars. When the protostars cluster transforms into a cluster of T-Tauri stars, the hot stellar winds and blazing surfaces of these stars heat the nearby gas forming an HII region. The stars develop as depicted in Fig. 1.3. This happens after the cluster has broken apart and the gas has been expelled from the HII region.

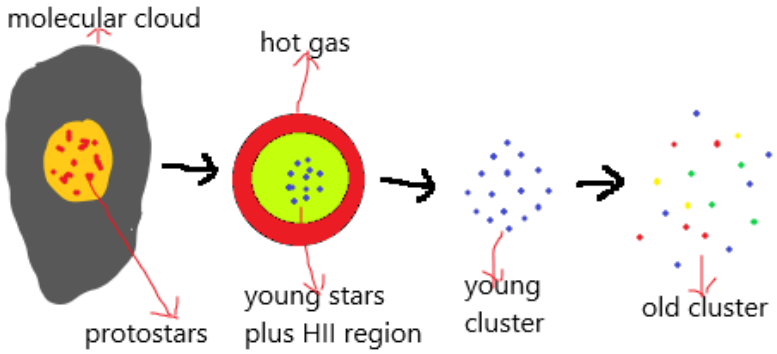

Figure 1.3: The birth of new stars begins in a dense concentration of protostars within a molecular cloud (Christensen 2019).

1.2 PROBLEM STATEMENT

One of the most perplexing issues in astronomy is how **massive stars** develop (McKee & Ostriker 2007). Even though massive stars are important and rare, little is understood about how they are formed, especially the conditions inside the cloud where they are generated and the very beginning of their evolution. The greatest density portions of molecular clouds are where these objects are thought to form, and their formation is thought to be distinct from that of objects of lower mass (Motte et al. 2018, Svoboda et al. 2019). The perspective of the surrounding environment is obscured because the nebulae in which massive stars develop are surrounded by dense matter, which absorbs visible light through dust and gas extinction and prevents us from seeing the surrounding environment (Krumholz 2015). Since the formation of stars is always connected with molecular clouds, it is essential to have an understanding of the ways in which diverse environmental variables can influence the features and structure of molecular clouds, as well as the ways in which molecular clouds themselves can influence the development of stars.

The fact that massive stars originate in clusters makes it difficult to attribute the many phenomena (disks, outflows, masers, UCH II regions, HMCs, etc.) with a single object, making identification of many of these stages challenging. Emission associated with these processes is intense at far-IR, millimeter, and radio wavelengths, although young massive stars themselves are not observable at optical wavelengths. Therefore,

these characteristics can be utilized to pinpoint regions where new, massive stars are being formed. As a result, the creation and early evolution of newborn massive stars can be better understood by combining multiwavelength, high angular resolution studies.

The 6.7 GHz methanol maser transition is studied in detail in this thesis since it is demonstrated to be an extremely potent maser in star-forming regions. Earlier evolutionary stages are linked to this maser. It only associates with enormous star formation and traces infrared black clouds, hot molecular cores, and other such phenomena.

1.3 OBJECTIVES

1.3.1 Main Objective

To probe the dynamics of massive star-forming region G188.95+0.89 using 6.7 GHz methanol masers.

1.3.1.1 Specific Objectives

(i) To investigate the spectra of 6.7 GHz methanol masers using radio data, so as to check variability which provides information about the dynamics of the on going accretion processes.

(ii) To plot the light curves of periodic methanol masers using radio data with a view to investigating the spatial movement of the gas.

(iii) To investigate the continuum, thermal line emissions and the chemical composition of the source in high mass star forming regions (HMSFRs) using the 1.3 mm ALMA data.

(iv) To investigate the morphology and kinematics of the source using high resolution ALMA data.

(v) To check the possible presence of other masers, within the extended region of

the source using archival infrared data.

1.4 MOTIVATION OF THE STUDY

HMSFRs are dynamic, which means that over time, the physical conditions in the regions change with time, resulting in brightening or quenching of the maser brightness. The lifetime of the 6.7-GHz methanol masers in HMSFRs is estimated to lie between 2.5×10^4 and 4.5×10^4 yrs (van Der Walt 2005). By the end of the lifetime of the masers, the environment around masers has significantly changed to either quench or destroy them. Thus, studying these masers is, therefore, an indirect probe of the physical properties and dynamics of a particular period during the early phase of High Mass Star Formation (HMSF) (Ellingsen 2006). It is also essential to ascertain whether the maser velocity components found to be periodic in the previous studies of the source still demonstrate periodicity behaviour at present (Goedhart et al. 2004). This could be an important contribution to our knowledge of the basic process that causes periodic masers in HMSFRs.

The following outline constitutes the framework of this thesis:

- In chapter 2 the fundamentals of star formation especially theories of massive star formation is presented. The astrophysical masers as tracers of star are elaborated. Phenomenological maser theory is explained.
- In chapter 3 describes the methodology. The observational aspects of the sources using single dish, interferometry and archival infrared data are presented. Data reductions and processing is undertaken.
- In chapter 4 describes the results of radio data observations using the single dish and interferometry. Results of archival infrared data are given. Discussions of results of radio, interferometry and archival IR is presented.
- In chapter chapter 5 discusses the findings and directions for further research. The findings are summed up.

CHAPTER TWO

THEORY AND LITERATURE REVIEW

The low - and intermediate - mass star formation are described briefly. Physical properties and formation processes of molecular clouds are discussed. Theoretical frameworks for understanding the mechanisms and conditions that give rise to massive star systems are laid out. The remaining part of the chapter describes maser theory and astronomical masers. The connection between methanol masers and stars with high masses is scrutinized.

2.1 LOW AND INTERMEDIATE - MASS STAR FORMATION

One of the many low-mass stars that may be seen in the night sky without a telescope is the Sun. Two reasons that make low-mass stars to be common than high-mass are:

(i) A star with a mass $< 8M_{\odot}$ is more likely to exist at any given time because stars with lower masses have longer lives and lifespan of a star decreases with increasing mass.

(ii) High-mass stars have a lower formation probability than low-mass stars.

In the process of forming low-mass stars, the proton-proton chain, or pp-chain, is employed to change hydrogen into helium. Deuterium is produced by the fusion of two protons, which is followed by the fusion of another proton to produce isotopes of helium-3. Stable helium-4 isotopes make up the bulk of the final products, but some lithium and beryllium are also created (Note that all of the elements discussed here and below are, in fact, ions because the star material has undergone ionization). As a consequence of this, the term "hydrogen" refers to the constituent particle of the hydrogen-1 isotope known as a proton (Freedman & William III 2008). Intermediate-mass stars have helium cores that are not degenerate, in contrast to low-mass stars,

which form a degenerate helium core when their supply of hydrogen runs out. When the core is degenerate, a runaway process known as core-helium-flash causes helium to burn (Freedman & William III 2008).

Helium combustion is thermally stable in a non-degenerate core. When helium burning is complete, low-mass and intermediate-mass stars undergo stellar wind annihilation, losing their outer layers. As a consequence of this, they transform into white dwarfs composed of carbon and oxygen, and surrounded by planetary nebulae that were formed from the remnants of their previous outer layers. Temperatures of 4×10^6 K to 4×10^7 K are optimal for the pp-chain, when the CNO-cycle has little effect, where C, N, O represents Carbon, nitrogen, and oxygen respectively. Low-mass stars with core temperatures comparable to those typically have a pp-chain as their dominant structure.

Protostars with luminosities dominated by accretion and cores with masses of a fraction of the Jeans mass create stars with masses significantly below $8M_\odot$ (McKee & Ostriker 2007). From the point on the "birthline," where they stop accreting and shift to the main sequence, low-mass stars experience substantial pre-main sequence evolution (Stahler & Palla 2004, McKee & Ostriker 2007). From this point on, we will concentrate on massive stars, or stars with $> 8M_\odot$.

2.2 HIGH - MASS STAR FORMATION

High-mass stars can be referred to as OB-type stars with enough mass to create a type II supernova, meaning M $> 8M_\odot$ (Zinnecker & Yorke 2007). In the studies made by Palla & Stahler (1993), it was shown that stars with M $> 8M_\odot$ do not go through a pre-main sequence phase. There are still many unclear points in the massive star formation, related to the fact that nuclear reactions in massive protostars begin much earlier than they reach the final mass (Gieser et al. 2022). High-mass stars are formed in optically thick environments and are embedded inside giant molecular clouds (GMCs) with high extinction in the V band, $A_V \geq 10$ mag

(Lada & Kylafis 1999). These GMCs in our Galaxy tend to be scattered over large distances $\geq$ few kpc from the Sun, except Orion, which is at a distance of 437 $\pm$ 19 pc from the Sun (Hirota et al. 2007). Factors like the great distances to HMSFRs, clustered environment in which they develop, the obscured regions undergoing massive star formation, and their strong interaction with their environment, it is difficult to interpret observational data of high-mass stars.

The CNO-cycle is used by high-mass stars to convert hydrogen into helium. The four protons are fused into one helium-4 with the aid of the elements C, N, and O acting as catalysts. High-mass stars behave differently from low-mass stars when it comes to hydrogen fusion since both chains of processes are highly temperature dependent. The CNO-cycle starts to function above 1.7×10^6 K, when core-hydrogen burning takes place in large stars. Massive stars are controlled by the CNO-cycle for as long as the three elements, are present in the plasma at the beginning of the star's life (which is true in almost all instances, with the exception of stars that are completely devoid of any metals).

Contrary to low mass stars, massive stars, that is stars with mass ($> 8M_{\odot}$), begin to burn carbon, oxygen, neon, and silicon in thermal equilibrium instead of developing degenerate helium (or carbon-oxygen) cores. Only when the core is made of iron, a metal that can no longer be burned by nuclear fusion, can they lose equilibrium. The process of nuclear fusion during massive star formation is depicted in Fig. 2.1. This is due to the fact that iron is such a stable metal that fusing it would need energy rather than producing energy, as stated by Freedman & William III (2008).

One stellar evolutionary sequence that spans the full evolution from conception (but excluding the star-formation process) through the final stages of life, can be computed in a few hours, thanks to modern computing power. The Hertzsprung-Russell (HR) diagram, which plots surface temperature against luminosity, is the most widely used tool for tracing the evolution of stars (for instance, see Fig. 2.2). The HR diagram organizes the stars in descending order of luminosity, with the moat luminous at the

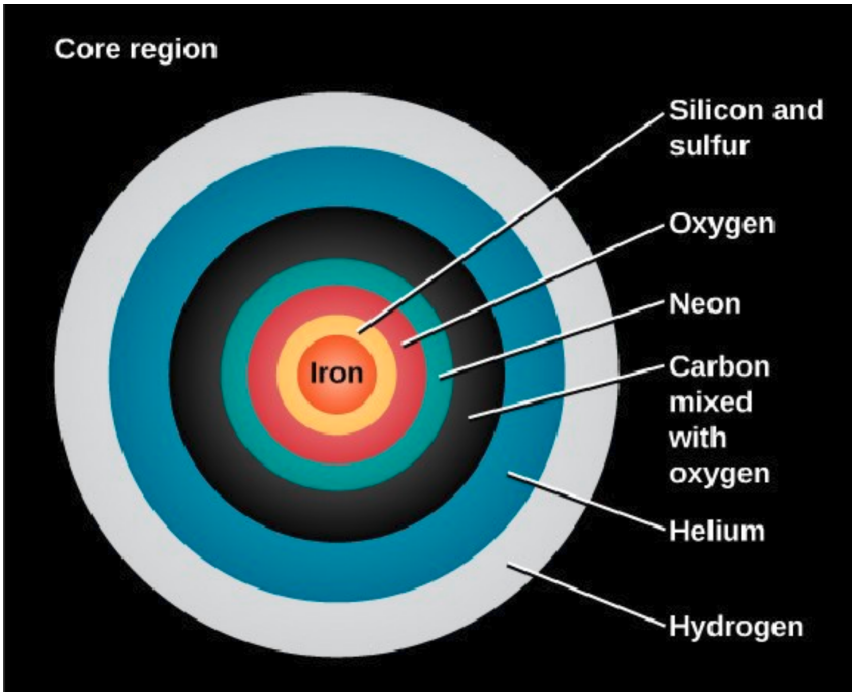

Figure 2.1: Core of a massive star showing core fusion processes. Only when the core is made of iron, which can no longer be created through nuclear fusion, does the amount of fallout reach an equilibrium.Credit: modification of work by ESO, Digitized Sky Survey(Jensen n.d.)

.

top and the least luminous towards the bottom. Stars with cooler spectral types are on the right, while stars with hotter spectral types, such as O and B, are on the left. Stars with the highest luminosities are located at the diagram's apex, while those with the lowest luminosities are located at its base. The graph's left side is dominated by hot stars in spectral classes O and B, while the right features cooler stars. $_{\odot}$ The earliest solid matter in the early Universe was created by massive stars ($> 8M_{\odot}$ and $> 10^3 L_{\odot}$), and these stars have a significant impact in the development of the galaxies in which they are hosted as well as the birth of following generations of stars (Dunne et al. 2003). Given the enormous impact giant stars have not only on their immediate surroundings but also on a cosmic scale, it is critical to comprehend the environmental ingredients and processes involved in their formation and early phases of evolution (Urquhart et al. 2011). By doing so, we can learn more about the molecular clouds in which they form, the stellar feedback loop at work in the star-forming environments nearby, and their fundamental impact on the Galaxies

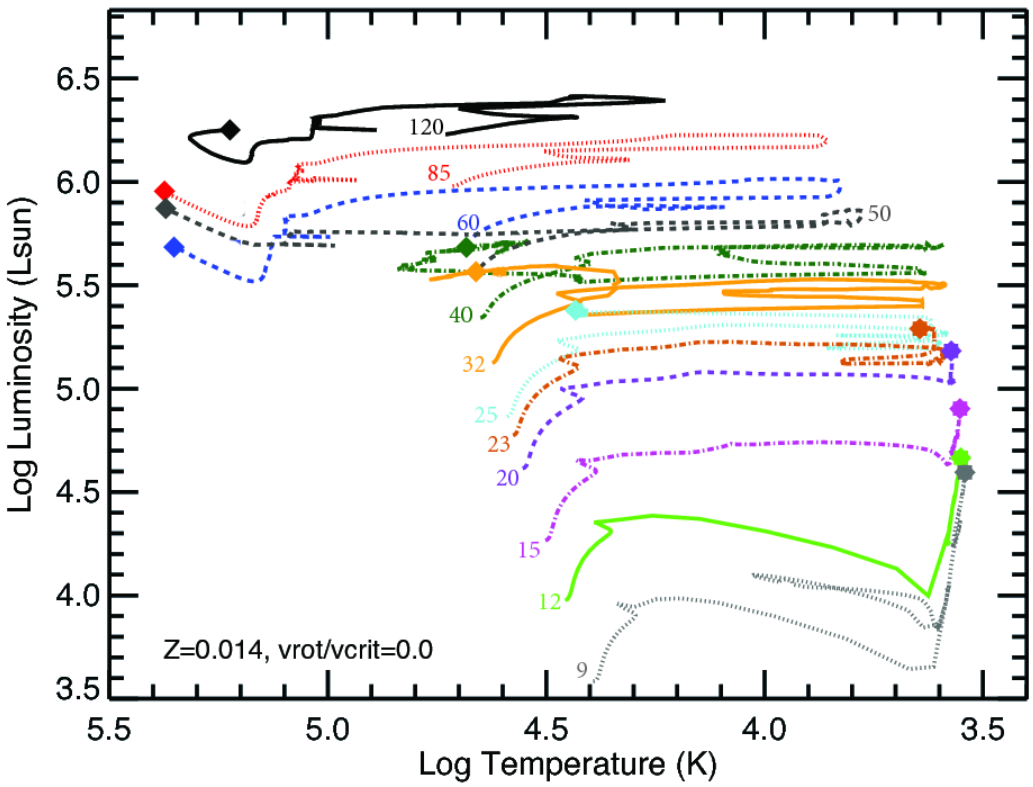

Figure 2.2: Stellar evolutionary model. On the ZAMS, the initial star mass (in solar-mass units) is designated. Diamond and octagram symbols denote the end of evolution (Groh et al. 2013)

.

that host them (Arce et al. 2011).

2.3 GIANT MOLECULAR CLOUDS

Atomic and molecular gases make up around 99 percent of molecular clouds, while dust makes up the remaining 1 percent. A GMC is a dense, cool (10–20 K), and predominantly hydrogen molecule-containing cloud (Peters et al. 2010). The interstellar material (composed primarily of hydrogen molecules and helium atoms) is generally compressible, magnetised, turbulent and fluid. The physical properties of the molecular cloud such as temperature, size, average number density and the total mass are determined from the molecular and atomic transitions. The rotational, electronic and vibrational transitions emit (or absorb) photons respectively at the UV/visible, infrared and radio (including submillimetre and millimetre) wavelengths. Therefore, a complete study of molecular clouds requires multi-wavelength observations.

Molecular clouds can be divided into four groups namely: diffuse, giant molecular, dark and dense core/Bok Globule clouds as given by Stahler & Palla (2008). Table 2.1 presents a list of the physical properties of these four groups of molecular clouds, in the order of increasing visual extinction. All star formation occurs in GMCs, hence GMCs formation is thus directly related to high-mass star formation (HMSF). Discussion on the criteria for the formation of a protostar from a collapsing molecular cloud is crucial, as it will provide the conditions for a star to form. As almost all star formation occurs in GMCs, in particular, high-mass stars, which are our specific interest, hence our discussion will be limited to GMCs (Montmerle & Townsley 2012).

Table 2.1: Classes of Galactic molecular clouds and their corresponding physical properties (Obtained from Stahler & Palla (2008), in Ch. 3.). The physical properties are line-of-sight visual extinction A_V , total number density n_{tot} , size Sz, temperature T and mass $M_\odot$.

Cloud type	A_V	n_{tot}	Sz	T	M
(mag)		(cm^{-3})	(pc)	(K)	($M_\odot$)
(1)	(2)	(3)	(4)	(5)	(6)
Diffuse	1	500	3	50	50
Giant Molecular	2	100	50	15	10^5
Dark (complexes)	5	500	10	10	10^4
Dark (Individual)	10	10^3	2	10	10
Dense cloud	10	10^4	0.1	10	10

According to Zhang et al. (1998), molecular clouds (MCs) are the primary locations for star formation in the galaxy and are referred to as Star Forming Regions (SFRs). Fig. 2.3 shows a giant molecular cloud known as the eagle nebula that has very low temperatures of just 10 to 20 K. The majority of the hydrogen in the GMC is made up of molecules. Giant molecular clouds are referred to as molecular clouds that are larger than 15 light years. A dark nebula (or dark cloud) is a highly dense region within a larger molecular cloud (MC).

2.3.1 GMCs Formation

The building blocks of galaxies, giant molecular clouds (GMCs), and their star offspring are constantly being created in our galaxy by a variety of mechanisms (Mélanie

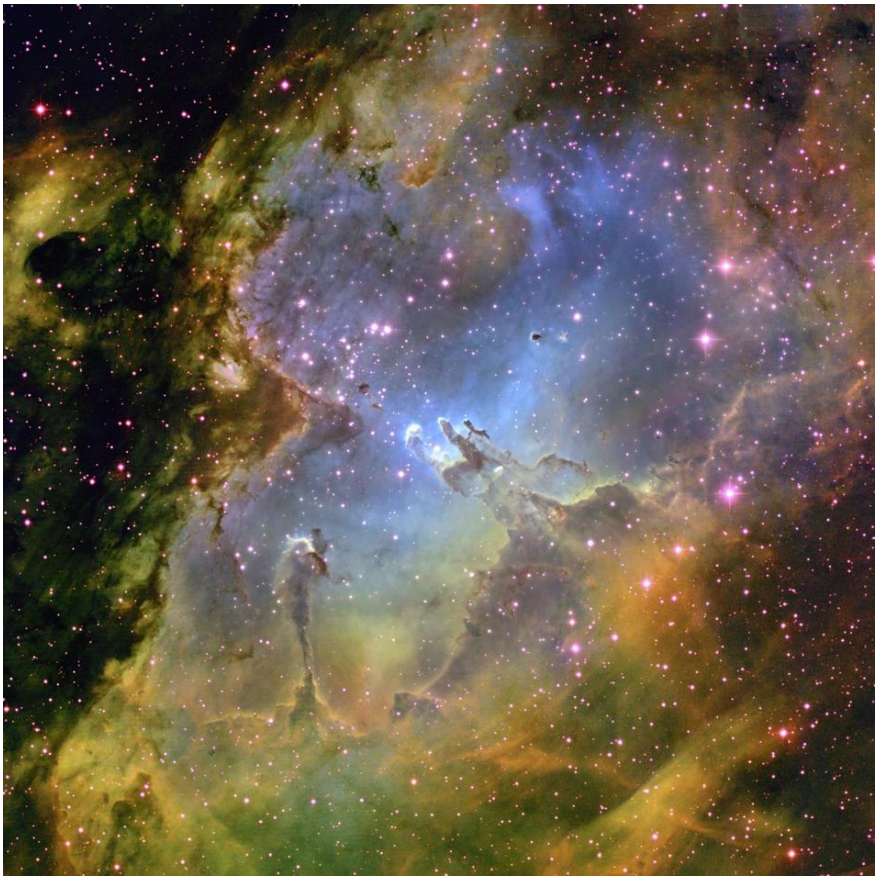

Figure 2.3: The Eagle Nebula lies within a molecular cloud that is roughly 20 light-years across. Credit:T. A. Rector and B. A. Wolpa, NOAO, AURA. A molecular cloud is an assemblage of interstellar gas and dust (Oliveira 2008)

.

et al. 2020). Their rate of formation has a direct link to the star formation rate in the galaxy, especially high-mass stars. Their lifespan is expected to be less than 3.0×10^7 yr (Stahler & Palla 2008). A brief description of proposed mechanisms to explain the formation of GMCs are:

(i) Parker instability model (Parker 1966). In the Parker (1966) instability, the magnetic field and cosmic ray pressure give substantial support to the gravitational collapse of the gas perpendicular to the galactic plane. A perturbation of the mass-to-flux ratio ($R = (M/\Phi)_{core}/(M/\Phi)_{envelope}$) is buoyant, which implies it will rise to the surface of the disk plane causing the mass to drift from the regions of high to low magnetic field strength. The regions with feeble magnetic fields condense to form GMCs.

(ii) Random coalescence model (Cowie 1980, Norman & Silk 1980), where randomly distributed small clouds collide inelastically and agglomerate into a GMC.

(iii) Pressurised accumulation in the shock model (Blitz & Williams 1999). The isolated supernovae, OB stars, and spiral density shocks condense the filaments, sheets and shells of a cloud into GMC.

(iv) Gravitational instability model (André et al. 2014, Elmegreen 1990). In this model, the rotation of a galaxy maintains the stellar component of a galactic disk, leaving the magnetised gas gravitationally unstable, which implies that it will collapse to form GMCs. A density wave is not necessary for initiating the collapse, but it can increase the instability growth. This is a top-down structure, where huge clouds are formed first and break up into GMCs due to the gravitational instability described by Toomre (1964).

(v) Thermal instability model (Balbus & Soker 1989, André et al. 2014, Field 1965). The system is isobaric, meaning that the pressure, P , is constant. A thermal instability in a homogeneous medium arises when the net energy loss per gram L is $\frac{\delta L/T}{\delta T}_P < 0$. L is the difference between energy loss and gain. Thermally unstable region, which is denser and cooler than its surroundings, cools and condenses to form dense, cold giant molecular complexes.

(vi) Spiral arm induced collision model (André et al. 2014, Blitz & Williams 1999). The spiral arms in the Galaxy urge collision of clumps in the disk to accumulate to form the GMCs.

2.3.2 Criterion For a Molecular Cloud to Collapse

A stable molecular cloud is held up against the pull of gravity by tumultuous motions of the molecular clumps, magnetic fields, rotational motion of the clumps and thermal pressure (Vink 2020). For star formation to occur, the cloud core must collapse first, allowing the denser parts to do so under their own weight and gravity. The cores comprise of 100,000 solar masses or less of gas and and dust. The cores collapse first

and fracture into clumps with a radius of 0.1 parsecs because they are denser than the surrounding cloud (Tan et al. 2014). The formation of protostars from these aggregates takes approximately 10 million years.

Material at centre of the cloud begins heating up as it breaks apart, creating a dense, hot core that starts to collect dust and gas as the cloud breaks apart (Rathborne et al. 2008). A portion of this material eventually becomes a star, while the remaining dust may either continue to exist as dust or transform into planets, asteroids, or comets (Gail & Hoppe 2010, Terrile 2017). The Virial theorem can be used to summarise the interaction between these forces in a molecular cloud. In the Lagrangian form, the Virial theorem as derived by Stahler & Palla (2004) is as follows;

$$\frac{1}{2}\ddot{I} = 2T + 2U + W + M, \tag{2.1}$$

where I ($I = \int r^2 dm$), T , U , W and M are: the moment of inertia of a molecular cloud, total kinetic energy of the internal motion, thermal motion, gravitational potential and energy associated with the magnetic field. $\ddot{I}$ is related to the acceleration of contraction or expansion of the molecular cloud. For a gravitationally stable molecular cloud, the equation on the left of 2.1 is zero, which implies $\ddot{I} = 0$. In a stable molecular cloud, which is supported only by thermal pressure against gravitational collapse, the Virial theorem in Lagrangian form in equation 2.1 becomes:

$$0 = 2U + W. \tag{2.2}$$

The total internal energy due thermal pressure of the cloud is $U = \frac{3M_{cl}k_BT}{2\mu m_H}$, where M_{cl}, T, k_B, μ and m_H are respectively the mass of a molecular cloud, uniform temperature of the cloud, Boltzmann constant, the average molecular weight and the mass of a hydrogen atom. The gravitational potential energy is given as, $W = (\frac{-3GM_{cl}^{cl}}{5})(\frac{4\pi\rho_o}{3M_{cl}})^{1/3}$, with ρ_o and G being the uniform density of the cloud and the universal gravitational constant, respectively. Utilizing U and W, that are given earlier, and equation 2.2,

the Jean's mass M_J of a molecular cloud can be derived as

$$M_J \simeq (\frac{5k_BT}{G\mu m_H})^{3/2}(\frac{3}{4\pi\rho_o})^{1/2} \tag{2.3}$$

If the mass of the cloud surpass its Jean's mass,it becomes gravitationally unstable, which implies it will collapse. It follows that if a stable molecular cloud is sufficiently perturbed, either 2U> W or 2U <W, it could either expand or collapse, respectively.

The temperature remains constant during the isothermal collapse, but the density of the core increases, meaning that M_J decreases (Battersby & Bally 2014). This could result in additional fragmentation of the core. The temperature stays constant because the cloud cools efficiently by transforming the kinetic energy of the atoms and molecules into far-infrared radiation, which is transparent to the cloud (Metzger 2010). This is a free-fall collapse phase and is designated by the free-fall timescale, t_{ff} (Smith 1995, Stahler & Palla 2004). In a self-gravitating spherical molecular cloud, the change in radius for infalling matter is governed by Newton's second law of motion (Smith 1995, Tohline 1982), from which the free-fall timescale can be determined as follows:

$$T_{ff} = \sqrt{\frac{3\pi}{32G\rho_o}} \simeq 2.1 \times 10^5 [\frac{\rho_o}{10^{-19} gcm^{-3}}]^{1/2} yr. \tag{2.4}$$

The free-fall timescale in equation 2.4 depends on the density of the cloud. Increasing the cloud's density decreases the free-fall timescale. When the free-fall collapse of the molecular cloud is complete, a protostar will have formed at its center. It is a star-like object that is close to being in gravitational equilibrium (Bonfand et al. 2019).

The Kelvin-Helmholtz timescale can be obtained from the gravitational energy of a near hydrostatic equilibrium and its luminosity L. From the Virial theorem, half of the gravitational energy of a near hydrostatic equilibrium object is used to heat the object, and the rest is radiated into space. The timescale for the radiation of gravi-

tational potential energy into space, is given as the ratio of half of the gravitational potential energy, and the luminosity of the protostar L, which is the Kelvin-Helmholtz timescale t_{KH} and it is given as;

$$t_{KH} = \frac{3}{10}\frac{GM^2}{RL} \simeq \frac{GM^2}{RL} \tag{2.5}$$

Equation 2.5 gives an estimation of the time in which a protostar enters the main sequence of the HR plot. It's time before nuclear or hydrogen fusion commences in the core, after a protostar has been formed (Zinnecker & Yorke 2007). The Jean's mass (equation 2.3) can be used to investigate the gravitational stability of molecular clouds. The free-fall (equation 2.4) and Kelvin-Helmholtz (equation 2.5) timescales can be compared for the low and high-mass protostars.

The Kelvin–Helmholtz timescale and time for accreting mass M_* at a specific accretion rate $\dot{M}_*$, which is $t_{acc} = M_*/\dot{M}_*$, comparisons between low-mass and high-mass stars are possible (Beuther et al. 2002). Considering a solar-like star, with 1 $M_\odot$, 1 $L_\odot$, 1 $R_\odot$ and a typical mass accretion rate of $\sim 10^{-7}$ $M_\odot$ yr^{-1}, the accretion time for 1 $M_\odot$ is $\sim 10^7$ yr. The Kelvin–Helmholtz timescale (using equation 2.5) is $\sim 3.0\times 10^7$ yr. The accretion and Kelvin–Helmholtz timescales are of the same order of magnitude $\sim 10^7$ yr.

For a high-mass star with M = 10 $M_\odot$, L = 3.0×10^3 $L_\odot$, R = 54 $R_\odot$ and typical mass accretion rate of $\sim 10^{-4}$ $M_\odot$ yr^{-1}, the accretion and Kelvin–Helmholtz timescale are 10^5 and 2.0×10^4 yr, respectively (Lada & Kylafis 1999, Beuther et al. 2002). The accretion timescale is greater than the Kelvin–Helmholtz timescale by a factor of ten. This means that a small percentage of mass is accreted before the main sequence phase, and a substantial fraction of mass is accreted as hydrogen burns in the core (Kahn 1974). These calculations reveal that the processes of HMSF differ from those of low-mass stars. The observations by Suri et al. (2021) for the first time, revealed fragmentation below ∼1000 AU toward the AFGL 2591-VLA 3 hot core. Three distinct low-mass (below one solar mass) cores were identified as;A, B,

and C. If a molecular cloud is held together against the pull of gravity by a magnetic field field only, Virial theorem in equation 2.1 will be W + M = 0. The magnetic field's energy is denoted by the expression $M = \frac{\Phi^2 B}{6\pi^2 R}$ or $M = \frac{|B|^2 R^3}{6}$ (Stahler & Palla 2004), where Φ is the magnetic flux. The Virial theorem can then be reduced to the following:

$$0 = \frac{|B|^2 R^3}{6} \frac{GM_{cl}^2}{5R}, = \frac{3G}{5R}[\frac{5\Phi_B^2}{18\pi^2 G - M_{cl}^2}], = \frac{3G}{5R}[M_\Phi^2 - M_{cl}^2], \tag{2.6}$$

where M_Φ is the critical mass (Crutcher 2012). Mass-to-flux ratio, $\frac{M_{cl}}{\Phi_B}$, can be derived from equation 2.6 as;

$$\frac{M_{cl}}{\Phi_B} = \sqrt{\frac{5}{18}} \frac{1}{\pi\sqrt{G}} \tag{2.7}$$

In the case where $\frac{M_{cl}}{\Phi_B} > \sqrt{\frac{5}{18}} \frac{1}{\pi\sqrt{G}}$ or $M_{cl}/M_\Phi < 1$, the magnetic field will stop the molecular cloud from gravitational collapse and the cloud is said to be magnetically subcritical (Lada & Kylafis 1999). When $\frac{M_{cl}}{\Phi_B} > 1$, the cloud is gravitationally unstable implying that it will collapse. This state of molecular cloud is said to be magnetically supercritical.

2.3.3 Stellar Initial Mass Function

The stellar initial mass function (IMF), also known as the number of stars per cubic parsec per unit logarithmic mass (Salpeter 1955, Miller & Scalo 1979, Rana 1987). Variation of initial stellar masses among a group of young stars is another name for it (Heyer et al. 2018). For stars with masses more than 5 $M_\odot$, the IMF is characterized by a power law; for stars with masses less than 1 $M_\odot$, it is flat (Myers 2000). At lower masses (0.1-0.5 $M_\odot$), there are still debates on whether the IMF is flat, continues to rise or turns. It is associated with the disintegration of a GMC into individual star-forming clumps. Fig 2.4 shows plots of various initial mass functions (IMF).

The IMF can be calculated using field stars and various sorts of stellar clusters

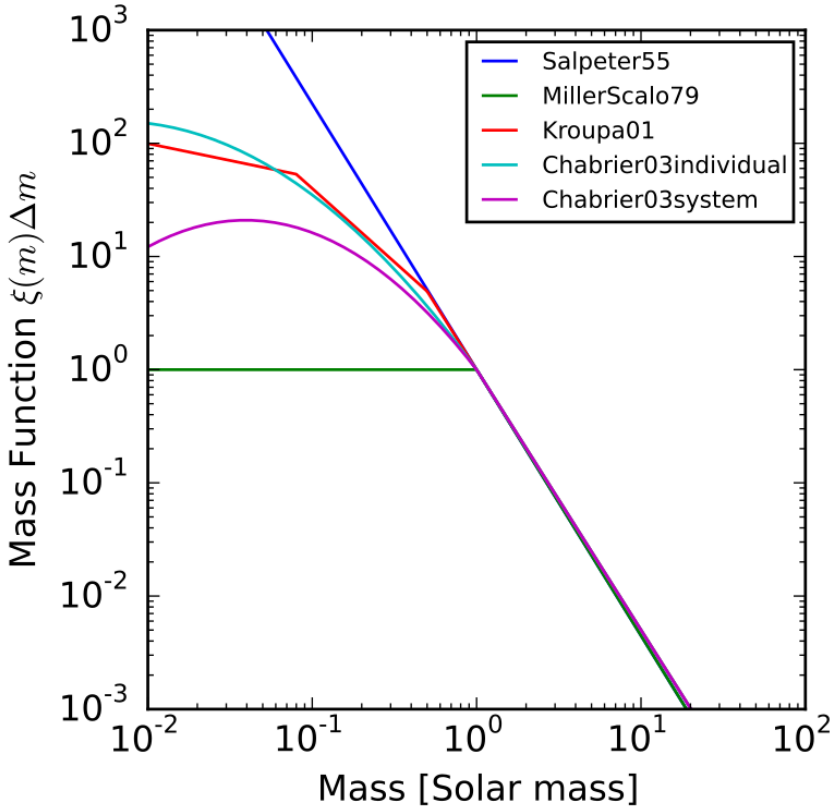

Figure 2.4: Plot of various initial mass functions (IMF). (The vertical axis is actually not $\xi(m)\Delta m$, but a scaled version of $\xi(m)$. For m greater than 1 solar mass, it is $(\mathrm{m}/\text{solar mass})^{-2.35}$). Credit: JohannesBuchner (Briceño et al. 2002)

(Chabrier 2003). The present-day mass function (PDMF), or the number of main sequence stars per unit logarithmic mass per cubic parsec, is used to calculate the IMF for the field stars (Karnik et al. 2001). The stellar birthrate history of the galaxy must be known in order to scale the PDMF, to be comparable to the IMF for stars with main sequence lifetimes (MSLs) younger than the age of the Galaxy (Boley 2013). However, the PDMF and IMF are equivalent for stars whose main sequence lifetimes are older than the age of the Galaxy. It is vital to know a star's stellar mass, which cannot be viewed, in order to comprehend its spectrum, lifetime, and demise (Williams et al. 2000).

Because the different elements that can be synthesized by stars in the mass range of m and m + dm are proportional to the slope of the stellar IMF, the stellar IMF is essential for calculating the star formation rate in a galaxy and the chemical evolution of the galaxy. The slope and associated mass range of the stellar IMF are crucial in

establishing the mass-to-light ratio for stars in a galaxy with a mass range of m and m+dm. Salpeter (1955) was the first to realize that the high-mass star region in the IMF shrinks as mass grows in size. This suggests that there are fewer high-mass stars in a narrow area of space (a few cubic parsec) (Boley 2013). The focus of research to comprehend the IMF has turned to understanding the genesis of the Core Mass Function (CMF) and the fragmentation features of molecular clouds because all known star formation occurs in dense molecular cores. The concept that the CMF is shaped like the IMF is actually supported by the majority of observational evidence (Testi & Sargent 1998, Motte et al. 1998, Alves et al. 2007). Ntormousi & Hennebelle (2019) concluded that that, while the resultant CMFs and IMFs have comparable slopes in all simulations, when a magnetic field is incorporated, the cores have somewhat different sizes and kinematical features, which impacts their gravitational stability. However, if thermal stability is ignored, a core selection based on the mass-to-flux ratio is insufficient to change the form of the CMF.

2.4 HIGH MASS STAR EVOLUTIONARY SEQUENCE

High-mass stars are formed inside GMCs, which are optically thick, meaning that optical and UV radiation can not escape the core. Therefore, the submillimetre, millimetre and centimetre astronomical observations are ideal for studying these regions. A brief summary of mid-infrared observations, through radio wavelengths toward regions where high-mass stars are forming or are still to be formed, was given by Van der Tak & Menten (2005). These authors categorised the observations into five groups, namely: (i) infrared dark clouds (IRDCs), (ii) high-mass protostellar objects (HMPOs), (iii) hot molecular cores (HMCs), (iv) ultracompact HII (UCHII) regions and (v) compact and classic HII regions. This categorisation was also adopted by Zinnecker & Yorke (2007).

These five groups form the sequence of events for how high-mass stars are formed, based on the observations. While there is still some disagreement over the evolutionary history, Churchwell (2002) and Zinnecker & Yorke (2007) provide summaries of

one hypothesised sequence. This history of evolution starts with prestellar cores or groups, which are held together by gravity over densities inside a molecular cloud and show signs of moving inward, but haven't yet started to form protostars. Prestellar cores have temperatures that are typically between 10 and 20 K, and the far-infrared region of the spectrum is where their spectral energy distributions reach their maximum.

Additional stages include the molecular cores, hyper-compact HII (HCHII), and ultra-compact HII (UCHII) regions. Compact and traditional HII regions make up the final phases. The embedded stellar population is now discernible in the optical and infrared as the HII region has developed and started to perturb the parent molecular cloud. According to Stahler & Palla (2008), there are four categories of molecular clouds: diffuse, giant molecular, dark, and dense core/Bok Globule clouds.

2.4.1 Infra-Red Dark Clouds and Filaments

It is believed that the conditions in the IRDCs are perfect for the birth of massive stars. They are molecular or dust clouds that are cold, thick, and visible in the mid-infrared (MIR). They serve as both the galaxy's molecular gas storage area and the site of star birth. The densest condensations in GMCs are IRDCs, which are also likely locations for massive star formation in the future (Churchwell et al. 2009). According to Kumar et al. (2022), they may contain young stars. It has come to light in recent years that not all IRDCs contain HMYSOs. The presence of HMYSOs is only detected in IRDCs that meet a specific mass-size requirement or, equivalently, are over a specific threshold density (Retes-Romero et al. 2020).

The observations toward the IRDCs show that these regions have high densities, n_{H2} 10^5 cm^{-3}, and low temperatures, T $<$ 20 K, suggesting that they exhibit the initial conditions for HMSFRs (Hull & Zhang 2019). The observations toward the dense cores of IRDCs also show that they are supported by both turbulent flow and magnetic pressure, implying the cores are magnetically subcritical (Pillai et al. 2015).

Infrared dark clouds typically have filaments as their main structural elements (IRDCs Rathborne et al. 2006). As putative precursors of cluster formation, filaments and infrared dark clouds (IRDCs) have drawn particular interest (Rathborne et al. 2006, Longmore et al. 2012, Russeil et al. 2013). Schisano et al. (2020) reported that many IRDCs are filamentous. By formalising the intuitive understanding of what a filament appears to be based on what the eye observes on a map, an extended region with a somewhat higher brightness contrast to its surrounding can be described as a filament. In the thick molecular gas of galaxies, filaments may contribute to control the star formation efficiency (Shimajiri et al. 2017). Magnetic fields, despite their weak confinement, undoubtedly play a considerable part in the formation, fragmentation, and growth of filaments (André et al. 2010).

2.4.2 High-Mass Protostellar Objects (HMPOs)

HMPOS can be described as dense cores that undergo gravitational collapse producing high-mass protostars with high luminosities, $L > 10^3 L_{\odot}$, and high accretion rates, $\dot{M} \geq 10^4 M_{\odot} yr^{-1}$ (Gieser et al. 2022). They are normally found in dense cores that experience gravitational collapse. The protostar's central heating causes the envelope's temperature to rise. Outflows are frequently seen, so disks ought to be there as well. Although they are frequently observed in the vicinity of low-mass protostars (Öberg et al. 2021), they remain difficult to observe due to their small diameters (1000 au) (Gieser et al. 2022). HMPOs emit strongly at millimeter wavelengths but weakly or not at centimeter wavelengths. Yoo et al. (2018) undertook a molecular line scan of 82 high-mass protostellar objects and discovered 27 inflow candidates, all of which lacked red asymmetry profile and had at least one blue one.

Ao et al. (2018) discovered 12 HMPO possibilities by studying how dense cores are linked to IRAS sources. Low FIR luminosity to virial mass ratios were found to be characteristic of HMPO sources, which agrees with the idea that these huge protostars are still in their early developmental stages. Similar to other main-sequence stars of zero age, these stars have not yet reached their full luminosity (Ao et al. 2018). 21

regions had bipolar molecular outflow morphology, according to the carbon monoxide CO (2-1), mapping observations towards 26 regions with HMPOs (Beuther et al. 2002). Bipolar molecular outflows were detected at a rate of about 80 per cent, indicating that they are a very plausible byproduct of HMSF (Ellingsen 2006). The accretion rates were derived to be between $\sim 10^{-4}$ and 10^{-3} $M_{\odot}$ yr^{-1}, and the estimated bolometric luminosity of $\sim 10^{4}$ $L_{\odot}$. Other CO mapping observations toward HMPOs have been conducted by, e.g. Henning et al. (2000) and Zhang et al. (2001).

2.4.3 Hot Molecular Cores (HMCs)

The HMCs, which are the hot, dense cores that surround high-mass YSOs, exhibit strong emission in a variety of rare and complicated organic compounds. The high-mass star-formation region's early processes known as hot molecular cores, are important for raising the ISM's chemical complexity (Shimonishi et al. 2021). For example, CH_3CN, CH_3OH, HCOOH, $HCOOCH_3$, CH_3OCH_3, CH_3CH_2 CN, CH_3COCH_3, NH_2CN and $(CH_2OH)_2$ have been detected in the HMCs associated with IRAS 20126+4104 (Palau et al. 2017). CH_3CN, CH_3OH, CH_3CH_2CN, HNCO, CH_3OCH_3 have been detected in the HMCs associated with IRAS 18566+0408 (Silva et al. 2017). It is possible that these molecules are formed in the extremely HMCs, where temperatures ($\gtrsim$150 K) via endothermic chemical reactions (Allen et al. 2017). HMCs are identified by a rich chemistry detectable in (sub)mm wavelength molecular line emission and gas temperatures above 100 K (Elmegreen & Palous 2007, Jørgensen et al. 2020).

Because the protostars are still rapidly accreting and the UCHII regions have not yet formed, it is thought that these HMCs represent an early evolutionary stage in the development of high-mass stars (Beuther et al. 2009). According to (Wootten 2001, Chen et al. 2006), hot molecular gas cores (HMCs) produced by young massive **star-forming regions** have a rich chemistry that makes it possible to study significant physical properties. Physical properties of hot cores include small source sizes ($\leq 0.1pc$), high densities ($> 10^{6}$ cm^{-3}), and greater temperatures of both gas and dust

(van der Tak et al. 2003). COMs are defined as molecules with six or more atoms. A hyper-compact HII (HCHII) zone may already exist in the center of the HMC because of the to the fact that protostar's ionizing radiation.

The high-mass star-formation region's early processes, known as hot molecular cores, are important for raising the ISM's chemical complexity (Manna & Pal 2023). The various complex organic molecules present in the HMCs can be recognized, along with their spatial distribution, using high spectral and spatial resolution data from sources like ALMA, VLA e.t.c (Manna & Pal 2023).

2.4.4 HII Regions

Regions in space known as HII regions are illuminated by the ionized hydrogen emission spectrum. HII Regions are made up of atomic hydrogen gas ionized by photons with energies $\geq 13.6eV$. Once they reach 10 $M_{\odot}$, HII regions begin to form around accreting protostars. Massive stars' ionizing radiation causes pronounced HII regions. Fig. 2.5 shows a schematic HII region.

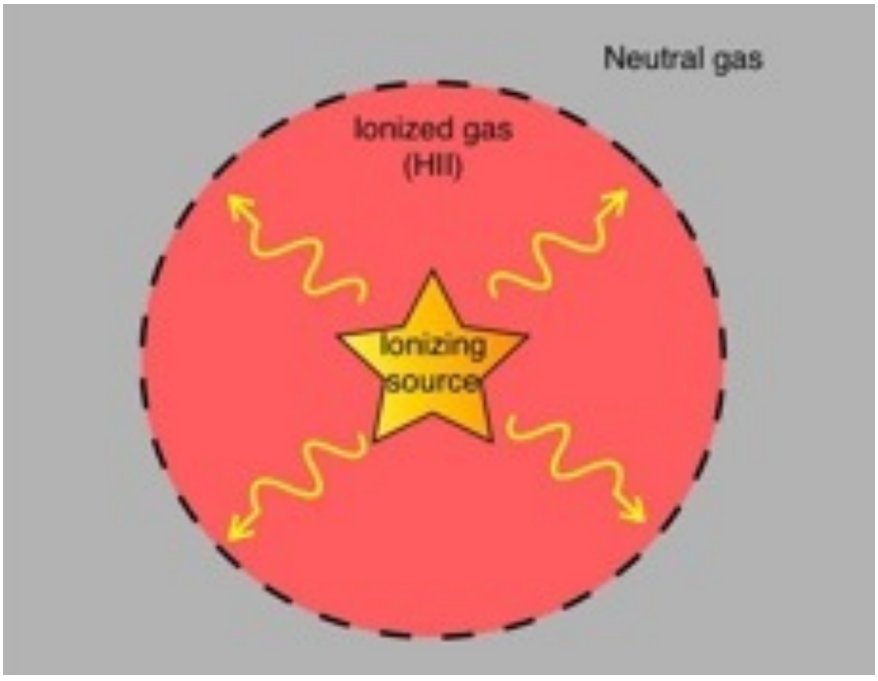

Figure 2.5: The schematic HII region (Deharveng et al. 2010)

The evolution of HII region is thought to be from Hyper-compact HII region (HCHII)

→ Ultra-compact HII region (UCHII) → compact and classical HII regions. This evolutionary sequence is driven by the expansion of the HII region. From the evolution of the HII regions, it can be deduced that younger and evolved protostars are associated with HCHII and compact HII regions, respectively. Table 2.2 lists the physical characteristics of each class of HII region.

Table 2.2: The physical characteristics of the ionized hydrogen regions: a brief overview (Obtained from (Kurtz 2005)

Class of Region (1)	Size (pc) (2)	Density (cm^{-3}) (3)	emission Measure (pc cm^{-6}) (4)	Ionised Mass ($M_\odot$) (5)
Hypercompact	$\lesssim 0.03$	$\gtrsim 10^6$	$\gtrsim 10^{10}$	$\sim 10^{-3}$
Ultracompact	$\lesssim 0.1$	$\gtrsim 10^4$	$\gtrsim 10^7$	$\sim 10^{-2}$
Compact	$\lesssim 0.5$	$\gtrsim 5.0 \times 10^3$	$\gtrsim 10^7$	~ 1
Classical	~ 10	~ 100	$\sim 10^2$	$\sim 10^5$
Giant	~ 100	~ 30	5.0×10^5	$\sim 10^3$ - 10^6
Supergiant	>100	~ 10	$\sim 10^5$	$\sim 10^6$ - 10^8

The physics of HII regions is controlled by three mechanisms:

(i) Photoionization - The state of equilibrium, where photoionization and recombination are in balance. This establishes both the nebula's structure and the general geographical distribution of the ionic states of the constituent elements in the ionised zone.

(ii) Thermal balance between heating and cooling - Photoelectrons with thermal energy of a few eV that are ejected from Hydrogen and Helium are the primary source of heating. Most HII regions cool primarily as a result of metal ion excitation by electron-ion impact, followed by "forbidden" line emission from low-lying fine structure levels. These cooling lines are responsible for the distinctive spectra of HII regions.

(iii) Hydrodynamics - which includes winds and outflows from the embedded stars as well as shocks, ionization and photodissociation fronts.

Summary of the physical properties of the ionised hydrogen regions are described in the paragraphs below:

HCHII regions: Murphy et al. (2010) identified HCHII regions, as regions that are soon after the star has just formed but before it develops into a UCHII region. The object is known as the hyper-compact HII region (HCHII) at this stage and is distinguished by more extreme electron densities (ne), emission measurements (EMs), and physical sizes. Sizes for this group are $\leq$ 0.05 pc (10,000 AU), while densities are $\geq 10^6$ cm^{-3} and emission measures are $\leq 10^{10}$ pc cm^{-6} (Hoare et al. 2006). Due to thermal and turbulence widening that is present in highly advanced HII regions, the objects often have wider radio recombination lines than expected (Murphy et al. 2010). High-mass stars are typically still completely enmeshed in their envelopes even in the most recent accretion stage, the HCHII region phase.

UCHII regions - UCHII regions are the physical manifestation huge newly created stars that are still ensconced in their native molecular clouds as stated by Churchwell (1990). UCHII regions can only be seen at radio, submillimeter, and infrared wavelengths due to dust in the molecular cloud core (Hoare et al. 2007). UCHII regions are small, intensely dense, and bright, as their name suggests. Due to the heated dust envelopes around them, which convert the whole star luminosity to far infrared light, at a luminosity of 100 μm, they are extremely luminous, ranking among the brightest objects in the Galaxy. UCHII regions are an important building block for large star systems. When the Lyman continuum emission from the enormous YSO is strong enough to ionize its birth environment, massive star formation occurs. (Hoare et al. 2007, de Carvalho 2013).

This spans the time between the central protostar's rapid accretion phase of star formation and, consequently, the time when the UC phase thanks the HII region for expanding, becoming more diffuse, and becoming less obscured, either by destroying the natal molecular core or by leaving the core (Churchwell 2002). UCHII regions were defined observationally by Wood & Churchwell (1989*b*) as regions with sizes $\leq$ 0.1 pc, densities $\geq 10^4$ cm^{-3} , and emission measures $\leq 10^7$ pc cm^{-6}. The ionized gas within the HCHII and UCHII regions not only lights up the immediate surroundings, but also reveals properties of the stars themselves (Hoare et al. 2006).

HII regions - HII regions are composed of atomic hydrogen gas that has been ionized by photons with energy $\geq 13.6eV$. According to (Peters et al. 2010), accretion and ionization happen at the same time when massive stars are born. Ionized outflows result from pressure of the 100000 K ionized gas being significantly higher than that of the 100 K accreting molecular gas (Peters et al. 2010).

Extreme UV photons ionise the hydrogen atoms in the vicinity of the YSOs, forming small growing pockets of HII regions. The Far Ultraviolet (FUV) radiation photodissociates molecules in the outermost regions of the HII regions. The exterior environment has has important impacts on the evolution of the HII regions. As a result a new intermediate region called a photodissociation region (PDR) which lies between the hot ionised region and colder molecular region.

In the Keto (2003) model, the HII region does not grow hydrodynamically because it is smaller than the critical radius, $r < GM/2c_s^2$, where c_s, G and M are the speed of sound in the ionised region, the universal gravitational constant and mass of the YSO, respectively. This means that the HII region is trapped by the gravitational field of the YSO. This is called a trapped HII region. The trapped HII region does not stop accretion, but the infalling material is ionised as it falls onto the YSO.

For a classical HII region around a YSO with a radius greater than the critical radius, $r < GM/2c_s^2$, it expands hydrodynamically, and the expansion disrupts the natal cloud (Zinnecker & Yorke 2007). Therefore, observations toward IRDCs, HMPOs, HMCs, HII regions and masers are important in probing the physical properties and dynamics of the evolution of HMYSOs at different epochs.

2.4.5 Maser-Based Evolutionary Timeline

After conducting in-depth analyses of several sources thought to be undergoing high-mass star formation, it was discovered that common maser transitions provide the greatest chance to identify an evolutionary scheme for these objects (Breen & Ellingsen 2012). Maser-based evolutionary allows qualitative investigations of the

related high-mass stars to be carried out, determining an evolutionary clock for high-mass star formation is a crucial step towards realizing a unified theory of star formation (Breen & Ellingsen 2012). Previous attempts to create a sequential history of the several common maser species in high-mass star formation areas have yielded inconsistent findings, mostly because they were based on tiny numbers of exceptional sources or severely biased samples (Ellingsen 2006). A rigorous maser evolutionary chronology has advanced significantly, thanks to the proliferation of fresh, huge, high-resolution, high-sensitivity maser datasets and related data. According to (Ellingsen et al. 2007), the various maser species are thought to reflect distinct evolutionary phases of massive star formation and favor various physical circumstances. Since many sources show emission from multiple maser transitions or species there must be significant overlap for the evolutionary phase traced by the most common types of masers as shown in Fig. 2.6. The class 1 and class II masers trace the earlier phases of star formation before the onset of other masers as shown in Fig. 2.6.

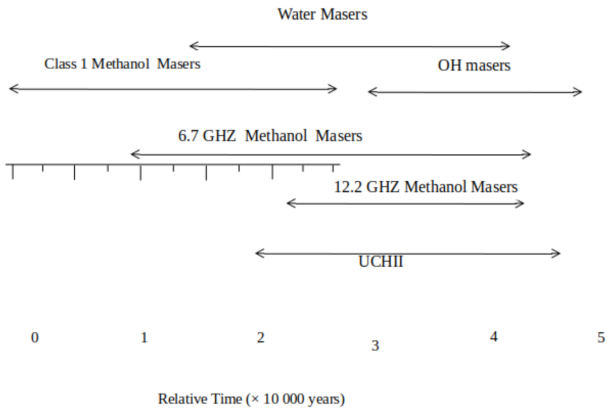

Figure 2.6: Evolutionary sequence for masers associated with massive star formation regions (Breen et al. 2010)

2.5 THEORIES OF THE FORMATION OF MASSIVE STARS

The observations toward the IRDCs, HMPOs, HMCs, and UCHII regions do not give us a complete picture of how a high-mass star is created, but point us in the direction of potential mechanisms at play of a high-mass star in a GMC. Therefore, a theory or theories are needed to try and finish the picture. Massive stars can enter the main

sequence while accretion is still taking place because they have short Kelvin-Helmholz periods. Because of this, large protostars become so luminous that radiation pressure may prevent further star formation. One fundamental issue with theories of massive star formation is this. There are three competing models to explain the high-mass star-forming process. These models are given by Zinnecker & Yorke (2007) as:

(i) core accretion (McLaughlin & Pudritz 1997, Yorke & Sonnhalter 2002, McKee & Tan 2003).

(ii) competitive accretion in a protocluster environment (Bonnell et al. 1997) and

(iii) stellar mergers in very dense systems.

Both the monolithic core accretion and the competitive accretion models are founded on accretion processes. Core Accretion and Competitive Accretion are the two major theories of massive star formation that are currently being researched.

2.5.1 Core Accretion

It is considered as a scaled-up version of low-mass star formation (Zinnecker & Yorke 2007). High accretion rates of the order 10^{-4} - 10^{-3} $M_{\odot}$ yr^{-1} can be achieved by considering a core with mass significantly higher than the thermal Jeans mass, requiring the gas in such a core to be turbulent and have strong magnetic fields. The strong magnetic fields may be important for suppressing fragmentation. A self-gravitating, centrally concentrated core initiates the accretion process by condensing a wide variety of masses from the clump-fragmenting environment around it. They then experience a somewhat orderly collapse using a central disc, eventually forming a single star or a small-N multiple. According to Tan et al. (2014), the stellar IMF is comparable to the pre-stellar core mass function.

Given that large stars are uncommon and only make up a modest mass fraction of the final star cluster, the circumstances that lead to this suppression should be rather uncommon. These large cores should start out with high densities, quick free-

fall periods, and fast accretion rates since they are projected to develop from highly pressurized clumps of gas. This situation is exemplified by the Turbulent Core Model (MT03) Tan (2005). Such a mechanism is anticipated to entail disc accretion and bipolar outflows, similar to the generation of low-mass stars (Jijina & Adams 1995).

The asymmetry helps to lessen the impact of radiation pressure on the accretion flow and escape of radiation in bipolar directions (Krumholz et al. 2005). Such a scenario is supported by some hydrodynamic simulations with varying implementations of radiation feedback, outflow feedback, turbulence, and magnetic field (Krumholz et al. 2007, Zhang et al. 2013). Disks and bipolar outflows are seen in these simulations and are important in reducing the radiation pressure barrier to form massive stars.

2.5.2 Competitive Accretion Model

At lower stellar densities, the competitive accretion model provides another possibility to form a massive star in a clustered environment (Bonnell et al. 2001, 2004, Bate 2009). In this case a massive star forms by not only accreting from its own core, but also initially unbounded material in the clump through Bondi-Hoyle accretion, competing with its stellar companions. Because of the interactions of the stellar companions in these coalescence models, the collapse is believed to be chaotic and not involving Keplerian disks and collimated bipolar outflow as in core accretion theory. The extent of a protostar's accretion domain, or the region from which gas can be gathered, determines how massive it can go. A star's ability to access gas is increased by being located in the protostellar cluster's centre, where gas flows down to the cluster's core. A protostar's early birth could give it an unfair advantage in the race to grow massive and enormous (Zinnecker & Yorke 2007). A mass segregated cluster and a direct relationship between a cluster's richness and the mass of its most massive star are also naturally produced via competitive accretion.

Considering a sizable, dense molecular gas cloud that contains several protostellar seeds that first condensed in some of the cloud's denser regions. Each of these con-

densations or cores has its own unique accretion zone, from which it can accrete cloud gas with a lower density (Larson 1978, Bonnell et al. 2001). The accretion domain of a protostar that is located in the cloud's center encompasses the entire cloud; however, the accretion domain of a protostar that is located off of the cloud's center is tidally confined by the total mass in the inner half of the cloud (Zinnecker & Yorke 2007). There will be competition among the protostellar masses for the cloud gas because of the cloud's finite mass because the supply is limited (Zinnecker & Yorke 2007). This will be especially true if the accretion zones begin to overlap.

Competitive accretion is a powerful mechanism because of two factors: (1) the cluster's ability to draw matter from farther away and concentrate it on the accreting stars; and (2) the expanding accretion radius of these stars as a result of their increasing mass (Zinnecker & Yorke 2007). However it is not clear if competitive accretion solves the radiation pressure problem (Edgar & Clarke 2004). An anisotropy of the thermal radiation field can be used to get around the radiation pressure issue that arises during the birth of massive stars (Kuiper et al. 2014). The development of a circumstellar disc inevitably results in the establishment of such an anisotropy. According to Kuiper et al. (2010), the anisotropy of the thermal radiation field lowers feedback onto the accretion flux, enabling the development of the most massive stars known. Competitive accretion has the benefit of providing a tangible means of gathering the material. There is a considerable amount of gaseous material that is gravitationally drawn to the center of the protocluster clump or cluster of stars, where it is accreted by the protomassive stars (Bonnell 2008).

2.5.3 Stellar Collisions and Mergers

Historically, there were two factors that led to the initial suggestion that large stars develop through stellar collisions. (a) At the time, it was believed that radiation pressure on dust prevented gas accretion, which was then thought to proceed spherically symmetrically. As of right now, this worry no longer exists (Zinnecker & Yorke 2007). (b) Because huge stars were packed too closely together in dense clusters, there was

concern that there might not be a large enough gas reservoir for monolithic collapse. Even though not all massive stars develop in closely packed clusters, many do so in widely dispersed OB associations, this is still a cause for concern (Zinnecker & Yorke 2007).

In the Stellar Merger scenario (Bonnell et al. 1998), massive protostars can directly collide and merge when the stellar densities of a forming star cluster are high enough ($\sim 10^8 pc^{-3}$). The explosive, wide-angle outflows from the Orion Molecular Cloud (OMC-1) core in the OMC may be an example of that produced by a protostellar merger event (Bally & Zinnecker 2005). The star density in the cluster centre (mass segregation at birth) is growing, as a result of sustained competitive accretion (mass loading), grazing collisions may become inevitable (Zinnecker & Yorke 2007). The most massive stars in the richest young clusters (such young globular clusters) will be the only stars in which stellar mergers will be significant and infrequent (Zinnecker & Yorke 2007). The fact that continuous competitive accretion (mass loading) raises the star density in the cluster center (mass segregation at birth) may eventually make grazing collisions inevitable, which is one reason to propose stellar mergers (Zinnecker & Yorke 2007). Small impact parameter stellar collisions may be the mechanism that gives rise to fast spinning massive stars, which are the precursors of (slow, long-duration) gamma-ray bursts.

2.6 MASER THEORY

MASER is an acronym for Microwave Amplification by Stimulated Emission of Radiation, and in astrophysical environments it is a naturally occurring phenomenon. The emission occurs in both the microwave and radio regimes of the electromagnetic spectrum. Within these wavelength regimes, the term "maser emission" refers to coherent emission at a certain frequency that is enhanced by the population inversion of the molecular energy levels. In an astrophysical context, the creation of a maser requires a level population inversion, pumping mechanism (radiative or collisional), velocity coherence along the line of sight, and a stimulating photon (Maswanganye

2018).

The occurrence of maser emission, according to Maswanganye (2017), takes place when molecules are stimulated by photons with energy (hν) to release new photons that have an energy level comparable to the photons that were initially released. Molecular collisions or interactions with non-black body radiation cause a population inversion between two energy levels, which is necessary for the production of masers. The principle of radiative transfer will be discussed first, due to the fact that astrophysical masers form in a gaseous media, taking into account the interactions that occur between the gaseous medium and radiation from a source is necessary (Gray 2012, Maswanganye 2017)

The preceding subsections provide an overview of the theories relating to maser emission, saturation of masers, radiative transfer in masers and pumping mechanisms (Batrla et al. 1987). It is necessary to describe the circumstances that must be met for population inversion to take place. The majority of the information shown below comes from Elitzur (1992*b*).

2.6.1 Rate Equations

Taking into account a two-level system with energy separation $\Delta E = E_2 - E_1$ where E_1 is the lower energy level and E_2 is the higher energy level as shown in Fig. 2.7, maser emission can be demonstrated. When matter interacts with radiation, one of three things may happen: (i) Einstein A-coefficient A_{ij} for spontaneous emission, (ii) Einstein B-coefficient B_{ij}, for absorption and (iii) for induced or stimulated emission,Einstein B-coefficient B_{ji} (ter Haar D. 1967, English version). Transition from energy level i to j is indicated by the subscript ij.

The energy levels can be populated and depopulated by radiation or collisional events as shown in Fig. 2.7. When the two-energy-level population model assumes thermodynamic equilibrium under the Boltzmann equation, the following equations connect

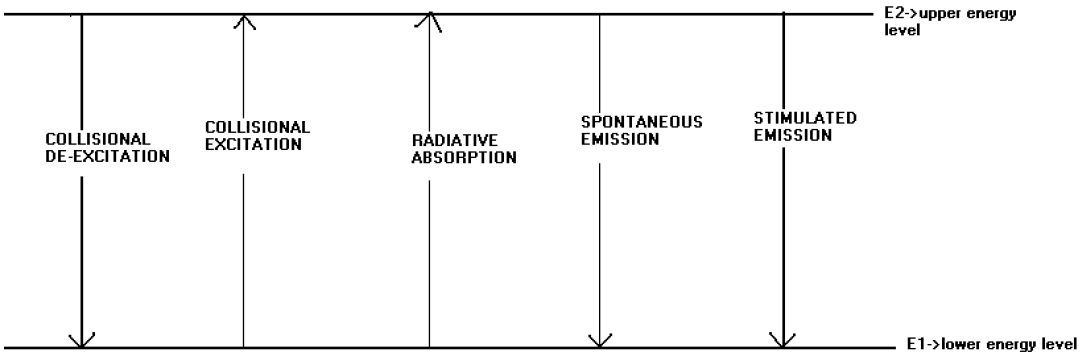

Figure 2.7: A schematic simple two level system with energy separation ΔE. The arrow identifies the energy level procedures that can increase and decrease their population (Maswanganye 2018)

.

the Einstein coefficients:

$$A_{ji} = \frac{2hv^3 B_{ji}}{c^2}; B_{ij} = \frac{g_j B_{ji}}{g_i} \tag{2.8}$$

where c is the speed of light in the vacuum, ν is the frequency and g_i is the statistical weight. Einstein's coefficients are demonstrated to be independent of the thermal equilibrium in Equation 2.8. They are depending on the system's tiny quantities despite being temperature independent.

The statistical weight as well as the dumping rate for all levels will be considered to be the same in our earlier described two-energy-level model shown in Fig. 2.7. Therefore, ($g_1 = g_2 = g$) and dumping rate ($\Gamma_1 = \Gamma_2 = \Gamma$). The system creates the dumping rate term to account for particles that can decay to non-masing levels. The set of equilibrium equations that are produced are as follows:

$$0 = p_{1v} - \Gamma n_{1v} + B_{12v} J_v n_{2v} - B_{12v} J_v n_{1v} + A_{21} n_{2v} - n_{1v} C_{12} + n_{2v} C_{21} \tag{2.9}$$

and

$$0 = p_{2v} - \Gamma n_{2v} - B_{12v} J_v n_{1v} + B_{12v} J_v n_{1v} - A_{21} n_{2v} - n_{1v} C_{12} + n_{2v} C_{21} \tag{2.10}$$

When equation 2.9 is substracted from equation 2.10, the population difference $\Delta n_v = n2_v - n1_v$, is represented as follows:

$$\Delta n_v = \frac{\Delta p}{\Gamma + 2B_{21}J_v}, \Delta n_v = \frac{\Delta n_0}{1 + \frac{J_v}{J_s}}\phi(V) \tag{2.11}$$

where $\Delta n_0 = \frac{p_2 - p_1}{\Gamma}$ is the emission line profile, and $J_s = \frac{\Gamma}{2B_{21}}$ stands for saturation intensity (Maswanganye & Gaylard 2012). The population inversion efficiency can be calculated using the formula in equation 2.12, ignoring the collision and spontaneous decay terms:

$$\eta = \frac{p_2 - p_1}{p_1 + p_2} \tag{2.12}$$

In equations 2.11 and 2.12, $p_2 > p_1$ is a non-thermal population inversion ($n_2 > n_1$) and maser activity is possible ($\eta > 0$), but when $p_2 \leq p_1$ (anti-inversion) maser activity not possible ($\eta \leq 0$) due to the absence of population inversion.

Radiative and collisional pumping are two recognised potential pumping mechanisms for masers. These two mechanisms excite the system to a higher state before allowing it to descend to the masing level (Maswanganye & Gaylard 2012). In equations 2.9 and 2.10, the pumping rate terms are denoted by $p_1 nu$ and $p_2 nu$. The absorption coefficient can be calculated using the equation presented in Elitzur (1992*b*) and also by Lo (2005) as follows:

$$k_v = \frac{hv}{4\pi} n_1 B_{12} (1 - \frac{n_2/g_2}{n_1/g_1})\phi(V) \tag{2.13}$$

In situations in which the absorption coefficient is negative , masers occur because it means the radiation will be magnified as it passes through the cloud or other medium.

2.6.2 Population Inversion

Astronomical masers can only develop when population inversion and velocity coherence occur. According to velocity coherence and population inversion, doppler shift along the line of sight must be small, and there must be fewer particles in the upper

energy level than in the lower (Maswanganye & Gaylard 2012). Astronomical masers require population inversion and velocity coherence for formation. Pumping is the method by which population inversions $p_2 > p_1$, develop in masers. System particles typically reside in the ground state in the absence of any interesting mechanisms. The pump rate per sub-level of the upper rate must therefore be greater than that of the lower rate in order for population inversion to occur (Maswanganye & Gaylard 2012).

The effectiveness of the pump process is defined by the fact that the populations n_u and n_l can become inverted under certain conditions. Such a deviation from thermodynamic equilibrium can be denoted as $n_u/g_u > n_l/g_l$. The populations of each energy level causing a maser transition can be described by considering a "three" energy level model, (see Fig. 2.8, where level "3" actually represents all levels above level "2" (Reid & Moran 1988).

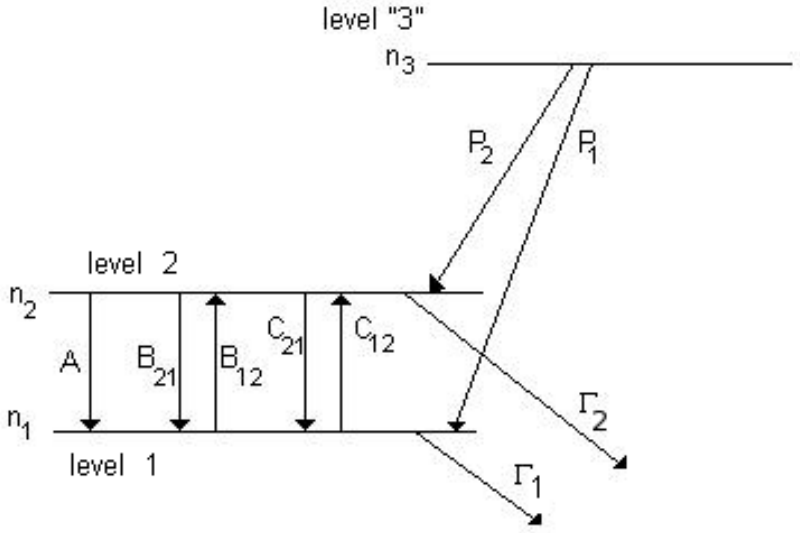

Figure 2.8: A schematic of a three energy level model showing the populations of each energy level causing a maser transition (Maswanganye 2018)
.

The values P_u represent the pumping from all other energy levels into the maser levels and Γ_i losses out of the maser levels into any other energy. This gives the level

populations as follows:

$$\frac{dn2}{dt} = P_2 - \Gamma_2 n_2 - A_{21} n_2 - I_{21}(n_2 B_{21} - n_1 B_{12}) - (n_2 C_{21} - n_1 C_{21}) \tag{2.14}$$

$$\frac{dn1}{dt} = P_1 - \Gamma_1 n_1 - A_{21} n_2 - I_{21}(n_1 B_{12} - n_2 B_{21}) - (n_1 C_{12} - n_2 C_{21}) \tag{2.15}$$

Under normal conditions the final three terms equations in 2.14 and 2.15, will not produce a population inversion. Meaning that either the pumping or loss rates must be different creating the population inversion (Elitzur 1982).

Population inversions can be produced by collisional mechanisms, radiative processes or chemical processes. Pumping mechanisms may be used to describe the processes. The relevance of each step might vary greatly depending on the type of environment, in particular the radiation and ambient density. The three processes can sometimes take place at the same time. The low densities predicted for megamaser regions allows radiative process only. Discussions of the processes is as follows:

- Radiative pumps can be viewed as 'converters' that absorb photons of frequency ν_p and change them into photons of frequency ν with a pump-dependent efficiency η. Each maser photon may require many photons, maybe of varying frequency. Considering the energy level system shown in Fig. 2.8, under normal conditions a population inversion due to radiation should not be possible, i.e. the pumping radiation is behaving as a blackbody. However, if the radiation deviates from this distribution population inversion is possible (Elitzur 1992*b*). One possibility is maser molecules mixed with optically thin dust where the intensity is frequency dependent, providing the population inversion by which more level 1 molecules are promoted to level 3 (Elitzur 1992*b*). Radiative pumping techniques need at least one pump photon for every maser photon generated. The strongest 6.7-GHz CH_3OH masers have an unusually high brightness, which could be problematic for radiative pumping schemes.

  High-resolution measurements of class II CH_3OH maser sources at these fre-

quencies are required to assess whether or not radiative pumping in the far infrared or submillimeter is feasible. If transitions have widely changing optical thickness and radiative rates are high relative to collisional rates (for example, when molecular densities are low), then pure radiative processes may result in population inversions.

- For collisional processes to create a population inversion, collisions with other species in the interstellar medium must occur with different collision cross sections. As presented in Fig. 2.8, it should be either the population of level 1 become depleted or transitions from level 3 into level 2 occur preferentially over those to level 1 leading to an over population in the upper maser energy level (Reid & Moran 1988). This form of pumping can be limited by the collision rates. High amount of collision would result in the thermalisation of the gas and stop the maser (Elitzur 1992*b*). By re-thermalizing the populations, higher collisional rates (for example, large densities) would typically extinguish population inversions.

- Chemical and photochemical reactions, including UV photodissociation (Andresen et al. 1984), which places molecules in an excited state where radiative decay is slow and collisional de-excitation is uncommon due to low densities, can cause population inversions (Andresen et al. 1984).

2.6.3 Maser Saturation

When $\frac{J_v}{J_s} << 1$, maser population difference Δn_v shown in equation 2.11 is referred to as an unsaturated maser and has no effect on maser radiation because it does not interact with it. Before interacting with radiation in the unsaturated maser instance, particles are pushed with pumping rate p and released with dumping rate Γ (Elitzur 1992*b*). Masers are highly brilliant and very compact because the unsaturated masing implies exponential amplification, which causes the spectral and spatial Full Width Half Maximum (FWHM) to become narrower (Maswanganye &

Gaylard 2012).

When $\frac{J_v}{J_s} >> 1$, saturated maser arises and how the maser radiations will impact the population inversion is depicted by the equations 2.11 and 2.12. The photon output rate will increase, the maser growth will be reduced (along with the absorption coefficient), the line profile will be re-broaden, and the FWHM will become more narrow (Elitzur 1992*b*). The expression that can be used to calculate the overall population of the maser system is n_v and $n_v = n\phi(V)$, where $\phi(V)$ denotes the emission line profile. The line profile contains information regarding the emission's broadening or narrowing (Elitzur 1992*b*).

2.6.4 Radiative Transfer in Masers

The radiative transfer equation 2.16, governs how radiation travels through space,

$$\frac{dI_v}{ds} = K_v I_v + J_v \tag{2.16}$$

where I_ν represents the specific intensity of photons at a given frequency ν, passing through area dA, with direction within solid angle $d\omega$, travelling along a distance s. The specific intensity at any point along s is affected by the material through which is passes. When passing through a volume dV equal to dAds, j_v gives the emission coefficient, i.e. the energy emitted by the volume element dV. The factor K_v represents the absorption of energy of specific intensity I_v passing through volume element dV (Spitzer Jr 1978).

2.7 ASTROPHYSICAL MASERS

Interstellar masers are among the most dependable indicators of the presence of recently formed high-mass star clusters (Breen et al. 2013, Hernández-Hernández et al. 2019). Masers are very well adapted to be used as probes of the regions because they have properties that make them good signposts of star formation zones. Due to their vast distribution throughout the galaxy and connections to both evolved stars

and star-producing regions, masers sources can shed light on the genesis and demise of stars. Masers are therefore ideal instruments for investigating the gas kinematics in which they are created (Torrelles et al. 2005). Since they occur at millimeter and centimeter wavelengths, they are numerous, powerful, and unaffected by the significant extinction that hinders research in other wavelength ranges (Ellingsen et al. 2007).

The ability to employ masers as an evolutionary clock would be highly desired because they are fairly obvious markers of star formation zones. Due to their intrinsically powerful radio emissions that are not reduced by the dust, maser sources are particularly helpful for research involving examinations of compact items that accrete dusty and compact material. The usage of astronomical masers is possible in measuring the precise distances to sources and to analyze interstellar scattering. Maser proper motions improve upon earlier approaches to measuring distance in terms of kinematics (Pestalozzi et al. 2005). Through the use of maser emission, one is able to investigate the dynamics of not only the associated star-forming source but also the ISM and the entirety of the Galaxy (Hill 2006).

Many molecular transitions have been found to exhibit masing characteristics. H_2O, OH, and CH_3OH are the three most common masers connected to HMSF regions (Churchwell 2002). A few compact HII regions and just a few transitions have also shown maser emission in the H_2CO, NH_3 and SiO molecular lines (Caswell, Vaile & Ellingsen 1995).

Masers are often restricted to very small (a few tens of AUs) and highly dense (10^6-$10^9 cm^{-3}$), clumps, making them superb scalar probes for investigating the physics and dynamics of HMSF regions on scale sizes where it would be exceedingly challenging or impossible to directly detect them (Churchwell et al. 1990). Refer to Reid & Moran (1981), Elitzur (1982, 1992*b*), Churchwell (2002) for reviews on masers. While methanol masers will be discussed in section 2.8, a brief explanation of masers connected to HMSF regions is investigated in this part.

Hydroxyl Masers (OH): There have been numerous studies of hydroxyl (OH) masers since Weaver et al. (1965) made discovery of OH emission in 1965 and Perkins et al. (1966) made postulation of this molecule's masing nature in 1966. Based on 1665 MHz OH maser emission studies in star-forming regions, we know that the OH maser is always identified in close proximity to the densest and most compact HII region, deep within the complex and far from the more brilliant stars (Hill 2006). This would suggest that the youngest UCHII regions are linked to OH masers.

The greatest OH maser emissions, are at frequencies 1665 MHz and 1667 MHz (Hill 2006). As a result, most OH maser observations are carried out at these frequencies. OH masers typically coexist with other maser types (specifically H_2O and CH_3OH), IR sources, and more broadly active regions of star formation, according to Caswell et al. (1980) and Slysh et al. (1995). Due to the fact that OH is the only paramagnetic masing molecule, it can be used to analyse both the velocity in masing regions and the magnetic field conditions on scales of 10^{13} to 10^{17} (Reid & Moran 1981). In the large star-forming regions ON 1, K3-50, and W51 Main/South, OH masers have been employed to estimate proper motion (Fish & Reid 2007).

Water Masers: H_2O maser emission arises from the $6_{16} \rightarrow 5_{23}$ rotational transition at 1.3 cm (22 GHz). It has been established that water maser emission is present everywhere in the Galaxy, since it was first detected by Cheung et al. (1969). Genzel et al. (1978), Codella et al. (1994), Colomer et al. (2000), Vorster et al. (2021) have undertaken studies on H_2O masers. It should be noted that the 22-GHz H_2O maser is not the only transition in H_2O that exhibits masing behavior. Examples of other H_2O masers include the 183 GHz rotational transition between $3_{13} - 2_{20}$ by Waters et al. (1980) and the 321 GHz transition $5_{15} - 4_{22}$ by Menten et al. (1990). Water masers are common in evolved star systems and around active star-forming regions of all mass ranges according to Elitzur (1992*a*), Reid & Moran (1981). Radiative pumping of H_2O masers was proposed by Goldreich & Kwan (1974), whereas collisional pumping was proposed by Deguchi (1977). The collisional pumping mechanism postulated by Deguchi (1977) is supported by observations toward the H_2O masers (Reid & Moran

1981, CooKE & Elitzur 1985).

Highly collimated molecular bipolar outflows have been linked to water masers in high-mass star-forming regions (Martí et al. 1999, Sridharan et al. 2002). Other maser species, like OH and CH_3OH, and UCHII regions are sometimes discovered in close proximity to H_2O masers. These H2O maser species and their related UCHII regions are not always colocated spatially. Other masers' geographic association with UCHII regions has been studied, for instance by Sridharan et al. (2002). They picked out 69 high-mass protostars. They also undertook imaging free-free (at 3.6 cm) and dust continuum (at 1.2 mm) emissions, they also scanned H_2O and looked for 6.7 GHz CH_3OH maser transitions. They identified H_2O masers at 29 sources, and CH_3OH masers at 6.7 GHz at 26 sources. The 6.7 GHz CH_3OH and H_2O masers had an emission velocity spread of 15 and 70 km s^{-1} respectively. The fact that H_2O and 6.7-GHz CH_3OH masers come from different settings explains their dissimilar velocity ranges. In addition, this suggests that their excitation methods are distinct. The high velocities of the H 2 O masers suggest that they follow the molecular bipolar outflow, while the 6.7-GHz methanol masers trace the innermost component of the cloud, the envelope of the central star or a disk.

The hypothesis that H_2O masers trace the outflows and are collisionally pumped is supported by multi-epoch VLBI observations of masers, which can yield the internal maser proper motion of a cloud. The G28.8+0.07 observations by Li et al. (2012) include VLBI observations at multiple wavelengths (for the H_2O and 6.7-GHz CH_3OH masers) and a single epoch (for the 1.665-GHz OH maser), as well as the 1.3- and 3-cm radio continuum, and the 24.5-m Subaru observations. A study towards massive protocluster NGC 6334I by Hunter et al. (2017) that is linked to both 6.7-GHz CH_3OH and H_2O masers increased dramatically in maser and dust emission, suggesting an abrupt accretion event in the development of the huge protostar.

Silicon Monoxide Masers (SiO): Snyder & Buhl (1974) discovered a collection of unexplained lines at 86, 245 MHz (3.48 mm) directed towards the Orion Nebula

molecular cloud (Hill 2006). They came to the conclusion that this strong emission was in agreement with the J = (2 - 1) transition of the first vibrationally excited state of $^{28}Si^{16}O$ at its rest frequency. Since then, reports of the finding of more SiO masing transitions have appeared in the literature. According to Snyder & Buhl (1975), SiO masers are typically found in close proximity to M-type variable stars, many of which also emit OH and H_2O masers. SiO maser emission toward Orion were reported by Snyder & Buhl (1974).

UCHII regios, infrared sources, OH masers, and H_2O masers have all been linked to SiO masers (Hill 2006). When Harju et al. (1998) targeted for UC HII regions, OH maser positions, and H_2O maser positions, they found that the most SiO maser emission was detected in the direction of the most intense H_2O masers. SiO masers are linked to molecular bipolar outflows in HMSFRs. Using 6.7 GHz CH_3OH maser detections, a molecular line survey towards EGOs resulted in the identification of the SiO(5-4) emission and HCO+ (3-2) line profiles, both of which indicate the existence of dynamic molecular outflows (Cyganowski et al. 2011). For a population inversion to occur, it is necessary to precisely tune a number of physical parameters, as noted by Elitzur (1992*a*) in his study of various pumping mechanisms for SiO masers. SiO masers, however, can form in a variety of physical situations if they are collisionally pushed. This suggests that collisional pumping of the SiO masers is more likely, while radiative pumping cannot be ruled out entirely.

Ammonia Masers (NH_3): The first definitive discovery of ammonia masers at several inversion transitions was reported by Madden et al. (1986). The NH_3 (6, 3) line looked the same in W51 but was absorbed in NGC 7538. The (J, K) = (9, 6) inversion transition, on the other hand, made maser-like emission that went toward W51, NGC 7538, W49, and DR 21(OH) (Hill 2006). Madden et al. (1986) says that these lines were found in regions with Strong infrared sources and dense H II regions, as well as H_2O and OH masers.

Formaldehyde Masers (H_2CO): Downes & Wilson (1974) discovered the first

formaldehyde masers. Since there are so few confirmed H_2CO Galactic masing sources, formaldehyde maser emission is a somewhat rare event in our Galaxy (Hill 2006). Mangum et al. (2008, 2013) found 13 targets with formaldehyde H_2CO transitions at 4.8 and 14.5 GHz, primarily in absorption but occasionally also in emission. The short lifetimes of the pumping source or the intrinsically low maser gain may be to blame for the tiny number of H_2CO masers that are known (Forster et al. 1985). 10 extragalactic H_2CO (mega) masers have been detected and are $\sim 10^5$ – 10^{10} times more luminous than their Galactic counterparts as pointed out by Pratap et al. (1994). The presence of H_2CO masers was investigated in a sample of 93 regions by Araya et al. (2015) to see if they are unique to HMSFRs. Out of the total of 93 regions, 22 were found to be young HMSFRs in the Hi-GAL. Of the 93 locations studied, 71 did not produce any high-mass stars; of these, 25 were low-mass star-forming regions, 31 were late-type stars, and 15 were either planetary nebulae or stars on the post-asymptotic giant branch. The 71 locations that were not HMSFRs did not show any signs of formaldehyde maser emission and just one new detection of H_2CO was made amongst the HMSFR in the sample. These findings from the 93 region survey are used to support the hypothesis that HMSFRs are the only places where the rare H_2CO is detected. They may also be tracking the origin of molecular bipolar outflows. This lends credence to the notion that H_2CO masers are pumped by collisions, however it does not rule out the possibility that they are pumped by radiative processes as well.There has been no definitive evidence about the pumping mechanism of H_2CO masers. The calculations of Van der Walt (2014) imply that the H_2CO masers are pumped by collisions, while Boland & De Jong (1981) proposed that free-free radio continuum pumps them.

2.8 METHANOL MASERS

When looking for N_2O absorption in the direction of Orion A, Barrett et al. (1971) announced the discovery of the first interstellar methanol (CH_3OH) maser emission (Hill 2006). Numerous novel masing transitions of CH_3OH have been found since the

discovery of methanol maser emission. The finding of two potent methanol maser emissions at 6.7 GHz by Menten (1991*a*) and 12.2 GHz by (Batrla et al. 1987) was particularly significant, arising from the $5_1 \rightarrow 6_0$ A^+ and the $2_0 \rightarrow 3_{-1}$ E transitions, respectively.

Interstellar methanol masers are among the finest markers of regions that are just beginning to generate high-mass stars. They possess characteristics that make them the best choice for usage as regional probes. The maser emission is concentrated and strong, allowing milliarcsecond precision observations with VLBI (Ellingsen et al. 2007). Thus, masers make excellent study instruments for dynamics of the gas in which they are produced (Torrelles et al. 2010). Despite the possibility that they are equally efficient physics probes in the same regions, the intricacy of maser pumping methods makes it challenging to confidently interpret the data (Cragg et al. 2002).

Batrla et al. (1987) proposed that methanol maser emission might be divided into two types, because the existence of a methanol maser operating at 12 GHz was unknown towards a 25 GHz maser (Hill 2006). Originally designated as classes A and B by Batrla et al. (1987). Menten (1991*a*) realized the potential for misunderstanding caused by CH_3OH species with A and E symmetry to be identified using this naming scheme and renamed the two classes I and II. The class I methanol masers (MMIs) are found offset from the UCHII region while the class II methanol masers (MMIIs) appear to be close to the UCHII region (Maswanganye 2017).

2.8.1 Class I Methanol Masers

The class I methanol masers are those operating at 9, 25, 27.4, 29.6, 36, 44.1, 84.5, 95.2, 104.3, 132, 146.6, 156.8, 218.4 and 229.7 GHz (Hunter et al. 2014, Yanagida et al. 2014, McCarthy et al. 2018) . According to Batrla et al. (1987), Menten (1991*a*), there are no overlapping lines between Class I and Class II sources.

Class I masers are often placed apart from compact continuum sources and are mostly collisionally pumped. As stated by Leurini et al. (2016) and the most recent discovery

of class I methanol maser operating at the $5_2 - 4_1$ E transition (266.8 GHz) by Chen et al. (2019) numerous different Class I transitions have been recorded. Submillimeter Array (SMA) measurements around the HMSFR G352.630-1.067 (distance 0.7 kpc) have identified this methanol transition. Southwest of W3(OH), the 84.5 and 95.2 GHz weak masers offer compelling evidence for collisional pumping and enable the determination of physical parameters (Sutton et al. 2004).

Supernova remnants, massive protostellar induced outflows, interactions between expanding HII regions and the surrounding molecular gas, places where shocks compress gas and heat it are just a few of the phenomena that may be linked to class I methanol masers (Voronkov et al. 2010, Pihlström et al. 2014). The masers may be related to earlier periods of stellar history before the creation of UCHII regions and other evidence of star formation. They might therefore represent real protostars that are still gaining mass. In both high- and low-mass stars, there have been sightings of Class I methanol masers (Kalenskii et al. 2010, Rodríguez-Garza et al. 2017). Voronkov et al. (2014) used the Australia Telescope Compact Array (ATCA) to create high angular resolution maps of 71 high-mass star-forming regions for 36- and 44-GHz MMIs, finding that these MMIs are correlated with molecular bipolar outflows, expanding HII regions, dark clouds, and shocks traced by 4.5 μm emission and 8.0 μm filaments. It was hypothesized that developed YSOs were related with the MMIs in the maps created by Voronkov et al. (2014), which showed MMIs that were dispersed both geographically and in velocity domains. Gómez-Ruiz et al. (2016) provided additional evidence that lends credence to this theory. In their study, they found that 16 of 42 regions with HMPOs had 44-GHz MMIs, which corresponds to a detection rate of 38%; conversely, 13 of 24 regions with UCHII contained 44-GHz MMIs, which corresponds to a detection rate of 54%. When compared to the detection rate in HMPO regions, the high detection rate of 44-GHz MMIs in UCHII regions suggests that MMIs are prevalent in highly advanced HMYSOs (Cyganowski et al. 2009). Gómez-Ruiz et al. (2016) suggest that the MMI might also be tracking shocked gas, which might originate from a variety of sources including cloud-cloud collisions and

increasing HII regions.

2.8.2 Class II Methanol Masers

The 6.7 GHz and 12.2 GHz lines are two examples of extremely bright Class II methanol masers, although maser emission has also been observed at 19, 23, 28, 37, 38, 107, and 157 GHz (Wilson et al. 1984, 1985, 1993, Slysh et al. 1995). At 108.8 GHz, a new, weaker class II maser line was discovered by Val'Tts et al. (1999). Class II CH_3OH masers are distinguished by their two strongest transitions at 6.7 GHz Menten (1991*a*), and and 12.2 GHz Batrla et al. (1987), both of which necessitate an abundance of methanol (Mohamed 2022).

Class II masers can be found in a variety of evolutionary stages, according to observations of methanol masers that are spatially associated with both millimetre and centimetre continuum emission (Pestalozzi et al. 2005). They are radiatively pumped and found in close vicinity to HII regions (Cragg et al. 1992, Sobolev et al. 1997). (Breen et al. 2013), reported that class II methanol masers are indicators of bright YSOs.

Table 2.3: Some masing transitions in Class I and II methanol masers. Source:Pandian (2006)

Class I		Class II	
Transition	ν (GHz)	Transition	ν (GHz)
$9_{-1} - 8_{-2}$ E	9.9	$5_1 - 6_0 A^+$	6.7
$J_2 - J_1$ E	25	$2_0 - 3_{-1}$ E	12.2
$4_0 - 3_1$ E	28.3	$2_1 - 3_0$ E	19.9
$4_{-1} - 3_0$ E	36.2	$9_2 - 10_1 A^+$	23.1
$7_0 - 6_1$ A +	44.1	$7_{-2} - 8_{-1}$ E	37.7
$5_{-1} - 4_0$ E	84.5	$6_2 - 5_3 A^-$	38.3
$8_0 - 7_1 A^+$	95.2	$6_2 - 5_3 A^+$	38.5
$9_0 - 8_1 A^+$	146.6	$3_1 - 4_0 A^+$	107.0

Some have reasoned that because methanol masers have linear structures with structured velocity structures, they must trace edge-on disks (Norris et al. 1993). Methanol masers are frequently oriented toward an outflow rather than a disc, according to investigations on maser proper motions by Fish (2007), shocked H_2 by De Buizer (2003),

and SiO De Buizer et al. (2005). These characteristics might be explained by the shock front's propagation into an area with expansive velocity structure, including rotation (Dodson et al. 2004).

Class II methanol masers are discovered along the surface of an outflow cavity, where shocked material is present, according to mid-infrared pictures of some sources (De Buizer et al. 2005, Fish 2007). Methanol masers have been shown to be offset from UCHII regions in some sources, which suggests that they are similar to hydroxyl masers in that, they manifest in the gas molecules outside the ionization front after being shocked (Phillips & van Langevelde 2005).

Theoretical studies by Cragg et al. (2005), reported that class II masers that are radiatively pumped were detected in less violent regions close to YSOs. HMYSOs are nearby and are the source of Class II methanol masers at 6.7 and 12.2 GHz (Chibueze et al. 2017). Such studies might help to improve the characterization of the local physical conditions when they are seen simultaneously (Durjasz et al. 2021). Theoretically, methanol masers of classes I and II cannot coexist because they are both radiatively pumped and the former are collisionally excited (Menten 1991*b*).

2.8.3 6.7 GHz Methanol Masers

The 5_1 - 6_0 A^+ line of methanol at 6.6685192 GHz, was identified by Menten (1991*a*), whose frequency was precisely determined by Breckenridge & Kukolich (1995). As the second brightest maser transition, it is also the brightest of the Class II methanol masers yet observed, for Galactic maser surveys, this is a frequently used line (Breen et al. 2015). For instance, Menten et al. (1992) discovered that a prototype source called W3(OH)'s multiple maser spots have brightness temperatures of 3×10^{12} K and higher. Methanol's 6.7 GHz transition has been shown to be an especially useful marker since it is both frequent and potent, and the only places it seems to be linked to are places where massive amounts of new stars are being formed (Minier et al. 2003*a*). The second-most powerful Class II methanol maser, the 12.178597 GHz

$2_0 - 3_1E$ line, sometimes accompany the 6.7 GHz masers.

In a sample of 535 IRAS color-selected candidates, Walsh et al. (1997) employed the Wood & Churchwell (1989*a*) color selection criterion to look for the 6.7 GHz methanol maser emission. They found evidence of methanol maser emission towards 201 of the targeted sites with a detection rate of 38%. The IRAS PSC was used by Szymczak et al. (2000*a*), Szymczak et al. (2000*b*), to color-select potential survey participants for a 6.7 GHz methanol survey. After looking through 1399 sources, a detection rate of 13% was discovered. It was discovered that there were many methanol maser sources to have colors that were significantly outside the conventional color ranges for UCHII regions. Szymczak et al. (2002) claimed that the number of CH_3OH maser sources is severely underestimated by IRAS-based searches by a factor of 2. The huge star-forming region G358.93-0.03's Class II CH_3OH maser line, which operates at 6.7 GHz, began to flare on January 14 of 2019, according to Sugiyama et al. (2019), the flux has grown to 99 Jy, an increase of an order of magnitude, after only two weeks.

2.8.4 Methanol Molecular Structure

Each atom or molecule has its own distinct set of energy levels. Quantum numbers characterize each possible energy level. Electronic, rotational, and vibrational eigenstates are the most common types of energy levels in molecules (Maswanganye 2018). HMSFRs are known to feature transitions in the CH_3OH molecule that exhibit massing behavior. The simplest member of the alcohol hydrocarbon family is methanol, which is made up of methyl (CH_3) and hydroxyl (OH) groups. It is an asymmetric top molecule, and Fig. 2.9 schematic depicts its chemical structure. The three major moments of inertia of CH_3OH have different values, making it an asymmetric top molecule (Flower 2007). Fig. 2.9 shows that the CH_3OH bond between carbon and oxygen can rotate, denoted by the double-headed arrow. Hindered internal rotation is the name the type of rotational motion seen here. Because of the potential barrier that depends on the angle and possesses three-fold symmetry, the torsional motion is not free and remains unchanged even after being rotated by 120 degrees (Flower

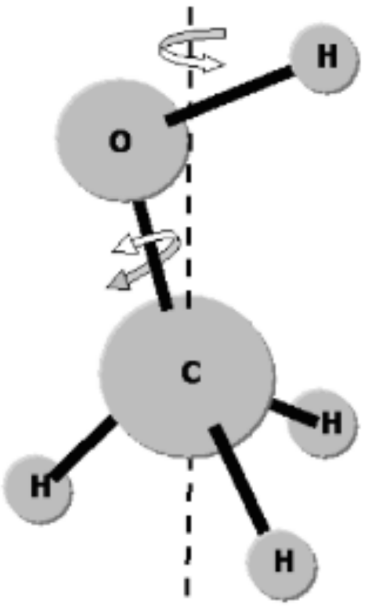

Figure 2.9: A representation of CH_3OH asymmetric top molecular structure (De Buizer 2000).

2007). Both ground-state and excited-state torsional CH_3OH transitions are seen. Quantum numbers J, representing the total angular momentum, and K, representing the projection of J onto the major axis of the molecule, further characterize the eigenstates of CH_3OH for the torsional state (ν_t). The eigenstate is either an E- or an A-type CH_3OH species, depending on the type provided by the J K type. Quantum mechanical selection criteria control the radiative transitions between states. Quantum mechanical selection criteria control the radiative transitions between states. A-type symmetry is $0 \leq K \leq J$, and $K > 0$ hasa double split by asymmetry denoted by the labels A^+ and A^-type CH_3OH (Maswanganye 2018). CH_3OH E-type has $-J \leq K \leq J$ where in E_1, $K \geq 0$ in E_12, $K \leq 0$. Two such transitions in CH_3OH are the 6.7- and 12.2-GHz $5_1 - 6_0$ A^+ -type and $2_0 - 3_{-1}$ E-type transitions. There is evidence that some CH_3OH molecule transitions exhibit masing behavior.

2.9 MASER VARIABILITY

Methanol masers connected to Massive Young Stellar Objects (MYSO) exhibit variability. Monitoring studies on variability have also been conducted on the 6.7 and

12.2 GHz lines (Goedhart, Gaylard & van Der Walt 2005). These investigations have revealed varied and plentiful sources of variability, such as periodic variations and a possible delay between features due to the length and speed of the light's travel (Goedhart, Gaylard & van Der Walt 2005, Goedhart, Minier, Gaylard & Van Der Walt 2005). 6.7 GHz CH_3OH masers were reported to be variable, according to MacLeod & Gaylard (1996) From January 1999 to March 2003, Goedhart et al. (2004) monitored 54 high-mass star formation regions (SFRs) carefully to learn more about what causes the variability at 6.7 GHz and how long it lasts. Eight of the sources were not variable, compared to 46 that were. Aperiodic, quasi-periodic, periodic, and monotonic growth and decrease were all parts of the masers' variability. The measurements of 6.7 GHz maser flux in multiple sources suggests that there is a substantial amount of variation and variability across time periods ranging from a few days to a number of years (Caswell, Vaile & Ellingsen 1995, MacLeod & Gaylard 1996, Goedhart et al. 2004, 2009, Sugiyama et al. 2008).

Changes in the pump rate, masing cloudlet and/or seed photons, or the maser path length, such as those brought on by large scale motions, are plausible reasons of variability (Caswell et al. 2010). Maser brightness monitoring programmes can reveal the types of variability in the strength of maser emission. The different types of variability observed in masers to date can be classified into stochastic, flaring and periodic variabilities, which are in most cases embedded in or superimposed on long-term variability. The flares can also occur periodically (e.g Araya et al. 2010, Goedhart et al. 2003, Fujisawa et al. 2014, Szymczak et al. 2016, 2011), and stochastically (e.g MacLeod & Gaylard 1996). Here, we give a brief discussion of the observed variability of maser's intensity of the few maser species found in HMSFRs. The stochastic variations and flares are discussed first, followed by the periodic variability.

2.9.1 Stochastic variations and flares

Stochastic variability is common in maser variability and sometimes can be embedded in long-term variability. These are small flux density variations with no clear, simple

pattern for predicting the next event. The stochastic, flares and long-term variability have been observed in many masers species.

Long-term 22 GHz H_2 O maser monitoring in Orion KL region by (Matveenko et al. 1988), reported flux density of the H_2O masers increased by an order of 10^6 Jy and then decayed back to the base flux density. The same source was also monitored by (Omodaka et al. 1999), using the 6m parabolic radio telescope from the Nobeyama Radio Observatory. The flux density was reported to have increased by an order of 10^6 Jy in a few weeks and then decreased slowly back to the initial flux density.

The third burst or flare occurred in 2011 (Otto & Gaylard 2012). The flares happened in 1985, 1998 and 2011. They could be quasi-periodic with a 13 yr period (Hirota et al. 2014). Orion KL is not the only source to show flaring behaviour in the 22-GHz H_2O masers. Another illustration is the flare described by Motogi et al. (2011) in the long-term study of H_2O masers using the 11m radio telescope in Hokkaido, University Tomakomai. Many different kinds of masers towards NGC 6334I flared at the start of 2015, and some of them are still in that state, according Hunter et al. (2017).

All these maser species were found to be variable with the methanol masers operating at 6.7 GHz showing strong flares superimposed on the long-term variability. The flares were observed to have time delays as a function of velocity between 10 and 35 days. The time delays were not observed in the OH masers. The methanol masers' time delays were thought to represent the projected physical motion (Sobolev et al. 2007). Stochastic and flare variabilities in masers can be expected in HMSFRs regions owing to the nature of the environment, e.g. high energy and constantly changing (Hull & Zhang 2019). Caswell, Vaile & Ellingsen (1995) were the first to identify variability in class II methanol masers. As a result, we can discover more about the environment surrounding stars as they develop by analysing long-term flux fluctuations of the 6.7 GHz methanol maser.

2.9.2 Periodic variation

The source G9.62+0.20E, which displayed simultaneous flares at 6.7, 12.2, and 107 GHz, was the first known periodic maser, according to (Goedhart et al. 2003). Seven more HMSFRs were found to have periodic 6.7 GHz CH_3 OH masers by Goedhart et al. (2014*a*) during the 10-year monitoring programme. These masers' durations were discovered to span from 132.8 to 668 days. The detection of periodic variable masers currently stands at about 26 as reported by Seidu (2020) and are listed in Table 2.4. Their periods vary in length from 29.5 to 668 days (Proven-Adzri et al. 2019). Four years of intensive monitoring by Goedhart et al. (2004) revealed various sources that showed periodic or quasi-periodic fluctuations.

An extensive study of 54 sources spanning a considerable amount of time revealed a variety of 6.7 GHz behaviours, comprising six objects with periodic flares at intervals ranging from 132 to 520 days (Goedhart et al. 2004). It is still unclear how the regular variations seen in these masers mirror modifications to the centre massive YSO or its environs.

The 4.8-GHz H_2CO maser associated with G37.55+0.20 was monitored together with the 6.7 GHz CH_3OH by Araya et al. (2010). Both were reported to show quasi-periodic flares with a 237 day period. G37.55+0.20 is amongst the sample of 16 sources which are known to have periodic methanol masers in HMSFRs. It was argued that the origin of the flares is unlikely to be close to either 4.8 GHz H_2CO or 6.7 GHz CH_3OH as their flares occur almost at the same time. It was argued that the origin of the flares is unlikely to be close to either 4.8 GHz H_2CO or 6.7 GHz CH_3OH as their flares occur almost at the same time (Araya et al. 2010).

The 22 GHz H_2O masers in G107.298+5.639 were monitored together with the 6.7 GHz CH_3OH masers by Szymczak et al. (2016). The periodic 6.7 GHz CH_3OH masers in G107.298+5.639 were first discovered by Fujisawa et al. (2014). It was found from the long-term monitoring programme by Szymczak et al. (2016) that the H_2O masers also show periodic variability which was anti-correlated to the 6.7

Table 2.4: Periods Of Periodic Methanol Masers. This table was taken from Table A.3 in Olech et al. (2020). References to individual sources can be found in Olech et al. (2020) and Proven-Adzri et al. (2019).

Source (Galactic Name)	Period (Days)	Distances (kpc)	Luminosity (L $\times$ 10^4)	References Period
G09.621+0.196	244	5.2±0.6	270±132	1
G12.681-0.182	307	2.4±0.17	5.2±1.3	2
G12.889+0.489	29.5	2.3± 0.13	21.5± 4.4	3
G14.23-0.005	23.9	2.0± 0.14	0.5± 0.1	7
G22.357+0.066	179.2	4.3± 1.4	8.4± 2.9	4
G24.14-0.01	182.0	13.5± 0.3	25± 5	10
G25.411+0.105	245	9.0± 0.3	18.7±5.6	8
G30.40-0.29	222.0	7.2± 0.7	5.9± 1.5	10
G33.64-0.22	540.0	7.6± 1.0	14.4± 1.9	10
G36.70+0.09	53.0	10.0± 0.4	10.8± 2.7	10
G37.550+0.200	237	4.9± 0.5	31.9± 4.8	5
G45.473+0.134	195.7	7.8± 0.4	56±14.0	8
G59.63-0.19	149.0	3.5±0.3	6.5±1.6	
G73.06+1.800	160	2.4±0.3	12±3.0	8
G75.76+0.340	199.8	3.5±0.3	138±33.0	8
G107.298+5.639	34.4	0.76±0.03	0.39±0.1	6
G108.76-0.99	163.0	3.2±0.2	48±12.0	
G188.946+0.886	395	2.1±0.27	25±6.0	1
G196.454-1.677	668	5.3±0.024	132±33.0	2
G323.46-0.079	93	-	-	10
G328.237-0.547	220.5	2.8±0.5	70±17.0	1
G331.132-0.244	504	5.0±0.5	53±27.0	1
G338.935-0.062	133	3.2±0.5	4.0±1.0	1
G339.622-0.121	201	2.9±0.5	12±3.0	1
G339.986-0.425	246	5.5±0.4	12±3.0	9
G358.460-0.391	220	2.8±0.7	3.0±0.8	9

GHz CH_3OH masers. The light curves of the H_2O masers were broader than the CH_3OH maser light curves. These two species are pumped differently - mid-infrared photons radiatively pump the 6.7 GHz CH_3OH masers (e.g Cragg et al. 2005) and the 22 GHz H_2O masers are collisionally pumped (e.g Elitzur et al. 1989). It was argued by Szymczak et al. (2016) that these (the 6.7 GHz CH_3OH and 22 GHz H_2O masers) species in G107.298+5.639 can co-exist in a constrained gas density range of 1 - $4\times10^8 cm^{-3}$ and at kinetic temperatures from 200 - 250 K. The anti-correlated periodic variabilities in these two species suggest that the origin of the periodicity is common, even though they are understood to be pumped by different mechanisms.

2.9.3 Origin of the Periodic Variability in Methanol Masers

The origin of periodicity in the masers found in HMSFRs is still not confirmed. However, five mechanisms which make an effort to explain the cause of the periodicity in masers have been proposed. Three of the five mechanisms use the variation in the dust grain temperature as the origin of the observed maser brightness variability (Sugiyama et al. 2017). The variability in dust temperature is caused either by the spiral rotation of material in the disk (Parfenov & Sobolev 2014, Sobolev et al. 2007), circumbinary accretion (Araya et al. 2010), or protostellar pulsational instability (Inayoshi et al. 2013). The remaining two mechanisms argue that the variation in seed photons is the origin of the maser brightness variability, which is caused by either the colliding wind binary (CWB) system (Van der Walt 2011, Van Der Walt et al. 2009) or a binary companion eclipsing the UV-radiation from the primary protostar (Maswanganye et al. 2015).

The Parfenov & Sobolev (2014) mechanism considers a protobinary system and methanol masers in the accretion disk. A protobinary system has high- and intermediate-mass YSOs, which form a bow shock as they orbit around the centre of rotation. As the bow shock rotates around the centre of rotation, a gap is formed. The base of the rotating bow shock is hot, dense, and luminous, producing a large amount of UV and optical photons which increase the temperature of the inner accretion disk. The rotating bow shock affects the gas column density, as it reaches its maximum when it is along the line of sight with the base of the bow shock. Rotating bow shock also affects the dust temperature, which is related to the pumping rate. This results in the variability of the maser brightness. It had been argued by Parfenov & Sobolev (2014) that different light curves of masers can be explained by the inclination angle, similar to results shown by Sytov et al. (2009).

It was proposed by Araya et al. (2010) that periodic accretion from a circumbinary disk gives rise to the observed maser periodicity. In their proposal, materials originating from the circumbinary disk is periodically accreted onto the YSOs or the

accretion disk. The periodic accretion heats the dust grains periodically, producing infrared radiation in the process. The periodic infrared radiation changes induce periodic variations in the maser's radiative pumping rate. This will cause variations in the intensity of the methanol masers.

In the Inayoshi et al. (2013) model, the pulsational instability of HMYSOs is argued to the source of periodic variability in maser brightness. The instability is assumed to be due to the high accretion rate, $\dot{M}_* \lesssim 10^{-3} M_\odot yr^{-1}$, in high-mass YSOs. The high-mass YSOs have a He^+ ionisation layer. In the k-mechanism, when the He^+ ionisation layer increases, the opacity also increases, which implies the temperature will rise and the high-mass YSO will expand. The expansion of the high-mass YSO decreases the temperature, which implies less ionisation of He. This will result in gravitational contraction. Inayoshi et al. (2013) argued that this process repeats for $\sim 10^3$ yr and the mass accretion rate, $\dot{M}_*$, is proportional to the period. However, high-mass YSOs with accretion rate $\dot{M}_* \lesssim 10^{-3} M_\odot yr^{-1}$ can not produce periodic pulsation even though they can be unstable. This could explain why periodic masers with periods of less than ten days have not been observed yet. The variations in temperature of HMYSOs affects the dust temperature which is related to the pumping.

In the CWB system model, Van der Walt (2011) proposed a protobinary system which is in an elliptic orbit. The primary YSO is more massive, has a stellar wind and emits ionising photons, which produce the HII region. The binary companion does not need to produce ionising photons but has a stellar wind. At periastron, the stellar winds from the two YSOs collide to produce ionisation pulses, which go through the fully ionised HII zone devoid of attenuation. As ionisation pulses reach the area of partial ionization, they are absorbed and raise the level of free-free emission and in turn, the size of the HII region. This process results in increasing the seed photon flux, which increases the intensity of the maser projected on the HII region. This will be exhibited in masers by a rapid ascent to the local optimum, then a decay hereafter, that behaves exponentially to reach minimal on a local scale. This behavior has been observed in those methanol masers that are connected to G9.62+0.20E (at both 6.7

and 12.2 GHz) and G37.55+0.20 (at 6.7 GHz) (Araya et al. 2010).

Maswanganye et al. (2015) suggested that there could be a young eclipsing binary system in the region, with the high-mass YSO and its bloated companion which does not emit UV radiation. As the bloated companion eclipses the high-mass YSO, it blocks the UV radiation emitted in the direction of the line of sight to the maser. This reduces the ionising photons which are proportional to the seed photon flux. The variation in the seed photon number affects the stimulating photons, which induces the changes in the brightness of the maser.

2.9.4 Masers as Evolutionary Probes of MSF

According to Ellingsen et al. (2007), the many types of masers have varied preferences for the physical conditions in which they thrive and are expected to trace different evolutionary periods of massive star creation. Taking into account the fact that various sources emit radiation from a diverse range of maser species or transitions, there must be a significant degree of evolutionary phase overlap that is detected by the majority of maser types. Methanol masers operating at 6.7 GHz and water masers operating at 22 GHz have both been identified as potential tracers of the birth of massive stars (Menten 1991*a*, Caswell, Vaile & Ellingsen 1995, Urquhart et al. 2009).

In addition, it has been discovered that both types of masers are present in the very early phases of a protostar, when the object is still accumulating mass, as well as prior to the time when it starts to ionize the medium in its surroundings. The above mentioned masers can frequently be seen at millimeter and centimeter wavelengths well in advance of the appearance of a UC HII region. OH masers arrive last in a compacted, presumably infalling, circumnebular shell that was described by Garay & Lizano (1999). 12.2 GHz Later on during the time when the emerging protostar is forming a detectable UC HII region, CH_3OH masers will begin to emerge. Class I CH_3OH masers are observed offset from strong radio continuous sources (i.e. young ionizing high-mass stars), and it is possible that they are pumped collisionally (Cragg

et al. 2005). According to Ellingsen (2006), class I methanol masers can be traced back to an earlier evolutionary phase. As the UC HII region transforms into a dispersed HII region, these masers eventually become extinct (Codella et al. 1994).

Phillips et al. (1998) proposes a different explanation for the weak association between UCHII regions and methanol masers. Instead, they argue that maser emission can be generated by intermediate-mass non-ionizing stars, which emit enough IR photons to pump the masing transition but not enough UV photons to generate a UC HII zone. The lack of evidence for class II methanol masers toward developed stars bolsters the contention that this maser is only present during the first stages of massive star formation.

Because none of the masing species (OH, H_2O, CH_3OH) are in the same place, different writers have suggested that every single one of these masers appears at various occasions in the life of a massive star (Genzel & Downes 1977). During the fast accretion phase, when a massive star is just starting to form, H_2O masers are thought to be present. The OH maser appears last in a squeezed circumnebular shell that appears to be collapsing in on itself, whereas the The formation of the protostar's UCHII region occurs after the CH_3OH maser has already been detected (Churchwell 2002). The masers go away when the UC HII zone transforms into a more dispersed HII region (Codella et al. 1994). The maser phenomenon occurs during the initial phases of the birth of massive stars (Garay & Lizano 1999).

CHAPTER THREE

METHODOLOGY

This chapter covers the methods used to collect radio data from the 26-m telescope at HartRAO and the ALMA. The lines software was used to reduce the radio data, and Python was used to analyze it. The sub-millimeter data was calibrated, CASA-reduced, and Python-analyzed. The archived IR data was retrieved from IR data archives and put through a Python analysis. The steps of data gathering, reduction, and calibration are covered. The methods were chosen because the observations could penetrate the highly opaque natal environments in which the early massive stars are born.

3.1 DESCRIPTION OF RADIO TELESCOPES

Radio astronomy is the study of the radio waves released by astronomical objects in space, according to Burke et al. (2019). Radio-astronomers' sources of study have extremely low radio wave intensities because they are so far away. Therefore, it is highly recommended to use an extremely sensitive system to identify and gather radio astronomy signals (Pandian et al. 2006). According to Ryle et al. (1959), radio telescopes can be employed singly or in groups.

The three fundamental components of every radio telescope are an antenna that gathers incident radiation, a receiver that detects this radiation, and a backend system that analyzes the data (Maswanganye 2018). How the backend system functions is determined by the observed signal type (Proven-Adzri et al. 2019). Either the signal is divided into many confined bands, with each narrow band's power being measured, or the total power in a broadband or continuous signal is measured, allowing one to construct the incident radiation's spectrum (Kooi 2008).

3.1.1 Single Dish

The most common kind of radio telescope concentrates radiation into the receiver using a parabolic dish, with or without a secondary reflector. Similar to their optical counterparts, dual reflector radio antenna systems can be of the Gregorian or Cassegrain type (Proven-Adzri et al. 2019). The various antenna reflectors used in telescopes are illustrated in Fig. 3.1. The size, effectiveness, and sensitivity of the antenna and the receiver together determine the system's overall sensitivity.

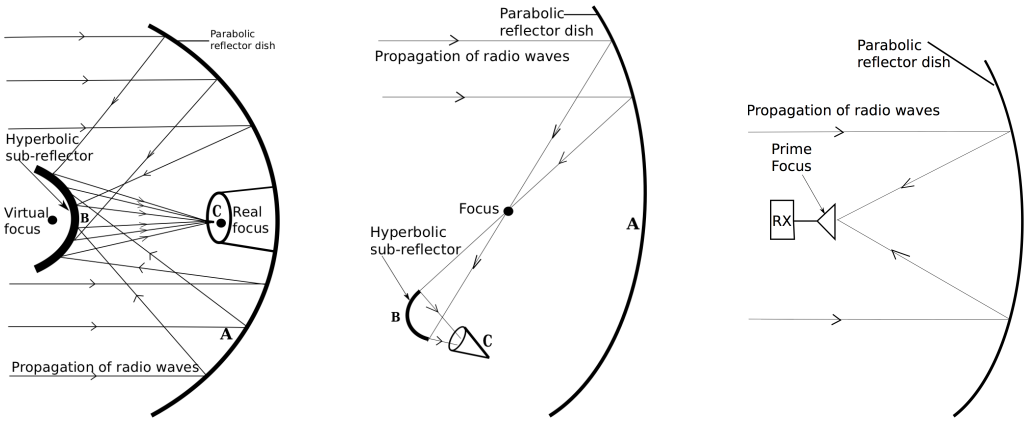

(a) Cassegrain (b) Gregorian (c) Prime focus

Figure 3.1: Several configurations of a reflector antenna. Image credit by Hazdra & Mazanek (n.d.)

.

3.2 SINGLE DISH OBSERVATION

3.2.1 Receivers

The HartRAO radio telescope has full polarisation receivers at 6.7 and 12.2 GHz (Maswanganye et al. 2014). These two receivers are circularly polarised which implies that each receiver has two feeds, which are left- and right-circular polarisations (LCP and RCP) (MacLeod, Chibueze, Sanna, Paulsen, Houde, van den Heever & Goedhart 2021*b*). For the 12.2 GHz receiver, the focused radio waves from the secondary reflector are coupled with the noise diode signal using a coupler (Combrinck 2014). The 12.2 GHz receiver has two noise diodes, low temperature one at 11.67 and 12.68 K for LCP and RCP respectively, and high temperature one at 62 and 68 K for LCP

and RCP respectively. The coupled signal is sent into a Low Noise Block (LNB) converter. The LNB converter amplifies the signal and down converts the radio-frequency (RF) to an intermediate-frequency (IF), which is important in reducing the attenuation during the transmission of the signal through a coaxial cable. Table 3.1 lists some of the fundamental structural elements of the 26m HartRAO radio telescope.

Table 3.1: Fundamental details about the HartRAO 26-m telescope. Credit:www.hartrao.ac.za

Owner and operating agency	HartRAO
Year of construction	1961
Radio telescope mount	Offset equatorial
Diameter	25.9
Focal length f	10.886 m
Focal Ratio (f/D)	0.424
Surface Tolerance	0.50-mm rms
Wavelength Limit	1.3-cm
Feed System	Cassegrain
Pointing Resolution	0.001°
Repeatability	0.004°
Slew Rate on each axis	0.5 $^{\circ}s^{-1}$

At the 26m HartRAO radio telescope back-ends is the radiometer which has a square-law detector. This squares the voltage input, $\mathbf{V}_{in}$, that bears a direct relationship to the measured noise power per bandwidth (Δ v) of the telescope $P_n \propto V_{in}^2$. The spectrometer back-end divides the passband into N narrow frequency ranges with a width of $\delta v (\leq v/N)$ and measures the power in each channel (Condon & Ransom 2016). The 26-m telescope at HartRAO has a spectrometer with 1024 channels.

6.7 GHz receiver has a cryogenic refrigerator Low Noise Amplifier (LNA), instead of an LNB, which minimises the noise contribution. It has only one noise diode, unlike the 12.2 GHz receiver. The LCP and RCP temperatures of the noise diode at 6.7 GHz for this receiver are 14.2 and 21.0 K, respectively. The radiometer and spectrometer are employed for the calibration and spectroscopic observations at 6.7 and 12.2 GHz, respectively. The radiometer, equipped with a square-law detector, or the spectrometer in the HartRAO control room send their data to the control

computer, where it is captured by the observing software.

3.3 HartRAO 26 m TELESCOPE INSTRUMENTATION AND SIGNAL PROCESSING

Fig. 3.3 depicts the 26 m single-dish. The 25.908-m Cassegrain design used in the 26-m HartRAO radio telescope was created by Blaw Knox in 1961 (Combrinck 2014). 25 53 ′14.4 ″(25.887 °C) South and 27 41 ′05.2 ″(27.685 °C) East are the coordinates for the telescope. Table 3.1 lists the fundamental characteristics of the 26-m telescope, and Fig. 3.2 illustrates the telescope's maximum elevation. Appendix **??** provides information on the fundamentals of a single dish radio telescope, such as the HartRAO.

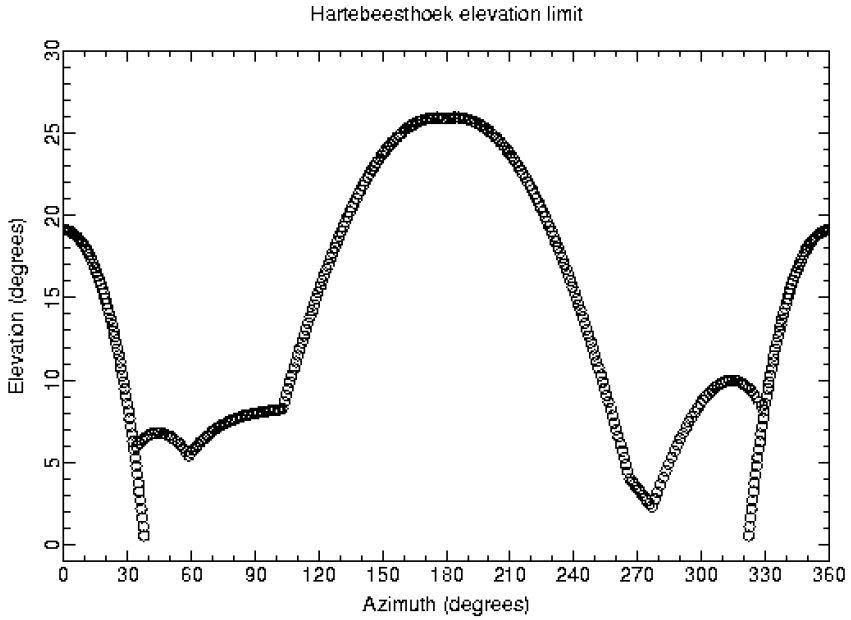

Figure 3.2: Elevation of HartRAO 26-m telescope. Credit: http://www.hartrao.ac.za/hh26m factsfile.html

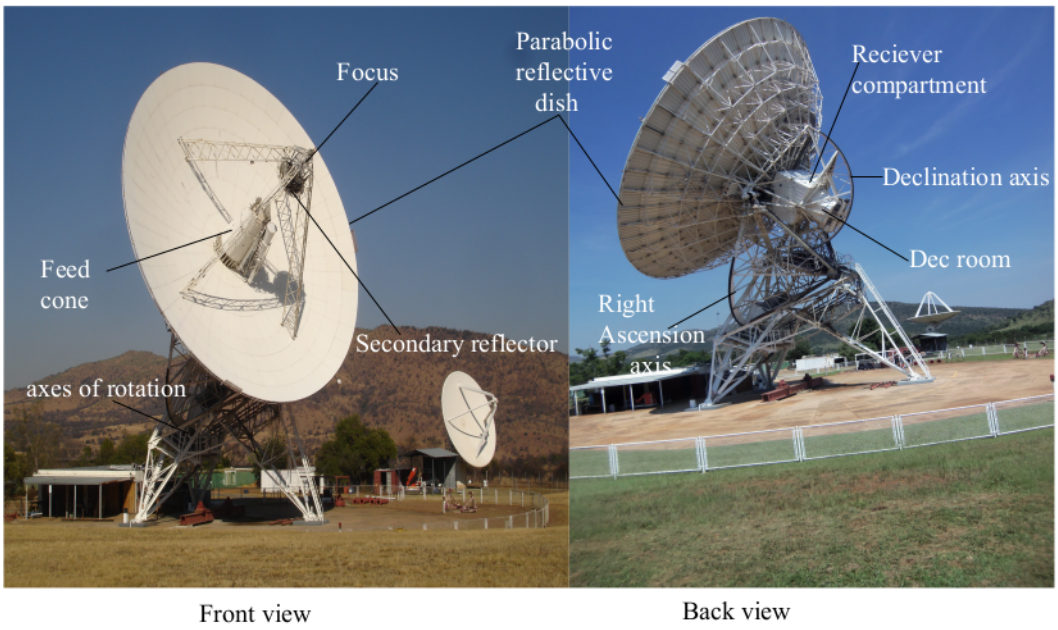

Figure 3.3: Image of HartRAO radio telescope dish. Image credit: http://www.hartro.ac.za/gallery/index.html

3.4 THE HartRAO OBSERVATIONS

3.4.1 The Drift Scan

The drift scans used to randomly collect the calibration data were performed once every three days, on average, while the telescope was available. This technique involves positioning the telescope in front of the source's path as shown in Fig. 3.3, in order to have the source cross the line of sight of the telescope. There was one nominal drift scan over the beam centre and two additional scans via the north and south half-power points. The amplitude was calculated from each of the three drift scans using a polynomial regression of the second order to the source peak in each of the three drift scans, as illustrated in Fig. 3.4. Each scan's amplitude can be described by a Gaussian function profile, $P_\theta = P_o exp(-ln(2)(\delta\theta/b)^2)$, in order to calculate the pointing error. These three scans can be mathematically defined as:

$$P_n = T\, exp(-ln(2)(\frac{\delta\theta + b}{b})^2) \tag{3.1}$$

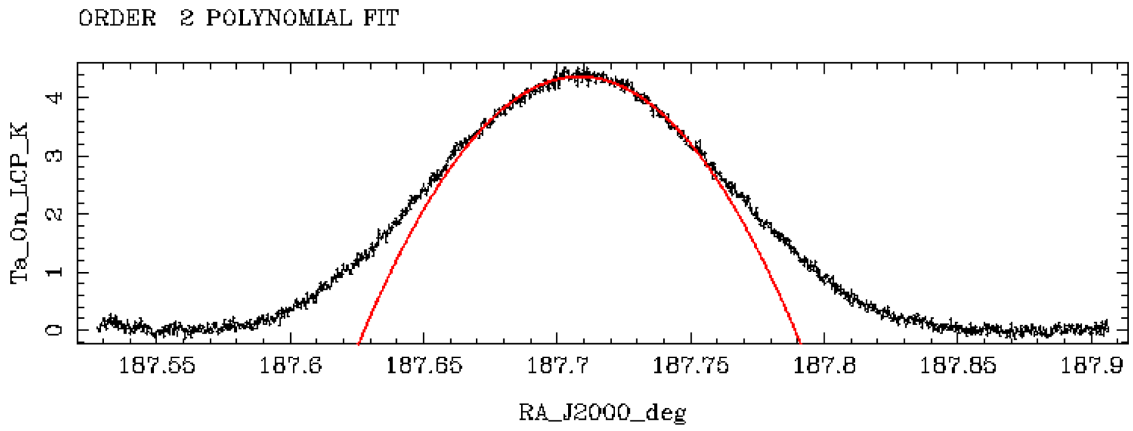

Figure 3.4: A second-order polynomial fit to the peak of the source.

$$P_s = T\,exp(-ln(2)(\frac{\delta\theta + b}{b})^2) \tag{3.2}$$

and

$$P_{on} = T\,exp(-ln(2)(\frac{\delta\theta + b}{b})^2) \tag{3.3}$$

The subscripts n, s and on represents North South and on source half-power points scans. The true antenna temperature T must be obtained from the drift scans in Equations 3.1, 3.2 and 3.3 respectively. The offset between the source and the beam's center is $\delta\theta$, and the beamwidth at the half power point is b. Equations The point source sensitivity (PSS) was computed using the corrected antenna temperature (T). One Jansky (Jy) of flux density produces a certain number of Kelvins of antenna temperature for each polarisation, according to the definition of PSS. PSS is calculated using equation 3.4

$$PSS = \frac{S}{2K_sT_A} \tag{3.4}$$

where K_s is the source correction factor ($K_s = 1$) for a point source, T_A is the true peak antenna temperature of a radio source and S is the observed flux from a radio source. Three sources, 3C123, Hydra A, and Virgo A, were used to calibrate the telescope's 4.5-cm (6668-MHz) receiver. Using Virgo A as the calibrator, it was

unable to accurately determine the telescope's point source sensitivity at 6668 MHz as a point source in the beam. Therefore, the point source sensitivity was calculated using 3C123 and Hydra A. Virgo A was chosen to determine if there is any variation in the sensitivity to a point source. because of its high signal to noise ratio and the fact that it is the brightest of the three sources. The flux densities of these sources were reported by Ott et al. (1994).

3.4.2 The 26-m HartRAO Telescope Calibration

The observations were made using the cryogenically cooled 4.5 cm full polarization receiver, which allowed for LCP and RCP operation. The masers were monitored with a velocity resolution of 0.044 km s^{-1} once every week or once every two weeks. However, when the maser was discovered to rapidly flaring, the amount of time spent observing was increased to multiple times each day or multiple times every observation. Error propagation was used to determine the level of uncertainty associated with the final PSS result (Taylor 1997). The uncertainty is given by:

$$\Delta(PSS) = \frac{1}{2}\sqrt{[\Delta(PSS_{3c1})]^2 + [\Delta(PSS_{hyd})]^2}, \tag{3.5}$$

where $\Delta(PSS_{hyd})$ is the standard deviation for the Hydra A PSS and $\Delta(PSS_{3cl})$ is the standard error of the mean of 3C123 PSS value.

Five pointing offset observations on G188.95+0.89 in spectral line mode were conducted before the frequency switched observations, as shown in Fig. 3.5. At 6.7 GHz, the pointing checks were performed within 3 arcmins. By fitting the peak's top with a second-order polynomial, as illustrated in Fig. 3.6, the pointing errors of the strongest maser peak located between10.5 km s^{-1} and 10.9 km s^{-1} were determined.

3.4.2.1 Pointing Offset Correction

The pointing accuracy of a radio telescope can be affected by factors such as deformation of the primary reflector due to gravity and thermal expansion of the primary and

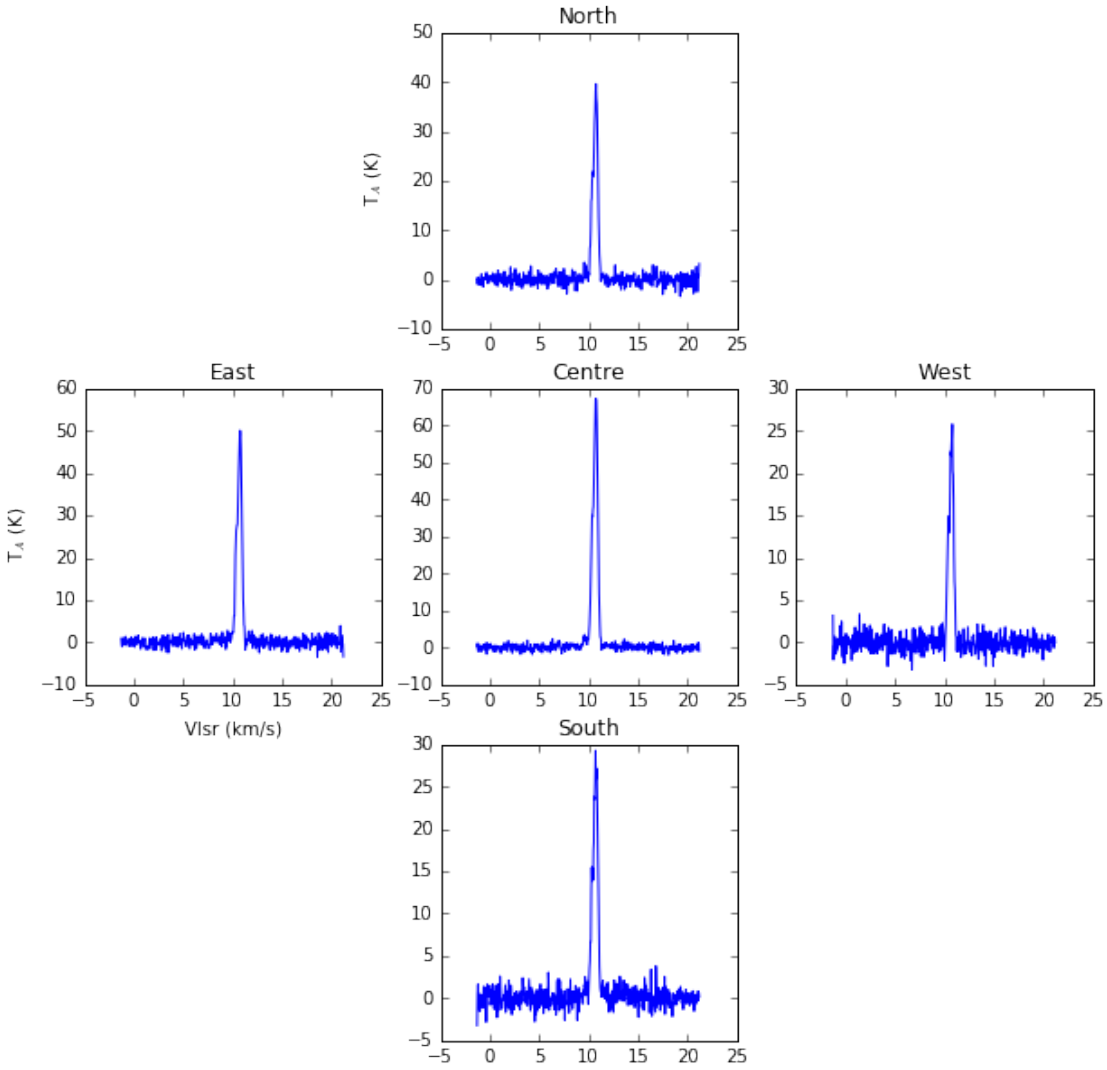

Figure 3.5: The G188.95+0.89 maser source was the target of a pointing observation.

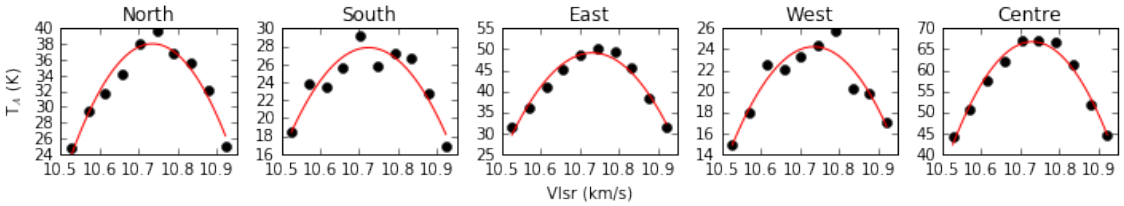

Figure 3.6: Using the highest peak power from the half-power measurements. Maser amplitude is shown as black dots, while the corresponding polynomial fit is shown in red.

secondary telescope reflectors. The deformation of the primary reflector of a radio telescope due to gravity can be minimised by conducting the observations near zenith, e.g. ~ 2 hours near zenith. However, some radio sources are off zenith. The pointing offset should be the same for both polarisations. To improve the signal-to-noise ratio, the polarisations were averaged together. When calculating the unpolarised flux density of the source, the two polarisations were added, after correcting for the gain.

In order to determine the pointing correction factor, four additional observations to the on-source observation were conducted to the north, south, east and west at the half power beamwidth levels. The top half of the telescope main beam cross-section can be approximated by a Gaussian profile, which implies that the five antenna temperatures from the five pointing observations, (i) on-source, T_A^{on}, (ii) north, T_A^{n}, (iii) south, T_A^{s}, (iv) east, T_A^{e}, and (v) west, T_A^{w}, can be approximated as shown in equations: 3.6, 3.7, 3.8, 3.9 and 3.10.

$$T_A^{on} = T_A exp(\ -ln(2)\frac{\delta\theta^2}{b^2})\ ) \tag{3.6}$$

$$T_A^{n} = T_A exp(\ -ln(2)(\ \frac{\delta\theta_{ns} + b}{b})\ ) \tag{3.7}$$

$$T_A^{s} = T_A exp(\ -ln(2)(\ \frac{\delta\theta_{ns} + b}{b})\ ) \tag{3.8}$$

$$T_A^{e} = T_A exp(\ -ln(2)(\ \frac{\delta\theta_{ns} + b}{b})\ ) \tag{3.9}$$

$$T_A^{w} = T_A exp(\ -ln(2)(\ \frac{\delta\theta_{ns} + b}{b})\ ) \tag{3.10}$$

All the observations, spectroscopic and driftscan, were conducted at hour angle < 3 h. These were done in order to reduce effects such as atmospheric absorption, gain variation with an hour angle, and dish deformation, which can affect the pointing error (Maswanganye 2018). By combining north-south T_A^{ns} and west-east T_A^{ew} pointing observations, the on-source peak may be calculated and then utilized to compute the pointing.

3.4.2.2 Calibration of a 4.5 cm receiver

The experiment that was performed in the laboratory to calibrate the equipment utilized liquid nitrogen, a 4.5-cm receiver, a radiometer, and an AIL7009 hot-cold standard noise generator. Liquid nitrogen was allowed to reach temperature equilibrium after being left alone for at least an hour. Fig. 3.7 displays a schematic diagram of the 4.5 cm receiver.

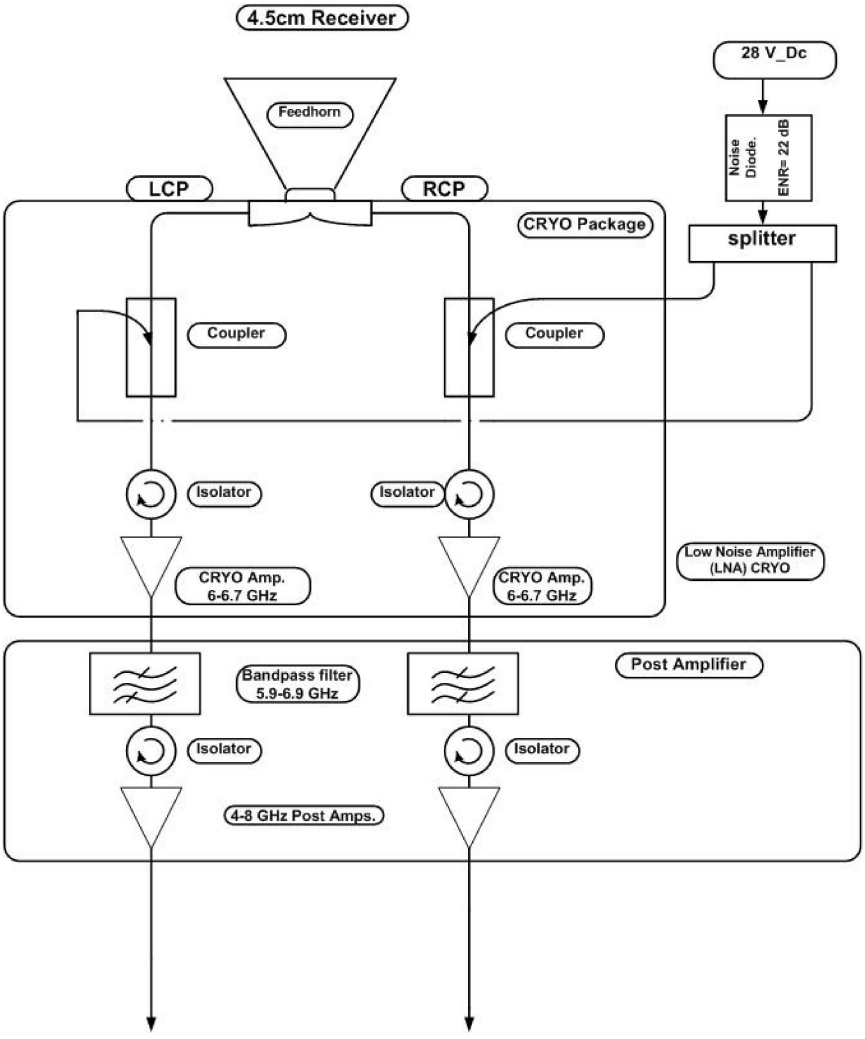

Figure 3.7: The 6668-MHz (4.5-cm) HartRAO receiver's schematic diagram. Source: (Maswanganye & Gaylard 2012).

3.4.3 Calibrating Continuum Drift Scans

Virgo A that it has frequency ranges between 1.408 and 10.550 GHz was used for calibration in this observation Maswanganye (2017). At frequencies over 5 GHz,

Virgo A has been suggested as an excellent calibrator due to its consistent flux density (Baars & Genzel 1977). This indicates that Virgo A exhibits slight variations as a result of the way it distributes the flux and has an accuracy of roughly 5%, according to Baars & Genzel (1977).

3.4.3.1 Flux Density Calibration

In radio astronomy, the gain of a radio telescope is typically expressed in terms of Kelvins per Jansky. (K Jy^{-1}), rather than using the units of effective area and it is dependent on frequency of the observation (Condon & Ransom 2016). It can also be calculated from the system equivalent flux density (SEFD). The effective areas for a fully circularly polarised (left and right) receiver of the telescope are:

$$A_e^{LCP} = \frac{1}{2}\frac{K_s K_B T_A^{LCP}}{S_o} \; and, \; A_e^{LCP} = \frac{1}{2}\frac{K_s K_B T_A^{RCP}}{S_o} \tag{3.11}$$

For each polarization, the Virgo A underwent three scans, two of which were drift scans carried out at half-power beam positions to the north and south of the target source. A source with a known flux density is observed with a radio telescope to measure its sensitivity. For each polarization, calibrators are radio sources used to calculate the PSS. Bright radio sources, point sources, or unresolved sources are ideal candidates for calibrators since their flux densities remain constant over very long time periods.

Based on driftscan measurements, PSS values were calculated for the 26m HartRAO radio telescope. Driftscan is an observing method in which the telescope is left stationary ahead of the calibrator's motion across the sky. With time, the calibrator will move through the field of view of the radio telescope. The noise diode is cycled on and off prior to bringing the calibrator into the radio telescope's field of view. The measured power per unit bandwidth in the square-law detector begins to climb toward its maximum as the calibrator begins to transit the telescope's field of vision.When the calibrator is positioned dead center in the telescope's beam, the power density

is maximized. Once the calibrator moves out of the sweet spot in the middle of the telescope's beam, the power per unit bandwidth begins to drop. Since we know the temperature of the noise diode, we can use the square-law detector to measure the power per unit bandwidth and then convert that to Kelvin.

Due to the detector receiving the sum of the antenna temperature T_A and the system temperature T_{sys}, the baseline of a driftscan measurement is not zero. Each driftscan's baseline was adjusted by subtracting a fitted n-order polynomial from the nulls at the beginning of the scans. For the baseline correction (or flattening), lower order polynomials were favored because of their little impact on the driftscan peak. The antenna temperature is located at the peak of the baseline-corrected driftscan measurement. Equation 3.11 uses the antenna temperature to determine the PSS. Since the PSS readings can be affected by the telescope's pointing offset, we also performed two additional driftscans, one to the north and one to the south, at the half power locations.

3.4.3.2 6.7 GHz receiver point source sensitivity

The 26m HartRAO radio telescope was calibrated at 6.7 GHz using two calibrators, Hydra A and 3C123. For both Hydra A and 3C123, the 6.7 GHz driftscan observations were conducted separately from the 12.2 GHz driftscan observations. Since VLBI observations take precedence, the observations were performed on a daily basis whenever the telescope was available. The driftscan peaks were calculated by fitting a second order polynomial to the upper half of the data. Finding the peak in a driftscan requires fitting a function to the upper half of the scan, and this function need not be a polynomial of the second order. It is also possible to find the driftscan's peak using Sinc $sinc(x) = sin(x)/x$ and Gaussian functions. The flux densities of Hydra A and 3C123 at 6.7 GHz were taken from Ott et al. (1994) because they were assumed to be point sources implying $K_s = 1$. Since the Hydra A and 3C123 PSS values for each frequency coincide in both polarizations, they are in good agreement with one another. various receiver components and square-law detectors will result

in various gains, hence the PSS values for the LCP and RCP will be varied.

The PSS values were averaged over the frequency range without any abrupt variations for each source. The PSS values in Table 3.2 were calculated by averaging the data for the 3C123 and the Hydra A, column 2 lists the days on which the average PSS values were determined. Mechanical adjustments in the 26m hartRAO radio telescope, such as the resetting of four surface panels on the primary reflector on the 2456300 JD (2013-01-07), are responsible for the step changes visible in the evolution of the PSS rather than variations in the flux density of the source. Target radio source antenna temperature is converted to Jy using the PSS parameters.

Table 3.2: Between the Julian dates listed in column 2, the point source sensitivity values average out.

Frequency	Julian Date (JD) Start-End	PSS LCP	RCP
1	2	3	4
GHz		Jy K^{-1}	Jy K^{-1}
	2455520 - 2455703	5.495	4.447
	2455704 - 2455744	6.542	5.012
	2455745 - 2455777	6.478	4.920
	2455778 - 2456299	5.715	4.445
	2456300 - 2458000	5.572	4.467

3.4.3.3 Baseline and Amplitude Correction

A linear function, or in certain situations, a second-order polynomial, was fitted through the beam's centre to establish the baseline (Seidu et al. 2022). Each scan's peak was thought to have a Gaussian profile. A beam of Gaussian shape with a width equal to the telescope beam's half power was fitted to each scan's peak in the North-South direction. Gaussian fitting was used to determine the pointing offsets between the source and the telescope beam's centre (Maswanganye 2017). The corrected antenna temperature is determined by multiplying the pointing correction factor by the drift scan antenna temperature, as shown in Fig. Fig. 3.8

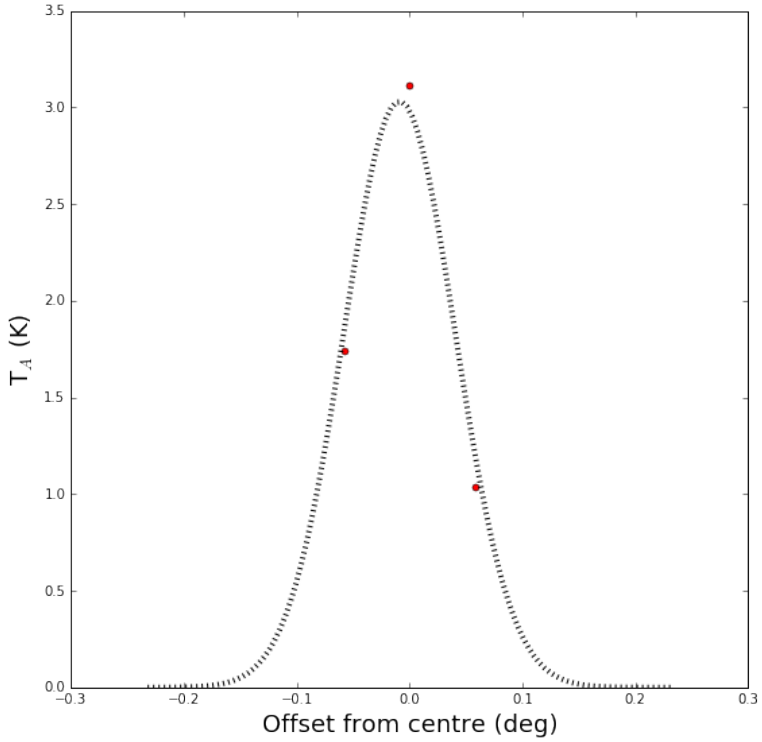

Figure 3.8: The peak amplitude of the continuum source was corrected by a factor of 1.05 due to pointing. The red dots show the measured temperatures of the antennas at the four cardinal directions. After applying the pointing correction factor, the resulting value is the amplitude.

3.4.4 Frequency to Velocity Conversion

In radio astronomy, frequency is transformed into V_{lsr}, for the spectrum units. surroundings. By converting frequencies to velocities, we can account for the Doppler shift caused by the Earth's orbit around the Moon, the Sun's orbit around the Earth, and the Sun's orbit around the local standard of rest (V_{lsr}). The relationship between the Line Rest Frequency (LRF) and speed of light in vacuum (c) determines the frequency shift brought on by velocity along line of sight. In our study, we used one Line Rest Frequency with a 6.668-GHz LRF and a Doppler conversion factor of 22226.7 Hz/km $^{-1}$. By multiplying bandwidth by Doppler shift conversion factor, one can determine velocity range (measured in km s^{-1}) that the receiver can detect. For the 6.7 GHz receiver, our spectroscopic observations had a spectral resolution of 0.044 km s^{-1}.

3.4.5 Bandpass Correction

Due to unstable system noise and poor antenna response, the bandpass of the entire power spectrum is not flat (Seidu 2020). A baseline correction must be done so as to eliminate any of such variations. In a single-dish observation, the bandpass correction can be performed using any of the spectral line techniques listed below:

1. **Position switching**: By using this method, a target can be seen both "on-source" and after the telescope has been relocated to a different part of the sky, where the two signals can be compared. Both the on and off-source times are the same. On-source and off-source positions both require about the same amount of time to reach. This observation method simply compensates for baseline effects since atmospheric influences are ignored and the best spectral baselines are acquired (Maswanganye & Gaylard 2012).

2. **Frequency switching**: The line spectrum is moved to the left (positive features) and right (negative features) sides of the spectral bandpass when the LO is switched during frequency switching observations. The signal-to-noise ratio is enhanced by adding the spectra of the two lines detected to the left and right of the bandpass (Maswanganye & Gaylard 2012). The frequency switching technique reduces systemic offsets and corrects frequency-dependent effects. The method is applied to sources whose angular diameters are less than the telescope's beam size. According to(Matthews et al. 2004), it is useful for both viewing narrow lines and differentiating spectral lines.

The frequency-switching method was used in the present investigation to examine the methanol masers operating at 6.7 GHz. The maser spectra acquired by the frequency switching observation are displayed in Fig. 3.9. A spike-like structure was visible in the bandpass's core from the figure. This might be a spectrometer effect. Before doing any additional data processing, that channel was removed. Appendix A.1.2 elaborates on single-dish observing methods in more depth. Total power is calculated by adding the left hand (P_{left}) and right hand (P_{right}) spectra as shown

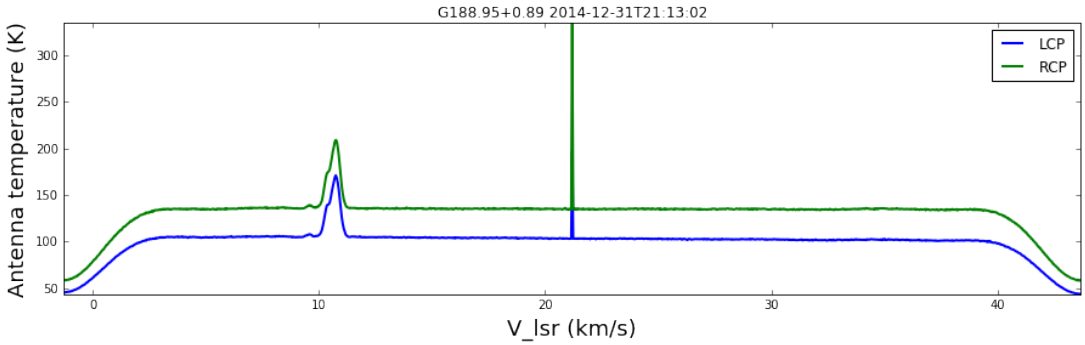

(a) Maser spectra on the bandpass's left side

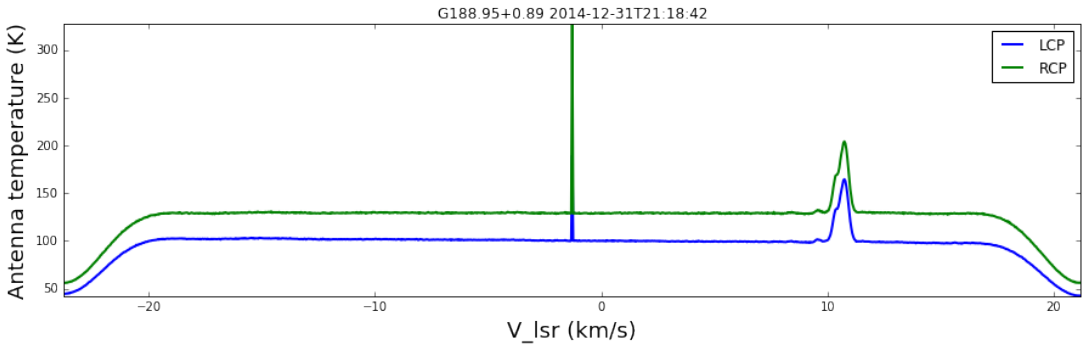

(b) Maser spectra on the bandpass's right side

Figure 3.9: Spectra of each polarisation for the frequency switched pair of the maser.

in equation 3.12

$$TotalPower = \frac{P_{left} - P_{right}}{P_{right}} T_{sys} \tag{3.12}$$

Due to the units of T_{sys} in equation 3.12, the total power of the spectrum derived from the difference of the left and right shifted spectra will be expressed in Kelvin as illustrated in Fig. 3.9. When an nth order polynomial is fitted to the non-emitting parts of the total power spectrum, the spectrum becomes flat. Baseline correction with low order polynomials is favored since they have a smaller impact on the peaks of the spectra. The flux density, expressed in Jy, is calculated by multiplying the total power by the power-to-size scale (PSS).

3.5 RADIO DATA REDUCTION PROCESSES

For HartRAO spectral line data, each integration were stored as a separate FITS file. This particular sequence of observations consists of quick pointing checks to the half-power cardinal points and the centre position, and a pair of frequency-switched

full-length scans on the central position. LCP and RCP are used to record data in dual polarization. The polarized spectra with similar velocities were added together. After that, the baselines are linearly fitted to account for any remaining variations. In our methanol maser source, the pointing error was calculated and adjusted. Two frequency-switched full-length scans on the central position are interspersed between rapid pointing checks to the half-power cardinal points and the central location. As the telescope is pointed away from the zenith, the gravitational pull of the earth may also be to blame. Large pointing values were rejected or regarded as unreliable data. The spectra with large pointing errors (> 1.3) were considered as bad data, and they were not included in the data set.

The on-source spectroscopic observation was reduced using similar steps to those used for the on-source pointing observations, but the polarisations were not averaged. The spectra were then multiplied by the PSS to convert them into Jy. The observations which had high system temperatures, $> 90K$, were considered to be bad data, as this could be due to bad weather, such as rain, or malfunctioning of some receiver component (Maswanganye 2018). Lines software and python were used for data reduction. A Gaussian was fitted to these measurements and the pointing offset figured out, on how much the amplitude of the on-source observation has been reduced by. Correction was then applied to the subsequent spectra.

3.6 MASER SLECTION

The chosen source was G188.95+0.89, which is one of the sources Caswell, Vaile & Ellingsen (1995) and Van Der Walt et al. (1996) listed as variable. From 1996 to 2004, G188.95+0.89 had been routinely observed by Goedhart et al. (2003), and its observation is still ongoing. Class II CH_3OH) masers are associated with the HMSFR G188.95+0.89, which is also known as S 252 or AFGL 5180, and demonstrated being dependable indicators of the first stages of HMSF by (Menten 1991*a*, Caswell, Vaile & Ellingsen 1995, Caswell 1996, Mutie et al. 2021). The parallax distance of the source is 1.76± 0.11 kpc, according to (Reid et al. 2009, Oh et al. 2010). Menten (1991*a*)

first identified the 6.7 GHz CH3OH masers of this source, and Goedhart et al. (2004), Goedhart et al. (2014*b*)) reported periodicity of the source τ =395±8 d. Table 3.3 shows some parameters of the source of study.

Table 3.3: G188.95+0.89 source linked with class II methanol masers.

Source Name(l,b)	G188.95+0.89
Equatorial Coordinates	
RA(h m s)	06 08 53.30
Dec (° ′ ″)	+21.38.30.0
Frequency (GHz)	6.7
Velocity range (km s^{-1})	
	V_L=7.5
	V_H=13.0
Monitoring Window	
Start (MJD)	52,820
End(MJD)	59,130
Number of Epochs	720

3.7 RADIO INTERFEROMETRIC OBSERVATIONS

In this section, in-depth explanations of fundamentals of radio astronomy interferometry is given, starting with a two-element interferometer, then followed by interferometric data collection and calibration techniques.

3.7.1 Interferometer Basics

The term "Interferometry" refers to the combining of signals from two or more radio telescopes to provide data that has the single-dish resolution, having a diameter that is proportional to the largest possible separation between the smaller dishes in the interferometer system, i.e;

$$\theta = 1.22\frac{\lambda}{D} \tag{3.13}$$

whereλ is the observation's wavelength. For instance, a telescope of ∼16 cm would be needed in order to accomplish a certain angular resolution of 1 arcsec at an optical wave length of 750 nm. A radio dish of about ∼15 km would be required to get the same level of resolution at a radio frequency of 5 GHz, which is not practical to build.

Therefore, the Rayleigh criterion (equation 3.13) indicates that a wider aperture is required to increase a radio telescope's resolving power, or to resolve smaller sources.

3.7.2 The Two Element Interferometer

These are two antennas, spaced apart by vector baseline b whereby radiation arrives from It was assumed that direction s would be the same for same for both (far-field) antennas. A system with two dishes separated along vector B is shown in Fig. 3.10. Consequently, the wave-front propagation delay (T) is expressed as;

$$T = \frac{B\,sin\theta}{c} \tag{3.14}$$

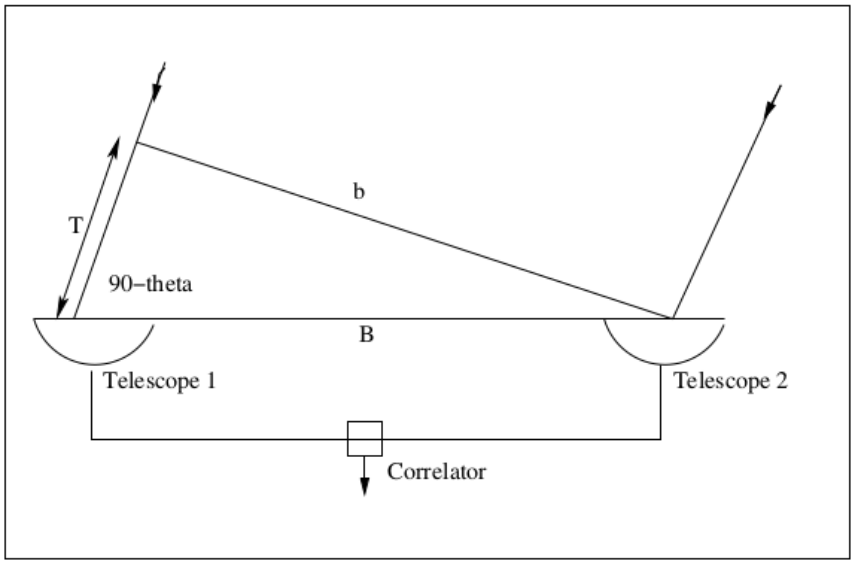

Figure 3.10: Illustration of a basic two-dish interferometer. The distance between telescopes 1 and 2 is B, the incoming signal has an angle of θ, and the time delay before reaching telescope 1 is T.

A two-dish interferometer with a simple schematic is shown in Figure 3.10. The distance between telescopes 1 and 2 is B, the incoming signal enters at an angle θ, and telescope 1 receives the signal with a time delay of T. In a two-element interferometer, the time delay (T) between the two antennas is determined by the baseline (B) and the angle (θ), the distance between the baseline and the source wave-front (b) Avison

(2011). A two-element interferometer's time delay can be depicted as demonstrated in Fig. 3.10. When the baseline B is equal to 2 kilometers and the angle of the incidence wave front is equal to zero degrees, the time delay, denoted by T, caused by an overhead source is zero. When θ is equal to 30 degrees, T is equal to ~ 3.3 μs; however, when T is measured at a greater baseline distance of 20 km, it is equal to ~ 33 μs, which is a factor of 10 greater than the initial value.

It is envisaged that the combined output of these several interferometer antennas will be a final signal. To do this, each signal's voltage output is sent into a correlator, which multiplies the voltages while taking into account temporal delays, and then averages the signal over time to provide the desired output (Avison 2011). The baselines in the interferometer array are connected to the correlator output voltage (R) as a sinusoidal output;

$$T = (\frac{V^2}{2})\, cos(\omega T) \tag{3.15}$$

where T is the received wavefront time delay, V is the voltage, and ω is the wavefront phase difference between the antennas. According to Ekers (2003), fringes are sinusoids with amplitude and phase that show wavefront interference. According to Rayleigh's traditional interpretation of the radiation law, the black-body temperature, also known as the brightness temperature, or T_B, of thermal emission is proportional to the radio brightness, also known as the flux density per unit solid angle, or B. This is the case (for (for $h\nu << kT_B$)) (Christiansen & Högbom 1987).

The radio brightness (B) of a source is its optimal intensity per unit solid angle. Equation3.16, Rayleigh's traditional formulation of the radiation law, connects it to the brightness temperature (T_B) and emission from a black body. The form of the antenna's reception pattern, P (l, m), or "beam," as well as A max, the antenna's maximum effective area, are what determine an antenna's effective area, A(l, m), where l, m are directional cosines as given by Christiansen & Högbom (1987):

$$A(l, m) = A_{max} P(l, m) \tag{3.16}$$

Extending a two-element interferometer's description to include extra elements increases the complexity of the correlation function.

3.7.3 Radio Interferometric Imaging

In interferometry, images of the target source are produced from visibility data using Fourier analysis. The images offer in-depth information that is impossible to obtain with a single-dish telescope alone. Instead of sampling in the image domain (l,m), Fourier domain (u, v) sampling is used by the interferometers. Sampling in Fourier space was done predict the distribution of sky brightness based on observations (I^{obs} (l,m)) derived from the observed visibilities (V^{obs} (u,v)) (Seidu 2020). A 2-D Fourier transform of V^{obs} (u,v) is I^{obs} (l,m). A definition of the complicated visibility is as:

$$V^{obs}(u,v) = \int I^{sky}(l,m)e^{-2\pi i(ul+vm)} \tag{3.17}$$

The uv-plane and observed complex visibility are converted into the sky brightness using the Fourier Transform. Equation 3.17 can be used to gauge sky brightness. By producing a dirty image (I^D), it is possible to determine I^{sky} (l,m) from the calibration. According to the Van Cittert-Zernike Theorem (Thompson et al. 2017, Zernike 1938), an image can be created by summing the cosine fringes in the Fourier sampling space. What follows is the imaging equation:

$$I^D(l,m) = I^{PSF}(l,m)\, I^{sky}(l,m) \tag{3.18}$$

In order to properly account for the I^{sky} (l, m), it is necessary to estimate the visibility function (S(u, v), V^{obs} (u,v)) in the regions of the uv-plane that have not been sampled (Seidu 2020).

The synthesized beam is produced by performing a Fourier Transform on the uv coverage. The flux density measurements need correct deconvolution (subtraction) of the instrument response, also referred to as the synthesized beam. The deconvolution

step is a reconstruction of the picture to produce the I^{sky}, whereas the imaging step is more of a convolution technique, as seen in Fig. 3.11. Deconvolution can be

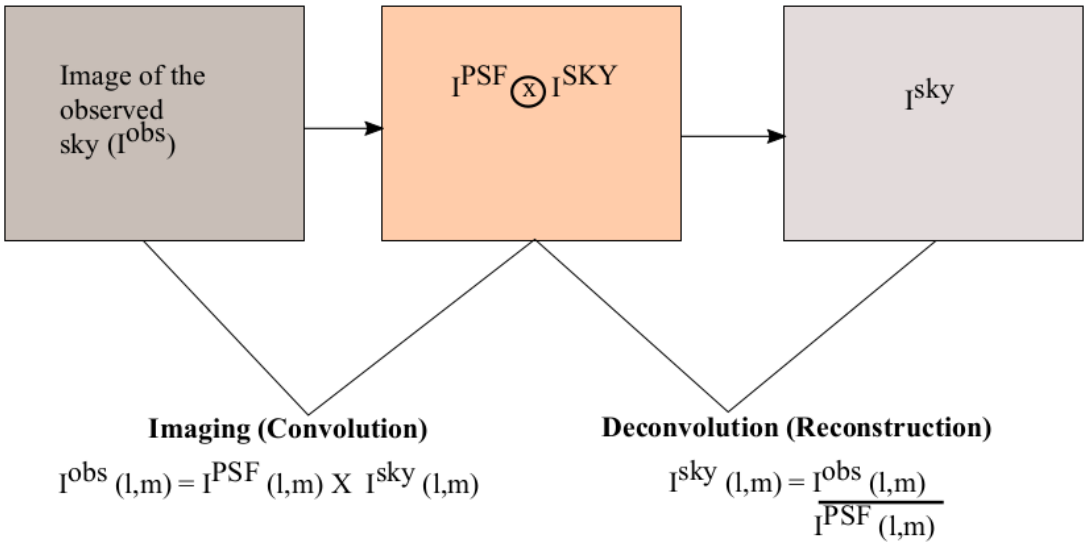

Figure 3.11: A graphical illustration of Deconvolution principle.

accomplished by the use of CLEAN algorithms in some situations. There are quite a few different CLEAN algorithms; nevertheless, for the purpose of this work, we shall present on the tCLEAN algorithm as stated by Garsden et al. (2015). An example of the image made using the tCLEAN algorithm is shown in Fig. 3.12. A 2D Gaussian fitting will give the integrated and peak flux as well as the the position angle.

3.8 BASELINES AND U-V COVERAGE

S (u, v) is the sampling function of the sky, and this is the uv coverage. As the radio telescopes follow the projected lm-plane target source across the sky, they create the uv-plane uv-tracks. Improvements to the sample function can reduce the number of holes in the uv coverage, but this is not a guarantee. As more radio telescopes are added to the interferometer and as more scans are performed on the target source, the sampling function will improve. Both of these methods for boosting uv coverage have their drawbacks, though. The first restriction is that the uv-plane is filled by rotation synthesis, so increasing the time spent monitoring the radio source won't increase the uv coverage if the track is completed from horizon to horizon (Maswanganye 2018).

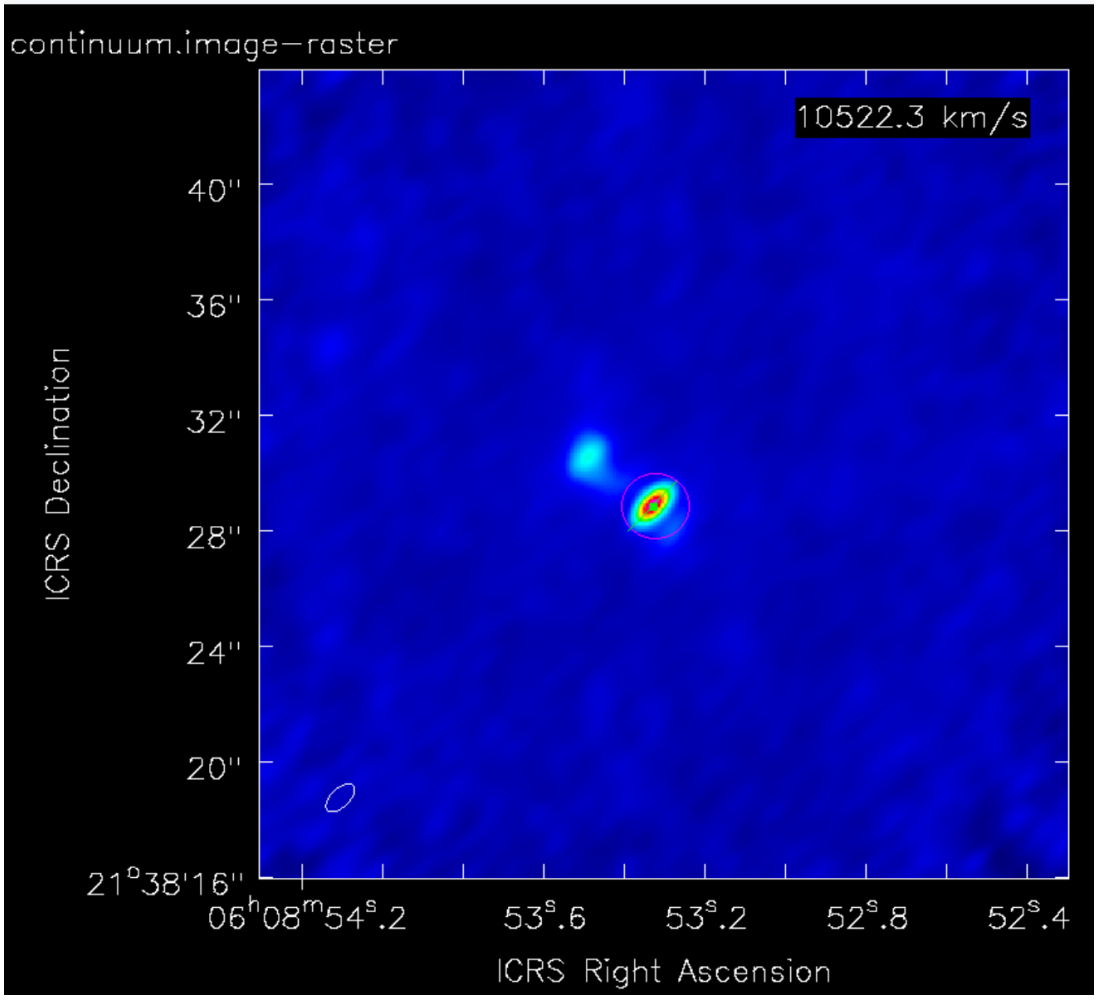

Figure 3.12: Imaging of the continuum

The second restriction is that the distance between the radio telescope and the target cannot be greater than the radio telescope's diameter. By cross-correlating voltages at the correlator, interference patterns are created when two or more telescopes are used together. Spatial coherence, also known as complex visibilities according to Seidu (2020), is the phenomenon in which voltages in distinct locations are correlated with one another. The visibilities comprise of both amplitude and phase and finer detais about u-v coverage are found in appendix A.2.1.

3.9 SUB-MILLIMETER INSTRUMENTATION

This thesis makes use of interferometric data obtained from the ALMA archives. The images were recreated at a better resolution that is not achievable using a single dish. The ALMA is a single, ground-breaking telescope that operates at wavelengths

between 0.32mm and 3.6 mm and is originally made up of 66 high-precision antennas. Its primary 12-metre array is made up of fifty antennas that work together as an interferometer or one telescope (Dent 2016). In order to examine light and signals from the universe's coldest objects, ALMA array was formed (Zainol 2021).

The Atacama Desert in Chile, with its dry climate and highest elevation of 5000 metres (16,500 feet), offers ALMA the ideal circumstances for detecting extremely weak signals from space. The ALMA array is depicted in Fig. 3.13, and The ALMA Telescope's primary features are summarized in Table 3.4. Its numerous radio dishes' surfaces are nearly flawless, with none deviating from an accurate parabola by more than 20 micrometres (approximately 0.00078 inches or 20 millionths of a metre). This prevents any incoming radio waves from being lost, allowing the final image to catch as much far-off cosmic light as possible.

The ultra-stable Carbon Fibre Reinforced Plastic (CFRP) reflector foundation and nickel panels with rhodium coating are used to create the radio dishes, which weigh roughly 100 tonnes apiece (Dent 2016). As an interferometer, ALMA combines the signals from its array of antennas, functioning as a single, enormous telescope the size of the entire array (Dent 2016). More details of the ALMA submillimeter More details of the ALMA submillimeter instrumentation, processing of radio signals with the ALMA and the frequency bands of ALMA receivers are found in appendices A.2.2, A.2.3 and A.2.4 respectively.

3.9.1 Submillimeter Observations

The ALMA data used in this thesis was extracted from: ADS/JAO.ALMA 2015.101454.S. after getting permission from the Principal Investigator (PI). Band 7 data that was extracted from ADS/JAO.ALMA 2017.1.00178.S. The observations of band 7 were done on 2017-12-02 and the archival data was released for use on 2019 -05-31. The band 7 data was observed at a wavelength of 0.93mm. Only continuum information was extracted from band 7 data hence discussion will major on band 6 data. The

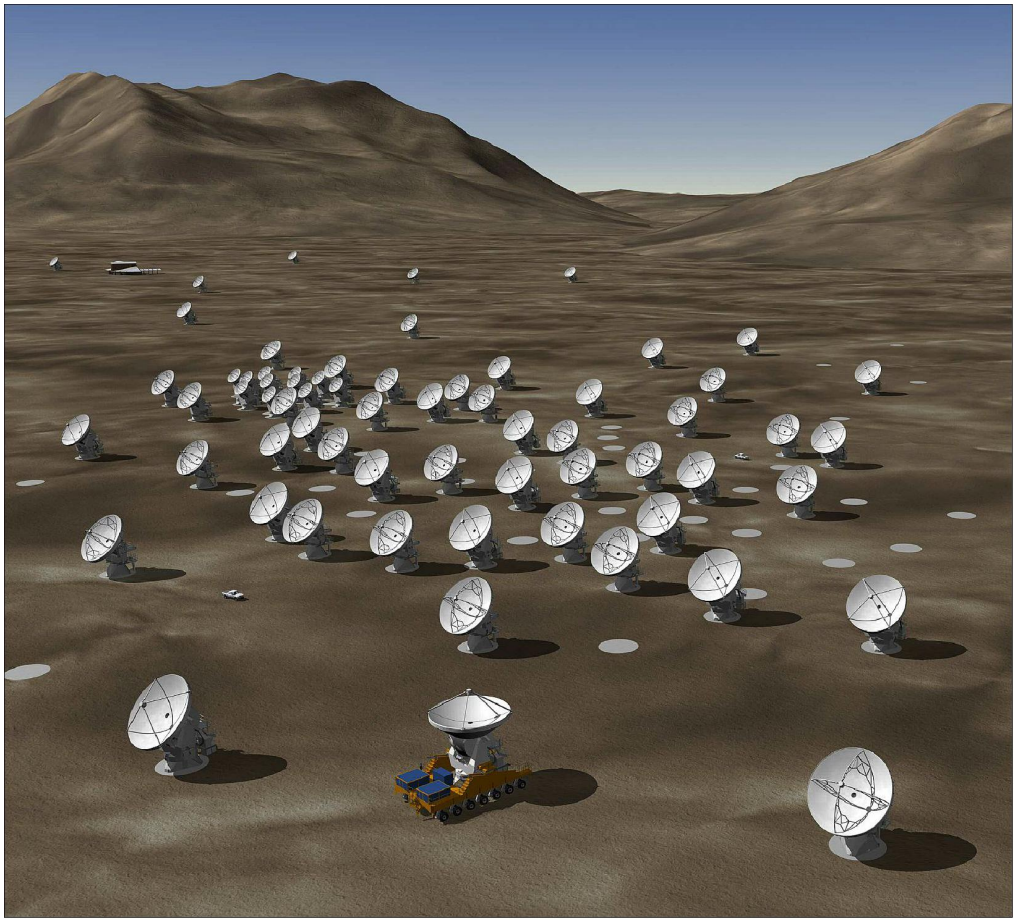

Figure 3.13: ALMA array. Credit:ALMA (ESO/NAOJ/NRAO)

Table 3.4: Basic specifications for the ALMA Telescope

Parameter	Quantity
Number of antennas	66
Dish sizes	Fifty-four 12 meter and twelve 7 meter
Antenna weight	100 tons
Total collecting area of array	71,000 square feet or 6600 square meter
Number of anetnna pads	192
Receiver frequencies	From 31 GHz to 950 GHz
Resolution	0.2 arcseconds to 0.004 arcseconds
Reconfigurable array	Minimum of 150 m, maximum of 16 km
Partners	United States, Chile, Japan, Europe Taiwan and Canada
Average annual rainfall	2.3in or 58mm
Average daily temperature at site	34° F or 1.1 ° C
Elevation	16,500 ft or 5000 m

observations of G188.95+0.89 were made with ALMA band 6 at 1.3 mm utilising two separate setups. According to Table 3.5, the Cycle 3 observations with 42 and 38 antennas, respectively, were carried out on various days. The anticipated baselines

ranged from 15 to 2600 m, and 31 minutes was the entire amount of time spent on the source. The two sets of data, Xca4 and Xf9b each included a brief examination of the bandpass calibrator as well as the flux scale calibrator, followed by a series of interleaved scans on a phase reference source and a number of targets within 15 degrees. Nine spectral windows (spws) were covered by the ALMA correlator. Using tasks from the CASA, the raw visibility data were calibrated using the conventional reduction script applied to the cycle-3 data. Version 4.7.2 of CASA, was used to manually calibrated the telescope data.

The sources J0510-1800 and J0750 - 1231 were put to use for in the bandpass calibration and the flux calibration. Eight spectral windows (SPWs) and their respective frequency ranges used in our study are; 216.643GHz, 217.104GHz, 218.760GHz, 218.440GHz, 219.560GHz, 230.538GHz, 231.900GHz and 234.000GHz respectively. The detected phase center of G188.95+0.89 in our study was R.A. (J2000.0) 06:08:53.300 and Dec. (J2000.0) +21.38.30.000. The spectral resolutions of the spectral windows was 15625KHz, 488 kHz, 488 kHz,122 kHz,122 kHz, 488 kHz and 488 kHz matching to resolutions of velocity of 20.3, 0.67, 0.17 and 0.67 km s^{-1}. The correlator was adjusted to span a wide range of spectral lines, with a focus on the CH_3OH $(4_{(2)}-3_{(1)})$, SiO $(J = 2 - 1)$, ^{12}CO $(J = 2 - 1)$ and $C^{18}O$ $(J = 2 - 1)$ rotational transitions.

Data from the science targets were extracted following calibration, and a pseudo-continuum dataset was created using line-free channels. For the continuum subtraction, a small number of line-free regions of the spectra were selected. The entire calibration process, including imaging the data cubes and self-calibrating to eliminate lingering phase and flux calibration inaccuracies, was carried out using CASA. A slightly larger synthesized beam of 42 mas $\times$ 42 mas with a position angle of 175° was produced by imaging the line data with a robust weighting of 0.5. After imaging, python scripts were used for the majority of the remaining analyses.

Table 3.5: ALMA Observational Parameters.

Parameter	ALMA 1.3mm
Observing date (UT)	2016-04-23
	2016-09-17
Configuration	C43-1
	C43-5
Phase Centre (J2000):	
R.A.	06h08m53.3000
Dec.	+21d38m30.00001
Project code	2015.1.01454.S
Time on Source (minute)	19,30
Number of antennas	42,38
FWHP Primary beam (″)	23
Baseband Freqs. (GHz)	216.6, 217.1, 218.8, 218.4,
	219.6, 230.5, 231.9, 234.0
Spectral windows	9
Channel width (MHz, km s^{-1}	0.488,0.635
Total bandwidth (GHz)	3.7
Continuum bandwidth (GHz)	0.39
Proj. baseline range (kλ)	11.5-2000
Gain calibrator(s)	J0603+21591
Bandpass calibrator	J0510+1800,J0750+1231
Flux calibrator	J0750+1231
Synthesised beam d	0.13
Continuum rms noise	2.0 mjy
rms noise (mJy beam $^{-1}$)	3

3.9.2 Sub-millimeter Data Calibration and Reduction

Noise, RFI, and the target source all contribute to the amplitudes and phases of the correlator's complex visibilities; as a result, data editing and calibration of complex visibilities are necessary before imaging the target source. Target source complex visibilities are calibrated using the calibrators. These radio sources are ideally unresolved, meaning that they are points, their flux density is relatively constant throughout the course of the observation, their locations have been precisely determined, and they are not masked by other sources in the vicinity.Because of this, we know their genuine, complex levels of visibility. The calibrators are employed to normalize the flux density and adjust for the target source's amplitudes and phases. During observations, the calibrators are used to monitor the sky and radio telescope gain for

accuracy. In order to minimise Radio Frequency Interference (RFI), the radio data that the interferometer received was reduced. Before creating an image, data reduction was done to calibrate the signals from each antenna. In order to post-process and reduce data from the current generation of radio astronomical telescopes, such as ALMA and VLA, Common Astronomy Software Applications (CASA) was employed. The CASA infrastructure is made up of several C++ programmes that are combined under an iPython interface to perform various data reduction tasks. The procedure for data reduction includes data analysis, editing, calibration, and imaging.

3.9.3 Calibration

Before calibration was done, SYSCAL table was fixed and time averaging of the Water Vapor Radiation (WVR) cal table was generated. The major calibration tasks undertaken were:

(i) setjy — Based on a flux density or model image, computes the model visibilities for a specific source, and is aware of conventional calibrator sources.

(ii) gencal —Generates a calibration table based on inputs of delay and antenna location.

(iii) bandpass — Finds complicated gains that vary with frequency (bandpass).

(iv) gaincal — Solves for time-dependent (frequency-independent) complex gains.

(v) fluxscale — Standard calibrators are used to bootstrap the flux density scale.

(vi) applycal — Calibration solutions that have been calculated are used. Bandpass and gain cal tables were applied.

(vii) plotcal — Plots calibration solutions, with the ability to flag them.

(viii) uvcontsub — complete the task of uv-plane continuum subtraction for spectral-line data.

(ix) split — For the specified sources, create a fresh (calibrated) MS.

3.9.3.1 Bandpass calibration

The process of measuring and correcting the gains of frequency-dependent component is known as bandpass calibration. The goal is to monitor the instrument response to fluctuation over time and at various frequencies. It is expected that a calibrator's bandpass will remain unchanged across the v_k frequency channels. For brief observations, the bandpass calibrator just needs to be seen once in advance because it is predicted to fluctuate slightly over time. Bright sources with a flat, featureless spectrum serve as the calibrators. Target source flux density scaling is another application for the bandpass calibrator. The ideal bandpass calibrator has high brightness and is a point source. The bandpass and flux density calibrator is the main calibrator.

Time and the radio telescope's altitude can cause the sky to shift during the observation. Changes in the sky are monitored by keeping a close eye on the secondary calibrator. A secondary calibrator that is both point-like and close to the primary source is ideal. When it is far away from the source, it may be tracking a different area of the sky than the target source, which would lead to an incorrect derivation of the amplitude and phase correction values. The interferometer frequently shifts focus from the primary calibrator to the secondary source. For bandpass calibration, J0750+1231 was employed as the source. Unlike the time-dependent effects handled by gain types 'G' and 'T', these frequency-dependent effects fluctuate across timeframes for a longer time. Therefore, using the bandpass task, it makes logical to solve for them as a single term 'B'. Signal amplitude and phase fluctuations on short time scales are primarily caused by the atmosphere, but there are similar variations across the band as a function of frequency predominantly due to instrumental effects.

3.9.3.2 Gain Calibration (gaincal)

The antenna-based gains were calibrated using gaincal as a function of time. Any multiplicative polarisation- and time-dependent complex gain effect downstream of the polarizers for a given spectral window is represented by Type G. Gaincal and

Bandpass algorithms used a model in the measurement set to compare with the actual data and determine the corrections to be applied per antenna so that the observed information closely matches the predicted one (model). The model has zero phase because it is expected that the calibration sources are point-like.

3.9.3.3 Time-dependent Phase/Amplitude Calibration

In our calibration J0750+1231 was used as a flux calibrator and J0603+2159 as a phase calibrator. A good phase calibration is key for image fidelity and good noise level. A good phase calibrator is a relative bright point source at well known position and need to be close to the scientific target in sky. While the flux standard's flux densities were determined, the default models of 1 were used for the bandpass and phase reference calibrators. Their flux densities were normalized using the task fluxscale. The gains from the other two sources are multiplied by an estimated factor based on the corrections for the flux standard, and a scaled table is written.

3.9.3.4 Imaging the complex visibilities

Following the completion of the data editing and calibration processes, the dirty image I^D can be deconvolved in order to locate the true intensity I. This is possible due to the fact that I D is the convolution of the desired intensity and the point spread function, as demonstrated by equation 3.18. Deconvolving the dirty intensity can be done with the help of the CLEAN algorithm (Högbom 1974). Since Högbom (1974) created the original CLEAN algorithm, many variants have been developed. The Högbom (Högbom 1974), Clark (Clark 1980), and Cotton-Schwab (Cornwell et al. 1999), algorithms are all examples of CLEAN algorithms. Since the Högbom CLEAN method was the first of its kind, we have decided to simply detail its implementation here:

1. The peak's location and intensity can be determined from the dirty image.
2. After multiplying the dirty beam, peak strength, and damping factor or loop gain γ (which is ≤ 1), we get the point source.

3. The dirty image is then corrected by subtracting the source from its peak location.

4. The intensity accumulation model $\dot{I}$ is then used to record the location of the point source.

5. The aforementioned procedures should be repeated until the dirty image reaches the user-specified threshold peak strength.

6. Finally, an elliptical Gaussian fitted to the central lobe of the dirty beam is used to construct the CLEAN image by convolving the accumulation model of the intensity $\dot{I}$ with the ideal CLEAN beam.

The leftover sidelobes from the dirty image can shed light on things like noise in the clean image (Cornwell et al. 1999). The radio astronomy interferometry data reduction software MIRIAD, CASA and AIPS all make use of CLEAN methods.

3.10 INFRARED OBSERVATIONS

Due to the embedded nature of massive young stellar objects, the dust surrounding them during their formation prevents observations of the earliest stages of development at optical wavelengths. Fortunately this same dust re-radiates the energy from the optical and UV emission at micron scale wavelengths (Tielens 2005) allowing observation of the regions surrounding the young stellar objects.

The infrared intensity takes the form of a modified blackbody for this dust emission (Tielens 2005) and as the massive young stellar object heats up, its peak will move toward shorter wavelengths. Therefore objects dominated by shorter wavelength infrared emission can be thought of as the more evolved "older" objects compared with those with spectral energy distributions dominated by longer wavelength emission. This is a key observing feature of both high and low-mass stars and is well represented in the low-mass star classification of Lada (1999) as shown in Fig. 3.14.

Infrared (IR) images of the regions surrounding the G188.95+0.89 methanol maser

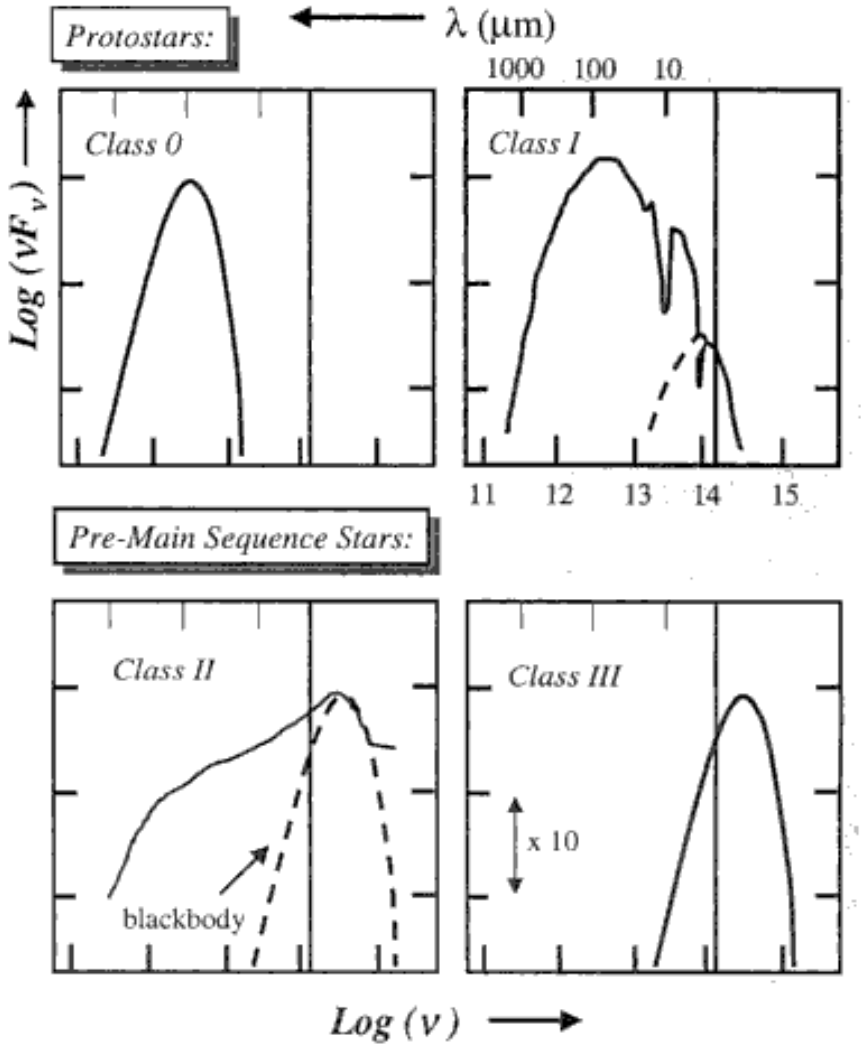

Figure 3.14: The classification system used to define the stages of low mass protostellar evolution from observable infrared characterisitcs (Lada 1999).

sites are presented. The purpose of imaging is to find out whether any IR sources can be associated with the methanol masers, as well as to see if there is anything unusual about the region in which the masers are being produced. Another reason of imaging is to investigate shocked gas in the massive star forming regions. The relationship of the methanol masers to IR objects, other maser species and H11 regions was examined.

3.11 INFRARED INSTRUMENTATION

Several Galactic plane scans, ranging from near-IR to radio, have detected G188.95+0.89. A multi-wavelength image mosaics has been to investigate the environment around

the maser source. Between the I-front and the PDR, we can easily pinpoint the emission related to the transition of polycyclic aromatic hydrocarbon (PAH) molecules as sytated by Povich et al. (2007). The main goals of the GLIMPSE survey were to further knowledge of star formation, interstellar dust physics, and the Milky Way's large-scale structure as revealed by stars (Churchwell et al. 2009). A combination of archival MIR, FIR, and milliimeter data was used to create a multiwavelength image of each location in the source.

3.11.1 Near Infrared Image Archives

The photometric data (J, H, and K_s) and near-infrared (NIR) images were obtained from 2MASS (Cutri et al. 2003). Near-infrared observations have several significant advantages over a wide range of observational methods, from X-ray to radio wavelengths. For instance, compared to those in the optical and numerous atmospheric windows, they are significantly less affected by interstellar extinction. Infra-red emission is useful since it pinpoints the locations of significant SFR features. Using the 2MASS photometric data, the SFR was examined for probable protostars and T Tauri stars, also referred to as class I and class II objects (Urquhart et al. 2004). The photometric precision of the 2MASS data is between 1 and 2 percent, and its positional accuracy is greater than $1''$. According to Cutri et al. (2003), the limiting magnitudes for J, H, and K_s are 15.8, 15.1 and 14.3, respectively. In order to concentrate on star formation in the AFGL 5180, we collected photometric data on sources from the 2MASS catalogue that were situated within a 60 $''$ radius of the location of the 06058+2138 IRAS point source. Any 2MASS sources found to have an SNR of less than 10 in any of the three frequency bands were ignored, as per Urquhart et al. (2004).

3.11.2 Mid- and Far-infrared Image Archives

The mid-infrared (MIR) image mosaics were acquired from the Midcourse Space Experiment (MSX) data repository Price et al. (2001), while the far-infrared (FIR)

images came from the InfraRed Astronomical Satellite (IRAS) data archives, according to Beichman et al. (1988). The MSX broad-band mid-IR images are used to investigate the nature of star formation within AFGL 5180 and the massive star development nearby. The Spitzer's Infrared Array Camera (IRAC), which has a high MIR resolution and sensitivity, supplied this information. This survey used Spitzer IRAC's four bands, which have bandwidths of 0.75, 1.0, 1.4, and 2.9 μ m and are centred at 3.6, 4.5, 5.8, and 8.0 μ m (Fazio et al. 2004).

Using the KARMA 2 program, the mid-IR flux values were approximated from the MSX images by estimating the flux in both the source and the background. By calculating the mean flux in boxes at various locations around the mm source, background residual flux was calculated. This method enables the removal of background noise as well as emission from local objects and extended regions as stated by Minier et al. (2005).

FIR observations between 70 and 500 m μm were obtained using the Photodetector Array Camera and Spectrometer (PACS), which were then used to examine the gas, the dust, and the imbedded points sources (Poglitsch et al. 2010). The Spectral and Photometric Imaging Receiver (SPIRE) on the European Space Agency's (ESA) far infrared and submillimeter observatory was also used to analyse gas and dust (Griffin et al. 2010). Source photometry (both point and extended) was obtained from the NASA/IPAC Infrared Science Archive (cited as (Berriman 2008). Hot cavities of dust left behind by HII regions were analyzed in the mid-infrared range (22 μm), while dust heated by YSOs can be traced in the far-infrared (70 μm) at the locations of young, cool protostellar objects (Azatyan et al. 2022). The locations with the hottest cavities are the ones best suited for star formation.

CHAPTER FOUR

RESULTS AND DISCUSSION

Three major sections make up this chapter. The findings of the single dish radio CH_3OH maser monitoring at 6.7 GHz for G188.95+0.89 are shown in the first part (4.1). Analysis was done on the variations of prominent maser characteristics. A description of the spectra and time series analysis was provided. The second part presents the interferometry imaging results of the 1.3 mm observations. Radio continuum emission results are presented in sections 4.4.2. The third part deals with the results of infrared archived data of the source G188.95+0.89 in which they are presented in Section 4.3. The radio, inteferometry and IR results are discussed in section 4.4.

4.1 SINGLE DISH RADIO RESULTS

4.1.1 Variability of the 6.7 GHz CH_3OH Maser Features

The chosen spectra of the G188.95+0.89, related to 6.7 GHz methanol maser observations that was collected at the maximum of three flares (Fl_n for n=6, 12, and 18) is presented in 4.1. The spectra is as a result of addition of right circular polarization (RCP) and left circular polarization (LCP) spectra however RCP and LCP spectra are shown in appendices A.1 and A.2. According to Bartkiewicz et al. (2016), Szymczak et al. (2018), claims that maser spectra obtained with a single dish exhibit a wide variety of features with Gaussian velocity profiles, all of which can be traced back to the presence of localized clouds. The velocity in which maser emission is detected ranges from v_{LSR} = 8.3 to 11.5 km s^{-1}. Change in the spectral profile that has occurred over the course of 18 years of observations is depicted in Fig. 4.1. This profile, upon closer inspection, was found to be constructed out of a large number of line blended masers, to be specific for $+10\,\mathrm{km\ s^{-1}} < v_{LSR} < +11.3\,\mathrm{km\ s^{-1}}$. Maser ve-

locity features were chosen because they are the brightest and mirror the behaviour of the nearby velocities (Mutie et al. 2019). Most of the time, the brightness of the cloud's brightest spot corresponds directly to the optimum flux density of each feature.

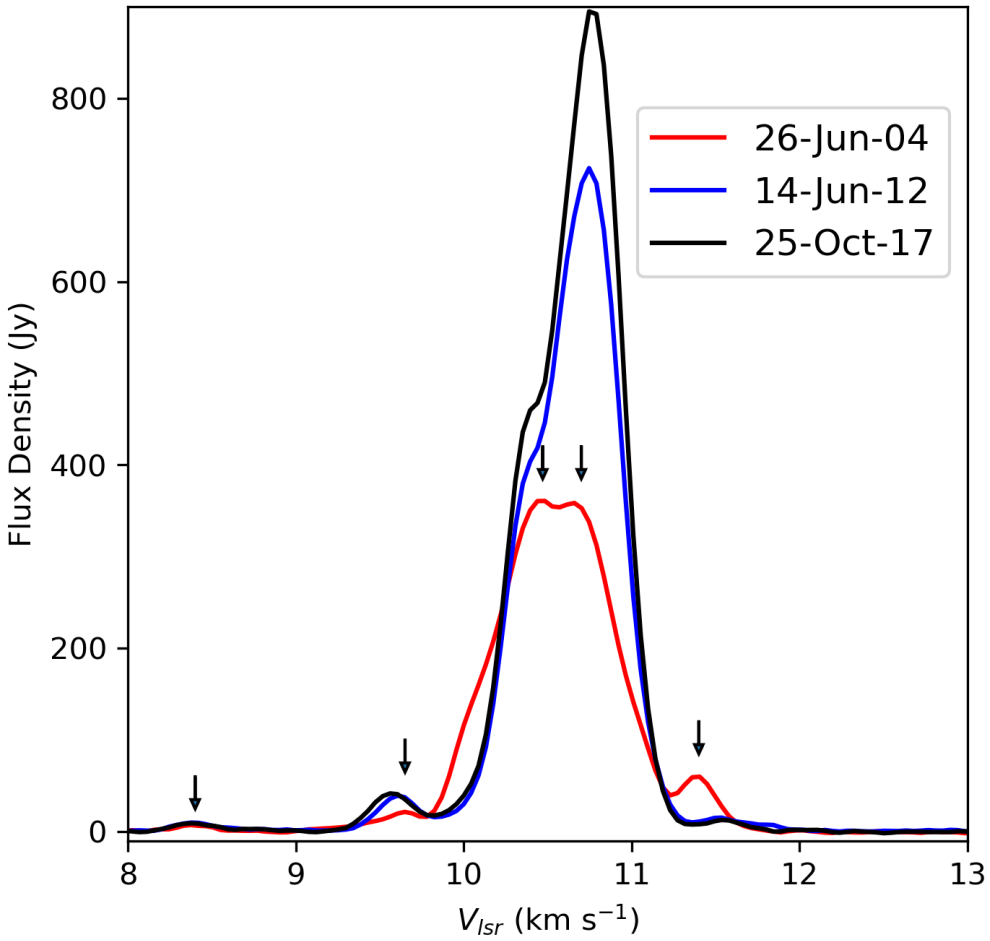

Figure 4.1: Variation in the G188.95+0.89 spectra related to 6.7 GHz methanol masers at the peaks Fl_6, Fl_{12}, and Fl_{18}.

The fluctuating circumstances on extremely fine angular scales in methanol masers can be probed easily, since the masers are very sensitive in slight environment changes. The maser features have strengthened others diminished, but most features have retained their periodicity during the observation. In some features there was variations in velocity and others experienced velocity drifts. In order to analyze these findings, five features were picked. In the velocity regime of highly combined lines, there are two at v_{LSR} =+10.44 km s^{-1} and +10.70 km s^{-1} respectively, and other three

bright velocity features at v_{LSR} =+8.42 km s^{-1}, +9.65 km s^{-1}, and +11.45 km s^{-1} were selected. On close scrutiny of Fig. 4.1 it was recognized that, the two features v_{LSR} =+10.44 km s^{-1} and +10.70 km s^{-1} are likely to be made up of multiple masers; the other three features are less likely. Integrated flux density time series graphs ($F_{\mathbf{Int_{6.7}}}$) were published in my earlier paper (Mutie et al. 2021).

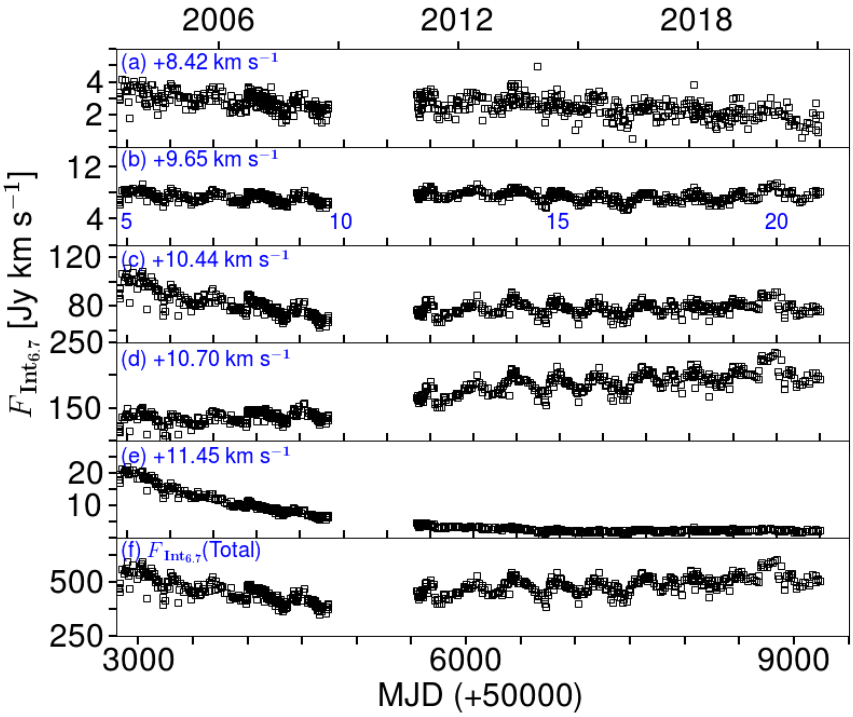

Figure 4.2: Light curves displaying time series plots of the chosen 6.7 GHz methanol maser features in G188.95+0.89. Integrated total flux density ($F_{\mathbf{Int_{6.7}}}$) of all the masers connected to G188.95+0.85 is shown in (f). According to Mutie et al. (2021), the x-axis in (a) to (e) denotes the flare maximum estimates, Fln where n ranges from 5 to 21 (for τ ∼395 d).

Although it is not immediately apparent for the feature v_{LSR} =+11.45 km s^{-1} in Fig. 4.2, the rest of the selected features are periodic. Two techniques, the Lomb-Scargle (LS) periodigram by Scargle (1982) and the Period04 software programme created by Lenz & Breger (2004), were utilized to calculate the period of each of the maser velocity features. Period outcomes were tabulated in Table 4.1 where the mean period for each method was included. The average values of the two methods are separated by no more than 3σ standard deviations, τ_{LS} =397.6±2.1 d (Mutie et al. 2021). Two features were found to be decaying between years 2003 and 2021, v_{LSR} =+8.42

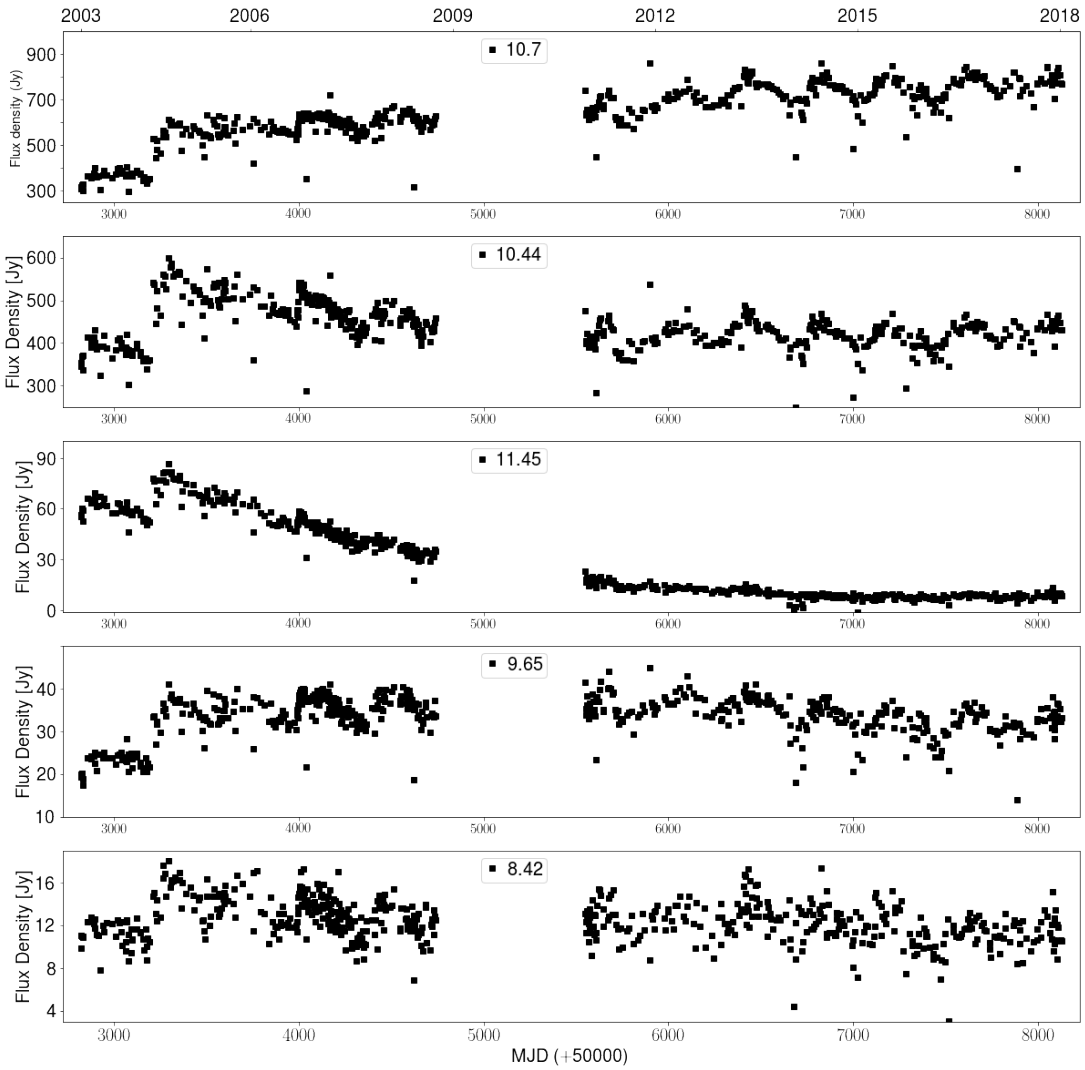

Figure 4.3: Flux density plots of selected five 6.7 GHz methanol velocity features pinpointed in Fig. 4.1. The five maser features have v_{LSR} =+8.42, +9.65, +10.44, +10.70 and +11.45 km s^{-1} respectively as labelled in each panel.

and +9.65 km s^{-1} and the v_{LSR} =+10.70 km s^{-1} feature has been monotonically increasing since 2003 as shown in Fig. 4.3. As soon as it was discovered by Menten (1991*a*), the +10.44 km s^{-1} was the brightest maser velocity feature, at present it is the second most powerful and it continued to deteriorate until MJD 5000. After that it is flattened out and then gradually began to increase, as seen in Fig 4.4. The increase was likely resulting from contributions made by the the +10.70 km s^{-1} feature are probably what led to the increase in brightness.

An exponentially decaying function was fitted for v_{LSR} =+11.45 km s^{-1} flux density

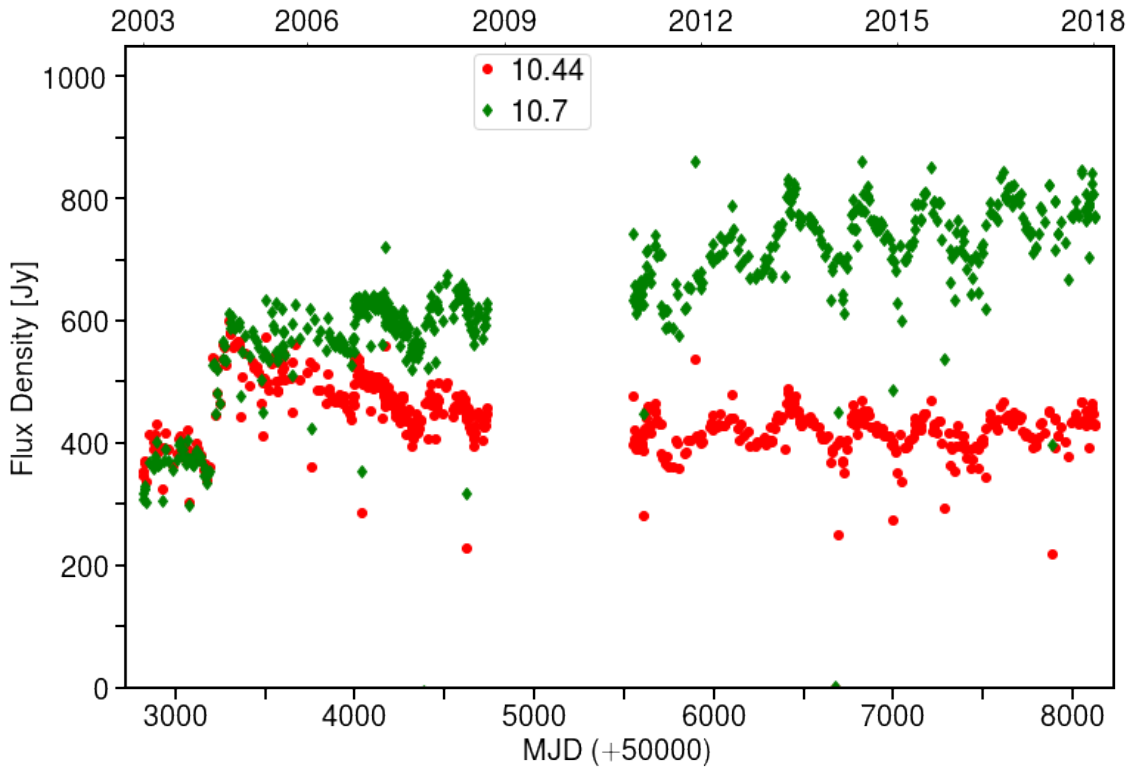

Figure 4.4: Flux density plots of the v_{LSR} =+10.70 and v_{LSR} =+10.44 km s^{-1} maser features. At present the v_{LSR} =+10.70 km s^{-1} feature is the brightest.

time series, as shown in Fig. 4.5. The fitted function is:

$$F_{\mathbf{Int_{6.7}}} = a \times e^{MJD/b} + c, \tag{4.1}$$

where a =150.0±4.0 Jy km s^{-1}, b = −1380.0±20.0, and c =1.740±0.050 Jy km s^{-1}. It was reported by Goedhart et al. (2004) this exponentially decaying feature reached a maximum on 2001 November 12 (MJD 2225), F_{Int} ∼45.2 Jy km s^{-1}. Based on equation 4.1,Mutie et al. (2021) estimate F_{Int} to be around 30 Jy km s^{-1} for MJD 2225. The values were outside estimated inaccuracies, and it was discovered that the projected value was much lower than the real value. This difference may be due to varying velocity resolution, during the current observation it was0.044 km s^{-1} while in Goedhart et al. (2004) it was 0.056 km s^{-1}. Line-merged features may also be a factor to consider contributing to the difference in integrated flux.

To test for periodicity in the +11.45 km s^{-1} feature, the original time series was subtracted using equation. 4.1 The residual was then shown in Fig. 4.5, indicating

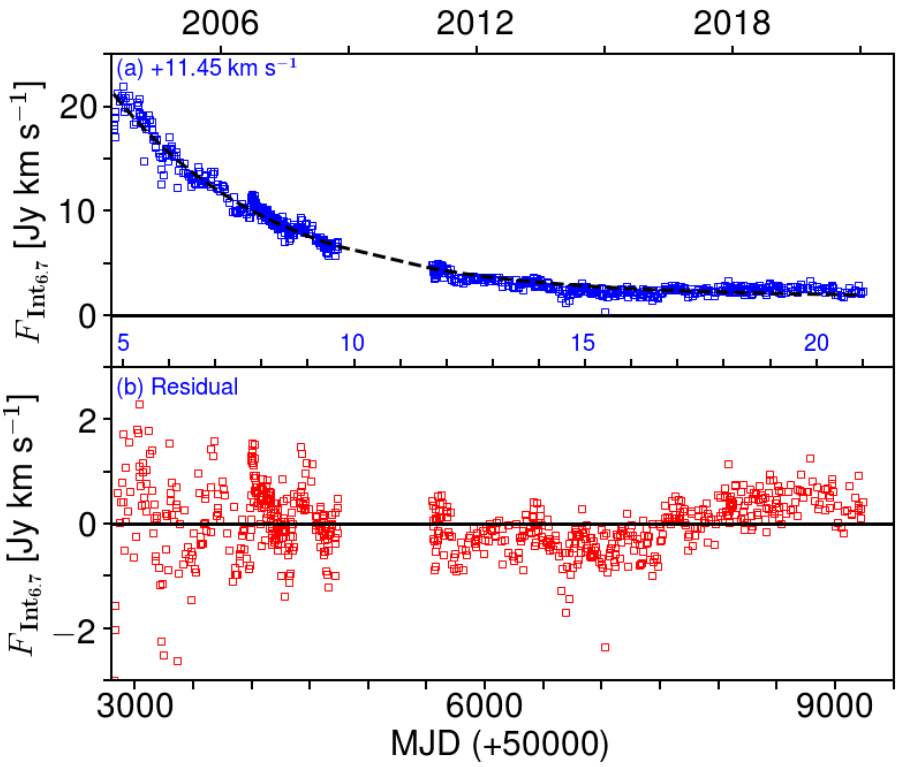

Figure 4.5: (a) Plot of the time series for the selected $F_{\mathbf{Int_{6.7}}}$ for the exponentially decaying v_{LSR} =+11.45 km s^{-1} maser feature fitted function in (black dashed line). (b) A plot is made showing the residual of the integrated flux density, which is the raw data less the exponentially decaying function that was fitted to those data. It is important to take note that the secondary x-axis in (b) denotes the predicted maximum of each flare, Fl_n for n=5 to 21 (forτ ∼395 d), respectively. Source: (Mutie et al. 2021).

that it might be periodic. After MJD 7500, there was a very tiny rise that may have been caused by changes in the V_{LSR} =+10.70 km s^{-1} velocity feature. The overall integrated flux density was first seen declining and then rising before MJD 5000, indicating that the maser velocity features were decreasing in brightness before brightening of the v_{LSR} =+10.70 km s^{-1} feature dominated (Mutie et al. 2021).

Each flare's relative amplitude variation was determined using the following formula:

$$R_{amp} = \frac{S_{max} - S_{min}}{S_{min}} = \frac{S_{max}}{S_{min}} - 1. \tag{4.2}$$

Table 4.1 contains the findings of the relative amplitude, denoted by the symbol (R_{amp}) for each of the five different velocity features that were chosen. This number

Table 4.1: The following are the specifics of each chosen 6.7 GHz maser feature:the feature central velocity, the velocity range over which F_{Int} is calculated, the velocity drift (1σ standard deviation in parenthesis), its goodness of fit (R^2), the period calculated using the Period04 and LS techniques and the explanation of long-term change. Standard deviations (1σ for the mean period of each methods are provided. Remarks on velocity drift are provided: uncertain (R^2 <50%), blue-shifting, and red-shifting. Each feature's flux density trends are commented. These details on maser velocity features were published in my earlier paper (Mutie et al. 2021).

	Velocity			Period		Relative	Comments	
Feature	Extent	Drift	R^2	τ_{Period04}	τ_{LS}	Amplitude	Velocity	Flux density
[km s^{-1}]	[km s^{-1}]	[$\times 10^{-5}$ km s^{-1} d^{-1}]	%	[d]	[d]			
+8.42	0.482	−1.181(7)	22.91	394.4	397.0	2.82	uncertain	gradually dwindling
+9.65	0.263	−2.381(3)	81.62	395.8	396.7	0.63	blue-shifting	Increasing Gradually
+10.44	0.182	+0.422(4)	30.41	393.5	398.3	0.12	uncertain	complex
+10.70	0.313	+0.392(5)	5.72	396.3	398.2	1.0	uncertain	increasing
+11.45	0.312	+1.881(4)	66.02		397.8	∼1	red-shifting	exponential decay
Mean				395(1)	397.6(7)			

fluctuates between 0.12 and 2.82 across the five velocity features. Take note that the amplitude is decreasing almost proportionally during the decay, as shown by the formula R_{amp} ∼1 for the $v_L SR = +11.45$ km s^{-1} feature. the R_{amp} value greater than one is an indicator of a likelihood of a flare. When comparing maser velocity components, no phase delays were seen.

4.1.2 Time Series and Light curves of Maser components in 2D Contour Form

A dynamic spectrum was created, as shown in Fig. 4.6, to visualize the variability of these G188.95+0.89-related 6.7 GHz methanol masers. The linked 6.7 GHz methanol masers' temporal behaviour was examined using the dynamic spectra (Proven-Adzri et al. 2019). On close scrutiny of the dynamic spectra, it was found that in most velocity channel between $v_{LSR} = +8.3$ and +11.5 km s^{-1} seems to experience periodic variability a clear indication that this source is highly variable. The findings are in agreement with earlier researchers who observed the source and found it to be periodic (Goedhart et al. 2004). The dynamic spectra contour plot covers the time-range 2003 June to 2021 January. A dynamic spectrum gives a clearer idea of how

light curve behaviour fluctuates with different velocity features. The fact that the 10.44 and 11.45 km s^{-1} masers began to fade about MJD 52000, while the other masers remained largely at the same flux level, is a highly intriguing feature of the masers in G188.95+0.89 (Goedhart et al. 2014*a*).

The 2-d plot in Fig. 4.6, displays the full flux density variations of the 6.7 GHz methanol features between 8.0 and 12.0 km s^{-1}. The intensity of the velocity features 8.42 km s^{-1} and 9.65 km s^{-1} decreased gradually overall during the monitoring period, whereas the velocity feature at 11.45 km s^{-1} appeared to experience an exponential decay (Mutie et al. 2019). By visual inspection, peak velocity seems to be drifting as from 2003 to 2021 as shown in Fig. 4.6. The mobility of the gas as reported by (Goddi et al. 2011) or the variability of a close pair of spectrally blended features as stated by (Szymczak et al. 2015) are thought to be the causes of the velocity drift, although this is not certain. While the 10.70 km s^{-1} velocity feature appears to be increasing brighter at the same time, the 10.44 km s^{-1} feature appears to be getting dimmer from 2003 to 2021. Peak flux density appears to be changing from 10.44 to 10.70 km s^{-1} as shown in Fig. 4.7.

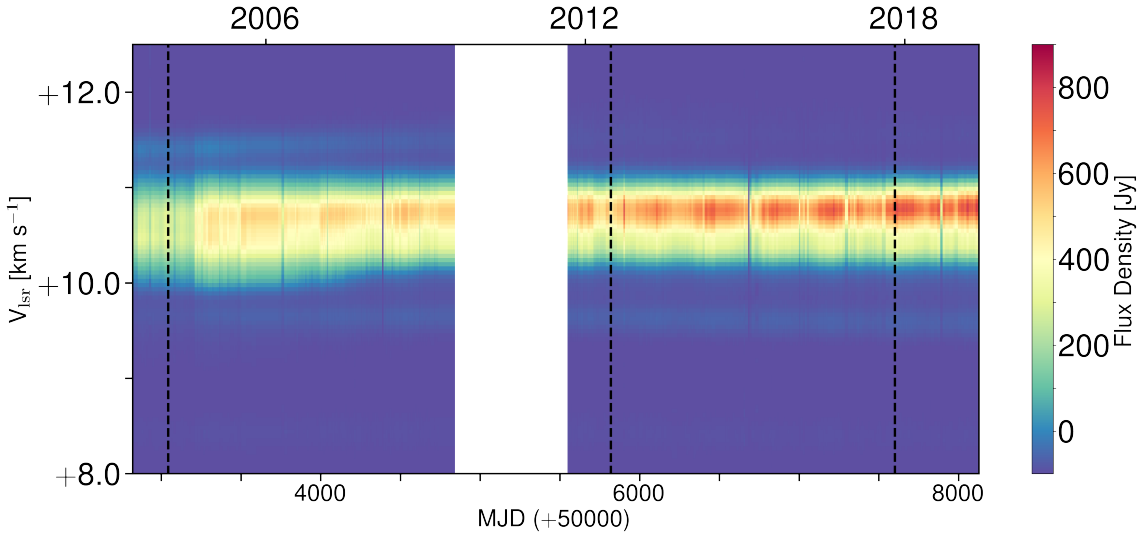

Figure 4.6: Dynamic spectrum of G188.95+0.89-associated 6.7 GHz methanol masers. The maximum spectra of Fl_6, Fl_{12}, and Fl_{17} are delineated by dashed lines in Fig. 4.1. Since the telescope was down for maintenance from September 2008 until December 2010, the corresponding blank region indicates that no observations were made during that time.

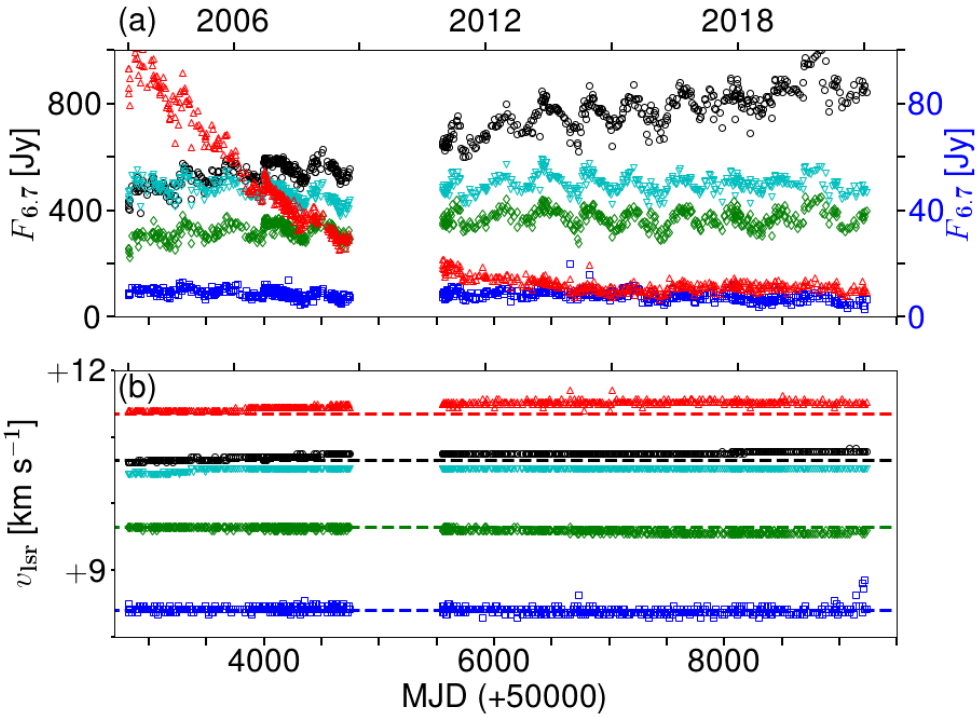

Figure 4.7: (a)The time series of the 6.7 GHz methanol masers associated with G188.95+0.89. (b) A fit to determine the extend of velocity drifts in the selected maser features.

4.1.3 Maser velocity drifts

Each velocity time series underwent linear regression analysis to ascertain the velocity drift, the findings are shown in Table 4.1. Among the features, two of the features had quantifiable velocity drifts, with "goodness of fit" values $R^2 > 50\%$. The v_{LSR} =+10.70 and v_{LSR} =+10.44 km s^{-1} velocity features' apparent drift may be due to fluctuations in the strongly line-merged masers that contribute to the features, as seen in Fig.4.1. A single Gaussian profile can be fitted for v_{LSR} =+9.65 and +11.45 km s^{-1} velocity features.

Numerous masers have reported velocity drifts. A velocity component of a water maser related with W75S red shifted 1 km s^{-1} over 3.5 yr, approximately 8×10^{-4} km s^{-1} d^{-1}, according to Lekht et al. (1995), who recommended that this change was caused by shocks brought on by increased wind activity. A single 6.7 GHz CH3 OH feature associated with G22.357+0.066 exhibited velocity change, according to

Szymczak et al. (2015), the feature endured for almost 520 days and had a velocity drift of 0.24 km $s^{-1} yr^{-1}$, or 6.5 $\times 10^{-4}$ km $s^{-1} d^{-1}$. They don't know for sure whether this is caused by the velocity of the gas or by extensively blended maser feature (MacLeod, Chibueze, Sanna, Paulsen, Houde, van den Heever & Goedhart 2021*b*). More 6.7 GHz methanol sources with velocity drifts were discovered by Szymczak et al. (2018). Again, they predict that these are caused by changes in close or blended features in the line, but some of them may actually be infalling gas. The features that were discovered to have systematic velocity drifts over a long period of time are shown in Fig. 4.1 and are summarized in Table 4.1.

One reason for the continuous velocity drifting in this source is that the variations of heavily line blended masers in a feature provide the appearance of velocity variation (Szymczak et al. 2018). In conclusion, the aforementioned velocity drifts make excellent candidates in upcoming VLBI researches to determine whether the features' radial velocity acceleration actually represents accreting gas, as was shown for AFGL5142 (Szymczak et al. 2018).

4.2 RADIO INTERFEROMETRIC RESULTS

The results of 230 GHz CH_3OH maser monitoring for G188.95+0.89 using ALMA telescope are presented in this section. Observation results of mm-wavelength, molecular line emission and high-resolution dust continuum were provided.

4.2.1 G188.95+0.89 Continuum Emission

The continuum image was created by collapsing all the spectral windows and channels. Fig. 4.8 and Fig. 4.9 presents the ALMA 1.3 mm solid and color continuum images of G188.9+0.89 (S252, AFGL 5180), obtained with ALMA band 6. The millimetre continuum reveals two cores namely MM1 and MM2 associated with G188.9+0.89 source. The two bright cores are elongated along the Northeast Southwest direction. Within a $4' \times 4'$ radius surrounding each methanol maser site, radio

continuum data was collected using Aladin and SIMBAD on CDS. The periodic 6.7 GHz CH_3OH masers seem to be near MM1 as indicated by the plus symbol. Core MM1 is where both the IR and radio sources shine brightest. The radio and IR sources corresponds with the most brilliant core MM1.

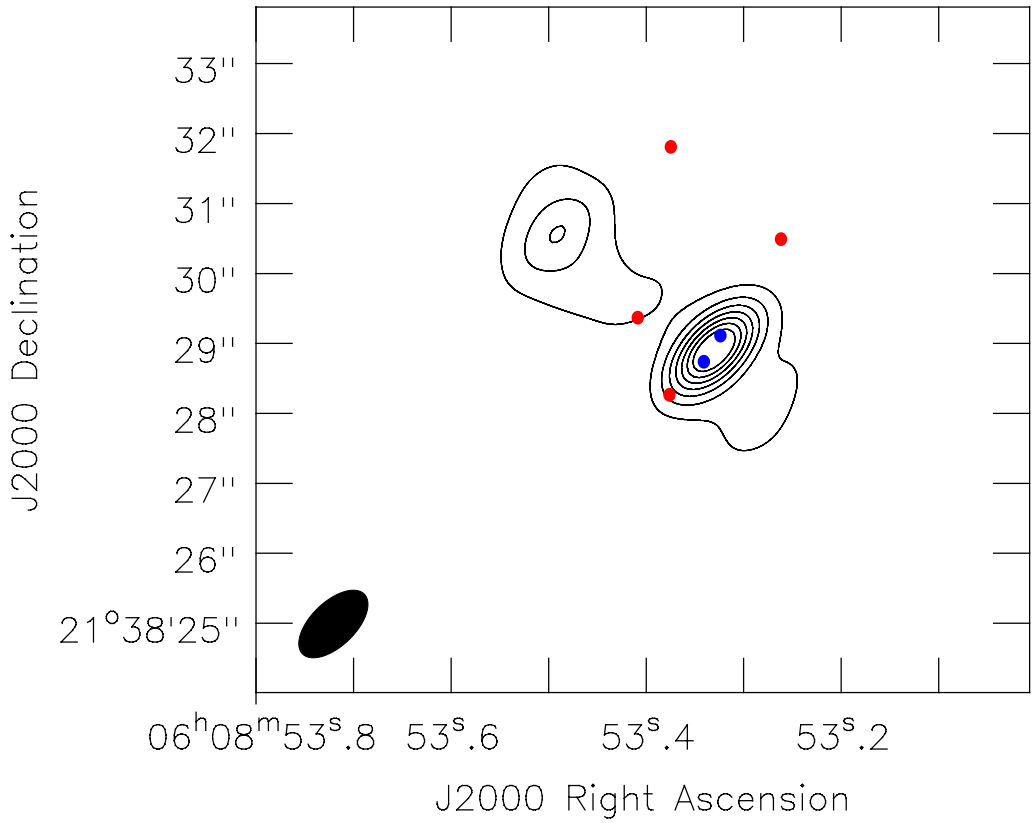

Figure 4.8: Solid contours represent the 1.3 mm continuum emission. The continuum contours are (9, 21, 33, 45, 57, 69 and 82) mJy beam^{-1}. The blue dots symbols depict methanol masers maser spots and the red dot symbol marks the positions of infrared sources (IRS) 1-4, where IRS 1 coincides with MM1 and IRS 2 with MM2. In the bottom left, an ellipse with a fill indicates the full width half maximum (FWHM) of the synthetic beam.

The AFGL-5180 continuum was imaged with higher resolution thanks to data of the source at 320 GHz. Eight millimeter continuum cores (MM1–MM8) were found in ALMA band 7 data, and the cores were found to be connected to G188.95+0.89 (Mutie et al. 2021). Figure 4.10 (top panel) shows a composite picture of G188.95+0.89 in WISE bands (3.4μm: red), (4.6 μm: green) and (12 μm: blue), as well as ALMA 1.3 mm dust continuum emission (Mutie et al. 2021). The 850 μm SCUBA MM2 object is represented by the green (4.6 μm) and it is the dominant object south of

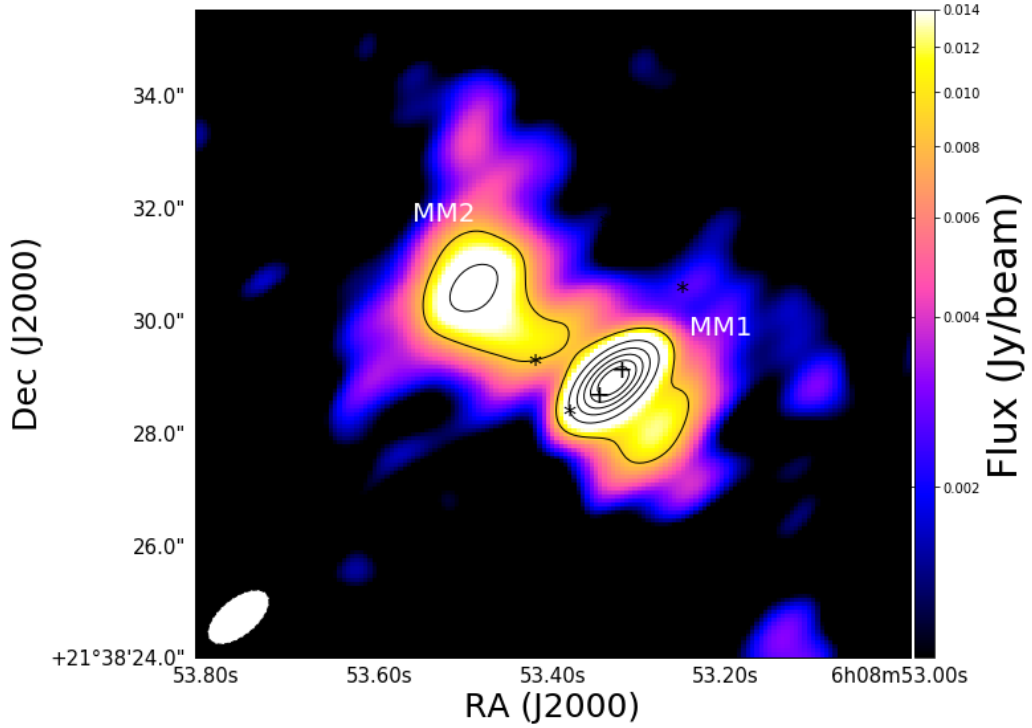

Figure 4.9: Solid contours shows band 6 ALMA 1.3 mm Continuum emission. The continuum contours are (9, 21, 33, 45, 57, 69 and 82) mJy beam^{-1}. The plus symbols depict methanol masers maser spots and the star symbol marks the positions of infrared sources. Synthesized beam at FWHM is shown as a filled ellipse in the bottom left corner.

the core object in the WISE image, which has a central infrared source equivalent to the 850 μm SCUBA MM1 object, that is brilliant in all three mentioned WISE bands (Mutie et al. 2021).

The use of ALMA band 7 data resulted to eight 1.3 mm objects (MM1-MM8) that were resolved from G188.95+0.89. 850 μm SCUBA MM1 and MM2 objects of Minier et al. (2005) are connected to MM1-MM4 and MM5-MM8 objects, respectively, as shown in in Fig. 4.10 (bottom panel). MM1 (the brightest dust continuum object) is linked to the periodic 6.7 GHz CH_3OH maser source (Mutie et al. 2021). MM2 was also found to be an important object at 1.3mm by ALMA. MM1 continuum core was resolved into a single object and MM2 was resolved by ALMA band 7 observation into two continuum cores (grey contours of Fig. 4.10 bottom zoom-in) as reported by Mutie et al. (2021). Based on the assumption of optically thin dust emission, the value of M_d in Table 4.2 was calculated using Hildebrand (1983):

$$M_d = \frac{S_\nu \, D^2}{\kappa_\nu \, B_\nu(T_d)} \tag{4.3}$$

Using D as the source distance of 1.76 kpc and the dust opacity per unit mass of $\kappa_\nu = 0.33$ cm^2 g^{-1} for 230 GHz according to Weingartner & Draine (2001), the dust continuum mass can be calculated. The dust continuum flux density S_ν at frequency ν is given in Table 4.2. At dust temperatures T_d, the Planck function is denoted as $B_\nu(T_d)$. The dust mass estimates are based on the temperatures used in Minier et al. (2005) for cores MM1–MM4, a temperature of 42 K was used, whereas for cores MM5–MM8, a temperature of 50 K was utilized. A gas-to-dust mass ratio of 100 was used to determine the core masses. The table 4.2 lists the observed continuum sources, along with their masses.

The table 4.2 lists the observed continuum sources, along with their masses.

Table 4.2: Parameters of the detected dust cores.

Object-name	R.A. (h m s)	Dec. (° ′ ″)	Peak flux (mJy beam^{-1})	Integrated flux (mJy)	V_{sys} km s^{-1}	Core mass ($M_\odot$)
MM1	06 08 53.33	21 38 28.9	71.7	71.1	5.0	8.2
MM2	06 08 53.49	21 38 30.5	22.5	41.3	2.0	4.8
MM3	06 08 54.13	21 38 34.4	5.6	9.4	3.0	1.1
MM4	06 08 52.86	21 38 29.5	3.2	3.8	4.5	0.5
MM5*	06 08 53.35	21 38 11.6	8.3	14.2	2.0	1.4
MM6*	06 08 53.42	21 38 13.7	1.9	3.6	4.0	0.4
MM7*	06 08 53.23	21 38 09.7	9.8	16.7	-	1.6
MM8*	06 08 52.97	21 38 11.1	5.8	6.0	4.0	0.6

On close scrutiny of Fig.4.10 it was found that due to their insufficient sensitivity, MM5-MM8 will not be explored in detail because they were so close to the primary beam's edge. By fitting a 2-D Gaussian in CASA, we were able to calculate the flux associated with the more localized emission in MM1. For the continuum imaging, a robust weighting of 0.5 was applied, corresponding to uniform weighting. This resulted to a synthesized beam of 1.11″× 0.64″(1950 AU× 11300 AU) at 1.76 kpc with a position angle (P.A) of 134°.

4.2.2 G188.95+0.89 Millimeter Line Emmission

The identified chemical species range from diatomic molecules to organic molecules with 6 atoms. There were many molecular lines seen in the direction of the 8

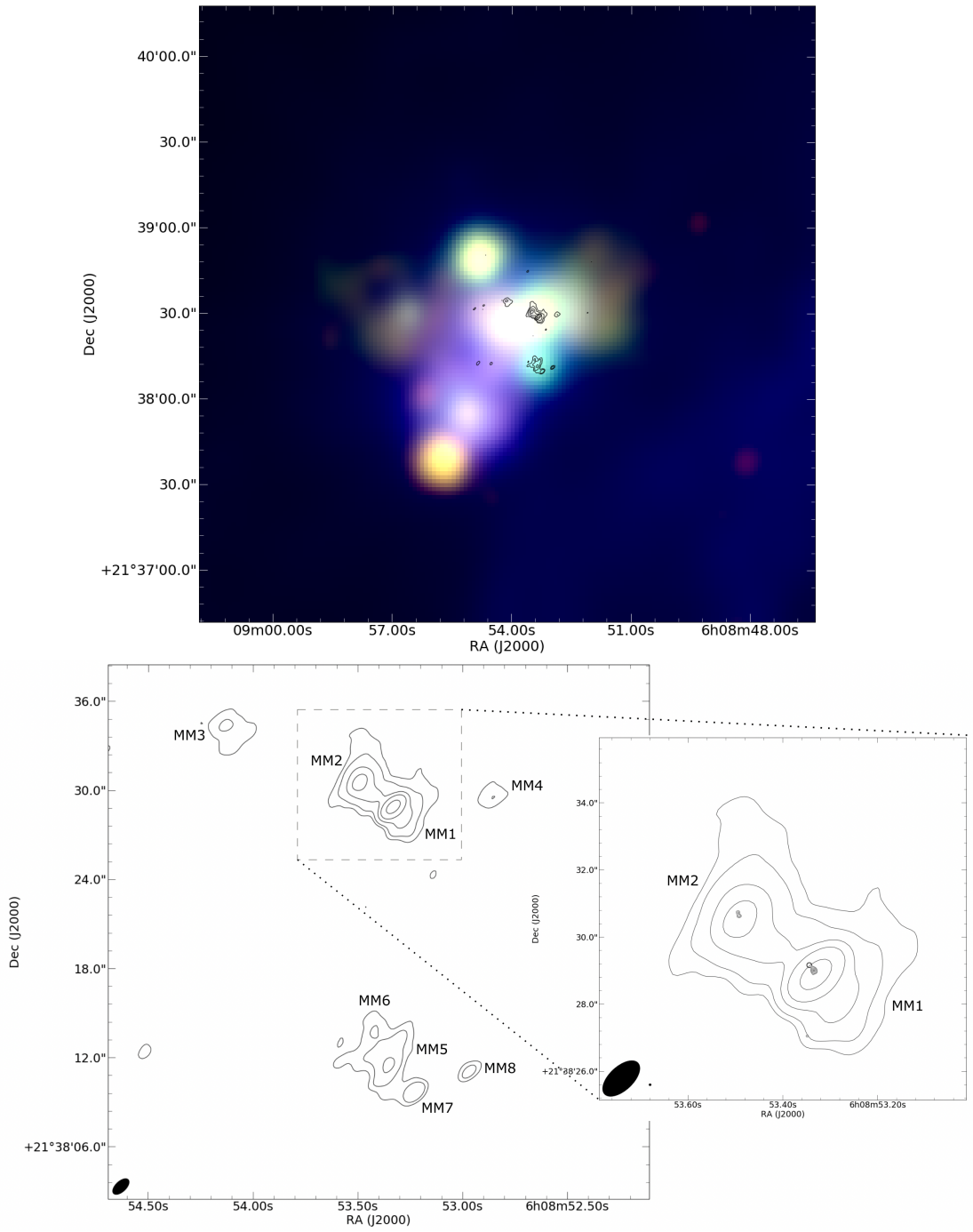

Figure 4.10: (top) G188.95+0.89 in a Three-Color WISE Composite Image. WISE band 1 (3.4 μm), 2, (4.6 μm) and 3 (12 μm) are shown in red, green, and blue, respectively. (bottom) G188.95+0.89 is the pseudo-color of the dust continuum emission seen in ALMA band 6 and band 7 (black contour, levels = [0.002, 0.004, 0.02, 0.06, 0.08] Jy beam^{-1}). Credit: (Mutie et al. 2021).

mm continuum objects. The identified emission lines includes 10 molecular transitions from 8 species including Carbon monoxide (CO) isotopologues ^{12}CO and C^{18}O, silicon dioxide (SiO), Methanol (CH_3OH), formaldehyde (H_2CO), glycolaldehyde (CH_2OHCHO), ethynyl (CCD), cyanogen (13CN) and acetaldehyde (CH_3CHO). Much focus only will be on the CH_3OH ($4_{(2)}-3_{(1)}$), SiO ($J = 2-1$), ^{12}CO ($J = 2-1$) and C^{18}O ($J = 2-1$) emissin lines that are more pronounced The spectra the other molecular lines are shown in appendix A.2.6. In addition to providing information on chemistry, molecular line analysis also reveals physical processes occurring in molecular clouds (Rivilla et al. 2019). The ascertainment of the evolutionary status of our target can be scrutinized through the identification, or lack thereof, of certain species among the molecular lines.

Towards HMSFRs the identified complex organic molecules (COMs) lines CH_3OH, CH_3CHO, and CH_2OHCHO are frequently seen. Although, Herbst & Van Dishoeck (2009) suggests that the actual sublimation temperature may vary somewhat across molecules, it is generally accepted that COMs form efficiently on grain surfaces at temperatures (T) greater than a few times 10 K, and that they sublimate to the gas phase at T $\gtrsim$ 100 K (Sakai et al. 2018). Common organic molecules (COMs) are crucial to periodic chemistry and may be inextricably tied to the beginning of life.

Previous molecular spectral line observation by Minier et al. (2005) towards G188.95+0.89 with a single pointing detected CH_3CN (92 GHz) and C^{18}O (109 GHz) lines. To identify different molecular species in the source, the CASSIS and Cologne Database for Molecular Spectroscopy CDMS, (Müller et al. 2005) spectroscopic databases were used (Chahine et al. 2022).

The splatalogue spectral line database's frequencies and line strengths are used to identify lines. If several candidates are present for identification of a particular spectral line or the exact source velocity is unknown, secondary criteria such as the Einstein A coefficient or the upper energy level must be taken into account. Higher Einstein spontaneous emission coefficients were analysed to determine which of the

analysed molecular lines is the most likely molecule (Guzmán et al. 2018). Lines with comparable lower energy and upper energy levels were revised so as to get the most likely molecule present. Integrated intensity maps of some of the detected lines were produced as illustrated below.

CH_3OH ($4_{(2)}-3_{(1)}$)

Fig. 4.11 shows the emission from the CH_3OH ($4_{(2)}-3_{(1)}$) line that was spotted going in the direction of each of the 8 cores. Southerly cores MM5-MM8 saw the most emission, whereas the MM4 core saw the least. The type of emission directed at MM5–MM8 cores was contaminated by the diminished sensitivity near the main beam's edge (Mutie et al. 2021). CH_3OH which is a Complex Organic Molecule (COM) frequently observed toward HMSFRs (Kleiner 2019). COMs are essential to periodic chemistry and may have a direct bearing on how life first developed (Caselli & Ceccarelli 2012). The presence of COMs in the source suggests an enhancement of shock waves as a result outflow passage.

The existence at the MM2 systemic velocity, of a second emission peak is an intriguing characteristic of the CH_3OH ($4_{(2)}-3_{(1)}$) emission towards MM2 (Mutie et al. 2021). With MM1, there is a CH_3OH ($4_{(2)}-3_{(1)}$) emission connected to it. According to Minier et al. (2005), the dust in the clump containing the 1.3 mm ALMA MM1–MM4 sources is approximately 150 K. Fig. 4.12 shows a Gaussian fit of the CH_3OH 4(2,2)-3(1,2) line. There is a little emission seen in the spectra from region outside the Gaussian. A blueshifted and a redshifted outflow emission of the CH_3OH are centered around MM1 and MM2. The outflow are centered around the dust continuum at the peak of the cores. More research was done on the methanol data in search of rotation in order to better comprehend the multi-outflow system seen in the ^{12}CO velocity channel map. There is no rotation in the structure traced by the CH_3 OH 4(2,2)-3(1,2) emissions because it has the same Gaussian fit and did not produce moment 1 maps.

SiO ($J = 2 - 1$)

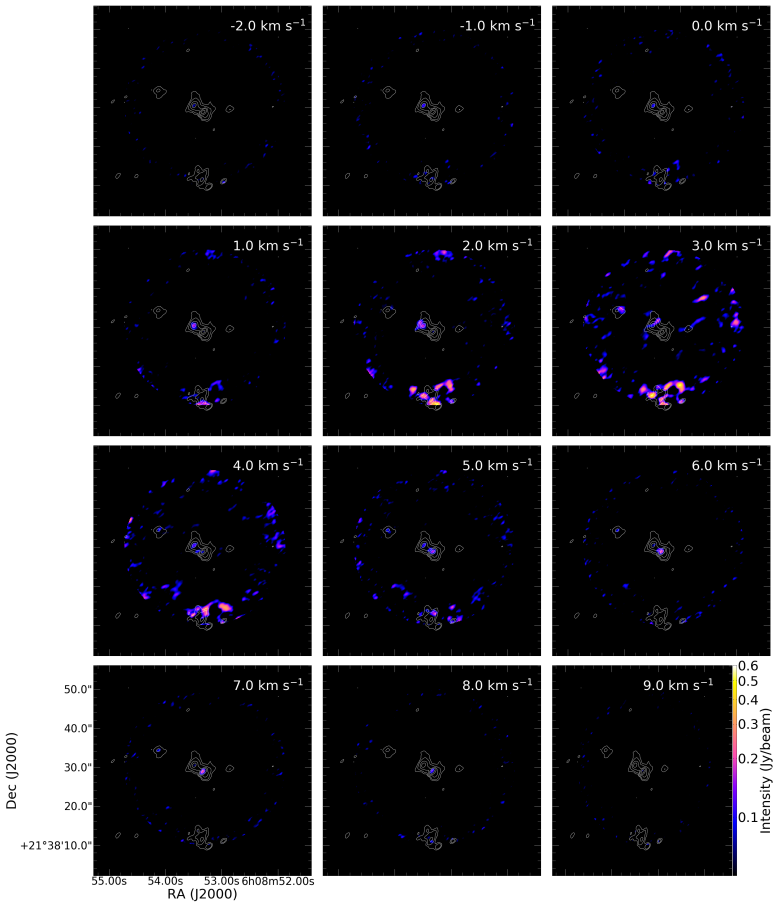

Figure 4.11: Dust continuum overlaid on a CH_3OH 4(2,2)-3(1,2) thermal line channel map (The black contour, levels = [0.002, 0.004, 0.02, 0.06, 0.08] Jy beam^{-1}). Beam intensity is represented by the color scale. Credit: (Mutie et al. 2021).

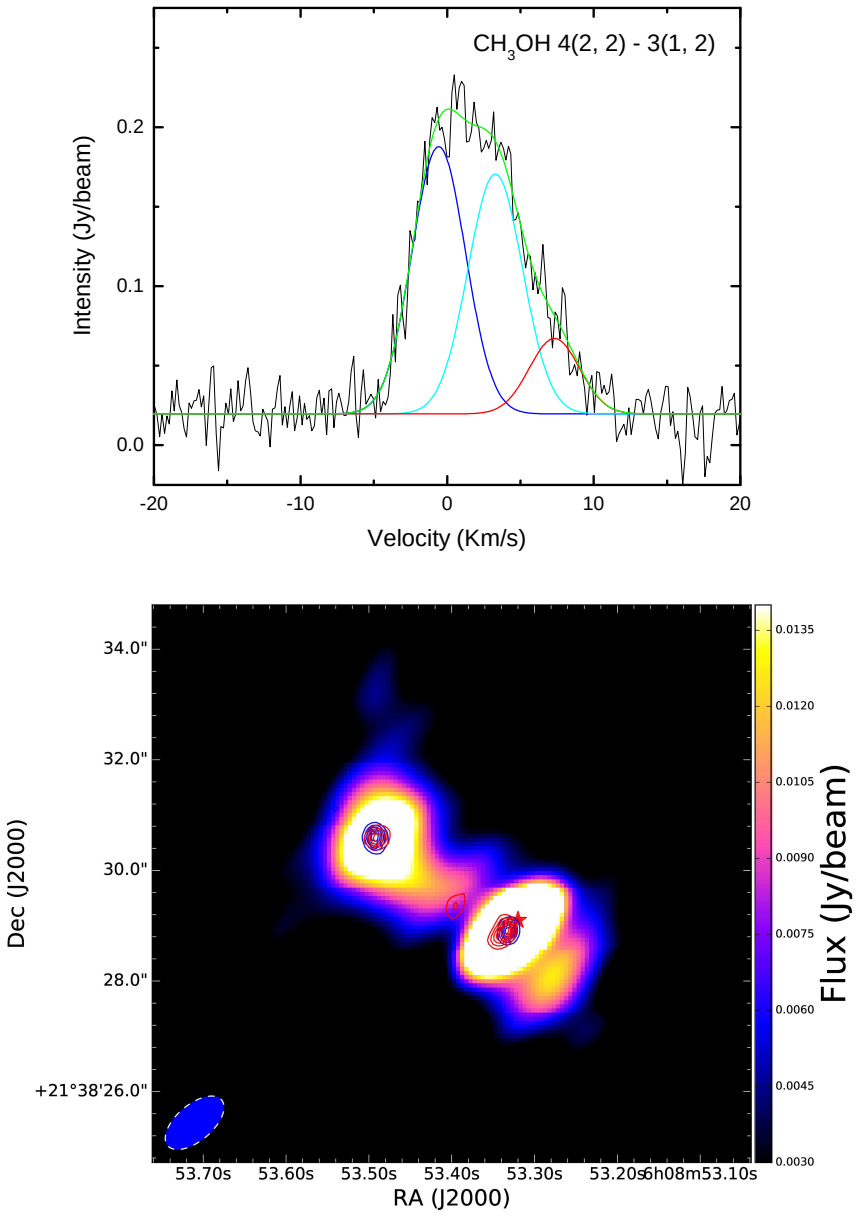

Figure 4.12: (top) Spectrum of CH_3OH 4(2,2)-3(1,2) shown in black. The red, blue and cyan are Gaussian fits and the green lines are the sum of the Gaussian fits. Little emission can be seen in the spectra from region outside the Gaussian. There is no rotation in the structure traced by the CH_3OH 4(2,2)-3(1,2) emissions because it has same Gaussian fit. (bottom) Integrated intensity (from -7 to 15 km s $^{-1}$) of CH_3OH 4(2,2)-3(1,2) shown by the contours. The blueshifted emission is integrated in the [-7 km s $^{-1}$ = 4 km s $^{-1}$] interval; the contours are (0.37, 0.73, 1.08, 1.44) x σ Jy beam^{-1}. The redshifted emission is integrated in the [5 km s^{-1}- 15 km s $^{-1}$] interval; the contours are (0.92, 1.79, 2.65, 3.52) x σ Jy beam^{-1}. The star sign show the position of the periodic methanol masers. 1.3 mm continuum shown as color image. Filled ellipse at the bottom left corner of the panel indicates the beam size.

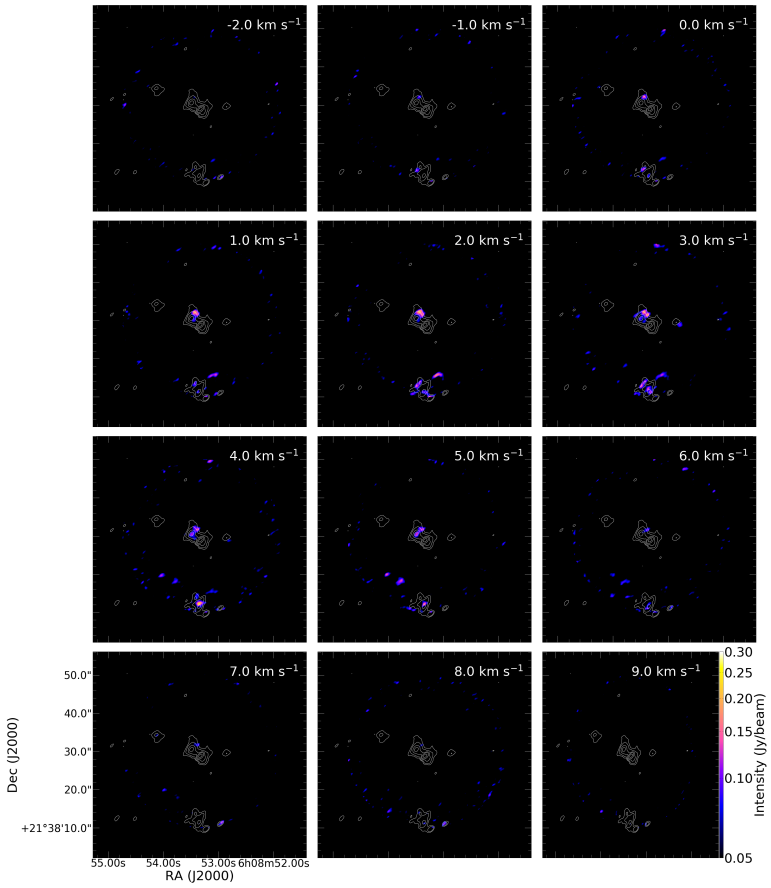

Figure 4.13: Dust continuum overlaid on a SiO ($J = 2 - 1$ thermal line channel map (The black contour, levels = [0.002, 0.004, 0.02, 0.06, 0.08] Jy beam^{-1}). Beam intensity is represented by the color scale. Credit: (Mutie et al. 2021).

.

According to Guzmán et al. (2018), the emission of SiO (J = 21) can be used to track shocks and outflows, especially in SFRs. The region of MM2's north-west where the major SiO emission was seen is shown in Fig. 4.13. In the channel map, the emission displays a bow-shock morphology that matches the systemic velocity of MM2. Each of the MM3 to MM8 objects has SiO emission (sometimes very feeble emission), However, SiO emission is not detected in the MM1 direction.

^{12}CO ($J = 2 - 1$)

The ^{12}CO ($J = 2 - 1$) emission in G188.95+0.89 is puzzling because of the highly self-absorbed characteristics in the line emission. It's also possible that all of the millimeter-scale objects are to blame for the convoluted distribution since they gen-

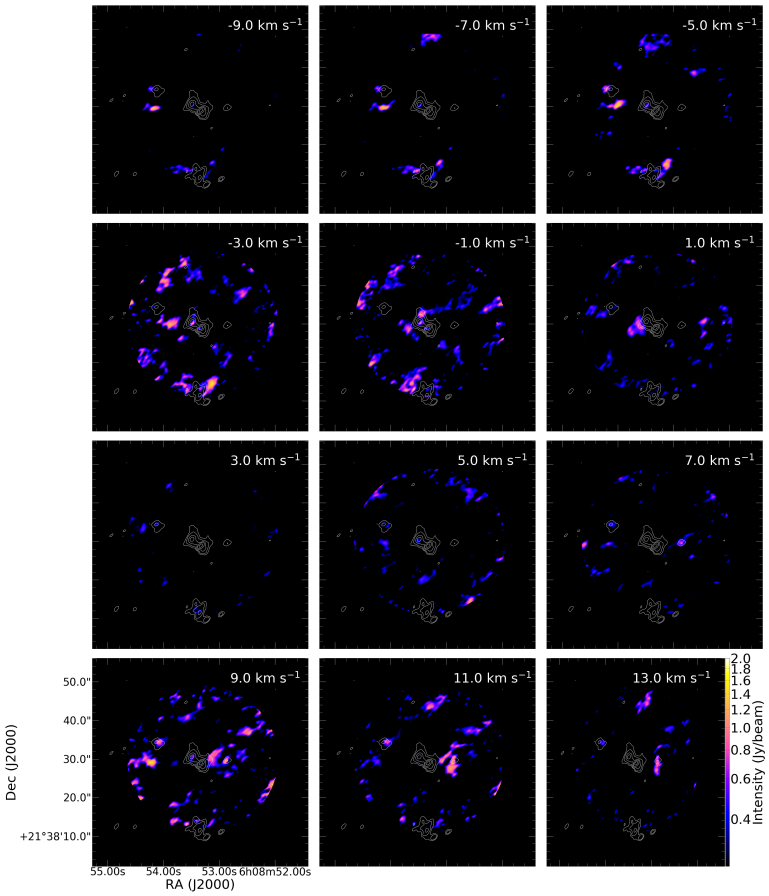

Figure 4.14: Dust continuum overlaid on a ^{12}CO ($J = 2 - 1$) thermal line channel map (The black contour, levels = [0.002, 0.004, 0.02, 0.06, 0.08] Jy beam^{-1}). Beam intensity is represented by the color scale. Credit: (Mutie et al. 2021).

erate outflows (Mutie et al. 2021). Fig. 4.14 shows that there may be an east-west bipolar outflow in MM2 coupled to the high emission in the -3 km s^{-1} channel to the east and the 9 km s^{-1} channel to the west. There are likely many young stellar objects (YSOs) in MM2, as well as emission to the north of the object, which may indicate a second outflow from the object (Mutie et al. 2021). The ^{12}CO ($J = 2 - 1$) emission is connected to each of the other millimeter objects.

C^{18}O ($2 - 1$)

C^{18}O ($2 - 1$), a tracer of high density, was identified in the direction of every MM1–MM8 as shown in Fig. 4.15. The main sources of the C^{18}O ($2 - 1$) emission are MM1 and MM2. It's worth noting that the distribution of the C^{18}O ($J = 2 - 1$)

emission in the brightest $C^{18}O$ (channel at 3 km s^{-1}), and can be located where the MM1 and MM2 cores meet. Table 4.3, provides information on the molecular line emissions that were found. The number of observed lines is heavily dominated by O-containing compounds, such as CH_3OH. Standard deviations of around 1.2 $km\,s^{-1}$ and 0.1 $km\,s^{-1}$ are observed for the source velocity of 9.4 km $s^{-1}$and the line width of 0.46 km s^{-1}, respectively.

The abundances of the organic molecules ^{12}CO, H_2CO and CH_3 OH are somewhat enhanced, whereas those of SiO and $C^{18}0$ molecules are slightly lower as shown in Fig. 4.16. The spectral lines point to a chemically active core with various molecules at various energies. The identified chemical species range from di- and triatomic molecules, to organic molecules with 8 atoms.

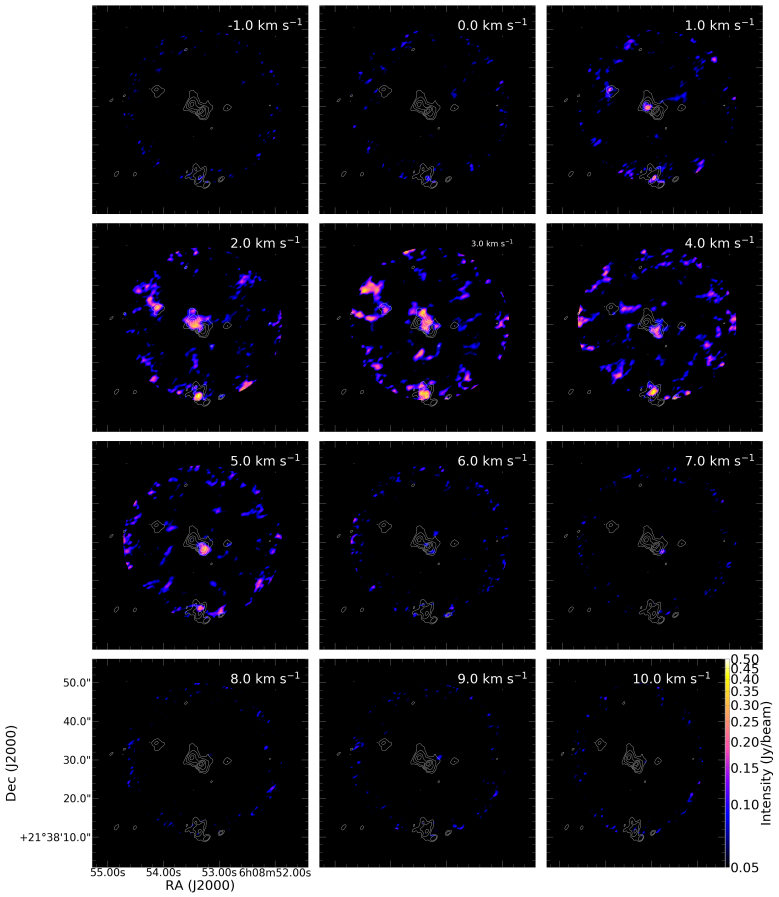

Figure 4.15: $C^{18}O$ ($J = 2 - 1$) channel map with G188.95+0.89 dust continuum emission overlaid (black contour, levels = [0.002, 0.004, 0.02, 0.06, 0.08] Jy $beam^{-1}$). The color scale is the intensity in Jy $beam^{-1}$ (Mutie et al. 2021).

Table 4.3: Note: The columns represent species, transition, rest frequency, energy at lower and upper levels, respectively. Source:Mutie et al. (2021)

Observed molecular species				
Molecule	Transition	Rest frequency (GHz)	E_{Lower} (K)	E_{Upper} (K)
CCD	N=3-2	216.564	14.65	20.78
^{13}CN	N=2-1	216.714	9.64	15.64
CH_3CHO	11(1,10)-10(1,9)	216.58	41.54	64.87
SiO	2-1	217.104980	20.842	31.264
H_2CO	3(2,1)-2(2,0)	218.764756	42.73	68.11
$C^{18}O$	2-1	219.5603541	5.273	15.812
CH_3OH	$4_{(2,2)}$-$3_{(1,2)}$	218.4400630	34.503	45.463
^{12}CO	2-1	230.5380000	5.534	16.604
CH_3CHO	12(3,9)-11(3,8)	231.97	63.64	92.63
CH_2OHCHO	4(4,1)-3(1,2)	231.99	8.54	15.27

Table 4.4: List of detected species in G188.95+0.89

2 atoms	3 atoms	4 atoms	6 atoms	7 atoms	8 atoms
$C^{18}O$	CCN	H_2CO	CH_3OH	CH_3CHO	CH_2OHCHO
SiO					
^{12}CO					
^{13}CN					

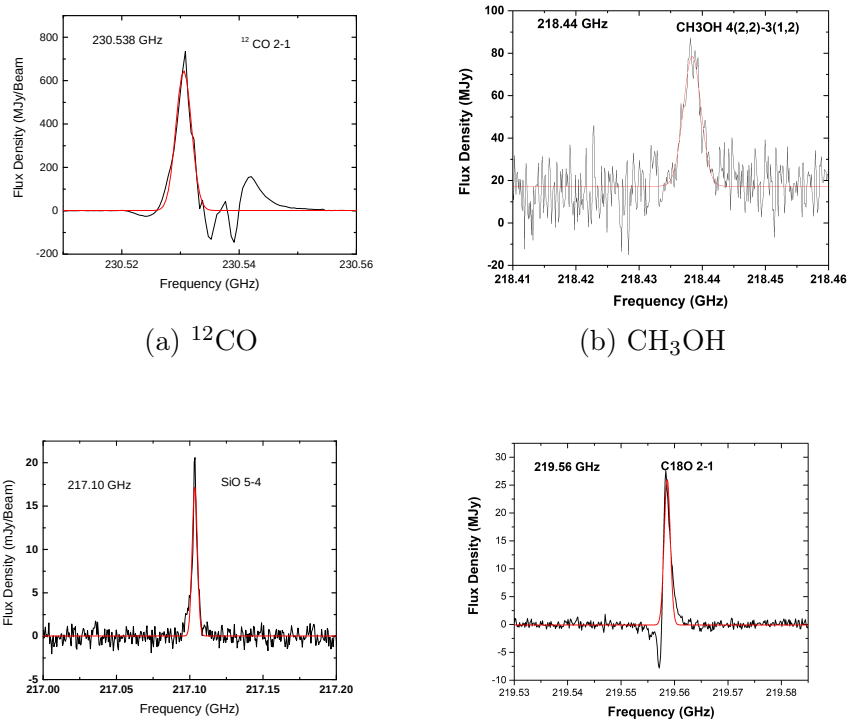

(a) ^{12}CO (b) CH_3OH

(c) SiO (d) $C^{18}O$

Figure 4.16: The spectra of the identified molecular lines are marked. The best-fit model's synthetic spectrum is shown in red, while the observed transitions are shown in black.

4.2.3 Main Morphological Features of G188.95+0.89

We analyzed the zero moment maps of each species' most important transitions to examine the morphology of the emission from the various species that was detected towards G188.95+0.89. The moment masking approach detailed in Dame (2011) and the CASA task moments were used to create the zero moment maps. ^{12}CO (2-1) and CH_3OH & $4_{(2,2)}$-$3_{(1,2)}$ zero moment maps are shown in Fig. 4.17. Both maps shows an elongated spatial emission coincident with the dust continuum. Emission directed towards the east-west direction. Other detected zero moment maps are shown in appendix A.2.5 in Fig. A.5.

4.2.4 Molecular Outflows

Good tracers of outflow include CO and SiO. One of the clearest indicators of protostellar emission is molecular outflows hence need to search for their presence in our

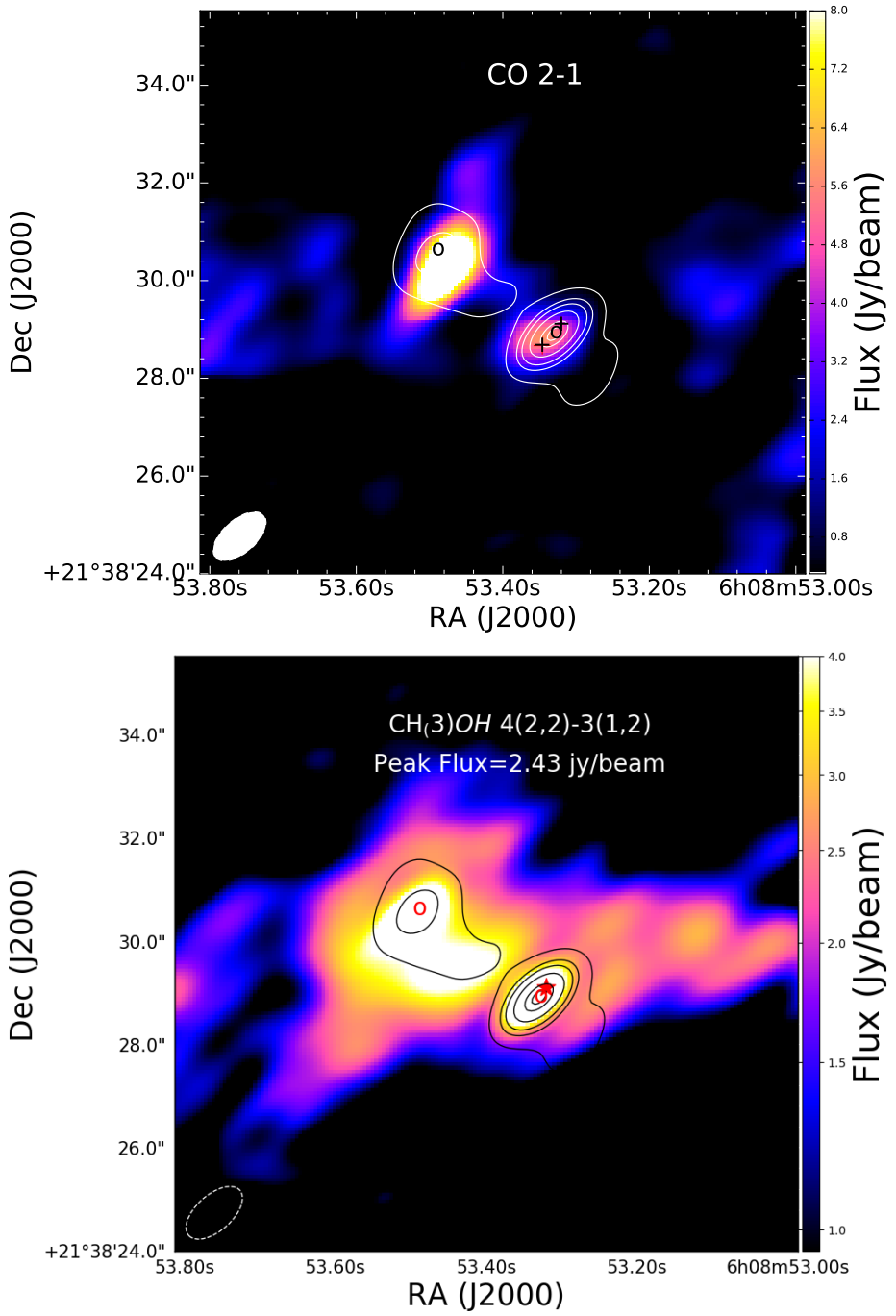

Figure 4.17: (top) Zero moment maps of detected molecular lines with emission at high velocities. Integrated map of ^{12}CO at 230.54 GHz from 2.5 km s^{-1} to 15.5 km s^{-1}. The contours represent the dust continuum of which the contour levels are the same as in Fig. 4.10. (bottom) Integrated map of CH_3OH 4(2,2)-3(1,2) at 218.44 GHz from 2.5 km s^{-2} to 9.0 km s^{-1}. The name of the molecular lines is shown at the top of the images. The plus and circles show the position of the methanol maser and the peak positions of the 1.3 mm dust-continuum respectively. Filled ellipse at the bottom left corner of the panel indicate the beam size.

source (Pillai et al. 2019). To identify molecular outflows in G188.95+0.89, the ^{12}CO (2-1) and SiO (5-4) channel maps emission were examined in various velocity bins across the region according to the depictions in Fig. 4.14 and Fig. 4.13. Both channels maps show the spatial configuration of the highly concentrated molecular gas. The ^{12}CO 2-1 channel map exhibits emission, tracing a bipolar molecular outflow in MM2, with an east-west velocity range of $\Delta v = 12$ km s^{-1}. Most of the SiO is being produced in the region to the north-west of MM2.

Fig. 4.18 (a) and (b) gives the average spectra of CO (2-1) and SiO (5-4) in region around the M1 and M2 dust cores. Three Gaussian lines clearly demarcate the outflow emission resulting from the ambient gas emission in both the CO (2-1) and SiO (5-4). The spectra of the region outside the Gaussian may be seen to include an excessive amount of blue-shifted and red-shifted emission and LSR velocity ranges from 2.5 to 20 Km s^{-1} with peak velocity at 10.7 Km s^{-1} for CO. Both blue and redshifted outflows are seen in MM1 and MM2 as shown in Fig. 4.18 (c) but the redshifted emissions are more pronounced in MM2.

The CO outflow's red and blue lobes closely overlap one another, and the redshifted emissions shows a double outflow. Both CO and SiO outflows dominate in MM2 while SiO outflow show blueshifted emissions in the MM1 core. The ^{12}CO emission shows lobes in NW-SE orientation displaying multiple outflows. Observations of the outflow map show that the source of the emission is located around the dust core. Self-absorption or foreground clouds along the line of sight causes the absorption features in CO spectra. The SiO emission shows bipolar outflow centered around MM2 core.

SiO molecule does not suffer from confusion with easily excited ambient material, like the more commonly used outflow tracer CO, hence it is particularly useful in observing outflows. As long as outflow is taking place, accretion will also be taking place, and the more ferocious the outflow, the higher the accretion rate. The presence of outflows in our source is a confirmation that accretion is taking place. SiO is

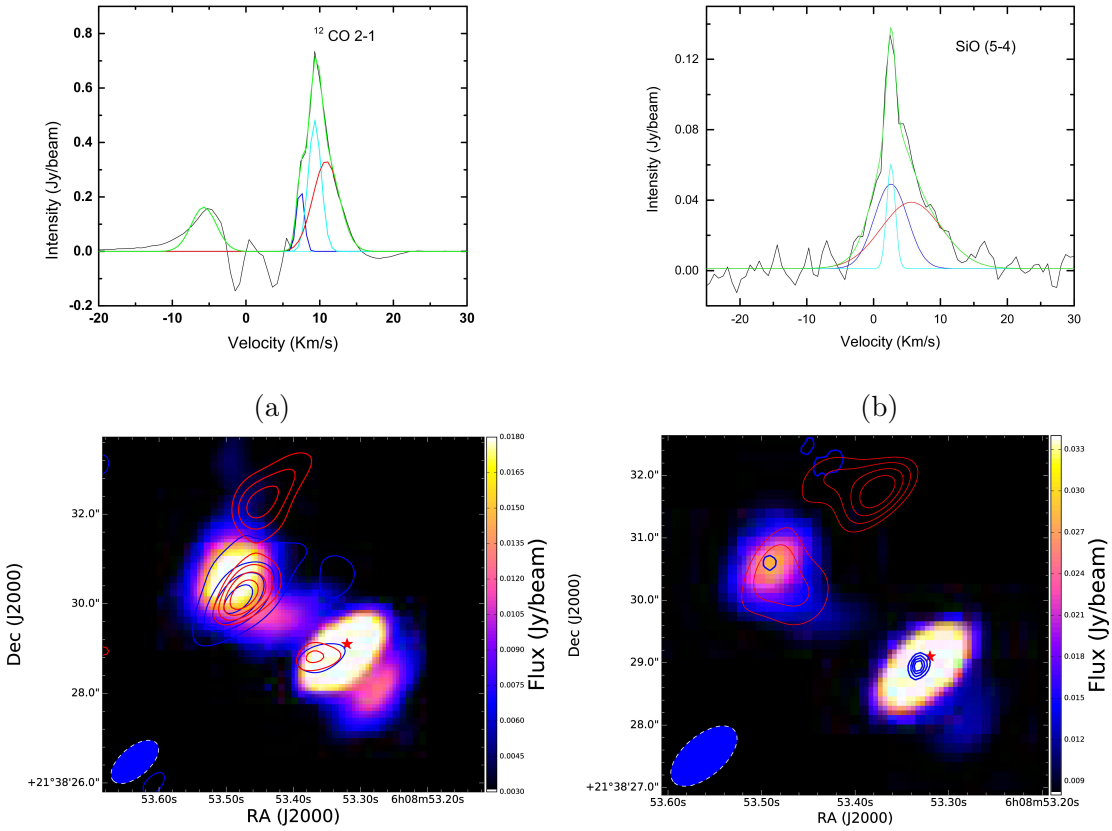

Figure 4.18: Upper panels (a) and (b): Spectra of ^{12}CO (2-1) and SiO (5-4) shown in black. Gaussian fits are shown in red, blue, and cyan. The sum of all the Gaussian fits appears as the green lines. Lower panels (c) and (d): Outflow traced by the ^{12}CO 2-1 and SiO (5-4) emission respectively. The CO blueshifted emission is integrated in the [-10 km s^1, 10 km s^{-1}] interval; the contours are (2.05, 2.54, 3.04, 3.53) $\times$ σ Jy beam^{-1}. The redshifted emission is integrated in the [11 km s^{-1}, 20 km s^{-1}] interval; the contours are (2.28, 2.72, 3.15, 3.59) $\times$ σ Jy beam^{-1}. SiO outflow blueshifted emission is integrated in the [-8.2 km s^1, 1.2 km s^{-1}] interval; the contours are (0.59, 1.10, 1.62, 2.13) $\times$ σ Jy beam^{-1}. The redshifted emission is integrated in the 1.5 km s^{-1} -10.5 km s^{-1}] interval; the contours are (2.58, 2.94 3.31, 3.67) $\times$ σ Jy beam^{-1}. The star symbol show the position of the methanol maser. The size of the beam is shown as a filled ellipse in the lower left corner of the display.

an unambiguous tracer of strong shocks and outflow (Daffern-Powell 2021). The shocks can modify the chemistry of the local ISM, by destroying dust grains and injecting silicon and SiO into the gas phase, therefore resulting in an abundance of SiO enhanced by orders of magnitude. The detection of SiO in our source is important as it represents an independent tool to test the presence of shocks and their relevance in the source(Daffern-Powell 2021).

Our final maps are shown in Fig. 4.18, and they allow us to calculate the system's total outflow mass, momentum, and energy. We assume that ^{12}CO is optically thin and disregard the (unknown) inclination angle of the outflow and spatial filtering of extended emission in our calculations. We also adopt an excitation temperature of 42 K that was used to calculate continuum mass.

All of these factors add up to a mass increase of the outflow of at least an order of magnitude when properly constrained and accounted for in the mass estimate (Dunham et al. 2014). The outflow parameters are shown in Table 4.5. According

Table 4.5: Note. Columns are lobes, mass(M), momentum(P), kinetic energy(E), P/M ratio.

Outflow parameters					
Lobes	$\int S_v dV$ (Jy km s^{-1})	M ($M_\odot$)	P ($M_\odot$ km s^{-1})	E $M_\odot$ (km s^{-1})^2	V_{char} (km s^{-1})
SiO Outflows					
Red	11.5	1910	6494	11039.8	3.4
Blue	2.8	437	393.3	176.9	0.9
CO outflows					
Red	8.9	1424	15521.6	84592.7	10.9
Blue	5.1	792	4910.4	15222.2	6.2

to Minier et al. (2001) the lines of masers in AFGL 5180 are roughly perpendicular to the outflows. The interactions between the masers and the larger scale structures, such as outflows, are linear in nature (Minier et al. 2001). Both the ^{12}CO (2-1) and SiO (5-4) emissions identify two high-velocity bipolar outflows heading towards the mm brightest centers, that are likely to be the youngest sources in this region. The outflow in G188.95+0.89-MM2 does not show a clear bipolar structure.

The ^{12}CO emission in G188.95+0.89 MM2 seems to be complicated, but channels

8.3 km s^{-1} and 10.7 km s^{-1}, of the ^{12}CO in Fig. 4.14, mark bipolar symmetry that crosses the peak of G188.95+0.89-MM2. Figure 4.18 shows that the red- and blue-shifted components of the ^{12}CO bipolar outflows are practically in the plane of the sky. This periodic maser source joins G9.62+0.19E and G22.357+0.066 that have similar bipolar outflow orientation (Tarchi et al. 2018).

Bipolar outflows are a strong indicator of disks being present (Reipurth et al. 2007). The out-flowing material creates shocks when it comes into contact with the still gas that makes up the envelope and the molecular cloud, which causes the grain mantles and refractory grains to (partially) sputter and evaporate. Once the molecules have entered the gas phase, their rotating lines can be studied to provide insight. The channel maps illustrate emission that extends in the directions of north-west and south-east, quite near to the position of the continuum peak.

After doing a study on the relationship between 6.7 GHz methanol masers and molecular outflows traced by ^{13}CO, De Villiers et al. (2015) came to the conclusion that the masers activate in hot core sources that already have outflows and deactivate during the UCHII phase of the reaction.

Molecular outflows play a significant role in the process of star formation for the following reasons: (i) it enables the infalling matter to shed its angular momentum and accrete onto the central object; and (ii) the ejected material interacts with its surroundings, profoundly altering it and, in some cases, completely obliterating the parental cloud. Both of these benefits are essential to the formation of stars (Arce et al. 2011, Shimajiri et al. 2008).

The ejected material creates shocks that are chemically rich places, exhibiting a chemical makeup that is extremely comparable to that of hot cores (Caselli & Ceccarelli 2012). In most times, high-mass stars are observed in binary or multiple systems. The source, AFGL-5180, has been shown to be a binary system by analyzing the structure of the continuum emission seen by ALMA. However, a better spatial resolution will be required to investigate the possibility of multiplicity in the source.

4.3 INFRARED RESULTS

4.3.1 Dust emission

A comprehensive and unbiased look at the Galactic plane's continuum emission was provided by the the Hi-GAL observations in 70, 160, 250, 350, and 500 μm bands. This wavelength range encompasses the peak of the spectral energy distribution (SED) emission of cold dust, which allows for the determination of crucial ISM parameters such as the hydrogen column density (N(H_2)) and the dust temperature (T_d) (Azatyan et al. 2022). A color-composite image of the molecular cloud can be seen in Fig. 4.19 (left panel). This image was created using data from three different Hi-GAL bands: (PACS 160 μm and SPIRE 350 and 500 μm). The right panel in Fig 4.19 shows the image of G188.95+0.89 Herschel 500 μm. The 060531.9+213706 and G188.935+00.804 HII zones are quite bright and noticeable. The plus (+) symbol shows the presence of 6.7 methanol masers at the center of the molecular cloud.

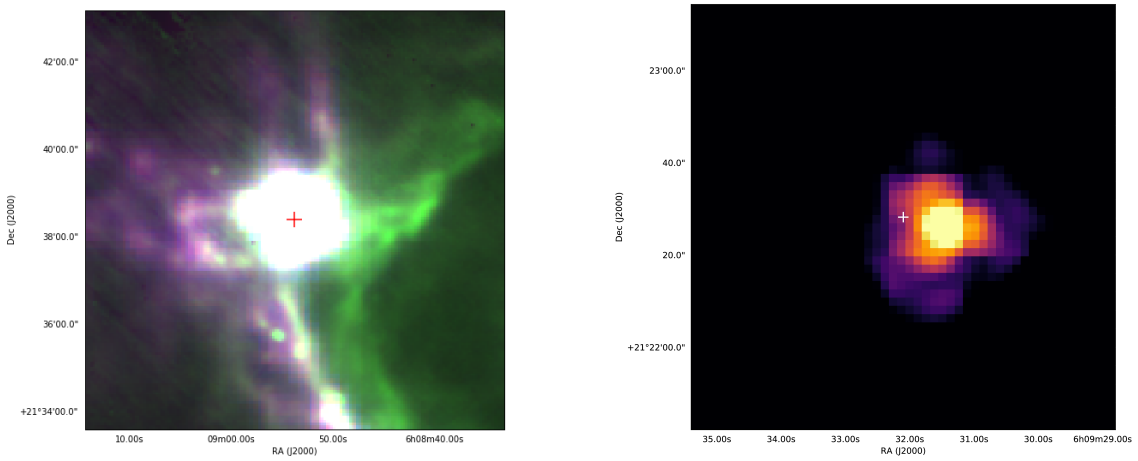

Figure 4.19: Composite 3-color images of the G188.95+0.89. Left panel: Herschel 160μm (blue), 350 μm (green), and 500 μm(red); right panel:zoomed image of G188.95+0.89 Herschel 500 μ m.

Fig. 4.20 shows a color-composite image of three WISE bands (3.4 μm, 4.6 μm and 12μm) represented by the colors blue, green and red covering the molecular cloud. A close view of Fig. 4.20 shows that in the MIR spectrum, HII regions are likewise quite luminous. This suggests that there is a large population of hot stars in the region around the UC HIIs, as shown by the comparatively high temperature of the

ISM in this region (Rivera-Ingraham et al. 2010).

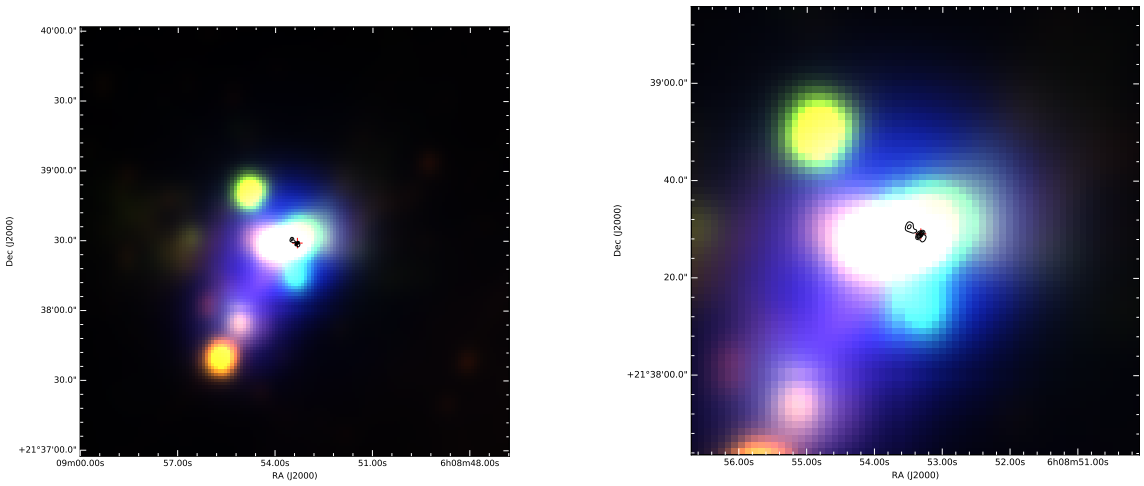

Figure 4.20: Composite 3-color WISE image of G188.95+0.89. WISE band (3.4 μm, 4.6 μm and 12 μm) are represented by colors red, green and blue. Right panel:zoomed image of G188.95+0.89 superimposed with continuum sources M1 and M2

4.3.2 Color–Color Diagrams

Star clusters are collections of stars that seem to be concentrated in little regions of the sky. Three basic characteristics are shared by all stars in a cluster since it can be assumed that they were all formed from a single primordial cloud of gas and dust at roughly the same time: (i) they are all the same distance from us; (ii) they are all the same age; and (iii) they are all the same chemical composition. Consequently, stellar clusters are perfect examples to examine the development of stars (Bacher & CHRISTENSEN 2001). A color-color (c-c) is what is used to describe a diagram where the horizontal variable is stated as the radiation difference observed from two distinct wavelengths, or the color index. The c-c diagram is a fundamental tool in both quantitative and qualitative studies of star evolution (Bacher & CHRISTENSEN 2001). The positioning of YSO candidates in color–color (c–c) diagrams allows for easy identification of these candidates. The colors that are used are determined by the data that is now at hand (Azatyan et al. 2022). As can be seen in Fig. 4.22, we produced a total of four c-c diagrams. The study into the star-forming region IRAS 05168+3634 has previously benefited from using the similar strategy, as stated

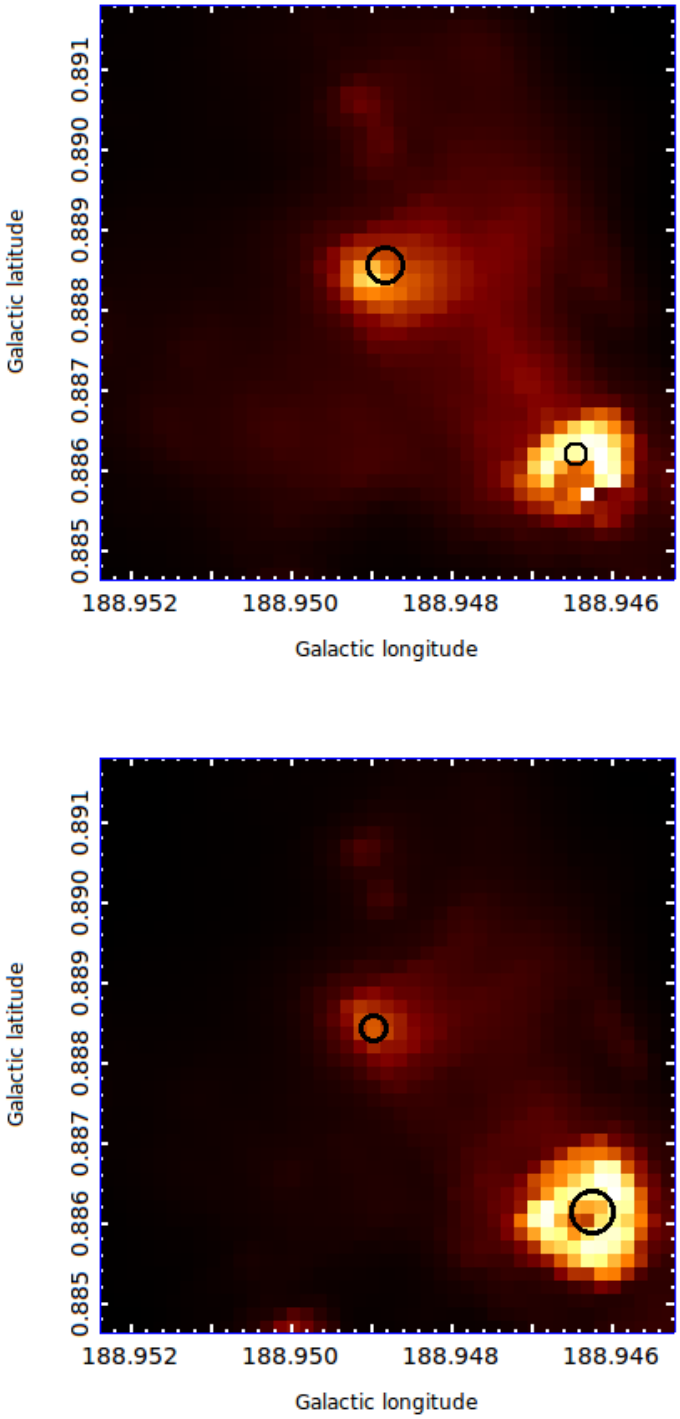

Figure 4.21: Spitzer/IRAC image of G188.95+0.89 (upper panel; 3.6 μm). Bottom panel: Spitzer/IRAC image of G188.95+0.89 at 4.5 μm. The location of the methanol masers in the SFR is shown by the circle.

by Azatyan (2019). The (J-H) versus (H-K) c-c diagram shown in Fig. 4.22 (top left panel) was initially used to detect objects with IR excess. The magnitude of the infrared excess offers a measurement of the amount of circumstellar material and, as

a result, an indication of the object's current stage of evolutionary development (e.g. Shu et al. 1987).

When choosing possible members of the cluster from stars pointing in the direction of the molecular cloud, it was believed that the majority of the residents of the examined active star-forming region are YSOs. (Azatyan et al. 2022). The existence of discs and envelopes around stars is responsible for the IR excess that is one of the most prominent observable features of YSOs (Lada & Lada 2003, Hartmann 2009). Class I and Class II YSOs can be distinguished from one another by the amount of IR excess they exhibit in either the near-infrared or the mid-infrared spectrum.

EGOs have mid-infrared colors that are located in the same regions of the color-color space that young protostars are in while still inside their infalling envelopes (Cyganowski et al. 2009). Extended 4.5 μm emission is a prominent and pervasive feature that may be seen in Spitzer photos of known HMSFRs, such as DR21 (Davis et al. 2007). With its extraordinary sensitivity at mid-infrared wavelengths, the Spitzer space telescope offers a novel way to detect dusty disks and envelopes near YSOs in SFRs. Using the infrared excess from circumstellar components to distinguish young stars from red background stars needs great sensitivity in the 3 - 24 μm bands (Allen et al. 2004, Gutermuth et al. 2008). Star and planet formation settings can be investigated and catalogued with the help of Spitzer's Infrared Array Camera IRAC and MIPS. Fig. 4.21 displays the color IRAC image of the source at 3.6 μm and 4.5μm. Two bright cores that were identified by ALMA band 6 as shown in Fig. 4.8 are clearly seen in the IRAC images.

4.3.3 Color-Magnitude Diagrams

The Color Magnitude diagram (CMd) is a valuable tool for determining the spectral types of stars and learning more about the stellar population in star-forming regions. All sources found in the JHKs bands and 56 fainter stars are plotted in the K versus H - K, CM diagram shown in Fig. 4.23. On the left side of Fig. 4.23 J versus J - H

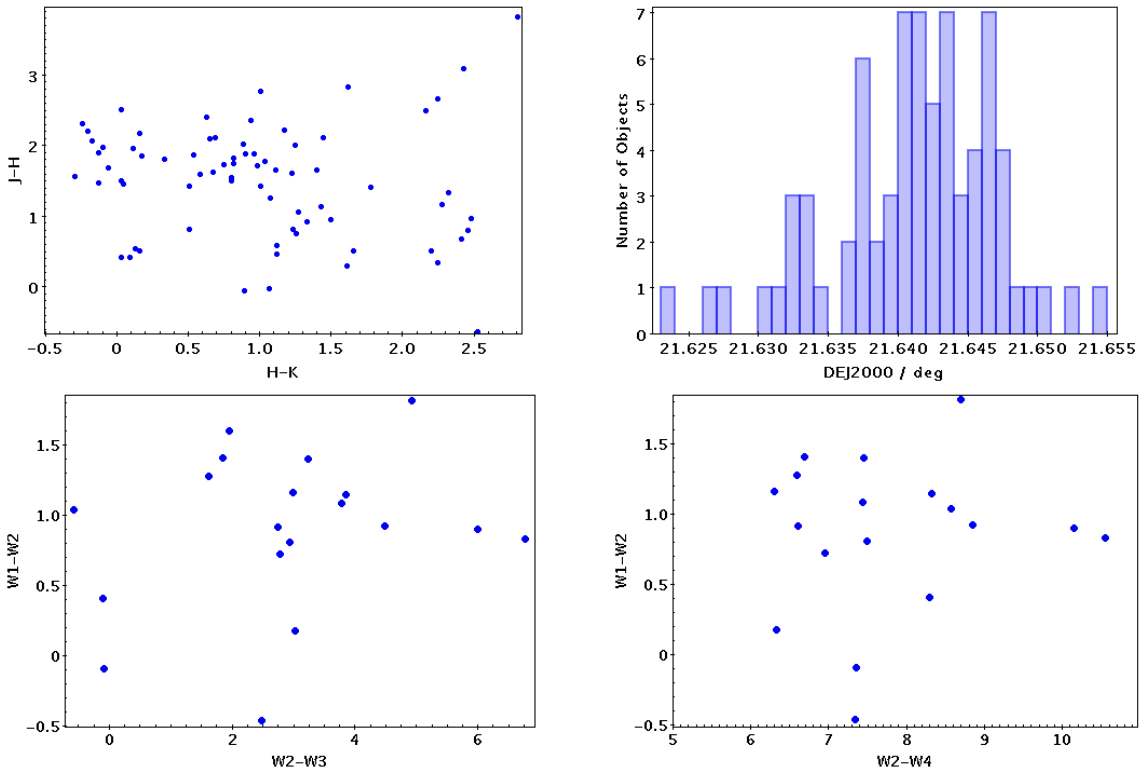

Figure 4.22: Color-color diagram showing (a) Top left panel: (J-H) vs. (H-K) diagram, (b) Top right panel: Histogram of sources within radius of 1$arcmin$, (c) Graphs comparing ranges [3.4]-[4.6] vs. [4.6]-[12] and [3.4]-[4.6] vs. [4.6]-[22] may be seen in the bottom left and right panels, respectively.

where 54 sources are plotted.

It is impossible for interstellar absorption to be the only factor contributing to the IR excess of the objects located to the right of the reddening vectors shown in Fig. 4.23. At least some of the IR excess of these objects is as a result of the existence of a circumstellar disc as well as an envelope (Azatyan et al. 2022). Among the items that are found in the reddening band of MS and giants, we have categorized as Class I evolutionary stage YSOs those that have a a $(J - K) > 3$ mag color index (Lada & Adams 1992). These elements can be found in the top right hand corner of the diagram.

4.3.4 Spatial Distribution of YSOs and Cool Red Sources

There are 9 extremely red sources found exclusively in the H and Ks bands in the NIR observations using the archival 2MASS data. These sources have colors redder

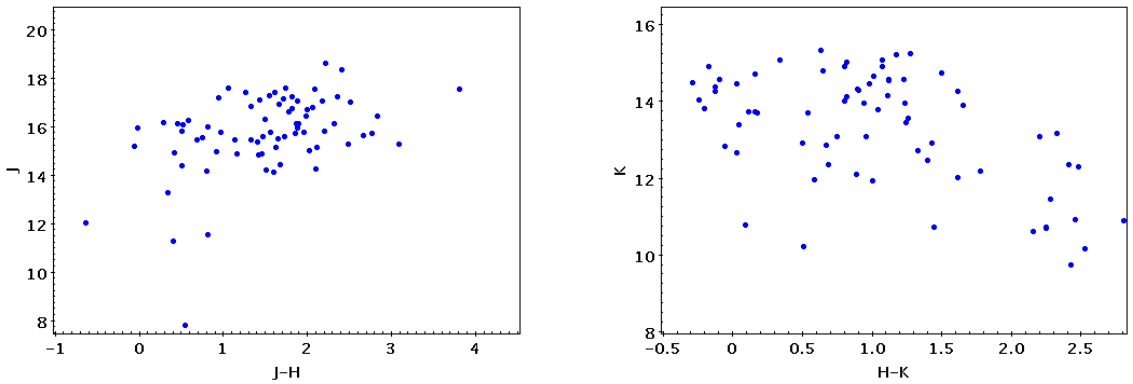

Figure 4.23: Left panel: CM diagram for the YSO candidates in AFGL 5180 showing J vs. (J-H). Right panel:CM diagram for the YSO candidates in AFGL 5180 showing K vs. (H-K). Red sources with $H - K > 2$ with J-band counterparts.

than $H - K > 2$ as shown in Fig. 4.24. The widespread distribution of very red sources in Fig. 4.24 shows that the vast majority are located to the west of the 6.7 GHz methanol maser region. It's intriguing to see how many highly red sources are within the boundary of the 6.7 GHz methanol maser and that of the IRAS source. The nine sources with the largest infrared excess were found to be part of the IR cluster after looking at the extinction corrected reddening values. According to the reddening values, the IR cluster is likely rather young, maybe sharing an age with the surrounding IRAS source (Urquhart et al. 2004).

4.3.5 Mid-infrared data

The region's overall structure on a galactic scale and the worldwide star creation occurring within the molecular cloud were investigated using the Wide field MSX images. It is possible to deduce the existence of a PDR based on the fact that the MSX band A image is predominately composed of Polycyclic Aromatic Hydrocarbons (PAH) (Urquhart et al. 2004). The MSX band E image shows that there are three hot embedded thermal sources can be found throughout the cloud. thermal sources embedded within the cloud. These sources are located at a distance from the bright rim in relation to the ionizing stars (Urquhart et al. 2004).

The bright source in the centre of Fig. 4.25 coincides with the location of AFGL 5180, suggesting that this object is being heated from the inside by the light of an embedded

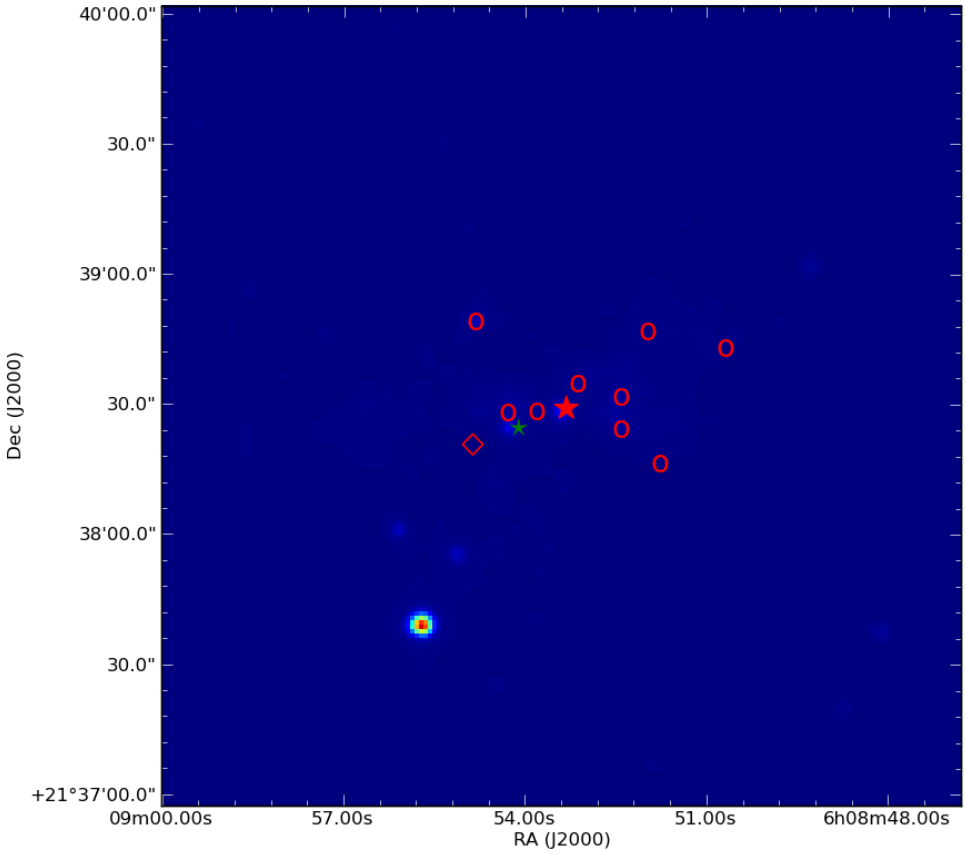

Figure 4.24: The spatial distribution of the candidates for YSOs with color excesses, superimposed over a logarithmic intensity scaled Ks-band image. Red and green stars indicate the position of 6.7 GHz methanol masers and the IRAS source. The diamond symbol indicate the position of the MSX source, and those sources are denoted by the red circles ($H - K > 2$).

main sequence star (Urquhart et al. 2004). The other bright sources located on the southwest are UC HII regions G189.0323+0.8092 and G189.0307+0.7821 respectively. These three images are colored green, red, and blue, respectively, as band A tracks emission from the local PDRs, thermal emission from hot dust is what band E focuses on, and band C tracks optically ionized gas. The intense red emission in the image's upper right corner plainly identifies the ionizing stars.

4.3.6 Counterparts at Other Wavelengths

Table 4.6 is a summary of the methanol maser counterparts in the IRAS, MSX, and NVSS catalogs. Indicators of star formation such as OH masers, H_2O masers, and NH_3 emission should be looked for within 1 arcsecond of the maser, and IRAS, MSX,

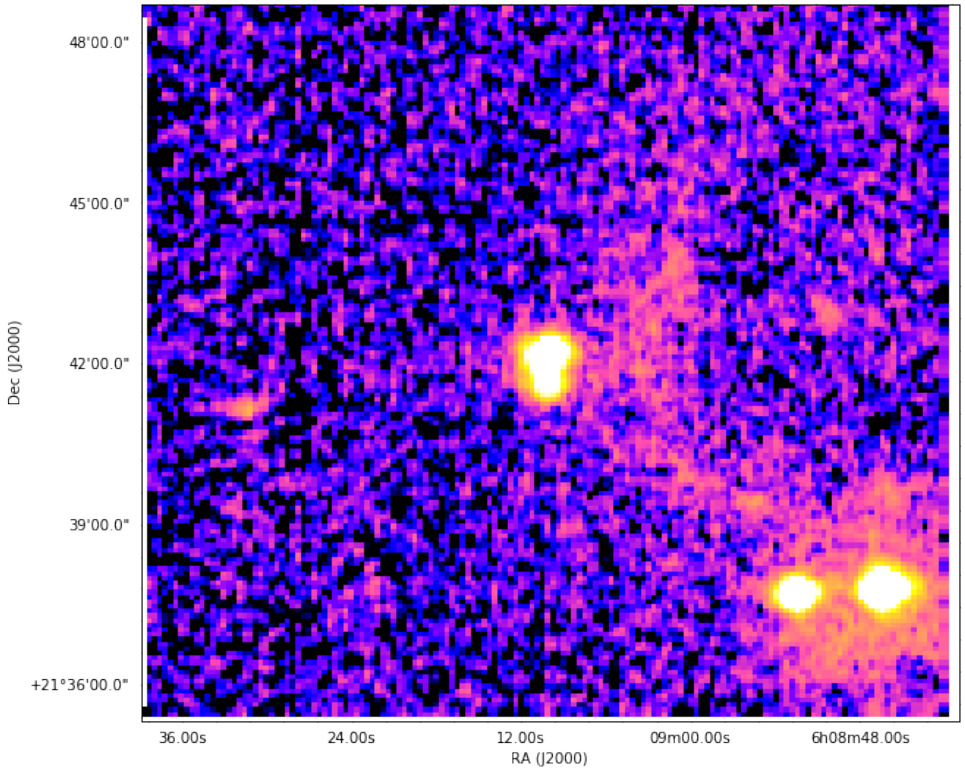

Figure 4.25: A composite image of band E (red), the MSX band A (blue) and the MSX band E (green). PDRs can be tracked using the band A image, thermal emission from warm dust can be tracked using the band E image, and optical ionized gas can be tracked using the DSS image.

and NVSS sources should also be considered, as they are likely to be associated with the emission. It is quite unlikely that sources more than 25 arcseconds from the methanol maser are connected to the maser emission.

In order to be consistent with the findings of earlier research on the topic conducted by Pestalozzi et al. (2005), a search radius of 1 arcmin was used. The goal was to relate any future discoveries of star formation tracers to the same complex as the YMSOs responsible for the emission of methanol maser. Table 4.7 shows the presence and absence of IRAS, MSX and NVSS counterparts from the source.

Astronomical sources thought to be producing 6.7 GHz methanol masers have been the subject of a multi-wavelength investigation during HMSF is necessary to comprehend the connection between the maser emission and its surroundings (Ellingsen 2006). In order to investigate the maser environment, we looked through catalogues that had previously been published in the scientific literature, in order to find coun-

terparts to the masers. New observations were carried out at wavelengths for which there was no previously collected data. At the moment, the catalogs that are of particular interest include 2MASS, GLIMPSE, MSX, IRAS, and NVSS.

Due to the excellent sensitivity of the 2MASS and GLIMPSE surveys and the abundance of stars in the near infrared, a substantial number of point sources from these catalogs (≥ 40 sources) will reside within the confines of any methanol maser. Therefore, unless the methanol maser placements are adjusted to subarcsecond accuracy, we will not include these two catalogs in our study.

Table 4.6: Potential matches between the methanol maser sample and sources listed in the IRAS, MSX, and NVSS catalogs. The IRAS, MSX, and NVSS sources within 25 ″ of the methanol maser are listed in the columns following the maser.

Methanol Maser	IRAS source	sep (″)	MSX source	sep(″)	NVSS source	sep(″)
G188.95+0.89	06058+2138	0.54	G188.9478+0.881	0.072	-	-

Table 4.7: Shows for each methanol maser the presence or absence of counterparts at 23 ″ and 60 ″ as well as other tracers. Letter y means present and n absence.

Methanol Maser	IRAS source? 23″, 60 ″	MSX source? 23″, 60 ″	NVSS source? 23″, 60 ″	H_2O maser?	OH maser?	other meth maser?	other SF tracers?
G188.95+0.89	y,y	y,y	n,n	n	y	y	y

Using a fiducial distance of $\sim$ 3 kpc to a major star-forming area, we find that a separation of 5″ in angular distance corresponds to a physical distance of 15,000 AU. Since the maser pump requires the warmed dust produced by the central star, a search radius of 5″ may be used as a rather safe upper bound on the likelihood of connection. When the error circle is taken into account, the 95% confidence interval for the location of a methanol maser is 18 $\sim$ 18 ″. Therefore, 25 ″ was chosen as the corresponding search radius.

4.3.7 Methanol Masers and Star Formation Tracers

Table 4.8 lists the distances to adjacent objects in the fields of the G188.95+0.89 region, including methanol masers. We can learn more about the surroundings of the

methanol masers by examining the locations of hydroxyl masers, HII regions, and water masers (Goedhart et al. 2002). If a H II region is present, then a high-mass ionizing star must be nearby. Even if the H II region is not observable, the existence of hydroxyl masers in the region's periphery is a positive indication of the existence of a high-mass star (Garay & Lizano 1999).

Shocks linked with fast outflows often contain water masers. Although water masers have been connected to both high- and low-mass star formation, conclusive proof of the connection requires measuring the outflows themselves, and can be located at considerable distances from the star causing the outflow (Garay & Lizano 1999).

Surveys in the mid-infrared 'have established that shocks, outflows, infall, and circumstellar disks are all traceable by maser emission from massive stars (Goedhart et al. 2002). There is no one activity or phenomenon that can be attributed to a certain maser species (De Buizer et al. 2005). Every methanol maser site has its surrounding environment meticulously analyzed. The goal of this detailed inspection was to calculate the exact distances to the methanol masers and other objects in the region (Goedhart et al. 2002).

Table 4.8: Locations of methanol masers in relation to nearby features. In the first column, you'll see the methanol maser's identification. In columns 5 we find the angular distance and its uncertainty between the field objects and the methanol maser.

Methanol Maser	Obiect Name	R.A. (h m s)	Dec. (° ′ ″)	A. sep ″
G188.95+0.89	Methanol maser	06 08 54.2	+21 38 25	0.66
	hydroxyl maser	06 08 54.14	+21 38 24.64	3.24
	HII region	06 08 53.81	+21 38 25.0	4.2
	water masers	06 08 53.4	+21 38 37	1.4

4.3.8 Infrared Sources Coincident with Methanol Masers

Table 4.10 provides a compiled summary of the findings obtained by doing the search over a wider area. It is more likely that methanol masers will be discovered in close proximity to radio sources that have a spectral index that is characteristic of an

Table 4.9: This table lists the presence and absence of infrared sources coincicent with masers IRAS, MSX .

Catalogue	Source	Separation (″)
IRAS	06058+2138	0.54
MSX	G188.9479+00.8871	3.84
2MASS	06085426+2138245	2.34

outflow (Zapata et al. 2006, Fish 2007).

4.3.9 Results from the Point Source Catalogues

G188.95+0.89 was searched through the MSX, 2MASS and IRAS catalogues. The various point source catalogues were searched through and, it was decided to not pursue 2MASS data. Since there were so many sources within 10 arcseconds of a Methanol maser site, it was hard to tell if one of them was at the same distance as the maser or in front of it.

The relationship between methanol masers, MSX sources, and IRAS sources, as well as the corresponding flux densities, is displayed in Table 4.10. Only MYSOs are discovered to be related with Class II 6.7 GHz methanol masers, which are radiatively pumped by IR emission from heated dust (Cragg et al. 2005, Chen et al. 2010).

Table 4.10: The relationship between Methanol masers, MSX, and IRAS sources, and flux densities in Jy.

MSX		
Band	Wavelength (μm)	Flux
B1	4.29	-1.309e+01
B2	4.35	-7.07065e+00
A	8.28	6.03e+00
C	12.13	9.840e+00
D	14.65	1.4e+01
E	21.34	6.71e+01
IRAS		
IRAS12	12	1.40e+01
IRAS25	25	1.4e+02
IRAS60	60	9.56e+02
IRAS100	100	1.67e+03

4.4 DISCUSSION OF RESULTS

4.4.1 Radio Results

4.4.1.1 Methanol Maser Variability Implications

It's interesting to note that historical observations indicate that the initially discovered peak flux density feature, v_{LSR} $\sim$+10.5 km s^{-1}, has changed noticeably since its discovery, ranging from less than 500 Jy before 1993 as reported by Menten (1991*a*), Caswell, Vaile, Ellingsen, Whiteoak & Norris (1995). It registered an amount of more than 600 Jy before 2009 as reported by Goedhart et al. (2004), Green et al. (2012) to $\sim$500 Jy on average in this observation. Currently, the optimum flux density is located at v_{LSR} =+10.70 km s^{-1} and not at +10.44 km s^{-1}as depicted in Fig. 4.4. Three features from Table 4.1 are decreasing in brightness, with the v_{LSR} =+11.45 km s^{-1} decaying exponentially in particular (see Fig. 4.5).

According to Caswell, Vaile, Ellingsen, Whiteoak & Norris (1995), between 1991 ($\sim$250 Menten (1991*a*)) and 1993 ($\sim$230 Jy), the feature v_{LSR} =+11.2 km s^{-1} marginally reduced. It was only y $\sim$100 Jy in August of 1999 as stated by Szymczak et al. (2000*b*), before reaching a maximum of 160 Jy in November of 2001 as reported by Goedhart et al. (2004), and then declining exponentially, as described here.

Both of these variations and the maximum reported by Goedhart et al. (2004), are inexplicable by equation 4.1. The periodic feature at v_{LSR} =+11.45 km s^{-1} appears to have experienced a modest flaring event between 1999 August and 2001 November, with an increase in flux density of a factor of 2.6. This periodic decay feature is comparable to the one seen in G323.460.08 (MacLeod, Smits, Green & van den Heever 2021).

Additional investigation of the past data and data from other transitions will be necessary to confirm the exponential decay of the maser velocity component (12.2 GHz CH_3OH and/or 22.2 GHz H_2O), is necessary (Mutie et al. 2021). Minier et al. (2000) and Hu et al. (2016) present spot maps of 6.7 GHz methanol masers; all velocity fea-

tures sit in an 180×180 au box around the bright reference feature v_{LSR} =+10.33 km s^{-1} which is assumed to be at a distance of 1.76 kpc.

Within a ∼50 au radius of the feature that serves as the reference is where you'll find the weakening features, v_{LSR} =+8.42 km s^{-1} seen somewhat north and +11.45 km s^{-1} a little to the south of the reference maser(Mutie et al. 2021). Towards the south-east of the maser used for reference ∼90 au is where you can locate the increasing component (+10.70 km s^{-1}). Further to the south-east (∼140 au) is where you'll find the constant feature, v_{LSR} =+9.65 km s^{-1} (Mutie et al. 2021). The masers in close proximity to the reference maser might be part of a disc-generated outflow according to Minier et al. (2000). The fluctuation of spectrally blended masers as suggested by Szymczak et al. (2014) or gas motion as stated by Goddi et al. (2011), may be the cause of velocity drifts like those shown here (Mutie et al. 2021). Infalling gas may infiltrate the accretion discs that surround large star-forming regions and may cause the drifts. Szymczak et al. (2014) describe a velocity drifting feature in Cepheus A and speculated that it might be the product of masers situated in regions of infalling gas or an artefact of fluctuating line-merged features.

The suggestion put forth by MacLeod, Chibueze, Sanna, Paulsen, Houde, van den Heever & Goedhart (2021*a*) was that the protostar G9.62+0.20E's accretion disk's inner radius was infalling, causing the associated methanol masers to drift in velocity in a predictable way. They do, however, add that masers in a processing disc could be the cause of the drifts.

Two features exhibit measurably observable velocity drift, as shown by Table 4.1. The blue-shifting velocity component, v_{LSR} =+9.65 km s^{-1} is shifting ($\sim -2.0 \times 10^{-5}$ km s^{-1} d^{-1}) while the other v_{LSR} =+11.45 km s^{-1}, is red-shifting ($\sim +2.0 \times 10^{-5}$ km s^{-1} d^{-1}) (Mutie et al. 2021). The drifts are identical to those seen in G9.62+0.20E and varying from −6 to +3×10^{-5} km s^{-1} d^{-1} (MacLeod, Chibueze, Sanna, Paulsen, Houde, van den Heever & Goedhart 2021*a*, Mutie et al. 2021). However, there aren't enough features with detectable velocity drift, making it impossible

to make a comparison to G9.62+0.20E. Still significant velocity drifts are reported and this in only the third source. Class II methanol masers, which are can only be found in association with HMSFRs, are present in the source (Minier et al. 2003*b*). Such locations undergo accretion events, which are indicated by flaring masers, as described in S255IR-NIRS3 (MacLeod et al. 2018), G323.46-0.08 (Proven-Adzri et al. 2019, MacLeod, Smits, Green & van den Heever 2021), G358.93-0.03 (Sugiyama et al. 2019, MacLeod et al. 2019) and G188.95+0.89, our current object of study (Mutie et al. 2021).

In the spot maps displayed in Minier et al. (2000), Hu et al. (2016), the two maser features undergoing velocity drifts are observed to be well separated by ∼200 au. It's likely that an outflow affects the central features, and this motion may cause velocity drift in the features at the edges according to Minier et al. (2000). Even the brightest feature at the moment is blue-shifting at v_{LSR} =+10.70 km s^{-1}, however this might just be as a result of changes in strongly line-merged features. These periodic masers are all connected to the MM1 in Fig. 4.9. To understand these variances, additional observation and analysis are necessary.

The maser spots for G188.95+0.89 are laid out on a curve, with the vertex having the maximum radial velocity and the velocity steadily decreasing away from it, according to interferometric data from Ellingsen et al. (1998). What we see is exactly what we would expect to see if we were looking at a bow shock pattern from a vantage point near enough to the bow-shock axis to witness each maser spot inside the paraboloidal shell traveling in the direction of us (Moscadelli & Catarzi 1996).

There is much debate about whether these masers are connected to outflow, as suggested by De Buizer et al. (2009), or circumstellar discs, as suggested by Norris et al. (1998) Findings of Sanna et al. (2015) demonstrates that they can be connected to both components of the same young star source environment.

4.4.2 Interferometric Results

4.4.2.1 Binary System of G188.95+0.89-MM2

It has come to light that there are a number of indicators in MM2 that point to the possibility of the presence of a binary system. First, the high-resolution ALMA band 7 dust continuum image separates MM2 into two cores that are 0.1" apart from one another (Mutie et al. 2021). Second, the CH_3OH 4(2,2)-3(1,2) emission occurs at both the systemic velocity and the spectral profile of the emission that is traveling towards MM2 have two prominent features (see channel at 2 km s^{-1} of Fig. 4.11). In Fig. 4.26, we see the 4" ellipse's spectra of ^{12}CO (solid lines) and CH_3OH 4(2,2)-3(1,2) (dashed line) from MM2. After a close inspection, it was noted that the ^{12}CO emission was optically thick. Self-absorption features are visible in the in the ^{12}CO spectra as shown in Fig. 4.26. This indicates that the ^{12}CO emission is being absorbed by cold foreground material.

Most notably in the ^{12}CO spectra is an absorption pattern that is analogous to the CH3OH CH_3OH 4(2,2)-3(1,2) absorption characteristic in v_{LSR}, which separates the 2 resolved cores in MM2 (Mutie et al. 2021). All of these features point to MM2 being composed of several (or at least two) young star objects.

The complicated orientation of the outflowing gas traced by ^{12}CO, as seen in Fig.4.26, is consistent with the presence of at least a binary, if not several, YSOs in MM2. It is shown that MM2 is intersected by an east-west outflow feature, a north-west outflow feature, and a south-east outflow feature. These data lend credence to the theory that MM2 contains at least a binary system.

4.4.3 Infrared Results

Numerous publications have discussed near-infrared (NIR) photometry of young star populations by utilizing NIR J-H, H-K two-color diagrams to distinguish between various object classes (Van der Walt et al. 2012). Here we follow the same practice.

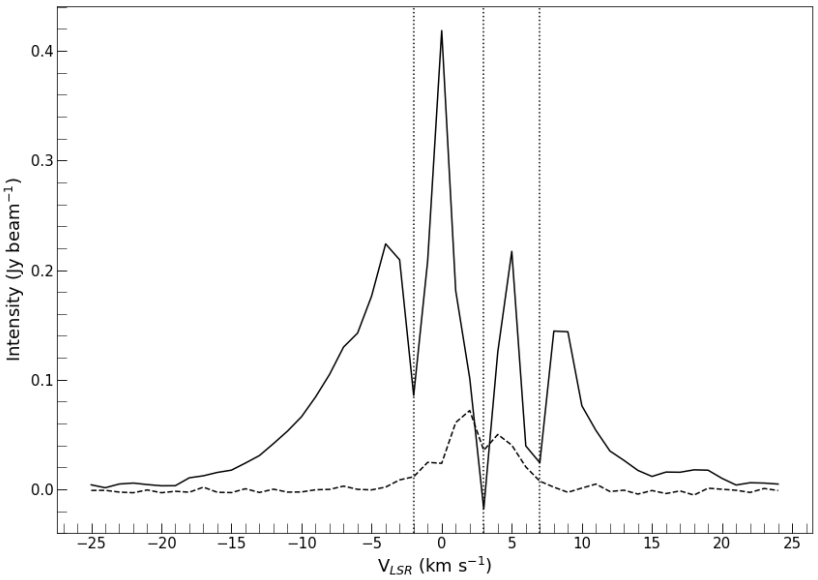

Figure 4.26: ^{12}CO (solid lines) and CH_3OH (dashed lines) the spectrum of G188.95+0.89 was taken using an ellipse of size ∼4" and centering on MM2. Multiple absorption patterns in the 12CO emission and a double peak in the CH_3OH line are indicators of a binary or more than two sources of propulsion in MM2. Source: (Mutie et al. 2021).

Fig. 4.22 (upper row on the left) presents the main results of the selected subset of 37 objects. The Objects that lie to the middle of the graph, above the T Tauri locus and with $0.2 < (H - K) < 1$. The infrared excess prevents these objects from being dereddened to the main sequence. Between the extremes of the T Tauri locus, each object was dereddened and placed at random position since the true unreddened intrinsic colors are not known. The objects continued lying on their individual dereddening line.

There may be doubts about the veracity of the grouping and the composition of the objects, given the distribution of the objects on the two-color diagram in Fig. 4.22 (top row, left). Dereddening would cause some of these stars to become ionizing, meaning they would have been detected as H II regions in radio continuum surveys or as strong infrared sources even though their optical extinction would be between 10 and 15 mag as reported by Van der Walt et al. (2012). Field stars and Class III objects with a minor NIR excess are the most common types of objects seen in the

reddening band. It's difficult to tell the difference between field stars and Class III objects, thus it's possible that the latter objects could be part of the SFR.

The list of objects with good WISE detections, defined as those with photometric uncertainty $< 0.2\ mag$ in WISE bands, were used to create two additional MIR c-c diagrams. The c-c diagram for [3.4]-[4.6] against [4.6]-[12] can be seen in the bottom right panel of Fig. 4.22. Class I YSOs have a color range of $[3.4] - [4.6] > 1.0$ and $[4.6] - [12] > 2.0$, making them the reddest objects.

Objects in the Class I YSO redness range have a color temperature of $[3.4][4.6] > 1.0$ and $[4.6][12] > 2.0$. Using the $[3.4] - [4.6]$ versus $[4.6] - [12]$ c-c diagram, a total of 19 YSO candidates were chosen for further consideration. The c-c diagram for [3.4]-[4.6] against [4.6]-[12] can be seen in the bottom right panel of Fig. 4.22

CHAPTER FIVE

CONCLUSIONS

5.1 SUMMARY

In this work, we presented the findings from 1.8 decades of observational tracking of 6.7 GHz CH_3OH masers towards G188.95+0.89. The summary of the results is as follows;

(i) The spectra of G188.95+0.89 was found to have five prominent velocity features at +8.42, +9.65, +10.44, +10.70 and +11.45 km s^{-1} are variable and periodic (however it is not immediately apparent for the velocity feature v_{LSR} =+11.45 km s^{-1}), suggesting a common background source. As this feature decays exponentially, its relative amplitude, R_{amp}, decreases approximately proportionally. Background free-free emissions, which are amplified by the masers, are likely responsible for the observed variations in the G188.95+0.89 masers.

(ii) A plot of light curves using radio data showed that the velocity drifts associated with the spatial movement of the gas depicted different variability patterns of close and blended features. It can be concluded that the velocity drifts were as a result of infalling gas to the inner radius of the accretion disk surrounding the star forming region of G188.95+0.89.

(iii) The continuum and thermal line emissions resolved G188.95+0.89 protocluster into eight 1.3 mm objects (MM1-MM8) of masses ranging from $0.4M_{\odot}$ to $8.2M_{\odot}$, indicating the presence of a massive star in the region. MM1 and MM2 are the central objects and MM1 (the brightest dust continuum object) is associated with the periodic 6.7 GHz CH_3OH maser source. Several molecular lines detected in the region included ^{12}CO, CH_3OH, SiO and ^{18}CO. The presence of this molecular lines is indicative that the objects under investigation are at

early phase of evolution.

(iv) Morphology of the emission from different species detected toward G188.95+0.89 were shown using the zero moment maps of the most prominent transitions of each species. ^{12}CO (2-1) and CH_3OH $4_{(2,2)}$-$3_{(1,2)}$ zero moment maps shows an elongated spatial emission coincident with the dust continuum MM2. MM2 hosts more than one YSO, likely a binary system. Strong emission of ^{12}CO at the east and west of MM2 point to the presence of an east-west bipolar outflow in MM2. Emissions north of MM2 also suggest a second outflow emanating from the object, which could signal multiplicity of YSOs in MM2. The detected outflows suggest the presence of accretion disks in the source.

(v) Hydroxyl and water masers were detected in close vicinity to the star forming region. Churchwell (2002) proposed that the most widespread masers associated with HMSF regions are H_2O, OH, and CH_3OH. The presence or absence of the different maser species can be used as an evolutionary clock, since masers are relatively easily observed signposts of star forming regions. A total of 36 candidate YSOs were detected within a 60″ radius of the G188.95+0.89 source. Nine of these YSOs form an IR cluster within the boundary of the UC HII region. Analysis of the extinction corrected reddening values would suggest that the IR cluster contains the most reddened YSO candidates detected in the region. All this points to the cluster being relatively young, considering the high number of potential protostars and the other two extremely reddened sources, the age is estimated to be of order of 10^5 yrs.

5.2 FUTURE RESEARCH PROSPECTS

In this section, a few recommendations which can be implemented to further the investigation of maser variability in HMSFRs are listed. These recommendations are:

- It is important to investigate potential causes of periodic variability and this

requires the use of Maser numerical modeling. It could help answer queries such as whether only changes in the photon flux of the infrared pump photons are responsible for these variations or if the seed photons at the frequency of the microwave line are also involved.

- At present only 26 periodic masers have been detected. Further monitoring programmes should be conducted in order to find more periodic masers. This could improve areas such as categorisation of light curves, add a possible mechanism for explaining the origins of maser periodicity. This will improve understanding of light curves or rule out other possible mechanisms for explaining the origins of periodicity in masers.

- Velocity drifts detected in G188.95+0.89 should be examined in other varying masers to investigate what causes them. These velocity drifts are excellent candidates for future VLBI investigations to determine whether the radial velocity acceleration of features actually traces the accretion of gas.

- There are presumably two YSOs in MM2, making it a binary system though it needs further investigation using VLBI to verify whether it is a binary.

References

Allen, L. E., Calvet, N., D'Alessio, P., Merin, B., Hartmann, L., Megeath, S. T., Gutermuth, R. A., Muzerolle, J., Pipher, J. L., Myers, P. C. et al. (2004), 'Infrared array camera (irac) colors of young stellar objects', *The Astrophysical Journal Supplement Series* **154**(1), 363.

Allen, V., Van Der Tak, F., Sánchez-Monge, Á., Cesaroni, R. & Beltrán, M. (2017), 'Chemical segregation in hot cores with disk candidates-an investigation with alma', *Astronomy & Astrophysics* **603**, A133.

Alves, J., Lombardi, M. & Lada, C. (2007), 'The mass function of dense molecular cores and the origin of the imf', *Astronomy & Astrophysics* **462**(1), L17–L21.

André, P., Di Francesco, J., Ward-Thompson, D., Inutsuka, S., Pudritz, R., Pineda, J., Beuther, H., Klessen, R. S., Dullemond, C. P. & Henning, T. (2014), 'Protostars and planets vi'.

André, P., Men'shchikov, A., Bontemps, S., Könyves, V., Motte, F., Schneider, N., Didelon, P., Minier, V., Saraceno, P., Ward-Thompson, D. et al. (2010), 'From filamentary clouds to prestellar cores to the stellar imf: Initial highlights from the herschel gould belt survey', *Astronomy & Astrophysics* **518**, L102.

Andresen, P., Ondrey, G., Titze, B. & Rothe, E. W. (1984), 'Nuclear and electron dynamics in the photodissociation of water', *The Journal of chemical physics* **80**(6), 2548–2569.

Ao, Y., Yang, J., Tatematsu, K., Henkel, C., Sunada, K. & Nguyen-Luong, Q. (2018), 'A search for high-mass protostellar objects in cold iras sources', *The Astronomical Journal* **156**(5), 210.

Araya, E., Hofner, P., Goss, W., Kurtz, S., Richards, A., Linz, H., Olmi, L. & Sewiło, M. (2010), 'Quasi-periodic formaldehyde maser flares in the massive protostellar object iras 18566+ 0408', *The Astrophysical Journal Letters* **717**(2), L133.

Araya, E., Olmi, L., Ortiz, J. M., Brown, J., Hofner, P., Kurtz, S., Linz, H. & Creech-Eakman, M. (2015), 'Formaldehyde masers: exclusive tracers of high-mass star formation', *The Astrophysical Journal Supplement Series* **221**(1), 10.

Arce, H. G., Borkin, M. A., Goodman, A. A., Pineda, J. E. & Beaumont, C. N. (2011), 'A bubbling nearby molecular cloud: Complete shells in perseus', *The Astrophysical Journal* **742**(2), 105.

Avison, A. M. (2011), Methanol masers and the environments of massive star formation, PhD thesis, The University of Manchester (United Kingdom).

Azatyan, N. (2019), 'Investigation of the stellar content in the iras 05168+ 3634 star-forming region', *Astronomy & Astrophysics* **622**, A38.

Azatyan, N., Nikoghosyan, E., Harutyunian, H., Baghdasaryan, D. & Andreasyan, D. (2022), 'Infrared study of the star-forming region associated with the uc hii regions g45. 07+ 0.13 and g45. 12+ 0.13', *Publications of the Astronomical Society of Australia* **39**, e024.

Baars, J. & Genzel, R. (1977), 'Pauliny-toth, iik, witzel', *A&A* **61**, 99–106.

Bacher, A. & CHRISTENSEN, L. L. (2001), 'The esa/eso astronomy exercise series', *EUROPEAN SPACE AGENCY-PUBLICATIONS-ESA SP* **491**, 49–50.

Balbus, S. A. & Soker, N. (1989), 'Theory of local thermal instability in spherical systems', *The Astrophysical Journal* **341**, 611–630.

Bally, J. & Zinnecker, H. (2005), 'The birth of high-mass stars: Accretion and/or mergers?', *The Astronomical Journal* **129**(5), 2281.

Barrett, A., Schwartz, P. & Waters, J. (1971), 'Detection of methyl alcohol in orion at a wavelength of˜ 1 centimeter', *The Astrophysical Journal* **168**, L101.

Bartkiewicz, A., Szymczak, M. & van Langevelde, H. J. (2016), 'European vlbi network imaging of 6.7 ghz methanol masers', *Astronomy & Astrophysics* **587**, A104.

Bate, M. R. (2009), 'The importance of radiative feedback for the stellar initial mass function', *Monthly Notices of the Royal Astronomical Society* **392**(4), 1363–1380.

Batrla, W., Matthews, H., Menten, K. & Walmsley, C. (1987), 'Detection of strong methanol masers towards galactic h ii regions', *Nature* **326**(6108), 49.

Battersby, C. & Bally, J. (2014), 'Astrophysics and space science proceedings'.

Beichman, C., Neugebauer, G., Habing, H., Clegg, P. & Chester, T. J. (1988), Infrared astronomical satellite (iras) catalogs and atlases. volume 1: Explanatory supplement, Technical report.

Berriman, G. B. (2008), The nasa/ipac infrared science archive (irsa) as a resource in supporting observatory operations, *in* 'Observatory Operations: Strategies, Processes, and Systems II', Vol. 7016, SPIE, pp. 379–387.

Beuther, H., Schilke, P., Menten, K., Motte, F., Sridharan, T. & Wyrowski, F. (2002), 'High-mass protostellar candidates. ii. density structure from dust continuum and cs emission', *The Astrophysical Journal* **566**(2), 945.

Beuther, H., Walsh, A. & Longmore, S. (2009), 'Hot high-mass accretion disk candidates', *The Astrophysical Journal Supplement Series* **184**(2), 366.

Blitz, L. & Williams, J. P. (1999), 'Molecular clouds (a review)', *arXiv preprint astro-ph/9903382* .

Boland, W. & De Jong, T. (1981), 'A model for the formaldehyde maser near ngc 7538-irs 1', *Astronomy and Astrophysics, vol. 98, no. 1, May 1981, p. 149-154. Research supported by the Nederlandse Organisatie voor Zuiver-Wetenschappelijk Onderzoek.* **98**, 149–154.

Boley, P. A. (2013), High-resolution studies of circumstellar material around massive young stellar objects, PhD thesis.

Bonfand, M., Belloche, A., Garrod, R., Menten, K., Willis, E., Stéphan, G. & Müller, H. (2019), 'The complex chemistry of hot cores in sgr b2 (n): influence of cosmic-ray ionization and thermal history', *Astronomy & Astrophysics* **628**, A27.

Bonnell, I. (2008), Competitive accretion and the formation of massive stars, *in* 'Pathways Through an Eclectic Universe', Vol. 390, p. 26.

Bonnell, I. A., Bate, M. R. & Zinnecker, H. (1998), 'On the formation of massive stars', *Monthly Notices of the Royal Astronomical Society* **298**(1), 93–102.

Bonnell, I. A., Vine, S. G. & Bate, M. R. (2004), 'Massive star formation: nurture, not nature', *Monthly Notices of the Royal Astronomical Society* **349**(2), 735–741.

Bonnell, I., Bate, M., Clarke, C. & Pringle, J. (1997), 'Accretion and the stellar mass spectrum in small clusters', *Monthly Notices of the Royal Astronomical Society* **285**(1), 201–208.

Bonnell, I., Bate, M., Clarke, C. & Pringle, J. (2001), 'Competitive accretion in embedded stellar clusters', *Monthly Notices of the Royal Astronomical Society* **323**(4), 785–794.

Breckenridge, S. & Kukolich, S. (1995), 'Precise laboratory measurements of methanol rotational transition frequencies in the 5 to 13 ghz region', *The Astrophysical Journal* **438**, 504–505.

Breen, S., Ellingsen, S., Caswell, J. & Lewis, B. (2010), '12.2-ghz methanol masers towards 1.2-mm dust clumps: quantifying high-mass star formation evolutionary schemes', *Monthly Notices of the Royal Astronomical Society* **401**(4), 2219–2244.

Breen, S., Ellingsen, S., Contreras, Y., Green, J., Caswell, J., Stevens, J., Dawson, J. & Voronkov, M. (2013), 'Confirmation of the exclusive association between 6.7-ghz methanol masers and high-mass star formation regions', *Monthly Notices of the Royal Astronomical Society* **435**(1), 524–530.

Breen, S., Fuller, G., Caswell, J., Green, J., Avison, A., Ellingsen, S., Gray, M., Pestalozzi, M., Quinn, L., Richards, A. et al. (2015), 'The 6-ghz methanol multi-beam maser catalogue–v. galactic longitudes 20°–60°', *Monthly Notices of the Royal Astronomical Society* **450**(4), 4109–4136.

Breen, S. L. & Ellingsen, S. P. (2012), 'Masers as evolutionary tracers of high-mass star formation', *Proceedings of the International Astronomical Union* **8**(S287), 156–160.

Briceño, C., Luhman, K., Hartmann, L., Stauffer, J. R. & Kirkpatrick, J. D. (2002), 'The initial mass function in the taurus star-forming region', *The Astrophysical Journal* **580**(1), 317.

Burke, B. F., Graham-Smith, F. & Wilkinson, P. N. (2019), *An introduction to radio astronomy*, Cambridge University Press.

Caselli, P. & Ceccarelli, C. (2012), 'Our astrochemical heritage', *The Astronomy and Astrophysics Review* **20**(1), 56.

Caswell, J. (1996), 'A new survey for 6.6-ghz methanol masers', *Monthly Notices of the Royal Astronomical Society* **279**(1), 79–87.

Caswell, J., Fuller, G., Green, J., Avison, A., Breen, S., Brooks, K., Burton, M., Chrysostomou, A., Cox, J., Diamond, P. et al. (2010), 'The 6-ghz methanol multi-beam maser catalogue–i. galactic centre region, longitudes 345° to 6°', *Monthly Notices of the Royal Astronomical Society* **404**(2), 1029–1060.

Caswell, J., Haynes, R. & Goss, W. (1980), 'Survey of oh masers at 1665 and 1667 mhz. i. galactic longitudes 326° to 40°', *Australian Journal of Physics* **33**(3), 639–672.

Caswell, J., Vaile, R. & Ellingsen, S. (1995), 'Variability of methanol masers', *Publications of the Astronomical Society of Australia* **12**(1), 37–53.

Caswell, J., Vaile, R., Ellingsen, S., Whiteoak, J. & Norris, R. (1995), 'Galactic methanol masers at 6.6 ghz', *Monthly Notices of the Royal Astronomical Society* **272**(1), 96–138.

Chabrier, G. (2003), 'Galactic stellar and substellar initial mass function1', *Publications of the Astronomical Society of the Pacific* **115**(809), 763.

Chahine, L., López-Sepulcre, A., Neri, R., Ceccarelli, C., Mercimek, S., Codella, C., Bouvier, M., Bianchi, E., Favre, C., Podio, L. et al. (2022), 'Organic chemistry in the protosolar analogue hops-108: Environment matters', *Astronomy & Astrophysics* **657**, A78.

Chen, H.-R., Welch, W. J., Wilner, D. J. & Sutton, E. C. (2006), 'A high-mass protobinary system in the hot core w3 (h2o)', *The Astrophysical Journal* **639**(2), 975.

Chen, X., Ellingsen, S. P., Ren, Z.-Y., Sobolev, A. M., Parfenov, S. & Shen, Z.-Q. (2019), 'Discovery of a new class i methanol maser transition at 266.8 ghz', *The Astrophysical Journal* **877**(2), 90.

Chen, X., Shen, Z.-Q., Li, J.-J., Xu, Y. & He, J.-H. (2010), 'A search for infall evidence in egos. i. the northern sample', *The Astrophysical Journal* **710**(1), 150.

Cheung, A., Rank, D. M., Townes, C., Thornton, D. D. & Welch, W. (1969), 'Detection of water in interstellar regions by its microwave radiation', *Nature* **221**(5181), 626.

Chibueze, J. O., Csengeri, T., Tatematsu, K., Hasegawa, T., Iguchi, S., Alhassan, J. A., Higuchi, A. E., Bontemps, S. & Menten, K. M. (2017), 'Class ii 6.7 ghz methanol maser association with young massive cores revealed by alma', *The Astrophysical Journal* **836**(1), 59.

Christensen, M. B. E. (2019), 'How do stars form?', *Frontiers for Young Minds* **7**.

Christiansen, W. N. & Högbom, J. A. (1987), *Radiotelescopes*, CUP Archive.

Churchwell, E. (1990), 'Ultracompact hii regions: the impact of newly formed massive stars on their environment', *The Astronomy and Astrophysics Review* **2**(2), 79–123.

Churchwell, E. (2002), 'Ultra-compact hii regions and massive star formation', *Annual Review of Astronomy and Astrophysics* **40**(1), 27–62.

Churchwell, E., Babler, B. L., Meade, M. R., Whitney, B. A., Benjamin, R., Indebetouw, R., Cyganowski, C., Robitaille, T. P., Povich, M., Watson, C. et al. (2009), 'The spitzer/glimpse surveys: a new view of the milky way', *Publications of the Astronomical Society of the Pacific* **121**(877), 213.

Churchwell, E., Wolfire, M. & Wood, D. O. (1990), 'The infrared emission from dust surrounding newly formed o stars', *The Astrophysical Journal* **354**, 247–261.

Clark, B. (1980), 'An efficient implementation of the algorithm'clean", *Astronomy and Astrophysics, vol. 89, no. 3, Sept. 1980, p. 377, 378.* **89**, 377.

Codella, C., Felli, M., Natale, V., Palagi, F. & Palla, F. (1994), 'The occurrence of h2o masers in hii regions', *Astronomy and Astrophysics* **291**, 261–270.

Colomer, F., Reid, M., Menten, K. & Bujarrabal, V. (2000), 'The spatial and velocity structure of circumstellar water masers', *Astronomy and Astrophysics* **355**, 979–993.

Combrinck, L. (2014), 'Hartebeesthoek radio astronomy observatory', *South Africa* .

Condon, J. J. & Ransom, S. M. (2016), *Essential radio astronomy*, Princeton University Press.

CooKE, B. & Elitzur, M. (1985), 'Water masers in late-type stars', *Astrophysical Journal, Part 1 (ISSN 0004-637X), vol. 295, Aug. 1, 1985, p. 175-182.* **295**, 175–182.

Cornwell, T., Braun, R., Briggs, D., Taylor, G., Carilli, C. & Perley, R. (1999), 'Synthesis imaging in radio astronomy ii', *Astron. Soc. Pac* **180**, 151–170.

Cowie, L. L. (1980), 'On the dynamics of agglomerating ensembles of clouds', *The Astrophysical Journal* **236**, 868–879.

Cragg, D. M., Johns, K. P., Godfrey, P. D. & Brown, R. D. (1992), 'Pumping the interstellar methanol masers', *Monthly Notices of the Royal Astronomical Society* **259**(1), 203–208.

Cragg, D. M., Sobolev, A. & Godfrey, P. (2005), 'Models of class ii methanol masers based on improved molecular data', *Monthly Notices of the Royal Astronomical Society* **360**(2), 533–545.

Cragg, D. M., Sobolev, A. M. & Godfrey, P. D. (2002), 'Modelling methanol and hydroxyl masers in star-forming regions', *Monthly Notices of the Royal Astronomical Society* **331**(2), 521–536.

Crutcher, R. M. (2012), 'Magnetic fields in molecular clouds', *Annual Review of Astronomy and Astrophysics* **50**, 29–63.

Cutri, R., Skrutskie, M., Van Dyk, S., Beichman, C., Carpenter, J., Chester, T., Cambresy, L., Evans, T. et al. (2003), 'Explanatory supplement to the 2mass all sky data release'.

Cyganowski, C., Brogan, C., Hunter, T. & Churchwell, E. (2009), 'A class i and class ii ch3oh maser survey of egos from the glimpse survey', *The Astrophysical Journal* **702**(2), 1615.

Cyganowski, C., Brogan, C., Hunter, T., Churchwell, E. & Zhang, Q. (2011), 'Bipolar molecular outflows and hot cores in glimpse extended green objects (egos)', *The Astrophysical Journal* **729**(2), 124.

Daffern-Powell, E. (2021), Dynamical Evolution of Stars and Planets in Star-Forming Regions, PhD thesis, University of Sheffield.

Dame, T. (2011), 'Optimization of moment masking for co spectral line surveys', *arXiv preprint arXiv:1101.1499* .

Davis, C., Kumar, M., Sandell, G., Froebrich, D., Smith, M. D. & Currie, M. (2007), 'Wfcam, spitzer/irac and scuba observations of the massive star-forming region dr21/w75–i. the collimated molecular jets', *Monthly Notices of the Royal Astronomical Society* **374**(1), 29–53.

De Buizer, J. M. (2000), *A mid-infrared imaging survey of star forming regions containing methanol and water maser emission*, University of Florida.

De Buizer, J. M. (2003), 'Testing the circumstellar disc hypothesis: a search for h2 outflow signatures from massive young stellar objects with linearly distributed methanol masers', *Monthly Notices of the Royal Astronomical Society* **341**(1), 277–298.

De Buizer, J., Radomski, J., Telesco, C. & Pina, R. (2005), 'Observations of massive star-forming regions with water masers: Mid-infrared imaging', *The Astrophysical Journal Supplement Series* **156**(2), 179.

De Buizer, J., Redman, R., Longmore, S., Caswell, J. & Feldman, P. (2009), 'Sio outflow signatures toward massive young stellar objects with linearly distributed methanol masers', *Astronomy & Astrophysics* **493**(1), 127–143.

de Carvalho, N. P. (2013), Massive Star Forming Regions at High Spatial Resolutions, PhD thesis, Universidade do Porto (Portugal).

De Villiers, H. M., Chrysostomou, A., Thompson, M., Urquhart, J., Breen, S., Burton, M., Ellingsen, S., Fuller, G., Pestalozzi, M., Voronkov, M. et al. (2015), '6.7-ghz methanol maser associated outflows: an evolutionary sequence', *Monthly Notices of the Royal Astronomical Society* **449**(1), 119–128.

Deguchi, S. (1977), 'Water maser and envelope of infrared stars.', *Publications of the Astronomical Society of Japan, Vol. 29, p. 669-681* **29**, 669–681.

Deharveng, L., Schuller, F., Anderson, L., Zavagno, A., Wyrowski, F., Menten, K., Bronfman, L., Testi, L., Walmsley, C. & Wienen, M. (2010), 'A gallery of bubbles-the nature of the bubbles observed by spitzer and what atlasgal tells us about the surrounding neutral material', *Astronomy & Astrophysics* **523**, A6.

Dent, W. (2016), Alma specifications and results: report at mid-cycle 3, *in* 'Ground-based and Airborne Telescopes VI', Vol. 9906, SPIE, pp. 320–331.

Dodson, R., Ojha, R. & Ellingsen, S. (2004), 'High-resolution observations of 6.7-ghz methanol masers with the long baseline array', *Monthly Notices of the Royal Astronomical Society* **351**(3), 779–790.

Downes, D. & Wilson, T. (1974), 'Formaldehyde line emission at 4.8 ghz near ngc 7538', *The Astrophysical Journal* **191**, L77.

Dunham, M. M., Arce, H. G., Mardones, D., Lee, J.-E., Matthews, B. C., Stutz, A. M. & Williams, J. P. (2014), 'Molecular outflows driven by low-mass protostars. i. correcting for underestimates when measuring outflow masses and dynamical properties', *The Astrophysical Journal* **783**(1), 29.

Dunne, L., Eales, S., Ivison, R., Morgan, H. & Edmunds, M. (2003), 'Type ii supernovae as a significant source of interstellar dust', *Nature* **424**(6946), 285–287.

Durjasz, M., Szymczak, M., Wolak, P. & Bartkiewicz, A. (2021), 'Observations of 12.2 ghz methanol masers towards northern high-mass protostellar objects', *Astronomy & Astrophysics* **648**, A118.

Edgar, R. & Clarke, C. (2004), 'The effect of radiative feedback on bondi–hoyle flow around a massive star', *Monthly Notices of the Royal Astronomical Society* **349**(2), 678–686.

Ediss, G., Carter, M., Cheng, J., Effland, J., Grammer, W., Horner Jr, N., Kerr, A., Koller, D., Lauria, E., Morris, G. et al. (2004), Alma band 6 prototype cartridge: Design and performance, *in* 'Proc. 15th Intl. Symp. Space Terahertz Tech', pp. 181–188.

Ekers, R. (2003), Astronomy at the fringe, *in* 'Radio Astronomy at the Fringe', Vol. 300, p. 301.

Elitzur, M. (1982), 'Physical characteristics of astronomical masers', *Reviews of Modern Physics* **54**(4), 1225.

Elitzur, M. (1992*a*), 'Astronomical masers', *Annual review of astronomy and astrophysics* **30**(1), 75–112.

Elitzur, M. (1992*b*), 'Astrophysics and space science library'.

Elitzur, M., Hollenbach, D. J. & McKee, C. F. (1989), 'H2o masers in star-forming regions', *The Astrophysical Journal* **346**, 983–990.

Ellingsen, S., McCulloch, P., Diamond, P. & Norris, R. (1998), Vlba imaging of 12.2 ghz methanol masers, *in* 'International Astronomical Union Colloquium', Vol. 164, Cambridge University Press, pp. 375–376.

Ellingsen, S. P. (2006), 'Methanol masers: Reliable tracers of the early stages of high-mass star formation', *The Astrophysical Journal* **638**(1), 241.

Ellingsen, S., Voronkov, M., Cragg, D., Sobolev, A., Breen, S. & Godfrey, P. (2007), 'Investigating high-mass star formation through maser surveys', *Proceedings of the International Astronomical Union* **3**(S242), 213–217.

Elmegreen, B. G. (1990), Theories of molecular cloud formation, *in* 'The Evolution of the Interstellar Medium', Vol. 12, pp. 247–271.

Elmegreen, B. G. & Palous, J. (2007), *Triggered Star Formation in a Turbulent Interstellar Medium (IAU S237)*, number 237, Cambridge University Press.

Fazio, G., Hora, J., Allen, L., Ashby, M., Barmby, P., Deutsch, L., Huang, J.-S., Kleiner, S., Marengo, M., Megeath, S. et al. (2004), 'The infrared array camera (irac) for the spitzer space telescope', *The Astrophysical Journal Supplement Series* **154**(1), 10.

Field, G. B. (1965), 'Thermal instability.', *The Astrophysical Journal* **142**, 531.

Fish, V. L. (2007), 'Masers and star formation', *Proceedings of the International Astronomical Union* **3**(S242), 71–80.

Fish, V. L. & Reid, M. J. (2007), 'Proper motions of oh masers and magnetic fields in massive star-forming regions', *The Astrophysical Journal* **670**(2), 1159.

Flower, D. (2007), *Molecular collisions in the interstellar medium*, Vol. 42, Cambridge University Press.

Fomalont, E., van Kempen, T., Kneissl, R., Marcelino, N., Barkats, D., Corder, S., Cortes, P., Hills, R., Lucas, R., Manning, A. et al. (2014), 'The calibration of alma using radio sources', *The Messenger* **155**, 19–22.

Forster, J., Goss, W., Gardner, F. & Stewart, R. (1985), 'A search for h2co emission towards oh masers', *Monthly Notices of the Royal Astronomical Society* **216**(1), 35P–39P.

Fraknoi, A., Morrison, D. & Wolff, S. (2016), 'Astronomy (the textbook)', *Houston: Open-Stax* .

Freedman, R. A. & William III, J. (2008), 'Kaufmann iii. universe'.

Fujisawa, K., Takase, G., Kimura, S., Aoki, N., Nagadomi, Y., Shimomura, T., Sugiyama, K., Motogi, K., Niinuma, K., Hirota, T. et al. (2014), 'Periodic flare of the 6.7-ghz methanol maser in iras 22198+ 6336', *Publications of the Astronomical Society of Japan* **66**(4), 78.

Gail, H.-P. & Hoppe, P. (2010), 'The origins of protoplanetary dust and the formation of accretion disks', *Protoplanetary Dust* p. 27.

Garay, G. & Lizano, S. (1999), 'Massive stars: their environment and formation', *Publications of the Astronomical Society of the Pacific* **111**(763), 1049.

Garsden, H., Girard, J., Starck, J.-L., Corbel, S., Tasse, C., Woiselle, A., McKean, J., Van Amesfoort, A. S., Anderson, J., Avruch, I. et al. (2015), 'Lofar sparse image reconstruction', *Astronomy & astrophysics* **575**, A90.

Genzel, R. & Downes, D. (1977), 'H2o in the galaxy: sites of newly formed ob stars.', *Astronomy and Astrophysics Supplement Series* **30**, 145–168.

Genzel, R., Downes, D., Moran, J., Johnston, K., Spencer, J., Walker, R., Haschick, A., Matveenko, L., Matveyenko, L., Kogan, L. et al. (1978), 'Structure and kinematics of h2o sources in clusters of newly-formed ob stars', *Astronomy and Astrophysics* **66**, 13–29.

Gieser, C., Beuther, H., Semenov, D., Suri, S., Soler, J., Linz, H., Syed, J., Henning, T., Feng, S., Möller, T. et al. (2022), 'Clustered star formation at early evolutionary stages-physical and chemical analysis of the young star-forming regions isoss j22478+ 6357 and isoss j23053+ 5953', *Astronomy & Astrophysics* **657**, A3.

Goddi, C., Moscadelli, L. & Sanna, A. (2011), 'Infall and outflow within 400 au from a high-mass protostar-3d velocity fields from methanol and water masers in aflg 5142', *Astronomy & Astrophysics* **535**, L8.

Goedhart, S., Gaylard, M. & Van Der Walt, D. (2004), 'Long-term monitoring of 6.7-ghz methanol masers', *Monthly Notices of the Royal Astronomical Society* **355**(2), 553–584.

Goedhart, S., Gaylard, M. & van Der Walt, D. (2005), Long-term monitoring of 6.7- and 12.2-ghz methanol masers, *in* 'Dense Molecular Gas Around Protostars and in Galactic Nuclei', Springer, pp. 197–202.

Goedhart, S., Gaylard, M. & Walt, D. v. d. (2003), 'Periodic flares in the methanol maser source g9. 62+ 0.20 e', *Monthly Notices of the Royal Astronomical Society* **339**(4), L33–L36.

Goedhart, S., Langa, M., Gaylard, M. & Van Der Walt, D. (2009), 'Short-period variability in the class ii methanol maser source g12. 89+ 0.49 (iras 18089- 1732)', *Monthly Notices of the Royal Astronomical Society* **398**(2), 995–1010.

Goedhart, S., Maswanganye, J., Gaylard, M. & van der Walt, D. (2014*a*), 'Periodicity in class ii methanol masers in high-mass star-forming regions', *Monthly Notices of the Royal Astronomical Society* **437**(2), 1808–1820.

Goedhart, S., Maswanganye, J. P., Gaylard, M. J. & van der Walt, D. J. (2014*b*), 'Periodicity in Class II methanol masers in high-mass star-forming regions', **437**(2), 1808–1820.

Goedhart, S., Minier, V., Gaylard, M. & Van Der Walt, D. (2005), 'Very long baseline array imaging of a periodic 12.2-ghz methanol maser flare in g9. 62+ 0.20 e', *Monthly Notices of the Royal Astronomical Society* **356**(3), 839–848.

Goedhart, S., Van Der Walt, D. & Gaylard, M. (2002), 'Near-infrared imaging of the environment of 6.7-ghz methanol masers', *Monthly Notices of the Royal Astronomical Society* **335**(1), 125–141.

Goldreich, P. & Kwan, J. (1974), 'Astrophysical masers. v. pump mechanism for h2o masers', *Astrophysical Journal, Vol. 191, pp. 93-100 (1974)* **191**, 93–100.

Gómez-Ruiz, A., Kurtz, S., Araya, E., Hofner, P. & Loinard, L. (2016), 'A catalog of methanol masers in massive star-forming regions. iii. the molecular outflow sample', *The Astrophysical Journal Supplement Series* **222**(2), 18.

Gray, M. (2012), *Maser Sources in Astrophysics*, Vol. 50, Cambridge University Press.

Green, J. A., Caswell, J. L., Fuller, G. A., Avison, A., Breen, S. L., Ellingsen, S. P., Gray, M. D., Pestalozzi, M., Quinn, L., Thompson, M. A. & Voronkov, M. A. (2012), 'The 6-GHz methanol multibeam maser catalogue - IV. Galactic longitudes 186°-330° including the Orion-Monoceros region', **420**(4), 3108–3125.

Griffin, M. J., Abergel, A., Abreu, A., Ade, P. A., André, P., Augueres, J.-L., Babbedge, T., Bae, Y., Baillie, T., Baluteau, J.-P. et al. (2010), 'The herschel-spire instrument and its in-flight performance', *Astronomy & Astrophysics* **518**, L3.

Groh, J. H., Meynet, G., Georgy, C. & Ekström, S. (2013), 'Fundamental properties of core-collapse supernova and grb progenitors: predicting the look of massive stars before death', *Astronomy & Astrophysics* **558**, A131.

Gutermuth, R., Myers, P., Megeath, S., Allen, L., Pipher, J., Muzerolle, J., Porras, A., Winston, E. & Fazio, G. (2008), 'Spitzer observations of ngc 1333: A study of structure and evolution in a nearby embedded cluster', *The Astrophysical Journal* **674**(1), 336.

Guzmán, A. E., Guzmán, V. V., Garay, G., Bronfman, L. & Hechenleitner, F. (2018), 'Chemistry of the high-mass protostellar molecular clump iras 16562–3959', *The Astrophysical Journal Supplement Series* **236**(2), 45.

Harju, J., Lehtinen, K., Booth, R. & Zinchenko, I. (1998), 'A survey of sio emission towards interstellar masers-i. sio line characteristics', *Astronomy and Astrophysics Supplement Series* **132**(2), 211–231.

Hartmann, L. (2009), 'Accretion processes in star formation second edition', *Cambridge Astrophysics Series* **47**(1), ALL–ALL.

Hazdra, P. & Mazanek, M. (n.d.), 'Horn antennas'.

Henning, T., Schreyer, K., Launhardt, R. & Burkert, A. (2000), 'Massive young stellar objects with molecular outflows', *Astronomy and Astrophysics* **353**, 211–226.

Herbst, E. & Van Dishoeck, E. F. (2009), 'Complex organic interstellar molecules', *Annual Review of Astronomy and Astrophysics* **47**, 427–480.

Hernández-Hernández, V., Kurtz, S., Kalenskii, S., Golysheva, P., Garay, G., Zapata, L. & Bergman, P. (2019), 'Apex millimeter observations of methanol emission toward high-mass star-forming cores', *The Astronomical Journal* **158**(1), 18.

Heyer, M., Wilson, G., Gutermuth, R., Lizano, S., Gomez-Ruiz, A., Kurtz, S., Luna, A., Serrano Bernal, E. & Schloerb, F. (2018), 'Early science with the large millimetre telescope: fragmentation of molecular clumps in the galaxy', *Monthly Notices of the Royal Astronomical Society* **473**(2), 2222–2233.

Hildebrand, R. H. (1983), 'The determination of cloud masses and dust characteristics from submillimetre thermal emission'.

Hill, T. L. (2006), Examining the evolutionary sequence of massive star formation, PhD thesis, UNSW Sydney.

Hirota, T., Bushimata, T., Choi, Y. K., Honma, M., Imai, H., Iwadate, K., Jike, T., Kameno, S., Kameya, O., Kamohara, R. et al. (2007), 'Distance to orion kl measured with vera', *Publications of the Astronomical Society of Japan* **59**(5), 897–903.

Hirota, T., Tsuboi, M., Kurono, Y., Fujisawa, K., Honma, M., Kim, M. K., Imai, H. & Yonekura, Y. (2014), 'Vera and alma observations of the h2o supermaser burst in orion kl', *Publications of the Astronomical Society of Japan* **66**(6), 106.

Hoare, M., Kurtz, S., Lizano, S., Keto, E. & Hofner, P. (2006), 'Ultra-compact h ii regions and the early lives of massive stars', *arXiv preprint astro-ph/0603560* .

Hoare, M., Kurtz, S., Lizano, S., Keto, E. & Hofner, P. (2007), 'Ultracompact hii regions and the early lives of massive stars', *Protostars and Planets V* **181**.

Högbom, J. (1974), 'Aperture synthesis with a non-regular distribution of interferometer baselines', *Astronomy and Astrophysics Supplement, Vol. 15, p. 417* **15**, 417.

Hu, B., Menten, K. M., Wu, Y., Bartkiewicz, A., Rygl, K., Reid, M. J., Urquhart, J. S. & Zheng, X. (2016), 'On the Relationship of UC HII Regions and Class II Methanol Masers. I. Source Catalogs', **833**(1), 18.

Hull, C. L. & Zhang, Q. (2019), 'Interferometric observations of magnetic fields in forming stars', *Frontiers in Astronomy and Space Sciences* **6**, 3.

Hunter, T., Brogan, C., Cyganowski, C. & Young, K. (2014), 'Subarcsecond imaging of the ngc 6334 i (n) protocluster: Two dozen compact sources and a massive disk candidate', *The Astrophysical Journal* **788**(2), 187.

Hunter, T. R., Brogan, C. L., MacLeod, G., Cyganowski, C. J., Chandler, C. J., Chibueze, J. O., Friesen, R., Indebetouw, R., Thesner, C. & Young, K. H. (2017), 'An extraordinary outburst in the massive protostellar system ngc 6334i-mm1: quadrupling of the millimeter continuum', *The Astrophysical Journal Letters* **837**(2), L29.

Impey, C. & Fraknoi, A. (2020), Key online resources for teaching astronomy, *in* 'Astronomy Education, Volume 2: Best practices for online learning environments', IOP Publishing.

Inayoshi, K., Sugiyama, K., Hosokawa, T., Motogi, K. & Tanaka, K. E. (2013), 'Direct diagnostics of forming massive stars: stellar pulsation and periodic variability of maser sources', *The Astrophysical Journal Letters* **769**(2), L20.

Jensen, L. (n.d.), 'The universe we see'.

Jijina, J. & Adams, F. C. (1995), 'Infall collapse solutions in the inner limit: Radiation pressure and its effects on star formation', *arXiv preprint astro-ph/9511095* .

Johnson, J. B. (1928), 'Thermal agitation of electricity in conductors', *Physical review* **32**(1), 97.

Jørgensen, J. K., Belloche, A. & Garrod, R. T. (2020), 'Astrochemistry during the formation of stars', *Annual Review of Astronomy and Astrophysics* **58**, 727–778.

Kahn, F. (1974), 'Cocoons around early-type stars', *Astronomy and Astrophysics* **37**, 149–162.

Kalenskii, S., Johansson, L. E., Bergman, P., Kurtz, S., Hofner, P., Walmsley, C. & Slysh, V. (2010), 'Search for class i methanol masers in low-mass star formation regions', *Monthly Notices of the Royal Astronomical Society* **405**(1), 613–620.

Karnik, A., Ghosh, S., Rengarajan, T. & Verma, R. (2001), 'Study of star formation in rcw 106 using far-infrared observations', *Monthly Notices of the Royal Astronomical Society* **326**(1), 293–302.

Keto, E. (2003), 'The formation of massive stars by accretion through trapped hypercompact h ii regions', *The Astrophysical Journal* **599**(2), 1196.

Kleiner, I. (2019), 'Spectroscopy of interstellar internal rotors: an important tool for investigating interstellar chemistry', *ACS Earth and Space Chemistry* **3**(9), 1812–1842.

Kooi, J. W. (2008), *Advanced receivers for submillimeter and far infrared astronomy*, Rijkuniversiteit Groningen.

Kraus, J. D. (1986), 'Radio astronomy, 2-nd ed', *Cygnus-Quasar Books, Powell, Ohio* pp. 7–12.

Krumholz, M. R. (2015), 'The formation of very massive stars', *Very Massive Stars in the Local Universe* pp. 43–75.

Krumholz, M. R., Klein, R. I. & McKee, C. F. (2005), 'Radiation pressure in massive star formation', *Proceedings of the International Astronomical Union* **1**(S227), 231–236.

Krumholz, M. R., Klein, R. I. & McKee, C. F. (2007), 'Radiation-hydrodynamic simulations of collapse and fragmentation in massive protostellar cores', *The Astrophysical Journal* **656**(2), 959.

Kuiper, R., Klahr, H., Beuther, H. & Henning, T. (2010), 'Circumventing the radiation pressure barrier in the formation of massive stars via disk accretion', *The Astrophysical Journal* **722**(2), 1556.

Kuiper, R., Klahr, H., Beuther, H. & Henning, T. (2014), A solution to the radiation pressure problem in the formation of massive stars, *in* 'The Labyrinth of Star Formation', Springer, pp. 379–383.

Kumar, V., Vig, S., Veena, V., Mohan, S., Ghosh, S., Tej, A. & Ojha, D. (2022), 'Investigating star-formation activity towards the southern h ii region rcw 42', *Monthly Notices of the Royal Astronomical Society* **515**(4), 5730–5742.

Kurtz, S. (2005), 'Hypercompact hii regions', *Proceedings of the International Astronomical Union* **1**(S227), 111–119.

Lada, C. J. (1999), The formation of low mass stars, *in* 'The Origin of Stars and Planetary Systems', Springer, pp. 143–192.

Lada, C. J. & Adams, F. C. (1992), 'Interpreting infrared color-color diagrams-circumstellar disks around low-and intermediate-mass young stellar objects', *The Astrophysical Journal* **393**, 278–288.

Lada, C. J. & Kylafis, N. D. (1999), *The origin of stars and planetary systems*, Vol. 540, Springer Science & Business Media.

Lada, C. J. & Lada, E. A. (2003), 'Embedded clusters in molecular clouds', *Annual Review of Astronomy and Astrophysics* **41**(1), 57–115.

Larson, R. B. (1978), 'Calculations of three-dimensional collapse and fragmentation', *Monthly Notices of the Royal Astronomical Society* **184**(1), 69–85.

Larson, R. B. (2003), 'The physics of star formation', *Reports on Progress in Physics* **66**(10), 1651.

Lekht, E., Mendoza-Torres, E. & Sorochenko, R. (1995), 'Time variations of h2o maser emission at w31a and w75s', *The Astrophysical Journal* **443**, 222–230.

Lenz, P. & Breger, M. (2004), 'Period04: A software package to extract multiple frequencies from real data', *Proceedings of the International Astronomical Union* **2004**(IAUS224), 786–790.

Leurini, S., Menten, K. & Walmsley, C. (2016), 'Physical characteristics of bright class i methanol masers', *Astronomy & Astrophysics* **592**, A31.

Li, J., Moscadelli, L., Cesaroni, R., Furuya, R., Xu, Y., Usuda, T., Menten, K., Pestalozzi, M., Elia, D. & Schisano, E. (2012), 'Massive star formation toward g28. 87+ 0.07 (iras 18411- 0338) investigated by means of maser kinematics and radio to infrared continuum observations', *The Astrophysical Journal* **749**(1), 47.

Lo, K. (2005), 'Mega-masers and galaxies', *Annu. Rev. Astron. Astrophys.* **43**, 625–676.

Longmore, S. N., Rathborne, J., Bastian, N., Alves, J., Ascenso, J., Bally, J., Testi, L., Longmore, A., Battersby, C., Bressert, E. et al. (2012), 'G0. 253+ 0.016: a molecular cloud progenitor of an arches-like cluster', *The Astrophysical Journal* **746**(2), 117.

MacLeod, G. C., Chibueze, J. O., Sanna, A., Paulsen, J. D., Houde, M., van den Heever, S. P. & Goedhart, S. (2021*a*), 'Systematic velocity drifts of methanol masers associated with G9.62+0.20E', **500**(3), 3425–3437.

MacLeod, G. C., Smits, D. P., Green, J. A. & van den Heever, S. P. (2021), 'Synchronized periodic maser flares of multiple OH and CH_3OH lines in G323.459-0.079', **502**(4), 5658–5667.

MacLeod, G. C., Sugiyama, K., Hunter, T. R., Quick, J., Baan, W., Breen, S. L., Brogan, C. L., Burns, R. A., Caratti o Garatti, A., Chen, X., Chibueze, J. O., Houde, M., Kaczmarek, J. F., Linz, H., Rajabi, F., Saito, Y., Schmidl, S., Sobolev, A. M., Stecklum, B., van den Heever, S. P. & Yonekura, Y. (2019), 'Detection of new methanol maser transitions associated with G358.93-0.03', **489**(3), 3981–3989.

MacLeod, G., Chibueze, J., Sanna, A., Paulsen, J., Houde, M., van den Heever, S. & Goedhart, S. (2021*b*), 'Systematic velocity drifts of methanol masers associated with g9. 62+ 0.20 e', *Monthly Notices of the Royal Astronomical Society* **500**(3), 3425–3437.

MacLeod, G. & Gaylard, M. (1996), 'Variable hydroxyl and methanol masers in g 351.78—0.54', *Monthly Notices of the Royal Astronomical Society* **280**(3), 868–876.

MacLeod, G., Smits, D., Goedhart, S., Hunter, T., Brogan, C., Chibueze, J., van den Heever, S., Thesner, C., Banda, P. & Paulsen, J. (2018), 'A masing event in ngc 6334i: contemporaneous flaring of hydroxyl, methanol, and water masers', *Monthly Notices of the Royal Astronomical Society* **478**(1), 1077–1092.

Madden, S., Irvine, W. M., Matthews, H., Brown, R. & Godfrey, P. (1986), 'New interstellar masers in nonmetastable ammonia', *The Astrophysical Journal* **300**, L79–L84.

Mangum, J. G., Darling, J., Henkel, C. & Menten, K. M. (2013), 'Formaldehyde densitometry of starburst galaxies: Density-independent global star formation', *The Astrophysical Journal* **766**(2), 108.

Mangum, J. G., Darling, J., Menten, K. M. & Henkel, C. (2008), 'Formaldehyde densitometry of starburst galaxies', *The Astrophysical Journal* **673**(2), 832.

Manna, A. & Pal, S. (2023), 'Detection of complex nitrogen-bearing molecule ethyl cyanide towards the hot molecular core g10. 47+ 0.03', *Astrophysics and Space Science* **368**(5), 44.

Martí, J., Rodríguez, L. F. & Torrelles, J. M. (1999), 'Cross-calibrated vla observations of h_2o maser and 1.3 cm continuum emission in iras 18162-2048 (= hh 80-81 irs)', *Astronomy and Astrophysics, v. 345, p. L5-L8 (1999)* **345**, L5–L8.

Maswanganye, J., Gaylard, M., Goedhart, S., Walt, D. v. d. & Booth, R. S. (2014), 'New periodic 6.7 ghz class ii methanol maser associated with g358. 460- 0.391', *Monthly Notices of the Royal Astronomical Society* **446**(3), 2730–2737.

Maswanganye, J., Gaylard, M., Goedhart, S., Walt, D. v. d. & Booth, R. S. (2015), 'New periodic 6.7 ghz class ii methanol maser associated with g358. 460- 0.391', *Monthly Notices of the Royal Astronomical Society* **446**(3), 2730–2737.

Maswanganye, J. P. (2017), 'An investigation into maser variability in high-mass star forming regions', *Ph. D. Thesis* .

Maswanganye, J. P. (2018), An investigation into maser variability in high-mass star forming regions, PhD thesis, North-West University.

Maswanganye, J. P. & Gaylard, M. J. (2012), 'The variability of cosmic methanol masers in massive star-forming regions', *Proceedings of the International Astronomical Union* **8**(S287), 108–109.

Matthews, H., Leech, J. & Friberg, P. (2004), Guide to spectral line observing at the jcmt, Technical report, Technical report, JAC.

Matveenko, L., Graham, D. & Diamond, P. (1988), 'The h2o maser flare region in the orion-kleinmann/orion-kl/nebula', *Soviet Astronomy Letters* **14**, 468.

McCarthy, T. P., Ellingsen, S. P., Voronkov, M. A. & Cimo, G. (2018), 'The relationship between class i and class ii methanol masers at high angular resolution', *Monthly Notices of the Royal Astronomical Society* **477**(1), 507–524.

McKee, C. F. & Ostriker, E. C. (2007), 'Theory of star formation', *Annu. Rev. Astron. Astrophys.* **45**, 565–687.

McKee, C. F. & Tan, J. C. (2003), 'The formation of massive stars from turbulent cores', *The Astrophysical Journal* **585**(2), 850.

McLaughlin, D. E. & Pudritz, R. E. (1997), 'Gravitational collapse and star formation in logotropic and nonisothermal spheres', *The Astrophysical Journal* **476**(2), 750.

Mélanie, C., Diederik, K. J., Vazquez-Semadeni, E., Fumitaka, N., Ralf, K., Ballesteros-Paredes, J., Shu-ichiro, I., Adamo, A. & Hennebelle, P. (2020), 'The molecular cloud lifecycle', *Space Science Reviews* **216**(4).

Menten, K. M. (1991*a*), 'The discovery of a new, very strong, and widespread interstellar methanol maser line', *The Astrophysical Journal* **380**, L75–L78.

Menten, K. M. (1991*b*), Methanol masers and submillimeter wavelength water masers in star-forming regions, *in* 'Atoms, Ions and Molecules: New Results in Spectral Line Astrophysics', Vol. 16, pp. 119–136.

Menten, K. M., Melnick, G. J., Phillips, T. G. & Neufeld, D. A. (1990), 'A new submillimeter water maser transition at 325 ghz', *Astrophysical Journal, Part 2-Letters (ISSN 0004-637X), vol. 363, Nov. 10, 1990, p. L27-L31.* **363**, L27–L31.

Menten, K., Reid, M., Pratap, P., Moran, J. & Wilson, T. (1992), 'Vlbi observations of the 6.7 ghz methanol masers toward w3 (oh)', *The Astrophysical Journal* **401**, L39–L42.

Metzger, B. D. (2010), 'Relic proto-stellar discs and the origin of luminous circumstellar interaction in core-collapse supernovae', *Monthly Notices of the Royal Astronomical Society* **409**(1), 284–304.

Miller, G. E. & Scalo, J. M. (1979), 'The initial mass function and stellar birthrate in the solar neighborhood', *The Astrophysical Journal Supplement Series* **41**, 513–547.

Minier, V., Booth, R. & Conway, J. (2000), 'Vlbi observations of 6.7 and 12.2 ghz methanol masers toward high mass star-forming regions. i. observational results: protostellar disks or outflows?', *Astronomy and Astrophysics* **362**, 1093–1108.

Minier, V., Burton, M., Hill, T., Pestalozzi, M., Purcell, C., Garay, G., Walsh, A. & Longmore, S. (2005), 'Star-forming protoclusters associated with methanol masers', *Astronomy & Astrophysics* **429**(3), 945–960.

Minier, V., Conway, J. & Booth, R. (2001), 'Vlbi observations of 6.7 and 12.2 ghz methanol masers toward high mass star-forming regions-ii. tracing massive protostars', *Astronomy & Astrophysics* **369**(1), 278–290.

Minier, V., Ellingsen, S., Norris, R. & Booth, R. (2003*a*), 'The protostellar mass limit for 6.7 ghz methanol masers-i. a low-mass yso survey', *Astronomy & Astrophysics* **403**(3), 1095–1100.

Minier, V., Ellingsen, S. P., Norris, R. P. & Booth, R. S. (2003*b*), 'The protostellar mass limit for 6.7 GHz methanol masers. I. A low-mass YSO survey', **403**, 1095–1100.

Mohamed, D. S. (2022), On the relation between cosmic masers and massive star-forming regions, *in* '2022 39th National Radio Science Conference (NRSC)', Vol. 1, IEEE, pp. 354–360.

Montmerle, T. & Townsley, L. (2012), 'Charge exchange in massive star-forming regions'.

Morison, I. (2013), *Introduction to astronomy and cosmology*, John Wiley & Sons.

Moscadelli, L. & Catarzi, M. (1996), 'Time variability of five strong 12 ghz methanol masers', *Astronomy and Astrophysics Supplement Series* **116**(2), 211–238.

Motogi, K., Sorai, K., Honma, M., Minamidani, T., Takekoshi, T., Akiyama, K., Tateuchi, K., Hosaka, K., Ohishi, Y., Watanabe, Y. et al. (2011), 'Intermittent maser flare around the high-mass young stellar object g353. 273+ 0.641–i. data and overview', *Monthly Notices of the Royal Astronomical Society* **417**(1), 238–249.

Motte, F., André, P. & Neri, R. (1998), 'The initial conditions of star formation in the rho ophiuchi main cloud: wide-field millimeter continuum mapping', *Astronomy and Astrophysics, v. 336, p. 150-172 (1998)* **336**, 150–172.

Motte, F., Bontemps, S. & Louvet, F. (2018), 'High-mass star and massive cluster formation in the milky way', *Annual Review of Astronomy and Astrophysics* **56**, 41–82.

Müller, H. S., Schlöder, F., Stutzki, J. & Winnewisser, G. (2005), 'The cologne database for molecular spectroscopy, cdms: a useful tool for astronomers and spectroscopists', *Journal of Molecular Structure* **742**(1-3), 215–227.

Murphy, T., Cohen, M., Ekers, R. D., Green, A. J., Wark, R. M. & Moss, V. (2010), 'Ultra-and hyper-compact h ii regions at 20 ghz', *Monthly Notices of the Royal Astronomical Society* **405**(3), 1560–1572.

Mutie, M., Chibueze, J., El Bouchefry, K., MacLeod, G., Morgan, J. & Baki, P. (2021), 'Massive protocluster of a periodic maser source g188. 95+ 0.89', *Monthly Notices of the Royal Astronomical Society* .

Mutie, M. M., Baki, P., Chibueze, J. O. & El Bouchefry, K. (2019), '14 years of 6.7 ghz periodic methanol maser observations towards g188. 95+ 0.89', *Proceedings of the International Astronomical Union* **15**(S356), 393–394.

Myers, P. (2000), 'Growth of an initial mass function cluster in a turbulent dense core', *The Astrophysical Journal* **530**(2), L119.

Norman, C. & Silk, J. (1980), 'Clumpy molecular clouds-a dynamic model self-consistently regulated by t tauri star formation', *The Astrophysical Journal* **238**, 158–174.

Norris, R., Byleveld, S., Diamond, P., Ellingsen, S., Ferris, R., Gough, R., Kesteven, M., McCulloch, P., Phillips, C., Reynolds, J. et al. (1998), 'Methanol masers as tracers of circumstellar disks', *The Astrophysical Journal* **508**(1), 275.

Norris, R., Whiteoak, J., Caswell, J. & Wieringa, M. (1993), Synthesis images of 6.7-ghz methanol masers, *in* 'Astrophysical Masers', Springer, pp. 203–206.

Ntormousi, E. & Hennebelle, P. (2019), 'Core and stellar mass functions in massive collapsing filaments', *Astronomy & Astrophysics* **625**, A82.

Nyquist, H. (1928), 'Thermal agitation of electric charge in conductors', *Physical review* **32**(1), 110.

Öberg, K. I., Guzmán, V. V., Walsh, C., Aikawa, Y., Bergin, E. A., Law, C. J., Loomis, R. A., Alarcón, F., Andrews, S. M., Bae, J. et al. (2021), 'Molecules with alma at planet-forming scales (maps). i. program overview and highlights', *The Astrophysical Journal Supplement Series* **257**(1), 1.

Oh, C. S., Kobayashi, H., Honma, M., Hirota, T., Sato, K. & Ueno, Y. (2010), 'Vera observations of ho maser sources in three massive star-forming regions and galactic rotation measurements', *Publications of the Astronomical Society of Japan* **62**(1), 101–114.

Olech, M., Szymczak, M., Wolak, P., Gérard, E. & Bartkiewicz, A. (2020), 'Long-term multi-frequency maser observations of the intermediate-mass young stellar object g107. 298+ 5.639', *Astronomy & Astrophysics* **634**, A41.

Oliveira, J. M. (2008), 'Star formation in the eagle nebula', *arXiv preprint arXiv:0809.3735* .

Omodaka, T., Maeda, T., Miyoshi, M., Okudaira, A., Nishio, M., Miyaji, T., Motiduki, N., Morimoto, M., Kobayashi, H. & Sasao, T. (1999), 'The enormous outburst of the 7.9 km s-1 water-maser feature in orion kl', *Publications of the Astronomical Society of Japan* **51**(3), 333–336.

Ott, M., Witzel, A., Quirrenbach, A., Krichbaum, T., Standke, K., Schalinski, C. & Hummel, C. (1994), 'An updated list of radio flux density calibrators', *Astronomy and Astrophysics* **284**, 331–339.

Otto, S. & Gaylard, M. J. (2012), 'Chasing the flare in orion kl: Observations of the 22 ghz h2o masers at hartrao', *International Astronomical Union. Proceedings of the International Astronomical Union* **8**(S287), 110.

Palau, A., Walsh, C., Sánchez-Monge, Á., Girart, J. M., Cesaroni, R., Jiménez-Serra, I., Fuente, A., Zapata, L. A. & Neri, R. (2017), 'Complex organic molecules tracing shocks along the outflow cavity in the high-mass protostar iras 20126+ 4104', *Monthly Notices of the Royal Astronomical Society* **467**(3), 2723–2752.

Palla, F. & Stahler, S. W. (1993), 'The pre-main-sequence evolution of intermediate-mass stars', *The Astrophysical Journal* **418**, 414.

Pandian, J. (2006), '6.7 ghz methanol masers: Properties, associations and tracers of galactic structure'.

Pandian, J. D., Baker, L., Cortes, G., Goldsmith, P. F., Deshpande, A. A., Ganesan, R., Hagen, J., Locke, L., Wadefalk, N. & Weinreb, S. (2006), 'Low-noise 6-8 ghz receiver', *IEEE Microwave Magazine* **7**(6), 74–84.

Parfenov, S. Y. & Sobolev, A. (2014), 'On the class ii methanol maser periodic variability due to the rotating spiral shocks in the gaps of discs around young binary stars', *Monthly Notices of the Royal Astronomical Society* **444**(1), 620–628.

Parker, E. (1966), 'The dynamical state of the interstellar gas and field', *The Astrophysical Journal* **145**, 811.

Perkins, F., Gold, T. & Salpeter, E. (1966), 'Maser action in interstellar oh', *The Astrophysical Journal* **145**, 361.

Pestalozzi, M., Minier, V. & Booth, R. (2005), 'A general catalogue of 6.7-ghz methanol masers-i. data', *Astronomy & Astrophysics* **432**(2), 737–742.

Peters, T., Banerjee, R., Klessen, R. S., Mac Low, M.-M., Galván-Madrid, R. & Keto, E. R. (2010), 'H ii regions: Witnesses to massive star formation', *The Astrophysical Journal* **711**(2), 1017.

Phillips, C., Norris, R., Ellingsen, S. & McCulloch, P. (1998), 'Methanol masers and their environment at high resolution', *Monthly Notices of the Royal Astronomical Society* **300**(4), 1131–1157.

Phillips, C. & van Langevelde, H. J. (2005), The extended methanol maser emission in w51, *in* 'Future Directions in High Resolution Astronomy', Vol. 340, p. 342.

Pihlström, Y., Sjouwerman, L., Frail, D., Claussen, M., Mesler, R. & McEwen, B. (2014), 'Detection of class i methanol (ch3oh) maser candidates in supernova remnants', *The Astronomical Journal* **147**(4), 73.

Pillai, T., Kauffmann, J., Tan, J. C., Goldsmith, P. F., Carey, S. J. & Menten, K. M. (2015), 'Magnetic fields in high-mass infrared dark clouds', *The Astrophysical Journal* **799**(1), 74.

Pillai, T., Kauffmann, J., Zhang, Q., Sanhueza, P., Leurini, S., Wang, K., Sridharan, T. & König, C. (2019), 'Massive and low-mass protostars in massive "starless" cores', *Astronomy & Astrophysics* **622**, A54.

Poglitsch, A., Waelkens, C., Geis, N., Feuchtgruber, H., Vandenbussche, B., Rodriguez, L., Krause, O., Renotte, E., Van Hoof, C., Saraceno, P. et al. (2010), 'The photodetector array camera and spectrometer (pacs) on the herschel space observatory', *Astronomy & astrophysics* **518**, L2.

Povich, M. S., Stone, J. M., Churchwell, E., Zweibel, E. G., Wolfire, M. G., Babler, B. L., Indebetouw, R., Meade, M. R. & Whitney, B. A. (2007), 'A multiwavelength study of m17: the spectral energy distribution and pah emission morphology of a massive star formation region', *The Astrophysical Journal* **660**(1), 346.

Pratap, P., Menten, K. M. & Snyder, L. E. (1994), 'Detection of formaldehyde maser emission near the ultracompact h ll region g29. 96-0.02', *The Astrophysical Journal* **430**, L129–L132.

Price, S. D., Egan, M. P., Carey, S. J., Mizuno, D. R. & Kuchar, T. A. (2001), 'Midcourse space experiment survey of the galactic plane', *The Astronomical Journal* **121**(5), 2819.

Proven-Adzri, E., MacLeod, G., Heever, S. v. d., Hoare, M., Kuditcher, A. & Goedhart, S. (2019), 'Discovery of periodic methanol masers associated with g323. 46-0.08', *Monthly Notices of the Royal Astronomical Society* **487**(2), 2407–2411.

Rana, N. C. (1987), 'Mass function of stars in the solar neighbourhood', *Astronomy and Astrophysics* **184**, 104–118.

Rathborne, J., Jackson, J., Zhang, Q. & Simon, R. (2008), 'Submillimeter array observations of infrared dark clouds: a tale of two cores', *The Astrophysical Journal* **689**(2), 1141.

Rathborne, J. M., Jackson, J. & Simon, R. (2006), 'Infrared dark clouds: precursors to star clusters', *The Astrophysical Journal* **641**(1), 389.

Reid, M. J. & Moran, J. M. (1981), 'Masers', *Annual review of astronomy and astrophysics* **19**(1), 231–276.

Reid, M. J. & Moran, J. M. (1988), Astronomical masers, *in* 'Galactic and extragalactic radio astronomy', Springer, pp. 255–294.

Reid, M., Menten, K., Brunthaler, A., Zheng, X., Moscadelli, L. & Xu, Y. (2009), 'Trigonometric parallaxes of massive star-forming regions. i. s 252 & g232. 6+ 1.0', *The Astrophysical Journal* **693**(1), 397.

Reipurth, B., Jewitt, D. & Keil, K. (2007), *Protostars and Planets V*, University of Arizona Press.

Retes-Romero, R., Mayya, Y., Luna, A. & Carrasco, L. (2020), 'Infrared dark clouds and high-mass star formation activity in galactic molecular clouds', *The Astrophysical Journal* **897**(1), 53.

Rivera-Ingraham, A., Ade, P. A., Bock, J. J., Chapin, E. L., Devlin, M. J., Dicker, S. R., Griffin, M., Gundersen, J. O., Halpern, M., Hargrave, P. C. et al. (2010), 'The blast view of the star-forming region in aquila (= 45°, b= 0°)', *The Astrophysical Journal* **723**(1), 915.

Rivilla, V., Beltrán, M., Vasyunin, A., Caselli, P., Viti, S., Fontani, F. & Cesaroni, R. (2019), 'First alma maps of hco, an important precursor of complex organic molecules, towards iras 16293–2422', *Monthly Notices of the Royal Astronomical Society* **483**(1), 806–823.

Rodríguez-Garza, C. B., Kurtz, S. E., Gómez-Ruiz, A. I., Hofner, P., Araya, E. D. & Kalenskii, S. V. (2017), 'A catalog of 44 ghz methanol masers in massive star-forming regions. iv. the high-mass protostellar object sample', *The Astrophysical Journal Supplement Series* **233**(1), 4.

Russeil, D., Schneider, N., Anderson, L., Zavagno, A., Molinari, S., Persi, P., Bontemps, S., Motte, F., Ossenkopf, V., André, P. et al. (2013), 'The herschel view of the massive star-forming region ngc 6334', *Astronomy & Astrophysics* **554**, A42.

Ryle, M., Hewish, A. & Shakeshaft, J. (1959), 'The synthesis of large radio telescopes by the use of radio interferometers', *IRE Transactions on Antennas and Propagation* **7**(5), 120–124.

Sakai, T., Yanagida, T., Furuya, K., Aikawa, Y., Sanhueza, P., Sakai, N., Hirota, T., Jackson, J. M. & Yamamoto, S. (2018), 'Alma observations of the irdc clump g34. 43+ 00.24 mm3: complex organic and deuterated molecules', *The Astrophysical Journal* **857**(1), 35.

Salpeter, E. E. (1955), 'The luminosity function and stellar evolution.', *The Astrophysical Journal* **121**, 161.

Sanna, A., Menten, K., Carrasco-González, C., Reid, M., Ellingsen, S., Brunthaler, A., Moscadelli, L., Cesaroni, R. & Krishnan, V. (2015), 'The environment of the strongest galactic methanol maser', *The Astrophysical Journal Letters* **804**(1), L2.

Scargle, J. D. (1982), 'Studies in astronomical time series analysis. II - Statistical aspects of spectral analysis of unevenly spaced data', **263**, 835–853.

Schisano, E., Molinari, S., Elia, D., Benedettini, M., Olmi, L., Pezzuto, S., Traficante, A., Brescia, M., Cavuoti, S., Di Giorgio, A. et al. (2020), 'The hi-gal catalogue of dusty filamentary structures in the galactic plane', *Monthly Notices of the Royal Astronomical Society* **492**(4), 5420–5456.

Seidu, M. (2020), Variability of methanol and OH masers associated with the star forming region G339. 62-0.12, PhD thesis, North-West University (South Africa).

Seidu, M., Goedhart, S. & van der Walt, D. (2022), 'Variability of methanol and oh masers in g339. 62- 0.12', *Monthly Notices of the Royal Astronomical Society* **511**(4), 5428–5435.

Shimajiri, Y., André, P., Braine, J., Könyves, V., Schneider, N., Bontemps, S., Ladjelate, B., Roy, A., Gao, Y. & Chen, H. (2017), 'Testing the universality of the star-formation efficiency in dense molecular gas', *Astronomy & Astrophysics* **604**, A74.

Shimajiri, Y., Takahashi, S., Takakuwa, S., Saito, M. & Kawabe, R. (2008), 'Millimeter-and submillimeter-wave observations of the omc-2/3 region. ii. observational evidence for outflow-triggered star formation in the omc-2 fir 3/4 region', *The Astrophysical Journal* **683**(1), 255.

Shimonishi, T., Izumi, N., Furuya, K. & Yasui, C. (2021), 'The detection of a hot molecular core in the extreme outer galaxy', *The Astrophysical Journal* **922**(2), 206.

Shu, F. H., Adams, F. C. & Lizano, S. (1987), 'Star formation in molecular clouds: observation and theory', *Annual review of astronomy and astrophysics* **25**(1), 23–81.

Silva, A., Zhang, Q., Sanhueza, P., Lu, X., Beltran, M. T., Fallscheer, C., Beuther, H., Sridharan, T. & Cesaroni, R. (2017), 'Sma observations of the hot molecular core iras 18566+ 0408', *The Astrophysical Journal* **847**(2), 87.

Slysh, V., Kalenskii, S. & Val'Tts, I. (1995), 'Detection of a series of methanol maser lines at 1.9 millimeter wavelength', *The Astrophysical Journal* **442**, 668–673.

Smith, R. C. (1995), *Observational astrophysics*, Cambridge University Press.

Snyder, L. & Buhl, D. (1974), 'Detection of possible maser emission near 3.48 millimeters from an unidentified molecular species in orion', *The Astrophysical Journal* **189**, L31–L33.

Snyder, L. & Buhl, D. (1975), 'Detection of new stellar sources of vibrationally excited silicon monoxide maser emission at 6.95 millimeters', *The Astrophysical Journal* **197**, 329–340.

Sobolev, A., Cragg, D., Ellingsen, S., Gaylard, M. J., Goedhart, S., Henkel, C., Kirsanova, M., Ostrovskii, A., Pankratova, N., Shelemei, O. et al. (2007), 'How do methanol masers manage to appear in the youngest star vicinities and isolated molecular clumps?', *Proceedings of the International Astronomical Union* **3**(S242), 81–88.

Sobolev, A., Cragg, D. & Godfrey, P. (1997), 'Pumping of class ii methanol masers. ii. the 5_1_-6_0_aˆ+ˆ transition.', *Astronomy and Astrophysics* **324**, 211–220.

Spitzer Jr, L. (1978), 'Review of publications: Physical processes in the interstellar medium', *Journal of the Royal Astronomical Society of Canada* **72**, 349.

Sridharan, T., Beuther, H., Schilke, P., Menten, K. & Wyrowski, F. (2002), 'High-mass protostellar candidates. i. the sample and initial results', *The Astrophysical Journal* **566**(2), 931.

Stahler, S. & Palla, F. (2004), 'The formation of stars. 2005', *Cited on* p. 30.

Stahler, S. W. & Palla, F. (2008), *The formation of stars*, John Wiley & Sons.

Sugiyama, K., Fujisawa, K., Doi, A., Honma, M., Isono, Y., Kobayashi, H., Mochizuki, N. & Murata, Y. (2008), 'A synchronized variation of the 6.7 ghz methanol maser in cepheus a', *Publications of the Astronomical Society of Japan* **60**(5), 1001–1006.

Sugiyama, K., Nagase, K., Yonekura, Y., Momose, M., Yasui, Y., Saito, Y., Motogi, K., Honma, M., Hachisuka, K., Matsumoto, N. et al. (2017), 'The shortest periodic

and flaring flux variability of a methanol maser emission at 6.7 ghz in g 014.23-00.50', *Publications of the Astronomical Society of Japan* **69**(4).

Sugiyama, K., Saito, Y., Yonekura, Y. & Momose, M. (2019), 'Bursting activity of the 6.668-ghz ch3oh maser detected in g 358.93-00.03 using the hitachi 32-m', *The Astronomer's Telegram* **12446**, 1.

Suri, S., Beuther, H., Gieser, C., Ahmadi, A., Sánchez-Monge, Á., Winters, J., Linz, H., Henning, T., Beltrán, M., Bosco, F. et al. (2021), 'Disk fragmentation in high-mass star formation-high-resolution observations towards afgl 2591-vla 3', *Astronomy & Astrophysics* **655**, A84.

Sutton, E., Sobolev, A., Salii, S., Malyshev, A., Ostrovskii, A. & Zinchenko, I. (2004), 'Methanol in w3 (h2o) and surrounding regions', *The Astrophysical Journal* **609**(1), 231.

Svoboda, B. E., Shirley, Y. L., Traficante, A., Battersby, C., Fuller, G. A., Zhang, Q., Beuther, H., Peretto, N., Brogan, C. & Hunter, T. (2019), 'Alma observations of fragmentation, substructure, and protostars in high-mass starless clump candidates', *The Astrophysical Journal* **886**(1), 36.

Sytov, A. Y., Bisikalo, D., Kaigorodov, P. & Boyarchuk, A. (2009), 'Observational manifestations of the common envelope in a close binary', *Astronomy reports* **53**, 428–435.

Szymczak, M., Hrynek, G. & Kus, A. (2000*a*), 'A survey of the 6.7 ghz methanol maser emission from iras sources-i. data', *Astronomy and Astrophysics Supplement Series* **143**(2), 269–301.

Szymczak, M., Hrynek, G. & Kus, A. J. (2000*b*), 'A survey of the 6.7 GHz methanol maser emission from IRAS sources. I. Data', **143**, 269–301.

Szymczak, M., Kus, A., Hrynek, G., Kepa, A. & Pazderski, E. (2002), '6.7 ghz methanol masers at sites of star formation-a blind survey of the galactic plane between 20° 40° and 052', *Astronomy & Astrophysics* **392**(1), 277–286.

Szymczak, M., Olech, M., Sarniak, R., Wolak, P. & Bartkiewicz, A. (2018), 'Monitoring observations of 6.7 ghz methanol masers', *Monthly Notices of the Royal Astronomical Society* **474**(1), 219–253.

Szymczak, M., Olech, M., Wolak, P., Bartkiewicz, A. & Gawroński, M. (2016), 'Discovery of periodic and alternating flares of the methanol and water masers in g107. 298+ 5.639', *Monthly Notices of the Royal Astronomical Society: Letters* **459**(1), L56–L60.

Szymczak, M., Wolak, P. & Bartkiewicz, A. (2014), '6.7 GHz methanol maser variability in Cepheus A', **439**(1), 407–415.

Szymczak, M., Wolak, P. & Bartkiewicz, A. (2015), 'Discovery of four periodic methanol masers and updated light curve for a further one', *Monthly Notices of the Royal Astronomical Society* **448**(3), 2284–2293.

Szymczak, M., Wolak, P., Bartkiewicz, A. & van Langevelde, H. (2011), 'Periodic variability of 6.7 ghz methanol masers in g22. 357+ 0.066', *Astronomy & Astrophysics* **531**, L3.

Tan, J. C. (2005), 'Clustered massive star formation in molecular clouds', *Proceedings of the International Astronomical Union* **1**(S227), 318–327.

Tan, J. C., Beltrán, M. T., Caselli, P., Fontani, F., Fuente, A., Krumholz, M. R., McKee, C. F. & Stolte, A. (2014), 'Massive star formation', *Protostars and Planets VI* **149**.

Tarchi, A., Reid, M. J. & Castangia, P. (2018), *Astrophysical Masers (IAU S336): Unlocking the Mysteries of the Universe*, Vol. 336, Cambridge University Press.

Taylor, J. (1997), 'An introduction to error analysis: The study of uncertainties in physical measurements, univ', *Science, Sausalito, CA* **45**, 92.

ter Haar D. (1967), 'The old quantum theory', *Pergamon Pres,Pergamon Pres* **18**, 167.

Terrile, R. (2017), 'Science mission directorate overview'.

Testi, L. & Sargent, A. I. (1998), 'Star formation in clusters: A survey of compact millimeter-wave sources in the serpens core', *The Astrophysical Journal Letters* **508**(1), L91.

Thompson, A. R., Moran, J. M. & Swenson, G. W. (2017), Van cittert–zernike theorem, spatial coherence, and scattering, *in* 'Interferometry and synthesis in radio astronomy', Springer, pp. 767–786.

Tielens, A. G. (2005), *The physics and chemistry of the interstellar medium*, Cambridge University Press.

Tohline, J. E. (1982), 'Hydrodynamic collapse', *Fundamentals of cosmic physics* **8**, 1–82.

Toomre, A. (1964), 'On the gravitational stability of a disk of stars', *The Astrophysical Journal* **139**, 1217–1238.

Torrelles, J., Patel, N., Curiel, S., Estalella, R., Gómez, J., Rodríguez, L., Cantó, J., Anglada, G., Vlemmings, W., Garay, G. et al. (2010), 'A wide-angle outflow with the simultaneous presence of a high-velocity jet in the high-mass cepheus a hw2 system', *Monthly Notices of the Royal Astronomical Society* **410**(1), 627–640.

Torrelles, J., Patel, N., Gómez, J., Anglada, G. & Uscanga, L. (2005), Vlbi water maser proper motion measurements in star-forming regions, *in* 'Dense Molecular Gas Around Protostars and in Galactic Nuclei', Springer, pp. 53–63.

Urquhart, J., Hoare, M. G., Lumsden, S. L., Oudmaijer, R. D., Moore, T. J., Brook, P., Mottram, J. C., Davies, B. & Stead, J. J. (2009), 'The rms survey-h2o masers towards a sample of southern hemisphere massive yso candidates and ultra compact hii regions', *Astronomy & Astrophysics* **507**(2), 795–802.

Urquhart, J., Moore, T. J., Hoare, M. G., Lumsden, S. L., Oudmaijer, R. D., Rathborne, J., Mottram, J. C., Davies, B. & Stead, J. J. (2011), 'The red msx source survey: distribution and properties of a sample of massive young stars', *Monthly Notices of the Royal Astronomical Society* **410**(2), 1237–1250.

Urquhart, J., Thompson, M., Morgan, L. & White, G. J. (2004), 'High-mass star formation within the bright-rimmed cloud sfo 79', *Astronomy & Astrophysics* **428**(3), 723–739.

Val'Tts, I., Ellingsen, S., Slysh, V., Kalenskii, S., Otrupcek, R. & Voronkov, M. (1999), 'Detection of new sources of methanol emission at 107 and 108 ghz with the mopra telescope', *Monthly Notices of the Royal Astronomical Society* **310**(4), 1077–1086.

van der Tak, F. F., Boonman, A., Braakman, R. & van Dishoeck, E. F. (2003), 'Sulphur chemistry in the envelopes of massive young stars', *Astronomy & Astrophysics* **412**(1), 133–145.

Van der Tak, F. & Menten, K. (2005), 'Very compact radio emission from high-mass protostars-ii. dust disks and ionized accretion flows', *Astronomy & Astrophysics* **437**(3), 947–956.

Van der Walt, D. (2014), 'Pumping of the 4.8 ghz h2co masers and its implications for the periodic masers in g37. 55+ 0.20', *Astronomy & Astrophysics* **562**, A68.

Van der Walt, D., De Villiers, H. & Czanik, R. (2012), 'A near-infrared study of the star-forming region rcw 34', *The Astronomical Journal* **144**(1), 13.

Van Der Walt, D., Goedhart, S. & Gaylard, M. (2009), 'Periodic class ii methanol masers in g9. 62+ 0.20 e', *Monthly Notices of the Royal Astronomical Society* **398**(2), 961–970.

Van der Walt, D. J. (2011), 'On the methanol masers in g9. 62+ 0.20 e and g188. 95+ 0.89', *The Astronomical Journal* **141**(5), 152.

Van Der Walt, D., Retief, S., Gaylard, M. & MacLeod, G. (1996), 'A search for 5 1–6 0 a+-methanol masers towards faint iras sources', *Monthly Notices of the Royal Astronomical Society* **282**(3), 1085–1095.

van Der Walt, J. (2005), 'On the number and lifetime of 6.7-ghz methanol masers', *Monthly Notices of the Royal Astronomical Society* **360**(1), 153–158.

Vink, J. (2020), *Physics and Evolution of Supernova Remnants*, Springer.

Voronkov, M., Caswell, J., Ellingsen, S., Green, J. & Breen, S. (2014), 'Southern class i methanol masers at 36 and 44 ghz', *Monthly Notices of the Royal Astronomical Society* **439**(3), 2584–2617.

Voronkov, M., Caswell, J., Ellingsen, S. & Sobolev, A. (2010), 'New 9.9-ghz methanol masers', *Monthly Notices of the Royal Astronomical Society* **405**(4), 2471–2484.

Vorster, J. M., Chibueze, J. O. & Hirota, T. (2021), Spatio-kinematics of the massive star forming region ngc6334i during an episodic accretion event, *in* 'South African Institute of Physics Conference at Potchefstroom', p. E1.

Walsh, A., Hyland, A., Robinson, G. & Burton, M. (1997), 'Studies of ultracompact h ii regions—i. methanol maser survey of iras-selected sources', *Monthly Notices of the Royal Astronomical Society* **291**(2), 261–278.

Waters, J., Kakar, R., Kuiper, T., Roscoe, H., Swanson, P., Rodriguez Kuiper, E., Kerr, A., Thaddeus, P. & Gustincic, J. (1980), 'Observations of interstellar h2o emission at 183 gigahertz', *Astrophysical Journal, Part 1, vol. 235, Jan. 1, 1980, p. 57-62.* **235**, 57–62.

Weaver, H., Williams, D. R., Dieter, N. & Lum, W. (1965), 'Observations of a strong unidentified microwave line and of emission from the oh molecule', *Nature* **208**(5005), 29.

Weingartner, J. C. & Draine, B. (2001), 'Dust grain-size distributions and extinction in the milky way, large magellanic cloud, and small magellanic cloud', *The Astrophysical Journal* **548**(1), 296.

Williams, J., Blitz, L., McKee, C., Mannings, V., Boss, A. & Russell, S. (2000), 'Protostars and planets iv'.

Wilson, T., Hüttemeister, S., Dahmen, G. & Henkel, C. (1993), 'Three transitions of methanol at 1 cm wavelength', *Astronomy and Astrophysics* **268**, 249–254.

Wilson, T., Walmsley, C., Menten, K. & Hermsen, W. (1985), 'The discovery of a new masering transition of interstellar methanol', *Astronomy and Astrophysics* **147**, L19–L22.

Wilson, T., Walmsley, C., Snyder, L. & Jewell, P. (1984), 'Detection of a new type of methanol maser', *Astronomy and Astrophysics* **134**, L7–L10.

Wood, D. O. & Churchwell, E. (1989*a*), 'Massive stars embedded in molecular clouds-their population and distribution in the galaxy', *The Astrophysical Journal* **340**, 265–272.

Wood, D. O. & Churchwell, E. (1989*b*), 'The morphologies and physical properties of ultracompact h ii regions', *The Astrophysical Journal Supplement Series* **69**, 831–895.

Wootten, A. (2001), 'Science with the atacama large millimeter array', *Science with the Atacama Large Millimeter Array* **235**.

Yanagida, T., Sakai, T., Hirota, T., Sakai, N., Foster, J. B., Sanhueza, P., Jackson, J. M., Furuya, K., Aikawa, Y. & Yamamoto, S. (2014), 'Alma observations of the irdc clump g34. 43+ 00.24 mm3: 278 ghz class i methanol masers', *The Astrophysical Journal Letters* **794**(1), L10.

Yoo, H., Kim, K.-T., Cho, J., Choi, M., Wu, J., Evans, N. J. & Ziurys, L. (2018), 'Inflow motions associated with high-mass protostellar objects', *The Astrophysical Journal Supplement Series* **235**(2), 31.

Yorke, H. W. & Sonnhalter, C. (2002), 'On the formation of massive stars', *The Astrophysical Journal* **569**(2), 846.

Zainol, F. D. (2021), Delving into massive stars: the colliding wind binaries, relations and various interferometric radio observations, PhD thesis, University of Birmingham.

Zapata, L. A., Ho, P. T., Rodríguez, L. F., O'Dell, C., Zhang, Q. & Muench, A. (2006), 'Silicon monoxide observations reveal a cluster of hidden compact outflows in the omc 1 south region', *The Astrophysical Journal* **653**(1), 398.

Zernike, F. (1938), 'The concept of degree of coherence and its application to optical problems', *Physica* **5**(8), 785–795.

Zhang, Q., Ho, P. T. & Ohashi, N. (1998), 'Dynamical collapse in w51 massive cores: Cs (3-2) and ch3cn observations', *The Astrophysical Journal* **494**(2), 636.

Zhang, Q., Hunter, T., Brand, J., Sridharan, T., Molinari, S., Kramer, M. & Cesaroni, R. (2001), 'Search for co outflows toward a sample of 69 high-mass protostellar candidates: Frequency of occurrence', *The Astrophysical Journal Letters* **552**(2), L167.

Zhang, Y., Tan, J. C. & McKee, C. F. (2013), 'Radiation transfer of models of massive star formation. ii. effects of the outflow', *The Astrophysical Journal* **766**(2), 86.

Zinnecker, H. & Yorke, H. W. (2007), 'Toward understanding massive star formation', *Annu. Rev. Astron. Astrophys.* **45**, 481–563.

APPENDIX A

APPENDICES

A.1 FUNDAMENTALS OF A SINGLE DISH RADIO TELESCOPE

A.1.1 Single Dish Radio Telescope

The radio waves can be linearly, elliptically or circularly polarised. Astronomical radio waves are either emitted by thermal, e.g. all objects with temperatures above zero Kelvin radiate blackbody energy, or non-thermal, e.g. maser emission, processes. The radio waves emitted by astronomical objects in space can be measured here on Earth by a radio telescope. In an ideal case, a radio telescope measures the noise power per bandwidth of a single-mode transmission line of a blackbody with temperature T which can be expressed as shown by Burke et al. (2019), Johnson (1928), Nyquist (1928).

Since radio waves are electromagnetic waves, the electric and magnetic fields of a propagating plane wave must be parallel to one another and the direction of propagation. The radio waves can be unpolarised, partially polarised, or fully polarised. Their polarisations are characterised by the Stokes parameters (Kraus 1986, Burke et al. 2019). The radio waves can be linearly, elliptically or circularly polarised. Astronomical radio waves are either emitted by thermal, e.g. all objects with temperatures above zero Kelvin radiate blackbody energy, or non-thermal, e.g. maser emission, processes. The radio waves emitted by astronomical objects in space can be measured here on Earth by a radio telescope. The noise power per bandwidth can be expressed as:

$$P_n = \frac{hv}{\frac{hv}{e^{K_B T_A} - 1}} \tag{A.1}$$

for the Rayleigh-Jeans approximation,

$P_n = K_B T_A$

where T_A is the temperature which a resistor would have had if it was to generate the same power per unit bandwidth from the voltage measured by the antenna. Note that T_A is not related to the receiver temperature. Equation A.1, called the Johnson-Nyquist (Johnson 1928, Nyquist 1928) formula, shows that the radio telescope measures the temperature of radio astronomical objects. The Johnson-Nyquist formula relates to the power of the resistor placed in the thermal bath. The power per unit bandwidth received from an unpolarised radio astronomical source (or black-

body radiation) subtended by the solid angle ω per polarisation unit is (Burke et al. 2019, Condon & Ransom 2016, Kraus 1986).

$$P_n = \frac{1}{2}A_e = \int\int B(\theta,\phi)P(\theta,\phi)d\Omega \tag{A.2}$$

where A_e , $B(\theta,\phi)$ and $P(\theta,\phi)$ are respectively the effective area of the radio telescope, Planck's blackbody intensity at the brightness temperature T_{br} (temperature of the source if it was a black-body) and the normalised telescope power pattern. For the 26m HartRAO radio telescope, $A_g = \pi\frac{D^2}{2} \sim 1030m^2$ using D as given in Table 3.1.

The Planck blackbody intensity at the brightness temperature T_{br} in radio astronomy is given by the Rayleigh-Jeans approximation, where $\frac{h\nu}{K_B T_{br}} << 1$, which implies that the Planck function of the blackbody radiator in equation A.3 will be:

$$B_v(T_{br}) = \frac{2k_B T_{br}\nu_2}{c^2} \tag{A.3}$$

the vacuum speed of light is denoted by the symbol "c." The observed flux density S_o, in Jy, of the brightness of the radio source is approximated by the Planck function of the blackbody radiation and is given by:

The Planck blackbody intensity at the brightness temperature T_{br} in radio

$$S_o = \int_{\Omega o} B(\theta,\phi)d\Omega = \frac{2K_B}{\lambda^2}\int_{\Omega_s} T_{br}(\theta,\phi)d\Omega \tag{A.4}$$

Radio astronomy sources are often approximated as blackbody radiators.

If we combine equations A.1, A.2 and A.3, the antenna temperature, T_A, can be shown to be

$$T_A = \frac{A_e}{\lambda^2}\int T_{br}(\theta,\phi)P(\theta,\phi)d\Omega \tag{A.5}$$

or

$$T_A = \frac{1}{\Omega_A}\int T_{br}(\theta,\phi)P(\theta,\phi)d\Omega \tag{A.6}$$

where Ω_A is the antenna beam area or beam solid angle. If the source is very small compared to the antenna beam pattern area then $P(\theta,\phi) \simeq 1$ (Kraus 1986). If the temperature of the radio source can be expressed as an average, T_{ave} , then the antenna temperature can be given by $T_A = \frac{\Omega_s}{\Omega_A}T_{ave}$ where,$\frac{\Omega_s}{\Omega_A}$ is called the beam filling factor (Condon & Ransom 2016, Kraus 1986). The combined temperature known as

the system temperature T_{sys} (Condon & Ransom 2016):

$$T_{sys} = T_{cmb} + T_{atm} + T_{spill} + T_{bg} + T_r \tag{A.7}$$

where T_{atm}, T_r, T_{spill} and T_{bg} are respectively: the temperatures of the atmosphere, the receiver, the spill-over (which arises from spill-over radiation that the feed picks up from beyond the edge of the reflector) and background radio sources. Root mean square (rms) is as follows:

$$\sigma_T \approx \frac{T_{sys}}{\sqrt{\Delta\nu_T}} \tag{A.8}$$

For an observation with $\Delta\nu\tau >> 1$, the voltage output is heavily smoothed (Condon & Ransom 2016). This implies that the telescope has to be calibrated, which leads to a discussion about the technique used for determining the aperture efficiency for the 26m HartRAO radio telescope at 6.7 and 12.2 GHz.

A.1.2 Single-dish observing techniques

The 26-m HartRAO radio telescope was used to observe the methanol maser source regions using the frequency switching technique. By adjusting the Local Oscillator (LO) frequency, the passband spectrum can be moved to the left or right using this method. It could fall within or outside of the receiver band. Total power is calculated as shown in equation A.9

$$TotalPower = [\frac{A_{N_{sig}} - A_{N_{ref}}}{A_{N_{ref}}}], \tag{A.9}$$

A.1.3 RCP and LCP of G188.95+0.89 Before Addition

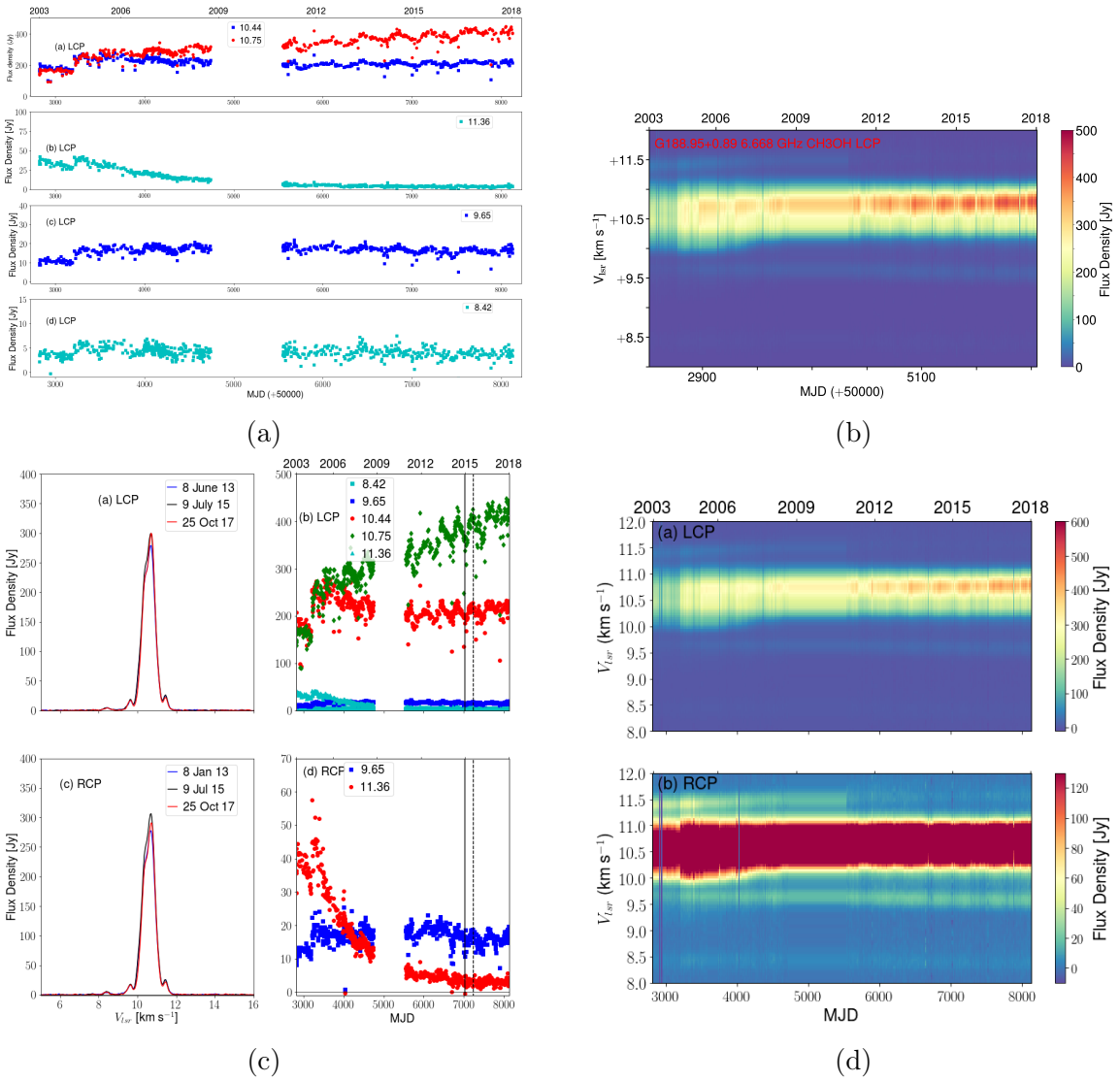

Figure A.1: Time series and dynamic spectrum of G188.95+0.89: (a) Top left panel: The time series in LCP, (b) Dynamic spectrum of the 6.7 GHz methanol masers linked with G188.95+0.89 LCP, (c) Bottom left panel: The time series in RCP and LCP before addition of the two, (d)Bottom right panel: Dynamic spectrum at LCP and RCP.

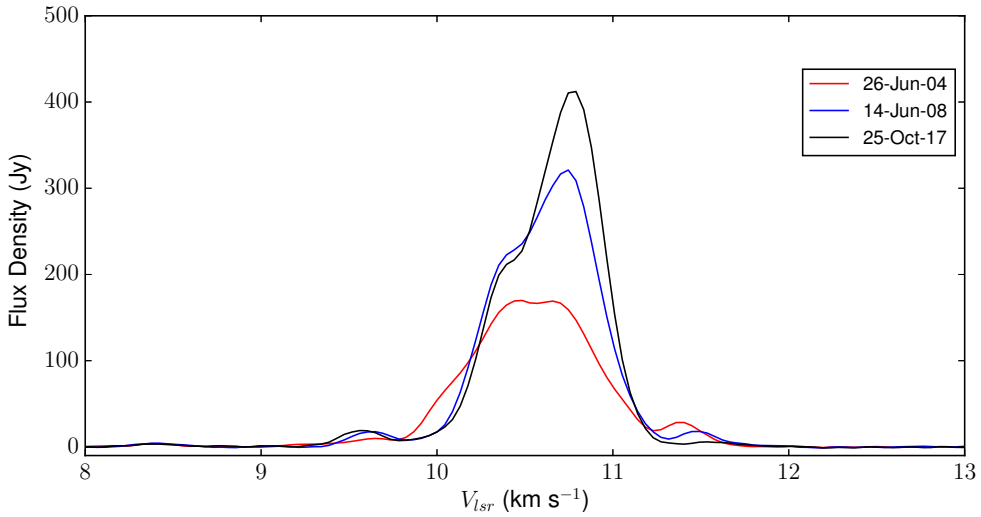

Figure A.2: LCP spectra.

A.2 FUNDAMENTALS OF INTERFEROMETRIC OBSERVATIONS

A.2.1 Baselines and U-V Coverage

When two or more telescopes are combined, the cross-correlation of voltages at the correlator results in interference patterns. The spatial coherence, also known as complex visibilities, is the cross-correlation of voltages at various regions. Phase and amplitude are also included in the visibilities. The placement and number of antennas in an array affect the source's visibility or u-v coverage. The coverage becomes more thorough and efficient as there are more baselines between antennas. When measuring distances on the ground rather than in the sky, a u-v plane is determined by the viewing wavelength λ, where u is measured from west to east and v is measured south to north, i.e:

$$u = (x_2 - x_1)/\lambda \tag{A.10}$$

$$u = (y_2 - y_1)/\lambda \tag{A.11}$$

Shorter baselines are preferable for resolving diffuse, extended sources while longer baselines will improve the resolution of a point source. At lower frequencies, radio interference, is produced by many devicesthat includes an unintended radio emissions from power lines, TV boosters, and other devices.

A.2.2 Sub-millimeter Instrumentation

The radio-wave portion of the electromagnetic spectrum contains the emission lines created by rotational transitions of numerous chemical species, which are our major diagnostic tool. The ALMA archives provided the interferometric data. With higher resolution, we can probe global features like the system tilt and the form of the gaseous envelope in addition to probing the velocity field in different parts of an object. The single-dish measurements complement the interferometric observations very well because, by simultaneously constraining the models with both types of observations, we ensure that our model is consistent with the facts on all explored spatial scales.

Cosmic light that oscillates between the radio and infrared spectrum can be studied by the ground-breaking ALMA radio telescope. Astronomers have been encouraged to detect this form of radiation for decades due to the fact that the Universe is filled with objects that release it. Water vapour in the atmosphere is a simple absorber of millimetre and submillimeter light. Water vapor in the atmosphere easily absorbs millimeter and submillimeter light. In Fig. A.3, the ALMA array is depicted

Figure A.3: ALMA array, in an extended configuration. Credit: ALMA (ESO/NAOJ/NRAO)

Astronomers may observe extremely far-off light that has been pushed towards the red end of the spectrum using ALMA's millimetre and submillimeter wavelengths as well as delve into the dense interiors of gas clouds to study the birth of stars and planets. ALMA functions as an interferometer, combining the signals from its array of antennas to create a single, enormous telescope the size of the entire array (Dent

2016).

A.2.3 Processing radio signals with the ALMA

An intricate chain of signal reception, conversion, processing, and recording begins with the ALMA front end equipment. Ten different frequency bands can be used to detect astronomical signals with this device. Any other system in use cannot compare to this one. The sensitivities of other radio telescopes all across the world are actually being improved by products produced from ALMA prototypes (Fomalont et al. 2014). Numerous components that are made in Chile, Europe, North America, and Eastern Asia make up the front end units.

Receivers, which are constructed in cartridges and are very simple to install or replace, will be housed in the cryostats. The Institut de Radio Astronomie Millim'etrique (IRAM) of France provided the required heated optics, windows, and infrared filters. The cryostats will have an operating temperature as low as 4 K (equivalent to -269°C).

A.2.4 Frequency bands of receivers

With all 10 receiver bands merged, the ALMA front end can detect signals with wavelengths ranging from 8.6 mm to 0.32 mm, or 35 GHz to 950 GHz in frequency. The characteristics of each ALMA receiver for science observations are shown in Table A.1 (as of Cycle 5). Figure A.4 illustrates a Band 6 receiver cartridge.

Table A.1: Specifications of individual ALMA receivers for science observation.

Band	Wavelength (mm)	Frequency (GHz)
1	8.57 - 6.00	035 - 050
2	4.48 - 3.33	067 - 090
3	3.57 - 2.59	084 - 116
4	2.40 - 1.84	125 - 163
5	1.84 - 1.42	163 - 211
6	1.42 - 1.09	211 - 275
7	1.09 - 0.80	275 - 373
8	0.78 - 0.60	385 - 500
9	0.50 - 0.42	602 - 720
10	0.38 - 0.32	787 - 950

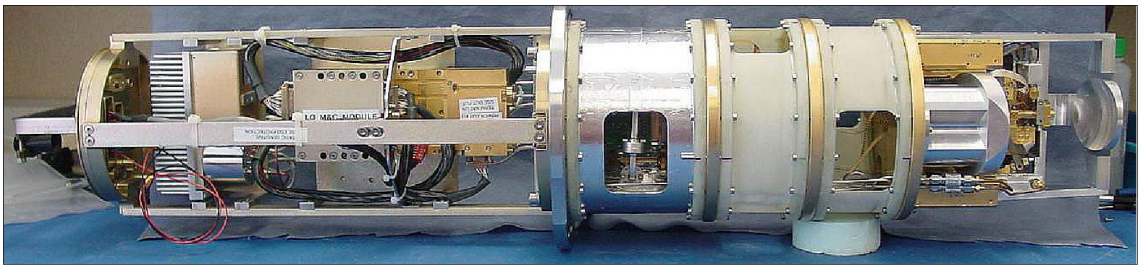

Figure A.4: Band 6, receiver cartridge. Credit: ALMA partnership (Ediss et al. 2004)

A.2.5 Zero Moment Maps of Some Detected Molecular Lines

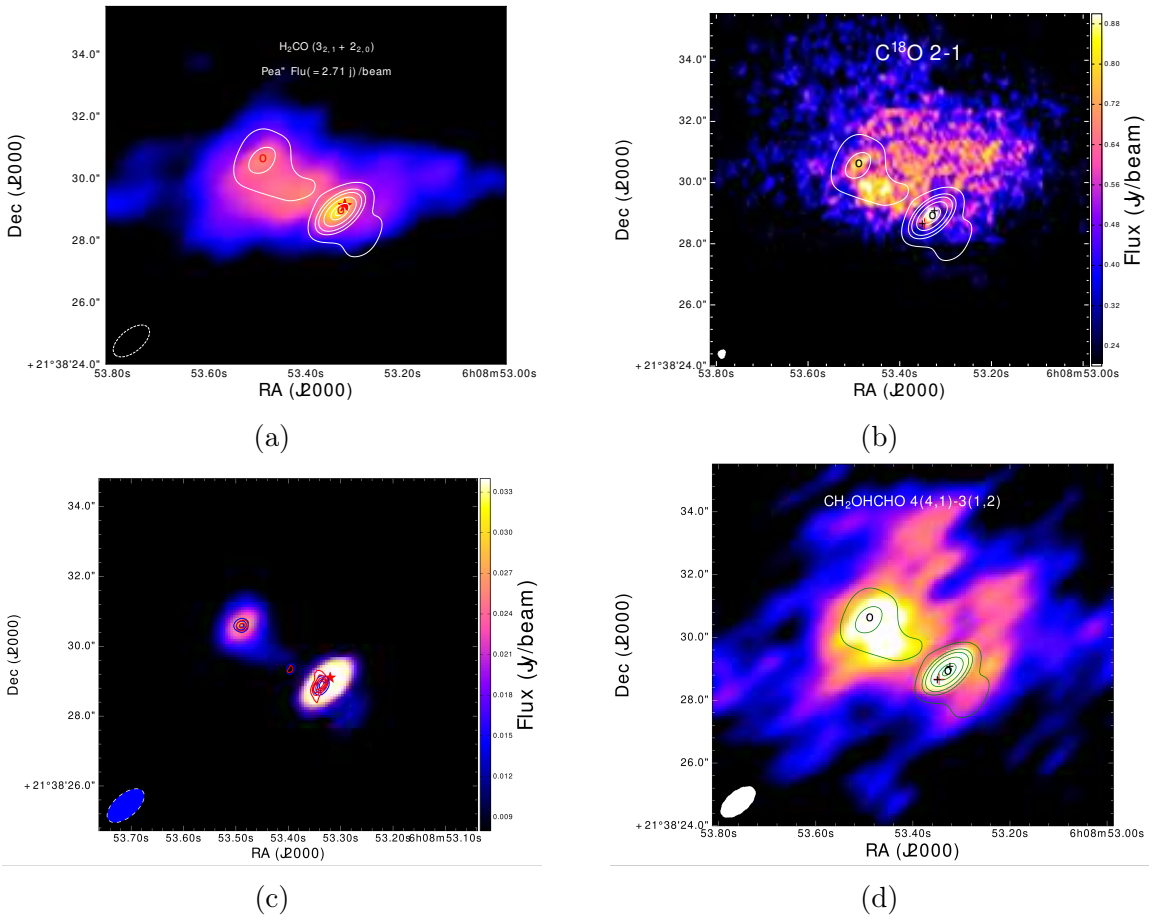

Figure A.5: (top) Zero moment maps of detected molecular lines with emission at high velocities. (a) Top left panel: Integrated map of H_2CO at 218.76 GHz, (b) Integrated map of ^{18}CO at 219.56 GHz (c) Bottom left panel: Integrated map of SiO at 217.104 GHz, (d) Bottom right panel: Integrated map of CH_2OHCHO at 231.76 GHz. The contours represent the dust continuum of which the contour levels are the same as in Fig. 4.9.

A.2.6 Spectra of Some Detected Molecular Lines lines

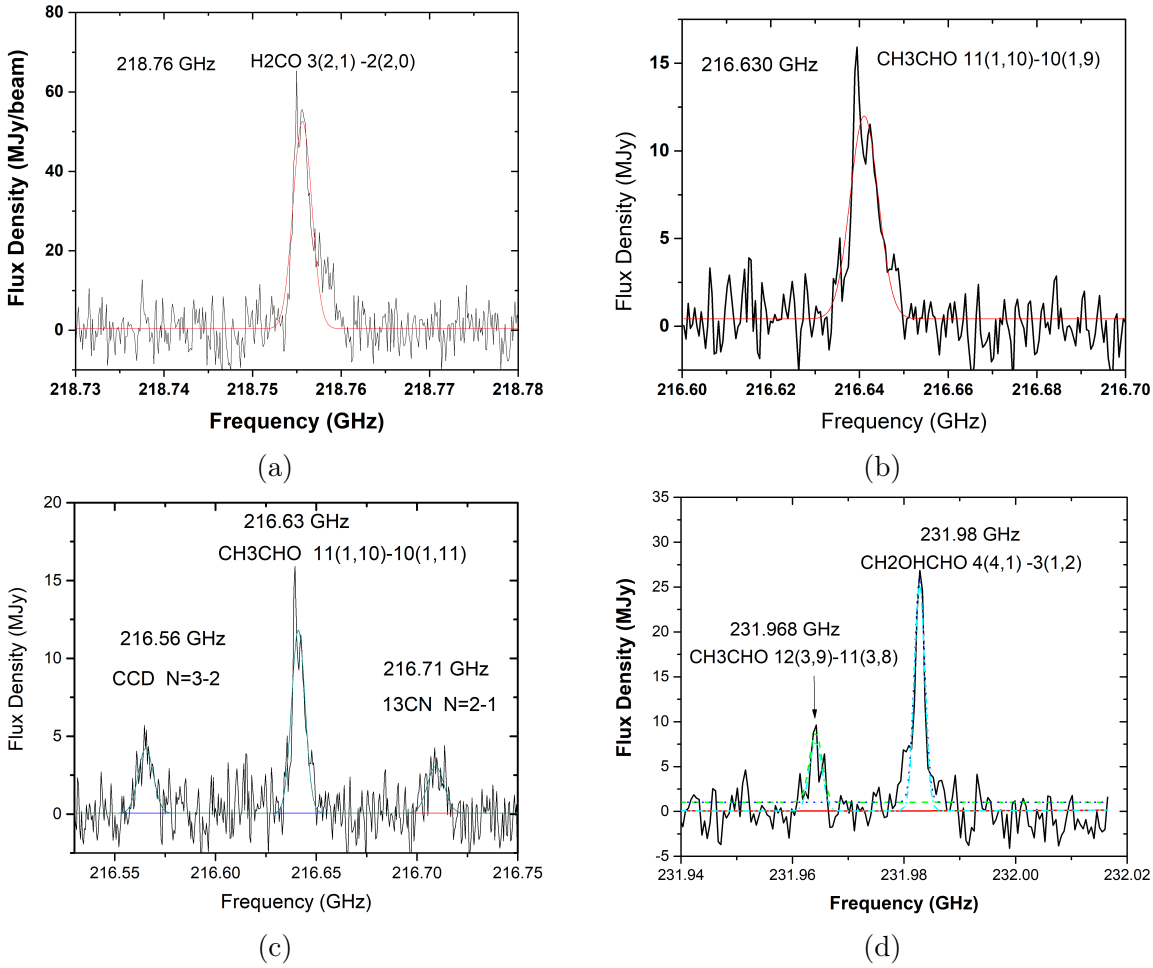

Figure A.6: Molecular line spectra that have been identified. The best-fit model's synthetic spectrum is shown in red, while the observed transitions are shown in black.

A.3 Publication-2019

Nuclear Activity in Galaxies Across Cosmic Time
Proceedings IAU Symposium No. 356, 2019
M. Pović, P. Marziani, J. Masegosa, H. Netzer, S. H. Negu & S. B. Tessema, eds.
doi:10.1017/S1743921320003543

14 years of 6.7 GHz periodic methanol maser observations towards G188.95+0.89

Martin M. Mutie[1,2], Paul Baki[1], James O. Chibueze[3,4] and Khadija El Bouchefry[5]

[1]Department of Physics, Technical University of Kenya, P. O. Box 52428-00200, Nairobi, Kenya

[2]Department of Physical Sciences, Chuka University, P. O. Box 109-60400, Chuka, Kenya

[3]Centre for Space Research, Physics Department, North-West University, Potchefstroom 2520, South Africa

[4]Department of Physics and Astronomy, University of Nigeria, Carver Building, 1 University Road, Nsukka, Nigeria

[5]South African Radio Astronomy Observatory, Rosebank, Johannesburg, South Africa
emails: martmulesh@gmail.com; paulbaki@gmail.com; james.chibueze@gmail.com and kelbouchefry@ska.ac.za

Abstract. We report the results of 14 years of monitoring of G188.95+0.89 periodic 6.7 GHz methanol masers using the Hartebeesthoek 26-m radio telescope. G188.95+0.89 (S252, AFGL5180) is a radio-quiet methanol maser site that is often interpreted as precursors of ultra-compact HII regions or massive protostar sites. At least five bright spectral components were identified. The maser feature at 11.36 km s^{-1} was found to experience an exponential decay during the monitoring period. The millimetre continuum reveals two cores associated with the source.

Keywords. ISM: individual (G188.95+0.89), ISM: molecules, stars: imaging.

Figure A.7: Publication-2019

.

A.4 Publication-2021

Monthly Notices of the ROYAL ASTRONOMICAL SOCIETY

MNRAS **00,** 1 (2021) https://doi.org/10.1093/mnras/stab1946
Advance Access publication 2021 July 9

Massive protocluster of a periodic maser source G188.95+0.89

M. M. Mutie [1,2★] J. O. Chibueze,[3,4] K. El Bouchefry [5], G. C. MacLeod,[6,7] J. Morgan [3] and P. Baki[1]

[1] *Department of Physics, Technical University of Kenya, P. O. Box 52428-00200, Nairobi, Kenya*
[2] *Department of Physical Sciences, Chuka University, P. O. Box 109-60400, Chuka, Kenya*
[3] *Centre for Space Research, Physics Department, North-West University, Potchefstroom 2520, South Africa*
[4] *Department of Physics and Astronomy, University of Nigeria, Carver Building, 1 University Road, Nsukka, 410001, Nigeria*
[5] *South African Radio Astronomy Observatory, Rosebank, Johannesburg, South Africa*
[6] *The University of Western Ontario, 1151 Richmond Street. London, ON N6A 3K7, Canada*
[7] *Hartebeesthoek Radio Astronomy Observatory, PO Box 443, Krugersdorp 1741, South Africa*

Accepted 2021 June 30. Received 2021 June 30; in original form 2021 March 30

ABSTRACT

We report the results of ongoing monitoring of the 6.7 GHz CH_3OH masers associated with G188.95+0.89. In these observations, five features are periodically varying and at least two exhibit evidence of velocity drifts. It is not clear the cause of these velocity drifts. The spectra have varied significantly since detection in 1991. The 11.45 km s^{-1} feature has decreased exponentially from 2003. Complementary ALMA 1.3-mm continuum and line observational results are also presented. Eight continuum cores (MM1–MM8) were detected in G188.95+0.89. We derived the masses of the detected cores. G188.95+0.89 MM2 was resolved into two continuum cores (separated by 0.1 arcsec) in ALMA band 7 observations. Also, CH_3OH ($4_{(2,2)}$-$3_{(1,2)}$) thermal emission associated with MM2 is double peaked. We propose the presence of multiple (at least binary) young stellar objects in MM2. SiO emission exhibits a bow-shock morphology in MM2 while strong emission of ^{12}CO at the east and west of MM2 suggests the presence of an east–west bipolar outflow.

Key words: masers – techniques: interferometric – stars: formation – ISM: individual objects: G188.95+0.89 – ISM: molecules – radio lines:stars.

Figure A.8: Publication-2021

.

A.5 Plagiarism Report

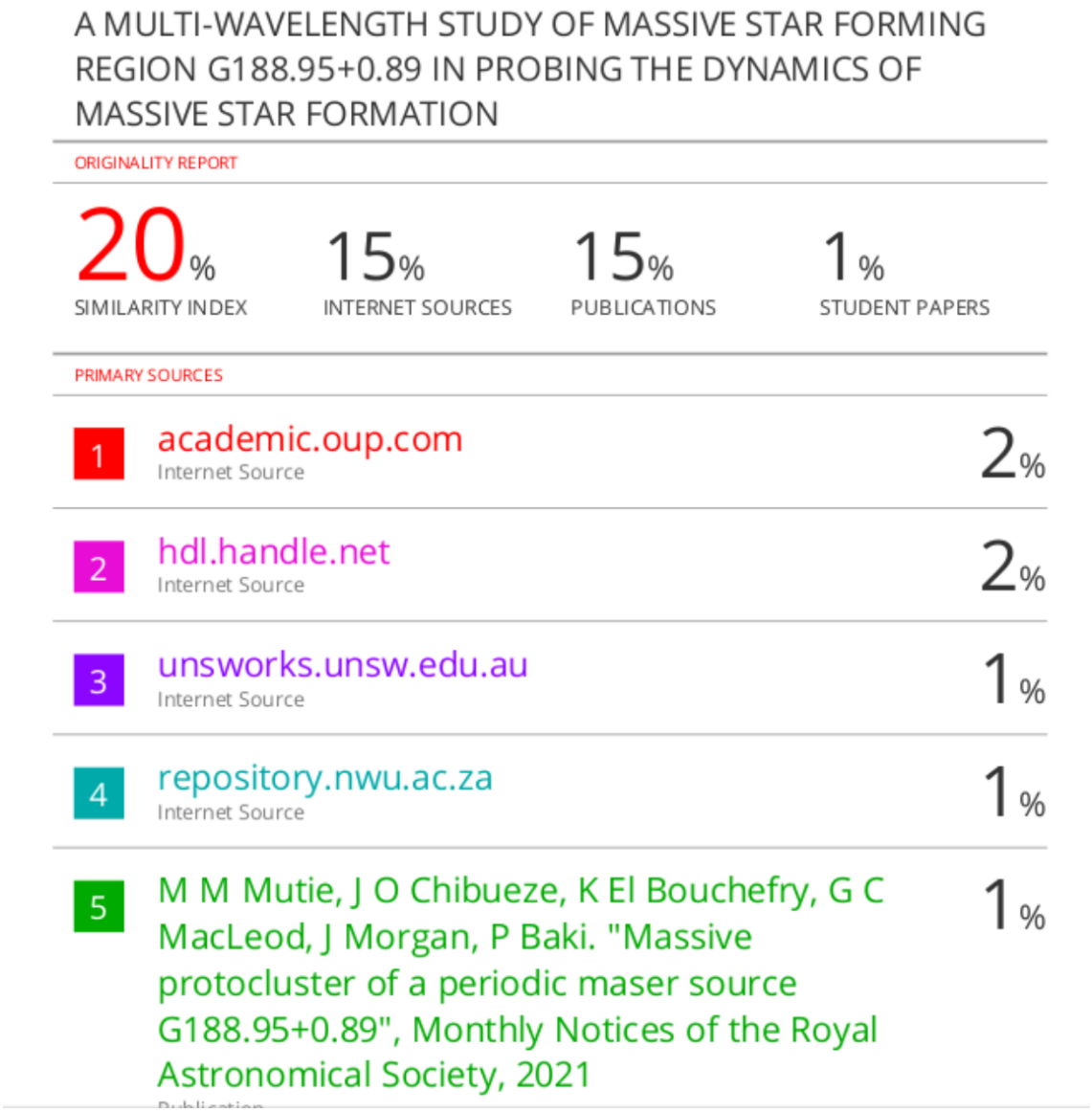
A MULTI-WAVELENGTH STUDY OF MASSIVE STAR FORMING REGION G188.95+0.89 IN PROBING THE DYNAMICS OF MASSIVE STAR FORMATION

ORIGINALITY REPORT

20%	15%	15%	1%
SIMILARITY INDEX	INTERNET SOURCES	PUBLICATIONS	STUDENT PAPERS

PRIMARY SOURCES

1	academic.oup.com Internet Source	2%
2	hdl.handle.net Internet Source	2%
3	unsworks.unsw.edu.au Internet Source	1%
4	repository.nwu.ac.za Internet Source	1%
5	M M Mutie, J O Chibueze, K El Bouchefry, G C MacLeod, J Morgan, P Baki. "Massive protocluster of a periodic maser source G188.95+0.89", Monthly Notices of the Royal Astronomical Society, 2021 Publication	1%

Figure A.9: similarity Report

.